

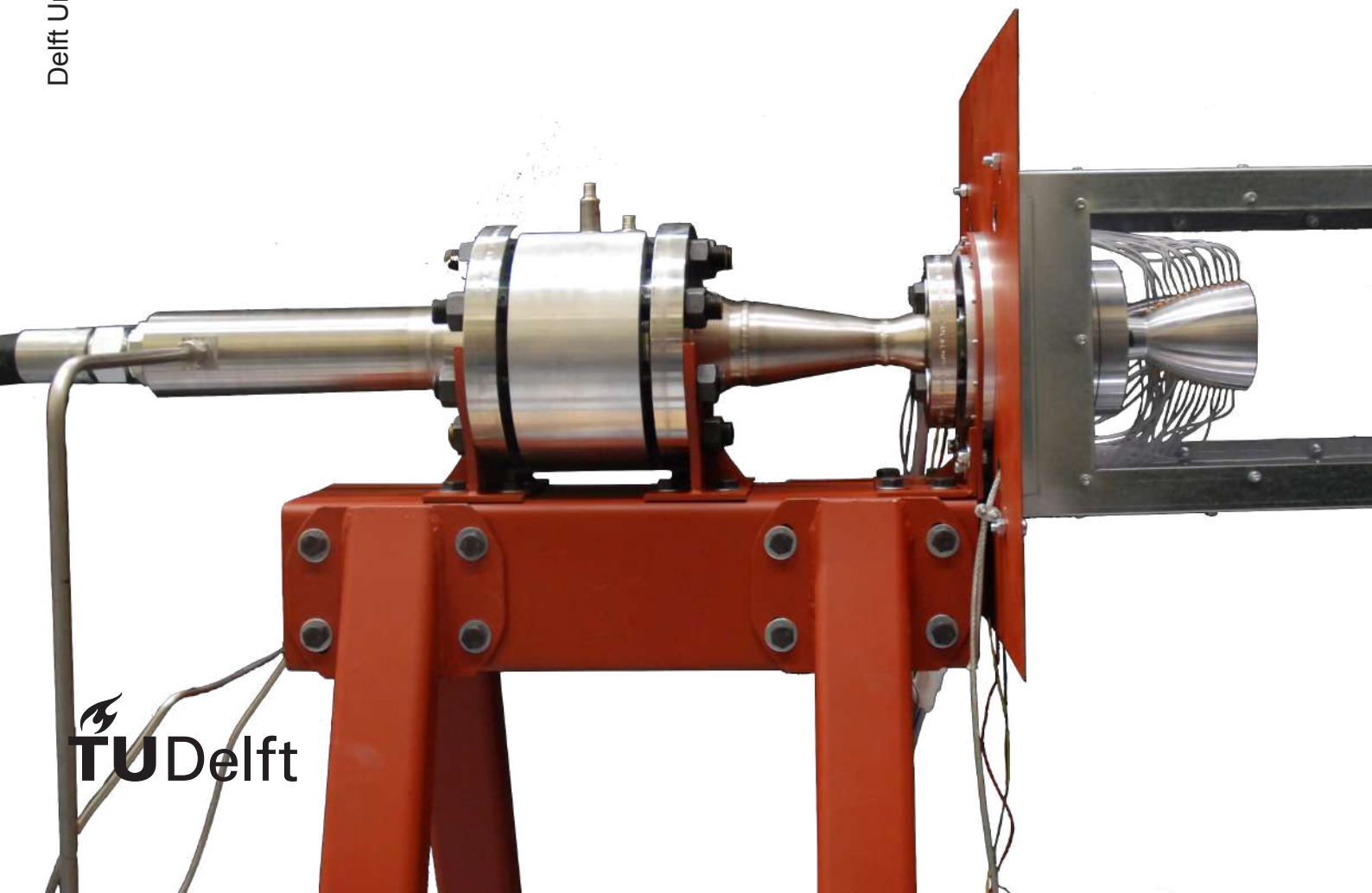
Master of Science Thesis

Development of a Rocket Nozzle Test Facility for Measurements of Fluid-Structure Interaction Phe- nomena

Krijn de Kievit

September 19, 2021

Delft University of Technology



Development of a Rocket Nozzle Test Facility for Measurements of Fluid-Structure Interaction Phenomena

Master of Science Thesis

by

Krijn de Kievit

Student number: 4441052
Thesis supervisors: Dr. ir. F. F. J. Schrijer TU Delft
Dr. ir. W. J. Baars TU Delft

An electronic version of this MSc. thesis report is available at <http://repository.tudelft.nl/>.

DELFT UNIVERSITY OF TECHNOLOGY
DEPARTMENT OF
AERODYNAMICS, WIND ENERGY AND FLIGHT PERFORMANCE AND PROPULSION

The examination committee certifies that the thesis project titled "*Development of a Rocket Nozzle Test Facility for Measurements of Fluid-Structure Interaction Phenomena*", submitted to the department of Flight Performance and Propulsion at the Aerospace Engineering faculty of the Delft University of Technology, in partial fulfilment for the award of the degree **Master of Science**, has been successfully completed by **Krijn de Kievit**.

Date: September 27, 2021

Committee Chair:

Dr. ir. B.W. (Bas) van Oudheusden

Supervisor:

Dr. ir. F.F.J. (Ferdinand) Schrijer

Supervisor:

Dr. ir. W.J. (Woutijn) Baars

Examiner:

Dr. A. (Arvind) Gangoli Rao

Abstract

Rockets are one of the most complicated machines ever built by mankind. A rocket uses extremely sophisticated engines in order to achieve the required velocity in order to stay in orbit around the Earth or another planetary body. Rockets normally consists of multiple stages, in order to optimise the amount of velocity that can be gained from a specific amount of propellant. The first stage, also known as the booster stage, does most of the work to put the later stages out of the Earth's atmosphere and into a horizontal ballistic trajectory. This means that the rocket engines on booster stages must be able to operate in varying atmospheric conditions, from the lighting of the engines at sea level to their shutdown close to the edge of space.

The exhaust of a rocket engine, known as a nozzle, is used to expel the gases burnt in the combustion chamber at the highest possible velocity. To achieve this, the gas is expanded along a carefully designed nozzle contour, where the velocity at the exhaust can reach up to Mach 5. The higher the degree of expansion, the larger the velocity of the gases and the higher the efficiency of the engine. However, it is not possible to expand the gas indefinitely, firstly because the nozzle would become extremely long and heavy, but secondly because the atmospheric pressure is pushing back on the exhaust gas, which is a problem only applicable to booster stage engines. Commonly, booster stage engines are designed such that the latter effect does not pose a problem at sea level, when the atmospheric pressure is highest. However, during the start-up of these engines, the pressure in the combustion chamber is still low, but the degree of expansion warranted by the contour of the nozzle is the same as for steady operational conditions, the high atmospheric pressure can cause the flow to separate on the inside of the nozzle wall. This separation causes a complex flow field and shock structure on the inside of the nozzle, which is asymmetric and can therefore cause significant loads on the nozzle in the direction perpendicular to the thrust force. These loads are commonly referred to as side loads.

The generation of side loads in stiff nozzles has been investigated since the 1960s, but never has the interaction between the deformation of a thin-walled nozzle and the flow structure during start-up been researched. This causes a large knowledge gap about the fluid-structure interaction inside the nozzle and its effect on the severity of the side loads, even though side loads in the past have caused significant damage to large rocket engines such as the space shuttle main engine [1] and the Vulcain engine. [2] Historically, this lack of knowledge has resulted in overdesigned nozzles, with higher mass than required. Moreover, design changes have been cancelled because of the unknown effect of the change in the structural properties of the nozzle on the severity of the side loads. This is why, for the current MSc. thesis research, a test setup to test flexible small scale nozzles has been built and data has been obtained on the fluid-structure interaction.

The purpose of this report is to describe the design process and the results from measurements on several different nozzles. Firstly, a short overview of the available literature is provided, of which a more elaborate description can be found in the literature survey connected to this research. [3] The design process resulted in a setup that can be used to test nozzles up to a total to atmospheric pressure ratio of 30, which is enough to capture the main phenomena related to side load generation. Moreover, the setup allows for the testing of flexible nozzles. These have been manufactured using SLA 3D printing, which allows for the printing of flexible resin materials. Using this setup, several different types of data can be obtained: (1) the longitudinal pressure distribution in a stiff nozzle at 15 points along 3 arrays each spaced 90 degrees apart around the circumference of the nozzle, (2) the lateral loads on the nozzle, (3) schlieren images in order to visualise the shock structure in the exhaust plume of the nozzle, (4) digital image correlation can be applied in order to track the deformation of the nozzle lip, such that vibrational modes and frequencies can be extracted and (5) particle image velocimetry can be used in order to extract 2D velocity field data of the exhaust plume flow.

Several tests with a stiff aluminium nozzle have proved that the setup can be operated safely and results in data that is similar to the data presented in literature. Thus, the setup has been validated to work correctly. Tests with flexible nozzles did not result in useful data since the vibrations were not representative of a real nozzle. However, it was shown that digital image correlation is an effective way of determining dominant modes which can provide great insight into the interaction between the fluid and the structure.

Contents

List of Figures	ix
List of Tables	xiii
1 Introduction	1
1.1 Research Objective and Questions	2
2 Literature Review	5
2.1 Fundamentals of Nozzle Flow	5
2.1.1 Ideal Nozzle Flow.	5
2.1.2 Shocks in Overexpanded Nozzles.	6
2.1.3 Shock Interactions and Reflections	7
2.1.4 Ideal and Parabolic Nozzle Contours	9
2.2 Flat Plate Shock Wave Boundary Layer Interaction	10
2.2.1 Interactions between Shocks and Boundary Layers	10
2.2.2 Unsteadiness in SWBLI	11
2.3 Flow Separation in Rocket Nozzles	12
2.3.1 Free Shock Separation.	12
2.3.2 Generalised Free Interaction Theory	13
2.3.3 Restricted Shock Separation.	15
2.3.4 FSS to RSS transition	16
2.3.5 Hysteresis Effects	17
2.3.6 Nozzle Exhaust Plume Flow	17
2.4 Nozzle Side Loads	19
2.4.1 FSS to RSS transition	19
2.4.2 Asymmetric Separation Line Model	22
2.5 Aeroelastic Effects	22
2.5.1 Deformation effects on nozzle flow	23
2.5.2 Structural Stability of Nozzle Eigenmodes	23
2.5.3 Stability of Higher Eigenmodes	25
3 Setup Design	29
3.1 Design Objective and Requirements	29
3.2 The TU Delft High Speed Laboratory Facility	30
3.3 Design Overview	31
3.4 Nozzle Design	32
3.4.1 Nozzle Contour Selection	32
3.4.2 Nozzle Sizing	34
3.4.3 Pressure Ports	36
3.5 Flexible Nozzle Design	38
3.5.1 Manufacturing	38
3.5.2 Material Selection	42
3.5.3 Structural Design	43
3.6 Fluid component design	46
3.6.1 Strain Tube	47
3.6.2 Settling chamber	49
3.6.3 Contraction and Diffuser	49
3.6.4 PIV tube.	51
3.6.5 Feed System	51

3.7	Structural Component Design	51
3.8	Electronic Component Design	53
3.9	Software Design	54
4	Measurement and Data Processing Methodology	57
4.1	Pressure, Temperature and Strain Measurements	57
4.1.1	Total Conditions.	57
4.1.2	Strain Gauges	58
4.1.3	Wall Pressure Measurements	59
4.1.4	National Instruments Modules	61
4.1.5	Data Post-Processing	62
4.2	Schlieren Imaging Setup	63
4.2.1	Working Principle.	63
4.2.2	Setup	64
4.2.3	Data Processing	65
4.3	Digital Image Correlation.	65
4.3.1	Setup	66
4.3.2	Data Processing	67
4.3.3	Modal Decomposition	70
4.4	Particle Image Velocimetry.	72
4.4.1	Working Principle.	72
4.4.2	Setup	75
4.4.3	Data Processing	78
4.5	Test Cases	80
5	Results	83
5.1	Aluminium Nozzle	83
5.1.1	Flow Development Analysis	83
5.1.2	Schlieren analysis	87
5.1.3	Velocity Fields	88
5.2	Flexible Nozzle Analysis	92
6	Conclusion and Recommendations	97
6.1	Design.	97
6.2	Conclusions from Experimental Results.	100
6.3	Research Objective	102
A	Additional Test Data	105
A.1	Pressure Data	105
A.2	Schlieren Data	111
A.3	PIV Data	113
A.3.1	NPR 10.52	113
A.3.2	NPR 16.42	115
A.3.3	NPR 22.21	116
A.3.4	NPR 24.48	117
A.3.5	NPR 25.98	118
A.4	DIC	120
A.4.1	NPR 2.07	120
A.4.2	NPR 7.88	121
A.4.3	NPR 8.66	122
A.4.4	NPR 9.55	123
A.4.5	NPR 9.81	124
B	Nozzle Parameters	125
B.1	Nozzle Wall Coordinates	125
B.2	Pressure Port Coordinates.	128

C	Sensor Calibration Data	129
C.1	Pressure Sensor	129
C.2	Strain Gauges	130
D	Technical Drawings	131
E	Test Procedures	153
	Bibliography	163

List of Figures

2.1	Simplified sketches of three different flow regimes in rocket engine nozzles [4]	7
2.2	Supersonic flow with a normal shock inside the divergent section of the nozzle [5]	8
2.3	Asymmetric lambda shock pattern in an overexpanded rocket nozzle [6]	8
2.4	Type 2 shock interaction [6]	9
2.5	Mach reflection [7]	9
2.6	Inverse Mach reflection [7]	9
2.7	Nozzle Contours	10
2.8	Inviscid strong shock wave interaction with boundary layer as suggested by Babinsky and Harvey [6]	11
2.9	Free Shock Separation inside a nozzle. [8]	12
2.10	Pressure distribution across separation shock in FSS [9]	13
2.11	Correspondence between experimental data and several separation criteria. Dotted = $1/M_i - 0.15$, dashed = Schmucker criterion (Equation 2.7), full = Stark criterion (Equation 2.8) [10]	14
2.12	Correlation function for generalised free interaction theory [11]	14
2.13	Schematic representation of restricted shock separation [8]	15
2.14	Pressure distribution during RSS [12]	16
2.15	Difference in axial location of separation and normal shock as a function of chamber pressure to nominal chamber pressure ratio [13]	16
2.16	Cap-shock pattern during start-up and shutdown, RSS occurs when the internal shock and reflected shock interact above the triple point (quadruple point is indicated) [14]	17
2.17	Flow patterns in the Vulcain engine during start-up [15]	18
2.18	Flow patterns in the RS-25 engine during start-up [16]	18
2.19	Comparison between simulation and HTV measurements of the cap-shock pattern [17]	19
2.20	Averaged side-load torque of a TIC and TOP nozzle during start-up [18]	20
2.21	Averaged side-load torque of a TIC and TOP nozzle during shutdown [18]	20
2.22	Dynamic response factor for the half-sine pulse	21
2.23	Dynamic response factor for the half-sine pulse [11]	22
2.24	Tepee formation during rocket engine start-up	23
2.25	Nozzle eigenmode shapes for bending loads [19]	23
2.26	Effect of wall deflection on pressure distribution and side loads in nozzle with separated flow [20]	24
2.27	Nozzle configuration for the first bending mode model [11]	25
2.28	Aeroelastic stability of the first bending mode for nozzles with different stiffness [21]	26
2.29	Wall displacement versus time for nozzles with different material properties [22]	26
3.1	Tank total pressure variation over 1 minute for different throat radii	31
3.2	Design Overview Schematic	32
3.3	PAR3 contour properties	34
3.4	J-2S nozzle contour and pressure distribution	35
3.5	Comparison of Schmucker load model with experimental data of the J-2S engine [23]	35
3.6	Average side loads for small-scale nozzle	35
3.7	Sound power for various rocket engines [24]	36
3.8	Separation location conditions with varying NPR according to Stark and Schmucker criteria	37
3.9	Dimensional nozzle contour and pressure distribution	38
3.10	Render of the nozzle design used by Tinney et al. The gray section is the flexible urethane-based nozzle. The blue section is the metal reinforcement around the throat section [25]	39
3.11	Shore hardness scale	40

3.12	Formlabs form 3 printer	41
3.13	Nozzle load case	45
3.14	Nozzle stresses for 5mm wall thickness	46
3.15	Assembly of flexible nozzle in nozzle clamp	46
3.16	Cut view of fluid components	47
3.17	Schematic of strain tube setup [26]	48
3.18	Design boundaries for diffusers [27]	50
3.19	PIV tube on the setup	51
3.20	Floor clamp block mechanism	52
3.21	Structural clamps in the setup	53
3.22	Schematic of electrical layout	54
3.23	NI LabView interface	54
4.1	Total condition sensors	58
4.2	Strain gauges	59
4.3	Nozzle pressure ports	60
4.4	ScaniValve 3217 pressure scanner (courtesy of Scanivalve)	61
4.5	Free interaction correlation curve fit to data obtained at NPR 24.03	63
4.6	Schematic of schlieren imaging setup	65
4.7	Schematic of the scheinpflug principle [28]	66
4.8	Schematic of DIC setup	66
4.9	Schematic of the plane camera model [29]	67
4.10	Perspective Transform on DIC images at NPR 2	68
4.11	Nozzle coordinate system	69
4.12	Intensity variation with radius from image centre	69
4.13	Lip detection for a section size of 2°	70
4.14	Mode shapes of different mode numbers	71
4.15	Schematic of planar PIV setup [30]	73
4.16	Schematic of PIV setup (top view)	76
4.17	Laser beam path	76
4.18	Lavision sCMOS imager looking at nozzle	76
4.19	Cyclone Seeder	78
4.20	Butterworth filtering of PIV images	79
4.21	Example of an instantaneous velocity field	79
5.1	Wall pressure contours for 5 minute ramp cases. The solid black line shows the separation point according to free interaction theory. The dotted black line shows the second degree polynomial fit and the dashed white line shows the separation point according to the Stark criterion	83
5.2	Separation location according to generalised free interaction correlation function fit, including second degree polynomial fit	85
5.3	Pressure distribution for varying NPR during increasing ramp at $\phi = 90$	85
5.4	Pressure distribution for varying NPR during decreasing NPR at $\phi = 90$	86
5.5	Pressure distribution for varying NPR close to FSS to RSS transition	86
5.6	Wall pressure contours at various azimuthal locations for different NPR values	86
5.7	Mean flow and fluctuations at NPR 23.84	87
5.8	Mean flow and fluctuations at NPR 24.65	87
5.9	Mean flow and fluctuations at NPR 25.03	87
5.10	Different flow conditions during FSS to RSS transition	88
5.11	Mean flow velocity components at NPR 16.42	89
5.12	Mean flow velocity components at NPR 22.21	89
5.13	Mean flow velocity components at NPR 24.48	89
5.14	Standard deviation of velocity components at NPR 16.42	90
5.15	Standard deviation of velocity components at NPR 22.21	90
5.16	Standard deviation of velocity components at NPR 24.48	90
5.17	Mach number contours at various NPR	91

5.18	Visualisation of nozzle flow at NPR 24.48	92
5.19	Estimated density, mass flux and mass flow distribution for a vertical plane at $x = 0$	93
5.20	Deformation over NPR ramp of flexible 80A 5 mm wall nozzle	93
5.21	Collapse of 3 mm elastic 50A nozzle	94
5.22	Collapse of 3 mm elastic 50A nozzle	94
5.23	Energy spectrum for 3 mm elastic 50A nozzle at various NPR	95
5.24	PSD for 3 mm elastic 50A nozzle at various NPR	95
6.1	Comparison between experiments from literature and current research data	101
6.2	Failure of the nozzle at NPR 10	102
A.1	NPR 14.83	105
A.2	NPR 23.84	105
A.3	NPR 24.23	105
A.4	NPR 24.65	105
A.5	Pressure distribution for varying NPR during increasing NPR for $\phi = 0$	106
A.6	Pressure distribution for varying NPR during increasing NPR for $\phi = 0$ compared to total pressure	106
A.7	Pressure distribution for varying NPR during decreasing NPR for $\phi = 0$	107
A.8	Pressure distribution for varying NPR during decreasing NPR for $\phi = 0$ compared to total pressure	107
A.9	Pressure distribution for varying NPR during increasing NPR for $\phi = 90$ compared to total pressure	108
A.10	Pressure distribution for varying NPR during decreasing NPR for $\phi = 90$ compared to total pressure	108
A.11	Pressure distribution for varying NPR during increasing NPR for $\phi = -90$	109
A.12	Pressure distribution for varying NPR during increasing NPR for $\phi = -90$ compared to total pressure	109
A.13	Pressure distribution for varying NPR during decreasing NPR for $\phi = -90$	110
A.14	Pressure distribution for varying NPR during decreasing NPR for $\phi = -90$ compared to total pressure	110
A.15	Mean flow and fluctuations at NPR 24.03	111
A.16	Mean flow and fluctuations at NPR 24.23	111
A.17	Mean flow and fluctuations at NPR 24.45	111
A.18	Mean flow and fluctuations at NPR 24.80	112
A.19	Normalised average velocity magnitude	113
A.20	Average Mach number	113
A.21	Normalised average horizontal velocity	113
A.22	Normalised average vertical velocity	113
A.23	Normalised standard deviation horizontal velocity	113
A.24	Normalised standard deviation vertical velocity	113
A.25	Vorticity in z direction	114
A.26	Streamlines	114
A.27	Normalised average velocity magnitude	115
A.28	Average Mach number	115
A.29	Vorticity in z direction	115
A.30	Streamlines	115
A.31	Normalised average velocity magnitude	116
A.32	Average Mach number	116
A.33	Vorticity in z direction	116
A.34	Streamlines	116
A.35	Normalised average velocity magnitude	117
A.36	Average Mach number	117
A.37	Normalised average velocity magnitude	118
A.38	Average Mach number	118
A.39	Normalised average horizontal velocity	118

A.40 Normalised average vertical velocity	118
A.41 Normalised standard deviation horizontal velocity	118
A.42 Normalised standard deviation vertical velocity	118
A.43 Vorticity in z direction	119
A.44 Streamlines	119
A.45 Energy Spectrum	120
A.46 Full PSD	120
A.47 Mode 0 PSD	120
A.48 Mode 1 PSD	120
A.49 Mode 2 PSD	120
A.50 Mode 3 PSD	120
A.51 Energy Spectrum	121
A.52 Full PSD	121
A.53 Mode 0 PSD	121
A.54 Mode 1 PSD	121
A.55 Mode 2 PSD	121
A.56 Mode 3 PSD	121
A.57 Energy Spectrum	122
A.58 Full PSD	122
A.59 Mode 0 PSD	122
A.60 Mode 1 PSD	122
A.61 Mode 2 PSD	122
A.62 Mode 3 PSD	122
A.63 Energy Spectrum	123
A.64 Full PSD	123
A.65 Mode 0 PSD	123
A.66 Mode 1 PSD	123
A.67 Mode 2 PSD	123
A.68 Mode 3 PSD	123
A.69 Energy Spectrum	124
A.70 Full PSD	124
A.71 Mode 0 PSD	124
A.72 Mode 1 PSD	124
A.73 Mode 2 PSD	124
A.74 Mode 3 PSD	124
C.1 Pressure sensor calibration curve	129
C.2 Horizontal strain calibration curve	130
C.3 Vertical strain calibration curve	130

List of Tables

3.1	Requirements	29
3.2	Parameters of nozzles used in transient investigations	33
3.3	Nozzle properties	36
3.4	Formlabs Form 3 printer specifications	41
3.5	Pugh chart to choose nozzle manufacturing option	42
3.6	Urethane properties used in experiments by Tinney et al. [25]	42
3.7	Formlabs printing materials	43
3.8	Validation of first natural frequency with data by Zhang et al. [22]	44
3.9	Settling chamber properties	49
3.10	Diffuser and contraction properties	50
4.1	Kyowa Strain gauge properties	59
4.2	Properties of various common seeding particle types [30]	74
4.3	PIV camera setup properties	77
6.1	Requirements	97
C.1	Pressure sensor calibration data	129
C.2	Strain gauge calibration data	130

Nomenclature

Acronyms

EER	End-Effect Regime
FSI	Fluid Structure Interaction
FSS	Free Shock Separation
HTV	Hydroxyl Tagging Velocimetry
IMR	Inverse Mach Reflection
NASA	National Aeronautics and Space Administration
NPR	Nozzle Pressure Ratio
PIV	Particle Image Velocimetry
pRSS	Partial Restricted Shock Separation
qRSS	Quasi-Restricted Shock Separation
RSS	Restricted Shock Separation
SWBLI	Shock Wave Boundary Layer Interaction
TIC	Truncated Ideal Contour
TOP	Thrust Optimized Contour

Roman Symbols

\bar{p}	Mean pressure	Pa
\dot{m}	Mass flow rate	kg/s
A	Area	m^2
a	Speed of sound	m/s
C_f	Shear stress coefficient	–
E	Young's modulus	Pa
e	Euler's number ≈ 2.718	–
F	Force	N
F	Free interaction theory correlation function	–
f	Frequency	Hz
I	Current	A
K	Gladstone-Dale constant	m^3/kg
k	Spring constant	N/m
L	Upstream influence length	m

M	Mach Number	–
n	Number of samples	–
p	Pressure	Pa
p'	Pressure fluctuation	Pa
q	Dynamic pressure	Pa
R	Specific gas constant	$J/kg/K$
r	Radius	m
R_d	Deformation response factor	–
Re	Reynolds number	–
St	Strouhal number	–
T	Temperature	K
t	Time	s
v	Velocity	m/s

Greek Symbols

β	Shock angle	deg
η	Efficiency	–
γ	Specific heat ratio	–
ν	Kinematic viscosity	m^2/s
ν	Prandtl-Meyer angle	deg
Ω	Coupled natural frequency	Hz
ω	Mechanical natural frequency	Hz
Ω_{nd}	Non-dimensional mechanical natural frequency	–
ϕ	Circumferential angle	deg
ϕ	Flow direction angle	deg
ρ	Density	kg/m^3
σ	Standard deviation	Pa
τ_n	Natural Period	s
θ	Flow deflection angle	deg
θ	Nozzle bending deflection angle	deg
ζ	Damping ratio	–

Subscripts

∞	Free stream
*	Nozzle throat
a	Aerodynamic

a	Ambient
c	Combustion chamber
cr	Critical
e	Nozzle exit
i	Incipient
m	Mechanical
max	Maximum
min	Minimum
NS	Normal Shock
p	Plateau
p	Pulse
sep	Separation
sl	Side load
st	Static
T	Thrust
t	total
w	Wall
x	axial location

Preface

All rocket engines use a nozzle to accelerate the combustion gases to supersonic speed at the nozzle exit. The higher the exhaust velocity, the higher the performance of the engine will be. This why the design of nozzles has been studied extensively over the past 80 years. During start-up and shutdown of a rocket engine, when the pressure in the combustion chamber is low, the flow on the inside of the nozzle wall can separate, causing lateral loads. A lack of understanding about the interaction between the deformation of the nozzle and the internal flow structure has lead to nozzles being designed with conservative design rules, resulting in increased nozzle mass. In order to design more light-weight nozzles, this interaction first needs to be understood.

This report presents the results of the development of a test setup at the Aerospace Engineering faculty at the Delft University of Technology, which allows for the testing of this fluid-structure interaction in small scale nozzles. I performed this research as part of my Master thesis, in order to obtain a Master's degree in Aerospace Engineering. After 6 years, the completion of this report is a significant milestone in the road to becoming an aerospace engineer. This road has been tough, and was not made easier by the appearance of the COVID 19 pandemic, but through my own perseverance and the help of many others I have managed to complete the program mostly within the set time.

Firstly, I would like to thank my supervisors, Dr. ir. F.F.J. Schrijer and Dr. ir. W.J. Baars, for their support and guidance during the entire research project. Without their support, the design of the setup would have been of much lower quality, while the extracted data would have been much less valuable. Moreover, the fact that both of them were extremely approachable made me feel part of the aerodynamics lab even though I had to do most of the work remotely. I am sure they will guide future students as well as they guided me in order to use this setup to gain knowledge in this field.

Secondly, I would like to thank the technical support staff at the high speed laboratory: Henk-Jan, Frits, Dennis, Peter and Nico. They helped me countless times with problems ranging from the design of the software to the installation of components to the critical safety assessment of the design. I also want to thank Giulio Dacome who, as a new PhD. candidate helped me set up the PIV system and assisted in taking the PIV measurements, which I could not have performed without him.

Thirdly, I would like to thank my girlfriend Iona, my friends and family, who have all been continuously supportive of my academic career and without whom I would not be the person I am.

The finalisation of this report brings me close to the end of a long period in my life in which learning was a central part. Now, I will start a new phase in which it is finally time to apply this knowledge to real-world problems. As Elon Musk says, you must wake up in the morning and be excited about the future, and this prospect definitely makes me excited for what is to come.

Krijn de Kievit
September 19, 2021

1

Introduction

Rockets are one of the most complicated machines ever built by humanity. Arguably, the rocket engines are the most complicated part of the entire rocket. A rocket engine basically consists of a propellant provision system, a combustion chamber and a supersonic exhaust nozzle. The current research focuses on the latter, specifically its aerodynamic performance during start-up and shutdown of the rocket engine.

The purpose of a nozzle is to accelerate the gases coming from the combustion chamber to the highest possible velocity before reaching the nozzle exit. The reason for this is encapsulated in the most famous equation in rocketry, the rocket equation:

$$\Delta v = v_e \ln \frac{m_i}{m_f}$$

This states that the change in the rocket velocity Δv , is directly proportional to the velocity of the combustion gases at the nozzle exhaust, also known as the exhaust velocity v_e . Another conclusion that can be drawn from this equation is that the largest velocity is changed when the ratio of starting mass m_i over mass after the engines burn out m_f is maximised. In other words, the rocket should lose as much mass, in the form of propellants, as possible during the time the engines burn, and the left over mass afterwards should be as small as possible. This is why the minimisation of structural mass is an important design factor in rockets, and also for nozzles.

The velocity of the combustion gases at the nozzle exit are a function of its shape and the ratio between the pressure in the combustion chamber and the ambient pressure. Another important consideration, the thrust of the engine, is maximised when the pressure of the gases at the exit of the nozzle are equal to the ambient pressure. Since the rocket is moving through the atmosphere during ascent, the ambient pressure is not constant, which means engineers have to decide the optimal point in the flight at which the exit pressure is equal to the ambient pressure. For rocket engines that have to operate at sea level, as well as at higher altitudes - which is typically the case for engines on booster stages of rockets - engines are generally optimised for relatively low ambient pressure, because of the specific trajectory of the rocket to orbit. During start-up and shutdown at sea level conditions, when the pressure in the combustion chamber ramps up from ambient to nominal operating pressure, the flow in the nozzle can experience extreme adverse pressure gradients for low combustion chamber pressures. This can cause flow separation inside the nozzle.

Asymmetric flow separation can cause significant structural loads, especially in the direction perpendicular to the thrust force, also known as side loads. These loads are transferred into the gimbal structure, which attaches the engine to the rocket, which means they can also be transferred all the way to the payload on top of the rocket. These loads are generally not steady, but instead cause severe vibrations, which have on some occasions lead to catastrophic failure of the engine. For example, during a test of the J-2S rocket engine, the engine broke off from its gimbal structure. [31] In another event, a propellant line running down the nozzle of the space shuttle main engine (SSME) was damaged. [1]

More recently, the European Vulcain engine [2] and the Japanese LE-7A engine [32] also experienced problems regarding these side loads.

Several solutions exist to address the problem of side loads. The most simple and obvious one is to design the nozzle such that it can withstand the side loads. However, this is easier said than done. Because of the complicated interactions between the exhaust gases and the structure, as well as the unsteady nature of turbulent boundary layer separation and shock wave boundary layer interaction, it is extremely hard to predict the side load magnitude for a specific nozzle design. Moreover, small scale tests generally do not accurately represent the loads observed in full scale engines. [2] Thus, the only way to determine the side load magnitude is to perform a full scale engine test. Since these tests are extremely costly, they are only performed at the last stages of the design process, when significant design changes to the nozzle are no longer possible. In practice this means that relatively high safety factors must be used in the structural design of the nozzle, which increases the mass.[33] Another solution would be to change the nozzle shape during the flight, but this would require an incredibly complicated mechanical system, which is likely very expensive and potentially unreliable.

The development of new engines for NASA's Space Launch System (SLS) and the European Ariane 6 rocket has sparked renewed interest in the flow structure in rocket nozzles during start-up and shutdown, and much numerical and experimental research has been published. [10, 22, 34, 35] The problem with most of the research, especially experimental, is that a stiff nozzle is used. Therefore, only fluid mechanics phenomena can be observed in these tests, while in reality nozzles are not particularly stiff and change shape during operation, and especially during start-up. Moreover, very little quantitative 1D and 2D velocity field data has ever been collected in experiments, which means that numerical research has very limited data to be validated.

In order to address this problem, it is decided that the Aerospace Engineering faculty should have its own nozzle testing facility, in which the knowledge about stiff nozzle flow can be used to test flexible nozzles to better observe and understand the fluid structure interaction during nozzle start-up and shutdown. Moreover, the affinity of the faculty with quantitative velocity field measurement techniques, specifically particle image velocimetry (PIV), allows for the best possible conditions to obtain quantitative field data.

This thesis report described the design process of the nozzle test setup and shows some of the data collected during initial tests. First, a short summary of the available literature is provided in chapter 2. Next, the design of the test setup is described in chapter 3. The data analysis methodology and results are described in chapter 4 and chapter 5. Finally, the conclusion is presented in chapter 6.

1.1. Research Objective and Questions

The objective of the research is defined as follows

The objective of this research is to build a nozzle test setup to be able to determine the effect of the stiffness of a rocket engine nozzle on the amplification of aerodynamic side loads due to fluid-structure interaction, while also providing critical validation data for numerical flow simulations on flexible rocket engine nozzles. This will be done by performing experiments on several flexible nozzles.

Based on this objective, several research questions have been posed

1. What is the performance of a stiff nozzle in this test setup?
 - (a) How does the flow development for a fixed shape nozzle compare to literature?
 - (b) At what NPR does FSS to RSS transition occur for this nozzle?
 - (c) To what extent is the separation and transition asymmetric?
 - (d) What does the velocity field look like during FSS?
 - (e) What does the velocity field look like during RSS?

-
- (f) How do PIV velocity fields compare to CFD simulations and other experimental data?
2. What is the best manufacturing method for flexible nozzles?
 3. What is the performance of a flexible nozzle in this test setup?
 - (a) At what NPR are vibrations present?
 - (b) At what NPR are vibrations most prevalent?
 - (c) What modes are dominant in nozzle vibrations?
 - (d) How does the frequency of dominant modes vary with NPR?
 - (e) How does the PIV tube affect nozzle vibrations?
 - (f) How does nozzle stiffness affect dominant mode frequencies?

2

Literature Review

This chapter presents a short overview of the available literature on the topic of nozzle fluid and structural dynamics during start-up and shutdown. A more elaborate review of literature is presented in the literature survey report associated with this research. [3]

2.1. Fundamentals of Nozzle Flow

Before elaborating on the more complicated flow physics of separation and side load generation in supersonic rocket nozzles, it is important to shortly discuss the fundamental, idealised flow model and some of the shock structures present in supersonic nozzles. Moreover, two types of nozzle contours important to this research are discussed.

2.1.1. Ideal Nozzle Flow

This model describes the flow in supersonic nozzles to incredible accuracy – about 1 to 6% error – considering the simplicity of the mathematics. The assumptions made in this model are listed in the literature survey [3]. Most importantly, it is assumed that the flow is isentropic and homogeneous, which is obviously not the case in the presence of a shock system in the nozzle. Nevertheless, the isentropic flow equations still allow for accurate calculation of thermodynamic conditions up to the location of the first shock.

Supersonic nozzles, also known as De Laval nozzles, consist of a converging section, a throat section, and a diverging section. In the converging section, the cross-sectional area of the nozzle decreases, while in the diverging section the nozzle cross-sectional area increases. The location of minimum area, right between the converging and diverging section, is known as the throat, with area A^* .

The nozzle is fed with air from a high-pressure section upstream of the nozzle, known as the settling chamber. Here, the flow velocity is practically zero, which means that the total thermodynamic conditions are equal to the static ones. The conditions at the throat are determined by the total conditions in the settling chamber. If the nozzle pressure ratio (NPR), which is defined as the ratio between the total pressure in the settling chamber and the ambient pressure at the exit of the nozzle, exceeds the critical pressure ratio, which for air is equal to 1.894, the flow at the throat and diverging section of the nozzle becomes supersonic. In the case of a supersonic nozzle, the Mach number at the throat is always equal to unity.

When the Mach number at the throat becomes equal to unity, pressure waves from downstream of the throat cannot travel upstream of the throat, such that information about downstream pressure cannot be communicated to the settling chamber. This condition is known as choked flow, and it defines the maximum mass flow rate through the nozzle. The mass flow can be calculated using

$$\dot{m} = A^* p_c \gamma \sqrt{\frac{\left(\frac{2}{\gamma+1}\right)^{\frac{\gamma+1}{\gamma-1}}}{\sqrt{\gamma R T_c}}} \quad (2.1)$$

It can be seen that the mass flow of the nozzle is directly proportional to the throat area and settling chamber pressure p_c . This fact is important in the design of the nozzle for the current research because the size of the nozzle therefore influences the maximum run-time of the setup. Moreover, the mass flow directly influences the thrust generated by the nozzle through

$$F_T = \dot{m} v_e + (p_e - p_a) A_e \quad (2.2)$$

where v_e is known as the exhaust velocity. The thrust determines the loads on the setup and therefore is also an important factor to consider. Sutton [4], states that the maximum thrust is achieved when the pressure at the exit of the nozzle, p_e , is equal to the ambient pressure p_a . The reason for this is elaborated upon in the literature review. [3] In this condition the nozzle is said to be optimally expanded. In case of supersonic flow, it is possible that the pressure at the nozzle exit is however not equal to the ambient pressure.

The pressure at the exit of the nozzle is fully determined by the conditions in the settling chamber, and the nozzle shape, most importantly the ratio between the area at the exit of the nozzle and the throat area. This ratio is also known as the nozzle expansion ratio ϵ .

$$\frac{A^*}{A_e} = \left(\frac{\gamma+1}{2}\right)^{\frac{1}{\gamma-1}} \left(\frac{p_e}{p_c}\right)^{\frac{1}{\gamma}} \sqrt{\frac{\gamma+1}{\gamma-1} \left(1 - \left(\frac{p_e}{p_c}\right)^{\frac{\gamma-1}{\gamma}}\right)} \quad (2.3)$$

Where the pressure ratio p_e/p_c is determined by the exit Mach number through the isentropic flow equation

$$\frac{p_e}{p_c} = \left(1 + \frac{\gamma-1}{2} M_e^2\right)^{-\frac{\gamma}{\gamma-1}} \quad (2.4)$$

In the case that the pressure at the exit of the nozzle is lower than the ambient pressure, the nozzle is said to be overexpanded. In this regime, shock waves are required to adapt the pressure at the exit of the nozzle to the ambient. This regime occurs when the ambient pressure is high, when the rocket is on the launch pad and during the initial phase of the flight. If the pressure difference is too large, the flow might separate from the nozzle walls because of the extreme adverse pressure gradient. Flow separation is the cause of extreme lateral loads on the nozzle structure, and therefore this flow structure is researched in this thesis. Normally, nozzles are designed such that during nominal operation, when the pressure in the settling chamber is high, no flow separation occurs. However, during start-up and shutdown of the engine, when the pressure in the settling chamber is still sub-nominal, flow separation can occur.

Figure 2.1 shows simplified sketches of all nozzle flow regimes. On the left-hand side, the flow regime at a specific altitude is depicted. The right-hand side shows the flow regime of the same nozzle at sea level. This would happen during static hot fire tests or at lift-off of the rocket. Rocket nozzles that have to operate in sea level, as well as vacuum, are normally of the type shown in the bottom row of the figure. The space shuttle RS-25, and Ariane V Vulcain engines, are examples of engines that belong in this category. For example, the RS-25 has an area ratio of 77.5, but the high pressure in the settling chamber in nominal operation prevents the flow from separating during high ambient pressure conditions.

2.1.2. Shocks in Overexpanded Nozzles

As stated before, nozzles are generally overexpanded at sea level. During start-up and shutdown, the NPR experiences a transient, which in the case of start-up is increasing, while during shutdown it is decreasing. The case of the start-up transient is used to describe the process of flow development.

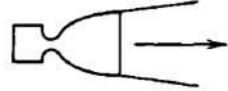

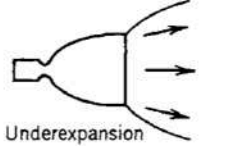
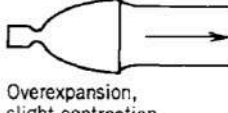
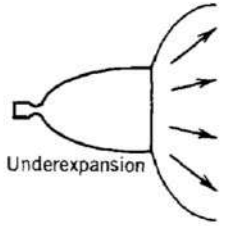
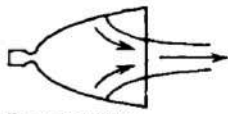
Stage	A_2/A_t	During flight		During sealevel static tests			
		$h(\text{km})$	$I_s (\text{sec})$	$h(\text{km})$	$I_s (\text{sec})$		
Booster or first stage	6		0	267		0	267
		Nozzle flows full, slight underexpansion			Nozzle flows full		
Second stage	10		24	312		0	254
		Underexpansion			Overexpansion, slight contraction		
Third stage	40		100	334		0	245
		Underexpansion			Flow separation caused by overexpansion		

Figure 2.1: Simplified sketches of three different flow regimes in rocket engine nozzles [4]

The ideal picture, which is illustrated by many textbooks [5, 36, 37], is one where the nozzle is initially fully subsonic, and becomes supersonic when the critical nozzle pressure ratio is reached. In this overexpanded state, a normal shock running from wall to wall, perpendicular to the flow direction, is present inside the nozzle to adapt the pressure of the flow to the ambient pressure. This shock moves downstream with increasing NPR and eventually moves outside of the nozzle. When a normal shock is no longer required, an annular oblique shock appears until the nozzle becomes optimally expanded.

A schematic representation of a normal shock present in the divergent section of the nozzle is shown in Figure 2.2. It is important to note that the representation of the shock gives the impression that the normal shock runs from one wall to the other.

In reality, a much more complicated shock structure appears inside overexpanded nozzles, as shown in Figure 2.3. This is mainly the result of the presence of the boundary layer in real cases, compared to the idealised model. The normal shock is still present, but interacts with the boundary layer, which can cause it to separate. The flow separation causes an oblique shock wave, which itself interacts with the normal shock wave. These interactions are unsteady and generally asymmetric, which makes them the main drivers for side loads in rocket nozzles. They are discussed in more detail in section 2.2.

2.1.3. Shock Interactions and Reflections

Two important shock phenomena to consider in the current study are shock interactions and shock reflections. Shock interactions involve the combination of two shocks, while shock reflections involve only one shock and a wall.

Edney [38] defines a total of six different types of shock-shock interactions. These shocks are governed by the $\theta - \beta - M$ relations, presented in the literature survey. [3] A graphical representation of these equations, known as a shock polar diagram, is a convenient way to display the behaviour

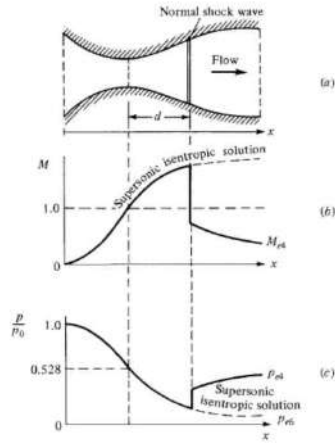


Figure 2.2: Supersonic flow with a normal shock inside the divergent section of the nozzle [5]

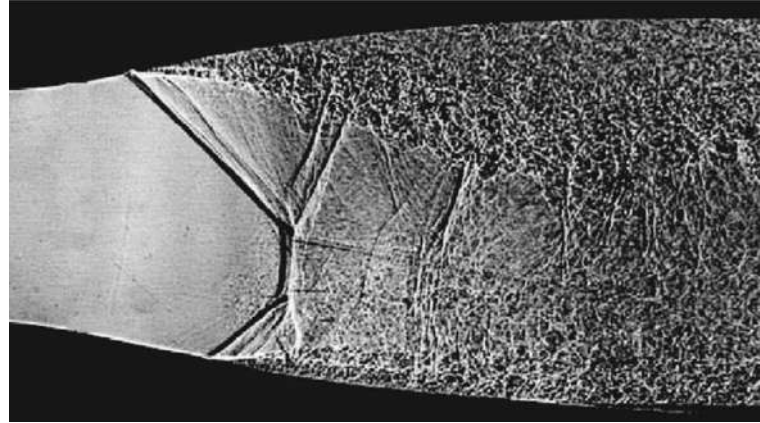


Figure 2.3: Asymmetric lambda shock pattern in an overexpanded rocket nozzle [6]

of shocks. A polar diagram shows the pressure jump across the shock on the vertical axis, and the flow angle on the horizontal axis. This plane is also known as the hodographic plane. For a specific upstream state p_1 and ϕ_1 , the polar represents all the possible downstream states. The shape of the polar depends on the upstream Mach number and the specific heat ratio γ through the characteristic equation.

$$v \pm \phi = \text{constant} \quad (2.5)$$

A shock can be represented as a jump from one location on the polar to another. The maximum amount of flow turning that can be achieved by an oblique shock is shown as the maximum flow angle on the polar. The polar representation is convenient because two parallel flows separated by a slip line occupy the same point on the diagram, since a slip line must have the same pressure and flow direction on either side. This fact can be used when determining the shock strength in case it is known that a specific region should have equal pressure and flow direction.

A type 2 shock interaction is most relevant in the current discussion. Its physical representation and shock polar are shown in Figure 2.4. In this case the strength of the oblique shocks C_1 and C_2 is so severe, that no overlap between their characteristic curves exists. In this case, a normal shock C_5 occurs around the centre line of the nozzle, also known as the Mach disk.

Two types of shock reflections exist, namely regular and Mach reflections. Regular reflections are the simplest kind of shock reflections, but generally do not occur in rocket nozzles. As explained by Mouton [7], in a regular reflection the reflected shock turns the flow the same amount as the incoming shock. In a channel with one side being a solid wedge this means that the incoming shock turns the flow to be parallel to the wedge, while the reflected shock turns the flow back to be parallel to the straight wall.

A Mach reflection, shown in Figure 2.5, occurs when the reflected shock has to turn the flow by more than the maximum flow angle ϕ_{\max} . In a polar representation this means that the characteristic of the reflected shock does not intersect the $\phi = 0$ axis. In this case a normal shock, or Mach Stem, is formed, with a curved almost normal shock originating from the wall. This reduces the flow turning required by the reflected shock, which can then be accommodated. It can be noted that the slip line behind the triple point is pointed towards the wall, causing an acceleration of the subsonic flow near the wall. Another type of Mach reflection, known as an inverse Mach reflection, shown in Figure 2.6, occurs when the Mach stem is curved upstream, meaning that the flow downstream of the triple point is inclined away from the wall. Hagemann et al. [18] suggest that the inverse Mach reflection is one of the main factors in side load generation in rocket nozzles, as discussed further in section 2.4.

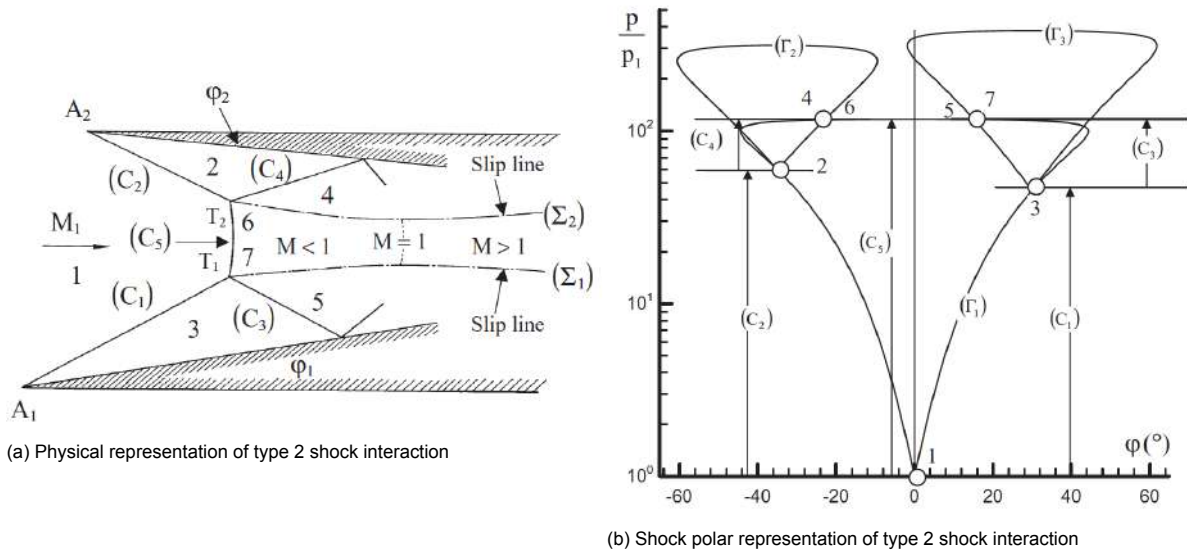


Figure 2.4: Type 2 shock interaction [6]

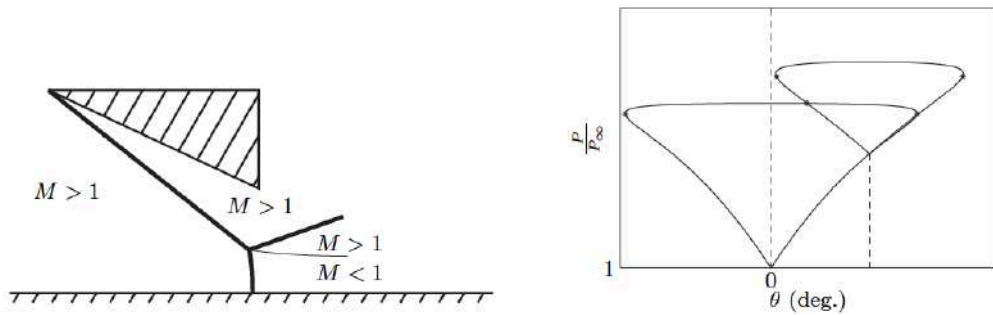


Figure 2.5: Mach reflection [7]

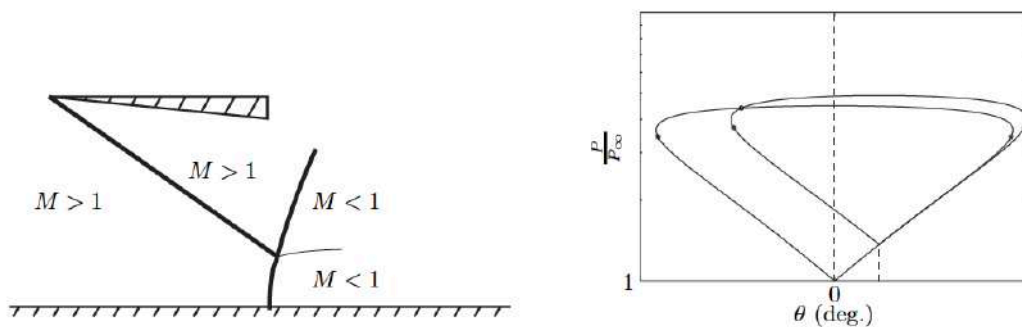


Figure 2.6: Inverse Mach reflection [7]

2.1.4. Ideal and Parabolic Nozzle Contours

From the previous paragraphs it can be concluded that the shape of the nozzle significantly affects the internal flow structure. Two types of nozzle contours are discussed in this subsection, the truncated ideal contour (TIC) and the thrust optimised contour (TOP). These two are discussed because the TIC contour has been used a lot in experiments available in literature [11, 18], and the TOP contour is the contour normally used for large rocket nozzles such as the one for the RS-25 engine, and therefore

gives a good impression of the flow physics inside the nozzles of large rocket engines.

The TIC contour is normally designed using the method of characteristics (MOC). An example of the contour is shown in Figure 2.7a. This contour is called truncated because an actual ideal contour would be extremely long and not practically feasible for real rocket engines. This is justified because the turning of the flow, and therefore the thrust contribution, in the final section is minimal. By truncating the nozzle at a certain point, the length and weight of the nozzle are kept manageable.

The TOP contour is shown in Figure 2.7b. It is used in most large modern rocket engines. This contour is optimised to generate the largest amount of thrust for minimum bell length (and thus weight). The nozzle consists of a circular section at the throat, reaching large wall angles of up to 60° . Afterwards, the contour follows a parabolic shape as proposed by Rao [39]. The transition from the circular part at the throat to the parabolic section in the divergent section causes a discontinuity in the second derivative of the wall slope. This discontinuity results in a large difference in axial pressure gradient, which in turn results in the formation of an oblique shock wave at the location of the discontinuity. This shock is called the internal shock. The formation of an internal shock is the biggest difference in internal flow structure between the TOP and TIC contours. [12, 34, 40] As explained later, it turns out that the internal shock has a very large effect on the downstream flow structure and the side loads during low NPR operation.

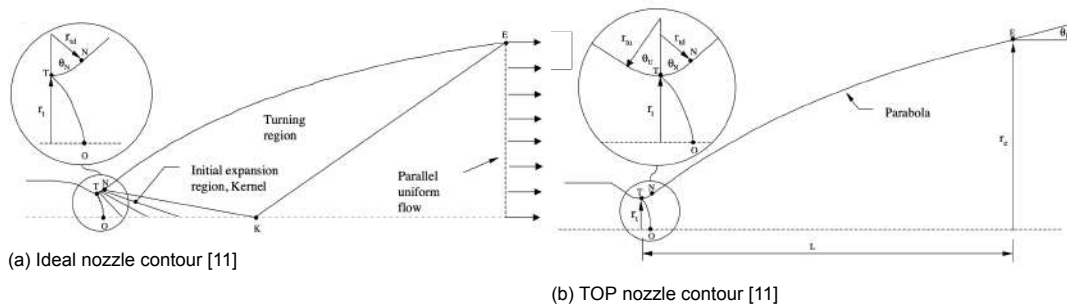


Figure 2.7: Nozzle Contours

2.2. Flat Plate Shock Wave Boundary Layer Interaction

It is important to understand some of the concepts of canonical flat-plate supersonic boundary layers and their interaction with incoming shocks to understand the flow field inside a rocket nozzle. Therefore, the concepts of shock wave boundary layer interactions (SWBLI) are discussed in this section before discussing nozzle flows.

2.2.1. Interactions between Shocks and Boundary Layers

The shape of the boundary layer greatly influences the effect of an incoming shock on the boundary layer. The boundary layer in the nozzle is normally turbulent, which means it has a low shape factor and a full velocity profile. The boundary layer shape factor is the most important parameter to consider in shock wave boundary layer interactions, and the Reynolds number is of minimal importance in high-speed turbulent boundary layers, because the flow is dominated by inertial forces.

A shock wave boundary layer interaction can be weak or strong. In the former situation, the boundary layer stays attached, while in the latter it separates. Weak interactions are discussed in the literature survey [3], but only strong interactions are discussed here because they involve flow separation. It might also occur that the flow reattaches further downstream, resulting in the formation of a separation bubble.

Babinsky and Harvey [6] mention that, because of the pressure distribution in the separation bubble, it can be represented by an isobaric region of dead air in the shape of a wedge, separated from the outer flow by a slip line. This representation is shown in Figure 2.8.

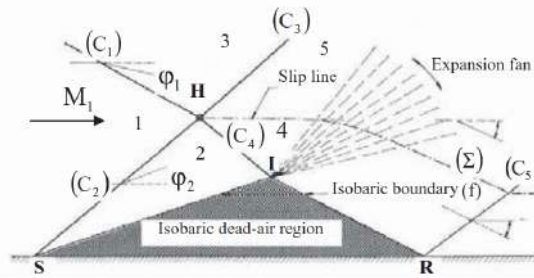


Figure 2.8: Inviscid strong shock wave interaction with boundary layer as suggested by Babinsky and Harvey [6]

The incoming shock (C_1) initially causes the separation. The isobaric wedge region causes an oblique shock at its base (C_2), which is known as the separation shock and interacts with the incoming shock. The reflected shock (C_4) hits the isobaric region in point I, but is immediately followed by an expansion fan to ensure no discontinuities in the pressure are present. In case the flow reattaches, another oblique shock wave (C_5) is formed. In rocket nozzles, the incoming shock can also be a normal shock. It turns out that whether or not the flow reattaches is significantly influenced by the type of incoming shock (normal or oblique).

2.2.2. Unsteadiness in SWBLI

The image sketched above would be an idealised average of the real shock wave boundary layer interaction. Shock wave turbulent boundary layer interactions are almost inevitably unsteady. [6, 41] The unsteady behaviour of these interactions an important driver in the generation of side loads. Moreover, the largest loads often occur at regions where heat transfer is high, does exacerbating the effect of unsteady separation. [42] Most studies about unsteady shock wave boundary layer interactions have been performed in flat plate compressive ramp studies, both experimental [41, 43–48] and numerical. [49]

From these experiments it is generally concluded that the unsteadiness frequency is much lower than the characteristic frequency of the turbulent boundary layer, U_∞/δ_i , and that the flow is intermittent in a specific region. In the unsteady interactions, an important frequency to consider is the maximum zero-cross frequency $f_{c,max}$, which is defined as the number of times that the shock foot crosses a specific location in the intermittent region in one second. [50] This frequency is not the same for the entire intermittent region, and so the maximum frequency is normally taken. Dolling found that the Strouhal number of this frequency normalised with the length of the intermittent region L_i and the free stream velocity U_∞ lies between 0.01 and 0.03 for flat plate, zero pressure gradient boundary layers. [51]

$$St = \frac{f_{c,max}L_i}{U_\infty} \quad (2.6)$$

Dussauge et al. [52] found that this Strouhal number remains relatively constant for different geometries and Mach numbers, meaning that it can be used in scaling considerations. This can be important when comparing full scale to small scale tests. When the natural frequency of a flexible nozzle is close to the maximum zero-crossing frequency, resonance of the two-way fluid structure interaction might occur, which could cause a significant increase in side loads.

Several causes of the unsteady behaviour are mentioned in literature. Erengil and Dolling [53] mention pressure fluctuations in the incoming boundary layer, Ünalmiş and Dolling [54] propose that the low frequency motion can be caused by low frequency thickening and thinning of the incoming boundary layer, while Beresh et al. [46] concluded from experiments that the low frequency fluctuation in shape factor are the cause instead. Ganapathisubramani et al. [47] state that the unsteadiness is caused by fluctuations between low- and high-momentum regions in the boundary layer. Other theories focus on the inherent unsteadiness of the separation bubble, and do not take into account upstream

unsteadiness of the flow. Piponniau et al. [55] suggest the unsteadiness of the separation bubble is caused by flapping caused by the shedding of vortices generated in the mixing layer after the separation point. This theory was confirmed with DNS simulations by Priebe and Martin. [56] It is likely that the cause of the unsteadiness is a combination of upstream and downstream effects, with large scale flapping motions being affected by the downstream separation bubble, but small-scale unsteadiness being affected by the upstream boundary layer.

2.3. Flow Separation in Rocket Nozzles

This section discusses the physics of internal flow separation in rocket nozzles. Furthermore, this section explains the complicated flow structures present in the nozzle at low NPR, as well as the difference between start-up and shutdown behaviour. Two types of flow structures are identified in rocket nozzles: (1) Free Shock Separation (FSS), which can occur in all types of rocket nozzles and (2) Restricted Shock Separation (RSS), which only occurs in TOP nozzles due to the interaction of the internal shock with the Mach disk. Both of these flow structures are discussed below. It must be noted that these flow structures are presented in 2D schematics in this section, but in reality they occur around the entire nozzle, creating annular flow structures.

2.3.1. Free Shock Separation

Free Shock Separation (FSS) was already identified in early rocket nozzle tests by Summerfield, because this shock pattern does not require the presence of an internal shock to occur. [57] Therefore, it occurs in nozzle contours of all types. For FSS, the flow in the nozzle separates from the internal wall due to the adverse pressure gradient at low NPR. A lot of numerical [58–63] and experimental [1, 9, 34, 64–67] studies, mostly in nozzles with an ideal or conical contour. Baars et al. provide a clear schematic of the flow field in the FSS regime, shown in Figure 2.9. [8]

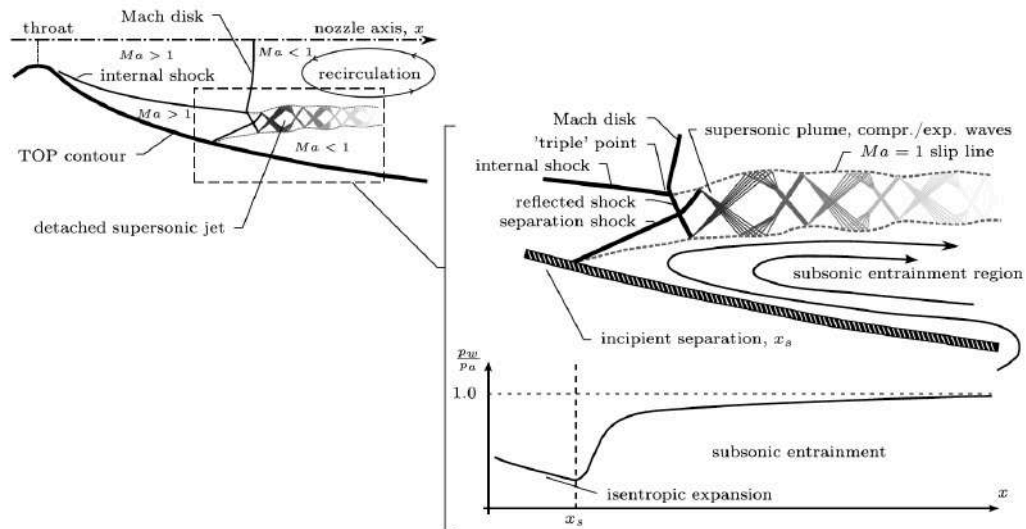


Figure 2.9: Free Shock Separation inside a nozzle. [8]

As in separation of supersonic flow off a flat plate, the process of separation causes the formation of an oblique separation shock, which in the case of a nozzle has a conical shape in three dimensions. [59] A direct Mach reflection of this shock from the centre line of the nozzle forms a Mach disk in the centre of the nozzle. This means that the flow around the centre line of the nozzle, also called the kernel [12], becomes subsonic, while the part of the flow that is further away from the centre line is still supersonic. Behind the separation shock, a recirculation region, designated the subsonic entrainment region in the figure, forms. It must be noted that this shock pattern only exists in TOP nozzles, because the internal shock does not occur in TIC nozzles.

The FSS regime has a very distinct wall pressure distribution in the vicinity of the separation location. This is shown in Figure 2.10.

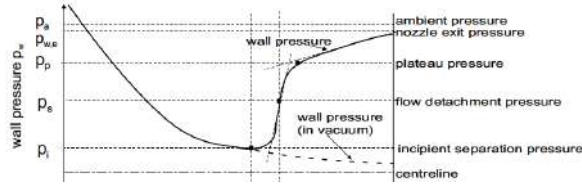


Figure 2.10: Pressure distribution across separation shock in FSS [9]

Five different pressure levels can be identified in this pressure distribution:

1. Vacuum wall pressure $p_{w,vac}$: The pressure that would exist at the wall if the flow is fully attached, as governed by the compressible nozzle flow equations.
2. Incipient separation pressure p_i : The pressure value at which the wall pressure p_w start deviating from the vacuum wall pressure.
3. Separation pressure p_s : The pressure at which the flow is regarded to have separated from the wall. This is also the pressure at the location where the separation shock starts. As explained in subsection 2.3.2, this pressure level is exactly defined using free interaction theory.
4. Plateau pressure p_p : The value of pressure at which the very rapid, almost linear, increase of pressure over the shock stops and transitions to a more gradual increase in pressure to the nozzle exit wall pressure. This pressure is also strictly defined in free interaction theory.
5. Nozzle exit wall pressure $p_{w,e}$: The pressure at the wall at the nozzle exit. This is generally very close, but still slightly lower than the ambient pressure (around 95% [18]). The lower pressure at this point allows for the formation of the subsonic entrainment region.

Over the years, many empirical criteria have been developed to determine the location of separation in the FSS regime. [57, 68, 69] These separation criteria allow for the determination of the values of NPR for which the flow separates inside the nozzle, and thus also tells something about the duration of increased loading for a known start-up or shutdown sequence. Two important criteria are mentioned here. Firstly, the criterion postulated by Schmucker, as presented in Equation 2.7. [40] To this day, this is still one of the most used criteria. [10]

$$\frac{p_i}{p_a} = (1.88M_i - 1)^{-0.64} \quad (2.7)$$

The second is the most recent, and more simplistic criterion suggested by Stark. [10]

$$\frac{p_i}{p_a} = \frac{1}{M_i} \quad (2.8)$$

Stark states that this criterion is in better agreement with experimental data than the Schmucker criterion for turbulent flows, as shown in Figure 2.11.

One model currently exists which describes the pressure distribution downstream of the incipient separation point, and is based on the flow physics. This is the generalised free interaction theory.

2.3.2. Generalised Free Interaction Theory

Carrière et al. [70] were the first to present the generalised free interaction theory, based on free interaction theory by Chapman et al. [71], but taking into account pressure fluctuations in the incoming flow. It is also presented by Östlund and Muhammad-Klingmann [21] and Reijasse and Birkemeyer. [72] This theory states that the pressure distribution around the separation location can be described using a correlation function F , through

$$F\left(\frac{x - x_i}{x_i - x_s}, p'\right) = \sqrt{\frac{p(x) - p_i}{q_i} \frac{\bar{v}(x) - v(x)}{C_{f_i}}} \quad (2.9)$$

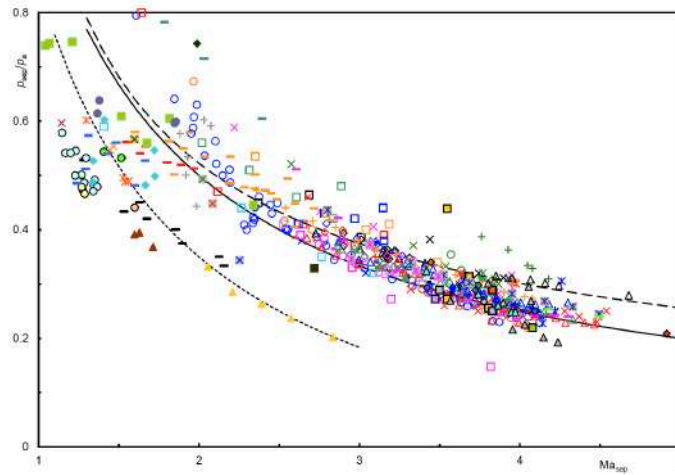


Figure 2.11: Correspondence between experimental data and several separation criteria. Dotted = $1/M_i - 0.15$, dashed = Schmucker criterion (Equation 2.7), full = Stark criterion (Equation 2.8) [10]

where $\bar{v}(x)$ is the value of the Prandtl-Meyer function at location x without separation and $v(x)$ the value of the Prandtl-Meyer function at location x with separated flow. It can be seen that the correlation function is a function of the non-dimensionalised distance $(x - x_i)/(x_i - x_s)$, which is the distance from the incipient separation point as a fraction of the separation length $x_i - x_s$. The correlation function is obtained from experiments, and shown in Figure 2.12. [11] The conditions at the incipient separation point p_i , q_i and C_{f_i} can be calculated using empirical relations such as the Schmucker criterion or a simple 2D solver.

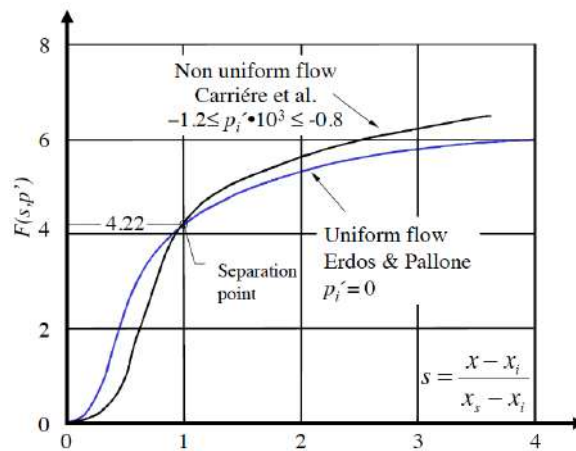


Figure 2.12: Correlation function for generalised free interaction theory [11]

Since $v(x)$ depends on $p(x)$, this equation is implicit and needs to be solved iteratively. From the correlation function, the separation location and plateau location are defined. Obviously, the separation location is present at the location where the dimensionless distance is equal to 1. The value of the correlation function is equal to 4.22. Östlund and Muhammad-Klingmann [21] define the plateau point as the location where the value of the correlation function is equal to 6.

This theory is useful because it describes the entire pressure distribution around the separation region. This also allows it to be used to determine a more accurate separation point from experiments of the longitudinal resolution of pressure measurements is insufficient. A least-squares regression fit with independent variables x_i and l_s allows for the determination of the exact separation location in between pressure measurement locations.

2.3.3. Restricted Shock Separation

Another shock pattern, known as restricted shock separation (RSS), is found at relatively high NPR in TOP nozzles. This shock pattern was first observed only in 1970 by Nave and Coffey during sub-scale tests of the J-2S engine [73], but they erroneously believed that this shock structure could not occur in full-scale hot-firing rocket engines, which is why it was not investigated much. They were proved wrong in 1998, when Frey and Hagemann showed that this type of shock structure does indeed occur in full-scale rocket engines. [74] After this discovery, many numerical [60, 67, 75–77] and experimental [1, 8, 12, 13, 15, 18, 34, 66, 78–85] studies has been done on RSS, and specifically on the transition from the FSS to RSS state. [13, 14, 86, 87] Again, a schematic of the flow structure is provided by Baars et al. [8]

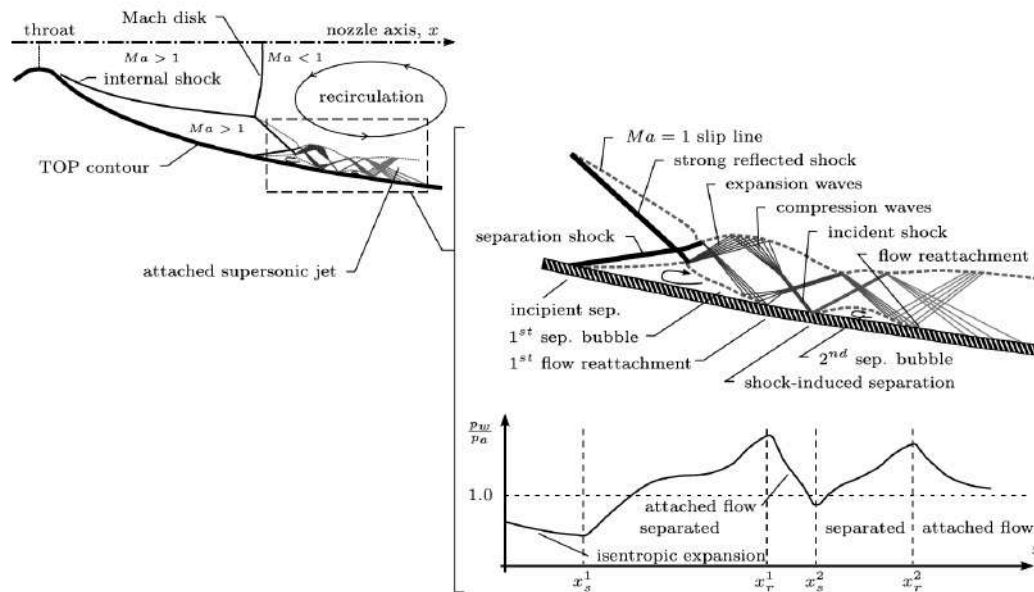


Figure 2.13: Schematic representation of restricted shock separation [8]

The schematic shows that in the RSS regime, the flow reattaches to the nozzle wall after separation. This results in the formation of one or multiple annular separation bubbles on the nozzle wall. Hagemann and Frey [12, 18] state that the presence of the internal shock is critical for this type of shock structure, because the internal shock forms an inverse Mach reflection with the nozzle centre line. This reflection results in a radially outward momentum, which during RSS is larger than the radially inward momentum resulting from the separation shock. This forces the flow back into the wall which causes it to reattach. The pattern of interaction of the internal shock, reflected (or conical shock) and the separation shock is known as a cap shock pattern.

Gribben et al. [88] and Welsh [89] found the existence of a recirculation region behind the Mach stem. Nasuti and Onofri [76, 87] explain this by stating that the Mach stem is not straight due to non-uniformities in the upstream kernel flow, resulting in a variable shock strength. This causes radial velocity and entropy gradients in the flow, which increase the downstream vorticity. This vortex can act as an obstruction of the kernel flow, by introducing a radial flow component in the direction of the wall.

The pressure distribution in the RSS regime is shown in Figure 2.14. [12] It can be seen that it is much more complex than the pressure distribution in the FSS state. The reattachment shocks causes pressure levels that are higher than atmospheric just behind the separation bubble. It can also be seen that the pressure increase across the separation shock is lower than for FSS. Because of the lower adverse pressure gradient in RSS, the separation point lies further downstream than during FSS. Thus, during transition from FSS to RSS or back, the separation point quickly jumps down- or upstream. It is also possible that the flow pulsates between FSS and RSS, which is known as partial RSS or pRSS. [90]

With increasing NPR, the separation bubble moves downstream, until the reattachment point reaches

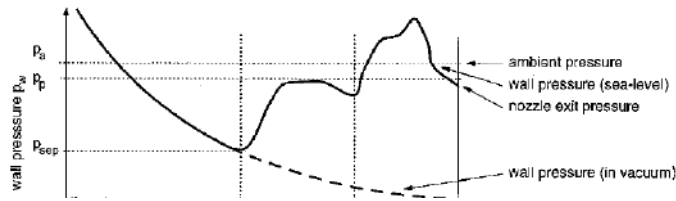


Figure 2.14: Pressure distribution during RSS [12]

the nozzle lip. When the reattachment point crosses the nozzle lip, the separation bubble opens up to ambient conditions, and the flow moves back into the FSS regime. As stated before, this results in an upstream jump of the separation point, which in turn allows for the closure of the separation bubble again. This pulsating behaviour between FSS and RSS when the separation bubble is at the nozzle exit is known as the nozzle end effect regime (EER). This is the regime in which the highest side loads are generated. [13]

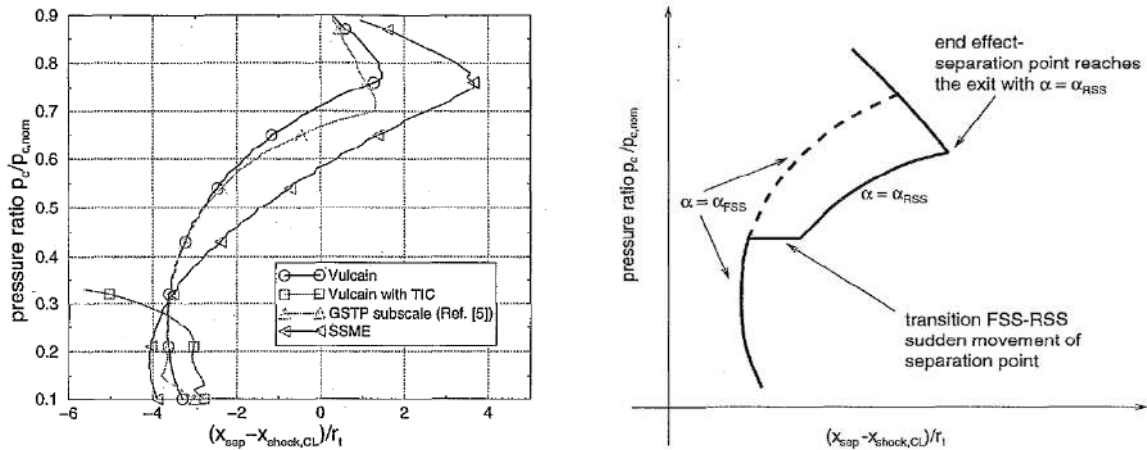
2.3.4. FSS to RSS transition

Several methods to predict the NPR at which transition from FSS to RSS occurs have been developed. Östlund and Bigert [86] presented a simple criterion

$$p_{c,transition} = p_{c,x_{RSS}=x_{NS}} \tag{2.10}$$

which states that the settling chamber pressure at transition is equal to the chamber pressure when the position of the normal shock at the nozzle centre line is the same as the RSS separation front, which can be determined using a 2D solver.

Frey and Hagemann developed a more sophisticated model, based on the cap-shock pattern being the driver of the transition. [13] They suggest that transition occurs at a slightly higher pressure than the pressure at which the difference in location between the separation and normal shock reaches a minimal value, as shown in Figure 2.15. EER occurs when this distance reaches its maximum positive value.



(a) Hypothetical situation with FSS only

(b) Real situation with FSS to RSS transition

Figure 2.15: Difference in axial location of separation and normal shock as a function of chamber pressure to nominal chamber pressure ratio [13]

Frey and Hagemann also based a side load model on this transition model, in which a momentum balance is used where the supersonic flow region is deflected in the direction of the wall at the reattachment point. The maximum side load occurs when only the flow on one side of the nozzle reattaches.

Another criterion is developed by Moríño and Salvá using results of a numerical study. [75] They state that transition occurs when the angle of the flow at the quadruple point - where the conical and separation shock interact - is greater than the nozzle wall angle at the lip.

Finally, Martelli [14] states that the flow transitions when the internal shock first forms an inverse Mach reflection, after which the conical shock interacts with the separation shock. This is shown in Figure 2.16.

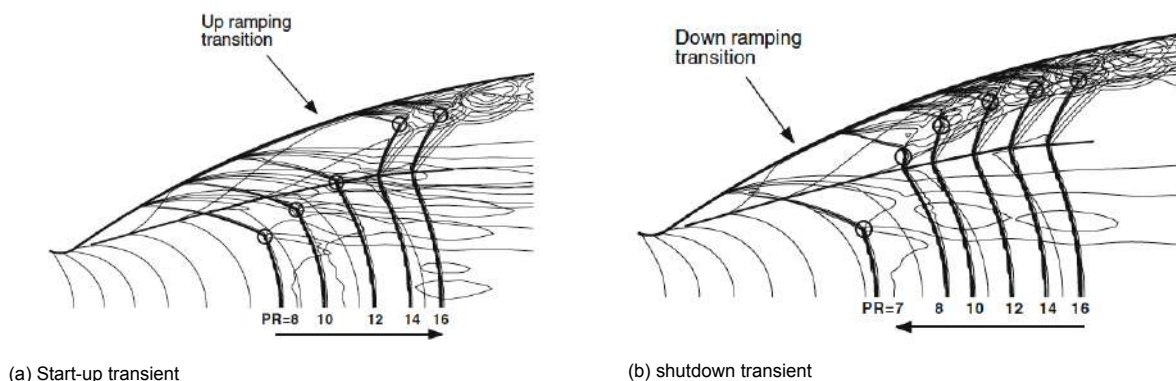


Figure 2.16: Cap-shock pattern during start-up and shutdown, RSS occurs when the internal shock and reflected shock interact above the triple point (quadruple point is indicated) [14]

During transient operation, it is Kwan and Start [79] showed that it is possible that the flow shortly and unsteadily reattaches while in the FSS regime. They called this quasi-RSS or qRSS. This state can occur in both TIC and TOP nozzles. Because the time scales of the transient are not even close to the time scales of the flow unsteadiness, experiments are normally performed for a sequence of constant NPR values. qRSS is therefore normally not captures, but since this regime does not generate the highest side loads, it is not detrimental to the validity of the research when left out.

2.3.5. Hysteresis Effects

Several experiments have shown that significant hysteresis exists in the FSS to RSS transition behaviour between start-up and shutdown. [12, 18] They show that transition from FSS to RSS occurs at a much higher NPR for start-up than for shutdown. The EER does not seem to be affected by hysteresis. The difference is quite extreme, with the transition NPR during start-up being 32, while during shutdown being only 14 in tests of Hagemann et al. [18] They mention that slight variations in the separation pressure ratio p_i/p_p occur between start-up and shutdown, which results in slightly different separation locations. Because the normal shock location remains constant, the conical shock generates a radially outward momentum for lower NPR, which means that the flow can stay attached for longer. It could also be the case that the recirculation region behind the Mach stem remains relatively stable even at lower NPR, which means it continues to act as an obstruction to the kernel flow.

Martelli et al. [14] mention that the hysteresis is only observed when considering the transition point as function of NPR, but completely disappears when the plateau pressure ratio p_c/p_p is used.

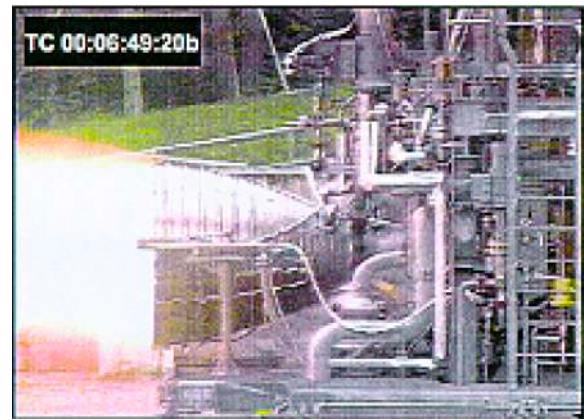
2.3.6. Nozzle Exhaust Plume Flow

Because the internal flow of the nozzle is hard to visualise in experiments, it is also important to discuss the structure of the exhaust plume. The FSS state can be clearly observed in the exhaust plume, because the flow is not attached at the nozzle lip. This is shown in Figure 2.17a. The transition is also clearly visible, as depicted in Figure 2.17b, where the top of the nozzle is in the RSS regime, while the bottom is still in FSS. At higher NPR, the cap-shock pattern can move outside of the nozzle until the internal shock is allowed to make a regular reflection with the nozzle centre line. At that point, a regular Mach disk appears in the exhaust plume. Figure 2.18 shows the development of the exhaust

plume during the start-up of the RS-25 Space Shuttle Main Engine (SSME). All different flow regimes are clearly distinguishable.



(a) FSS



(b) RSS at the top, FSS at the bottom

Figure 2.17: Flow patterns in the Vulcain engine during start-up [15]



(a) FSS



(b) RSS



(c) FSS, external cap shock



(d) Mach Disk, full flowing

Figure 2.18: Flow patterns in the RS-25 engine during start-up [16]

Very little quantitative data is available on the exhaust plume flow during low NPR operation. Yoon et al. [82] and Ramsey et al. [17] are the only ones to present quantitative data of the velocity field obtained using hydroxyl tagging velocimetry (HTV), a technique that uses lasers to track hydroxyl ions in the flow. They used this technique on a hot-firing hydrogen-peroxide mono-propellant thruster, with a throat radius of 20.4 mm and a relatively limited expansion ratio of 7.4. They still achieve a clear RSS pattern in the exhaust plume, shown in Figure 2.19. [17] It can be seen that the results match the results from the simulation relatively well, and a large low velocity region is observed close to the centre line of the nozzle, while supersonic jets are present further away from the centre. Yoon et al. do mention that the trapped vortex is not observed in the experiments, and this vortex is also not observed in the measurements by Ramsey et al. although this is not specifically mentioned in their paper.

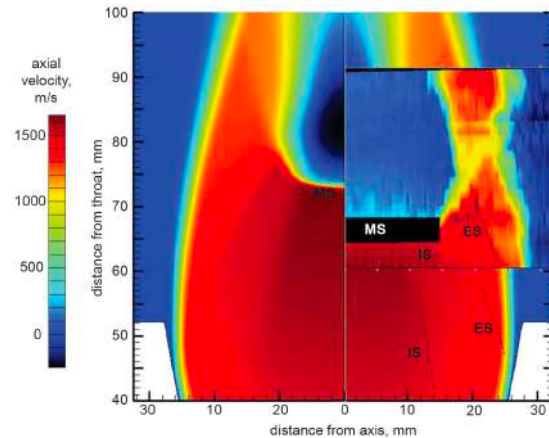


Figure 2.19: Comparison between simulation and HTV measurements of the cap-shock pattern [17]

2.4. Nozzle Side Loads

The lateral loads on a rocket nozzle are commonly referred to as side loads. These loads are generated whenever the nozzle is operational, but are at their maximum during the start-up and shutdown phase. Hagemann et al. identified several causes of increased side loads during start-up and shutdown transients. [18]

1. The transition from an FSS to RSS flow structure, and back during the EER
2. A globally asymmetrical separation line
3. Unsteady pressure pulsations at the separation location or in the downstream flow
4. Aeroelastic coupling between the flow and the nozzle structure
5. Pressure instabilities in the ambient outside of the nozzle
6. Asymmetric hardware

Of these, the first four are relevant to the current research. It must be noted that aerodynamic side loads, of which the causes are described above, are different from the structural side loads experienced by the nozzle. As explained in later sections, aerodynamic side loads can be amplified because of the flexibility of the structure through fluid-structure interaction (FSI). This section further explains the side loads generated due to each of the causes described above. Moreover, several models have been developed to determine the magnitude of the side loads. Of these, the asymmetric separation line model is discussed as well. Lastly, the effects of FSI and aeroelasticity are discussed as well.

2.4.1. FSS to RSS transition

Mattson et al. [66] were the first to determine that the aerodynamic side loads are significantly higher during FSS to RSS transition than during the rest of the start-up and shutdown phase. Furthermore, the side loads during EER are potentially even higher. This warrants that the focus of most research about nozzle side loads lies on these two phenomena in the start-up and shutdown sequences. These loads are often the critical load case for the nozzle, and therefore very important to understand. The fact that transition and EER cause the highest side loads can be concluded from Figure 2.20 and Figure 2.21, which show the side loads for a TIC nozzle (squares) and a TOP nozzle (triangles). [18]

For the start-up phase, shown in Figure 2.20, it can be observed that the TIC nozzle experiences higher side loads at low NPR, but that the TOP nozzle experiences significant side load peaks at transition and the EER (designated as re-transition). It is interesting to note that the side loads are lower for the TOP nozzle than for the TIC nozzle for most NPR values, apart from the peaks. This could be caused because the TIC nozzle was longer, meaning that the lateral force of both nozzles could be

similar. During shutdown, presented in Figure 2.21, the same peaks are observed at transition and EER, obviously at different NPR than during start-up. However, more side load peaks are also observed between NPR 35-0, which are left unexplained.

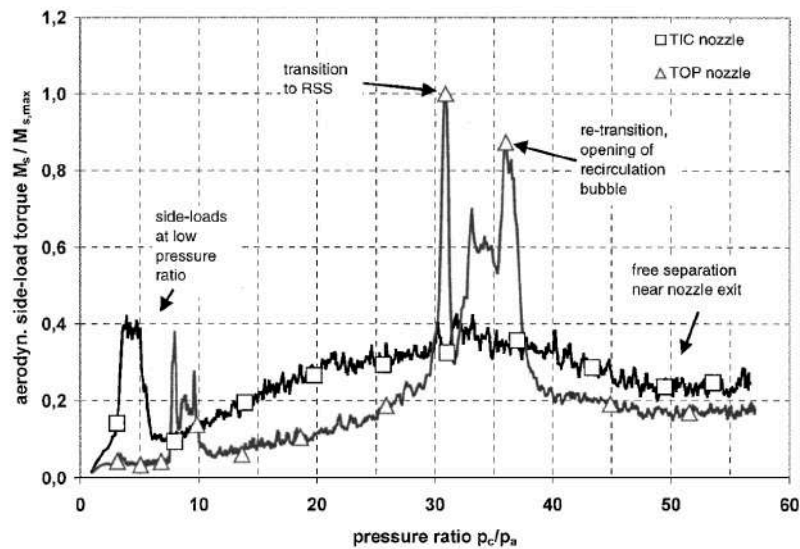


Figure 2.20: Averaged side-load torque of a TIC and TOP nozzle during start-up [18]

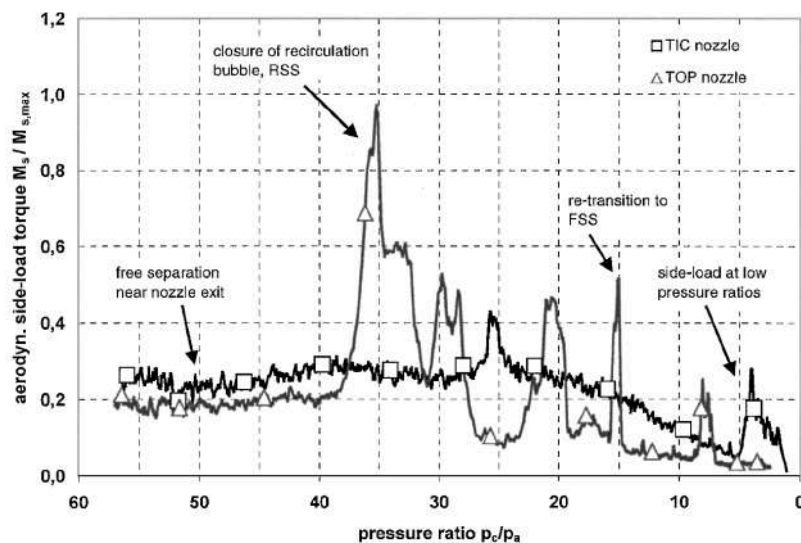


Figure 2.21: Averaged side-load torque of a TIC and TOP nozzle during shutdown [18]

The peak in side load during transition and EER is caused by asymmetric flow structures in the nozzle and the vast difference in pressure distribution for these structures. The transition between states requires a certain amount of time, which was found to be at least 50 ms by Nguyen et al. [80] but other data suggests this could be as low as 20 ms. [15]

Because the transition time between FSS and RSS and for EER is short, and thus the asymmetric flow structure is also only present for a short time, the side load can be considered a pulse load. Since this load cannot be considered static, the structural properties of the nozzle affect the dampening or amplification of the magnitude of the load. Pulse excitation theory can be used to model these loads, using a half-sine or triangle pulse. [11] The system can then be modelled as a single degree of

freedom (SDOF), mass-spring system with mass m and spring constant k . The system is assumed to be undamped because damping usually has very little influence on the initial response, and the force amplification. [91] The system is then described by the following equation of motion

$$m\ddot{x} + kx = \begin{cases} F_0 \sin(\pi t/t_p) & t \leq t_p \\ 0 & t \geq t_p \end{cases} \quad (2.11)$$

where x is the position of the mass relative to its equilibrium position, F_0 is the peak load and t_p is the pulse duration. The solution of this equation is separated in a solution for the forced vibration, where load is applied, and free vibration, where no load is applied. The deformation of the structure relative to a static load of the same magnitude $x_{st,0}$ is then given by the following response functions:

$$\frac{x(t)}{x_{st,0}} = \frac{1}{1 - (\tau_n/2t_p)^2} \left[\sin\left(\pi \frac{t}{t_p}\right) - \frac{\tau_n}{2t_p} \sin\left(2\pi \frac{t}{\tau_n}\right) \right] \quad t \leq t_p \quad \text{forced vibration} \quad (2.12)$$

$$\frac{x(t)}{x_{st,0}} = \frac{(\tau_n/t_p) \cos(\pi t_p/\tau_n)}{(\tau_n/2t_p)^2 - 1} \sin\left[2\pi \left(\frac{t}{\tau_n} - \frac{1}{2} \frac{t_p}{\tau_n}\right)\right] \quad t \geq t_p \quad \text{free vibration} \quad (2.13)$$

where $\tau_n = 2\pi/\omega_n$ with ω_n being the natural frequency of the structure. And for $t_p/\tau_n = 1/2$

$$\frac{x(t)}{x_{st,0}} = \frac{1}{2} \left(\sin \frac{2\pi t}{\tau_n} - \frac{2\pi t}{\tau_n} \cos \frac{2\pi t}{\tau_n} \right) \quad t \leq t_p \quad \text{forced vibration} \quad (2.14)$$

$$\frac{x(t)}{x_{st,0}} = \frac{\pi}{2} \cos 2\pi \left(\frac{t}{\tau_n} - \frac{1}{2} \right) \quad t \geq t_p \quad \text{free vibration} \quad (2.15)$$

From these equations it can be concluded that the response of the structure and the amplification of the loads greatly depends on the ratio of the pulse duration and the natural period of the structure t_p/τ_n . Assuming that the pulse duration time is similar for similar conditions in the nozzle, the only driver of the load amplification is the natural period of the nozzle structure.

The deformation response factor R_d is defined as the maximum value of the response function for each specific value of t_p/τ_n , through

$$x_{\max} = R_d x_{st,0} \quad (2.16)$$

which means that the aerodynamic force is amplified by the deformation response factor. Figure 2.22 shows the deformation response factor as a function of t_p/τ_n . The peak lies close to 1.75 at $t_p/\tau_n \approx 0.8$. For stiff nozzles with very small τ_n , which are normally used in cold flow tests, $t_p/\tau_n \rightarrow \infty$ and so no force amplification is present. However, when the natural period of the nozzle lies close to the pulse duration time, significant amplification might occur.

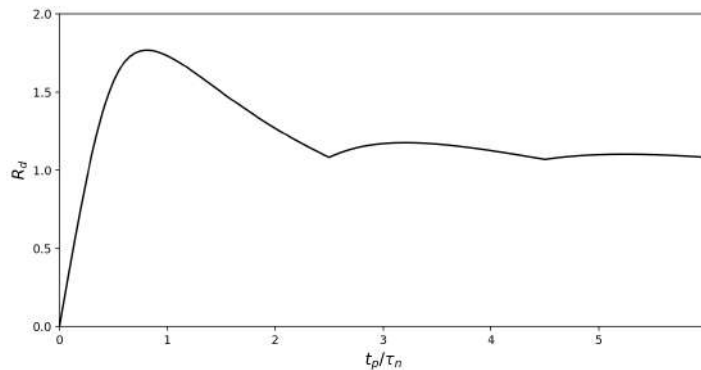


Figure 2.22: Dynamic response factor for the half-sine pulse

2.4.2. Asymmetric Separation Line Model

Schmucker developed the first model to estimate the magnitude of the side load based on the asymmetry of the separation line. [23] This model mainly focuses on the FSS regime, and a schematic is shown in Figure 2.23. [11]

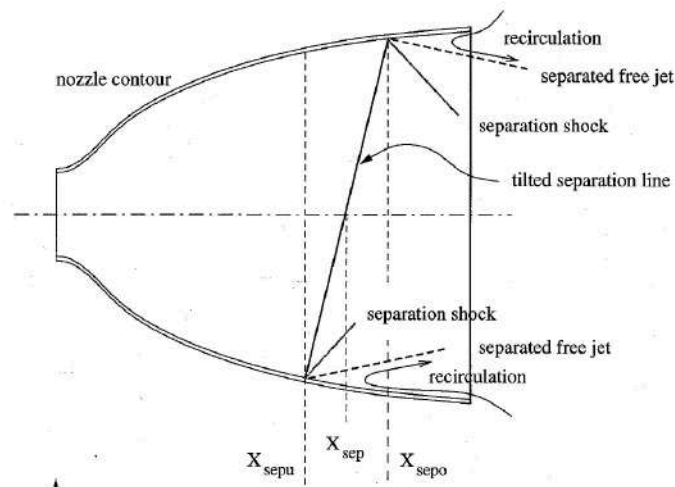


Figure 2.23: Dynamic response factor for the half-sine pulse [11]

Using a derivation described in the literature survey [3], one arrives at the final equation to determine the side load.

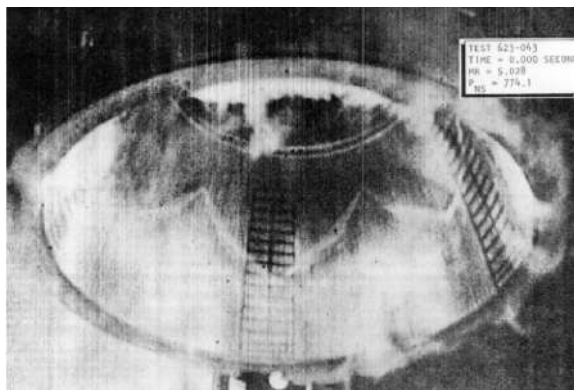
$$F_{sl} = 2K_g K_i \frac{r_i}{r_t} r_t^2 \frac{p_i}{p_a} \frac{p_a}{p_c} p_a \left(1 - \frac{p_i}{p_a}\right) \frac{1}{\frac{d(p_w/p_c)}{d(x/r_t)}} \frac{1}{1 - \frac{1 + \frac{\gamma-1}{2} M_i^2}{(1.88M_i-1)M_i} \frac{1.2032}{\gamma}} \quad (2.17)$$

Several contributing factors to the side load can be identified from this equation. First, the geometry of the nozzle determines the conditions at the incipient separation point and also directly affect the side loads through the r_t^2 term. The most important thing to note is that the side load is inversely proportional to the wall pressure gradient $d(p_w/p_c)/d(x/r_t)$. Since the wall pressure gradient generally decreases towards the nozzle lip, the side load will increase as the separation point moves downstream. This effect is amplified by the fact that the side load is proportional to the NPR, which is higher when the separation point lies further downstream. Consequently, Schmucker experimentally found that the maximum side load is achieved at a chamber pressure 10 to 20% below the full flowing chamber pressure.

Obviously, this 2D image is idealised. In 3D, the separation line follows a zig-zag pattern in the azimuthal direction. These triangular features are called "tepees" and are usually unsteady. They were observed in the J-2S engine by Nave and Coffey, as can be seen in Figure 2.24a [73] and in the RS-25 engine as shown in Figure 2.24b. The separation line in hot-firing engines is so clearly visible because of condensation at the separation point. It is not fully understood why tepees form in the nozzle.

2.5. Aeroelastic Effects

When a flexible nozzle is loaded for a short period of time, the nozzle will not deflect according to static deformation laws, but instead it can start to vibrate as was already discussed in subsection 2.4.1. When assuming that the nozzle is fixed at the throat, just like a string, a nozzle in free vibration will have very specific natural frequency and eigenmode shape and several harmonics. The eigenmode with the lowest natural frequency has the lowest number, and a nozzle has several lowest number eigenmodes depending on the type of deformation: bending, torsional or axial. Side loads mostly affect the bending modes of the nozzle, which is why these are discussed further.



(a) J-2S engine [73]



(b) RS-25 engine (courtesy of NASA)

Figure 2.24: Tepee formation during rocket engine start-up

The lowest eigenmode in bending deformation is pure bending around the nozzle throat. This is known as the first eigenmode. Sometimes, a 0th eigenmode is identified, which is the azimuthally uniform expansion and contraction of the nozzle wall. The deflection of points on the nozzle relative to the undeflected state can be described by a single sine wave around the azimuth. The second mode, known as ovalization, can be described by two sine waves around the azimuth and so on. The first several modes contain most of the energy and therefore modes higher than number four are not considered. [19] These are shown below.

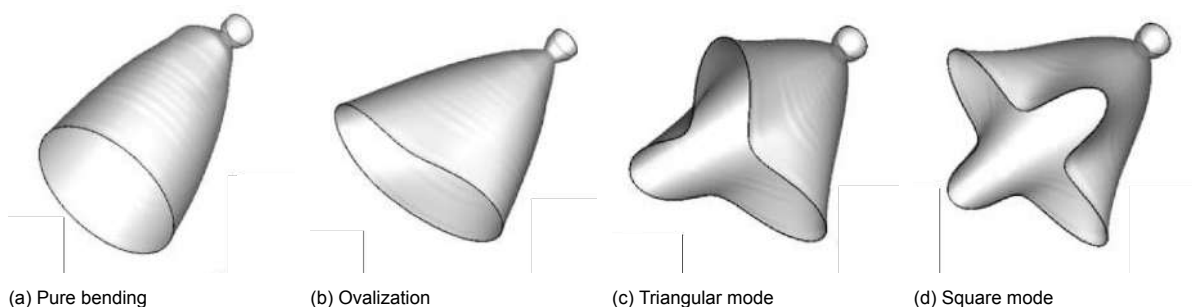


Figure 2.25: Nozzle eigenmode shapes for bending loads [19]

In the ideal case, only the first eigenmode is asymmetric, and therefore the main contributor to side loads. In reality, other modes might also contribute to the side loads.

2.5.1. Deformation effects on nozzle flow

Genin et al. performed several experiments investigating the effect of a deformed nozzle on the internal flow structure. [20, 92, 93] They mention that the dynamic deflection of the nozzle wall in case of internal separation is not always damped. This is shown in Figure 2.26. In the case that the wall of the nozzle is deflected radially inward, the separation point will move downstream because of the lower degree of expansion. Assuming that the side loads act at the separation point, this will also move the inward side load lever arm downstream, which causes further inward deflection. In the case of an outward deflected wall, the lever arm of the inward directed side load will be decreased, thereby also further increasing the outward deflection.

Moreover, these experiments have shown that the asymmetry of the nozzle separation line is increased when increasing out-of-roundness of the nozzle. This makes sense because of the direct effect of the nozzle shape on the location of the separation point.

2.5.2. Structural Stability of Nozzle Eigenmodes

The introduction of fluid flow in the nozzle changes its structural properties, specifically the natural frequency. A system is aeroelastically stable if the forced response of the combined system is the same

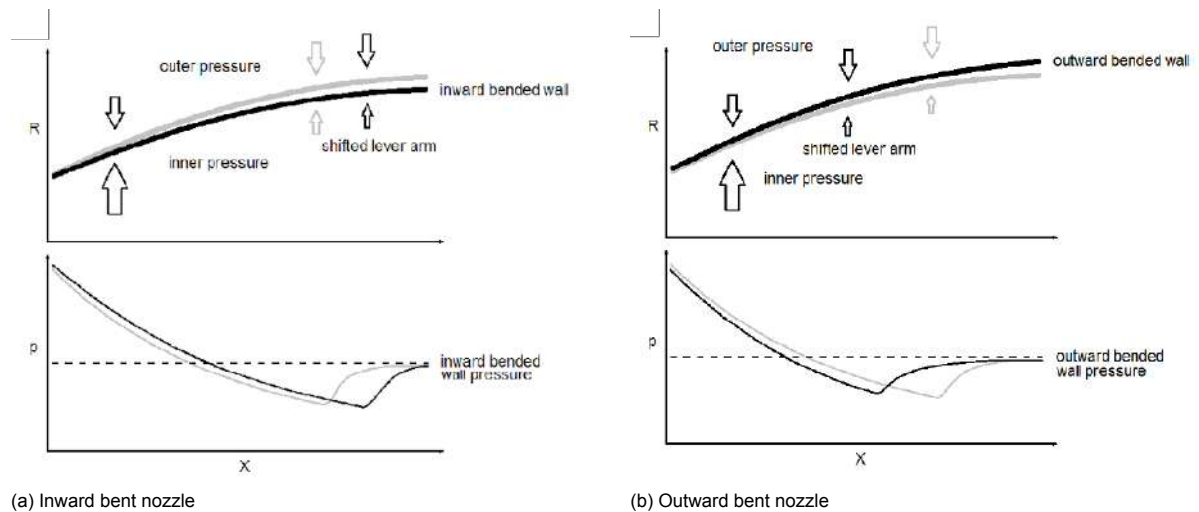


Figure 2.26: Effect of wall deflection on pressure distribution and side loads in nozzle with separated flow [20]

as the isolated structural system response, although potentially at a different natural frequency. The change in natural frequency depends on the degree of coupling between the structural system and the aerodynamic forces. [21] Structural loading increases if the natural frequency of the combined system is lower than that of the structural system and decreases when the natural frequency is higher. When the natural frequency of the combined system becomes imaginary, the system becomes statically unstable, and the deformation amplitude grows exponentially until the motion is damped or the nozzle fails.

The combined system can also be statically stable, but dynamically stable. In flat plate aerodynamics this condition is known as flutter. The aerodynamic forces act as restoring forces, but enter a positive feedback loop with the deformation. [94] In nozzles, dynamic aeroelastic instability can cause severe vibrations of the nozzle wall, potentially resulting in structural failure.

The only bending mode of which the degree of coupling and stability can be determined with relative ease is the first bending mode. This is also the only bending mode that has been investigated experimentally in nozzles by Östlund et al. [95] and Mattson et al. [66] A model to determine the change in natural frequency of the first bending mode resulting from aeroelastic coupling was developed by Pekkari [96, 97] and later improved by Lefrançois [98, 99] and Östlund [11]

These models consist of two separate parts: the first modelling the deformation of the nozzle due to a specific load and the second part modelling the change of the flow structure due to the deformation of the nozzle. A schematic of this idea is presented by Zhao. [35] The nozzle is represented as a rigid convergent and divergent section, connected by a torsional spring with spring constant k at the throat. This representation is shown in Figure 2.27. [11]

The system is considered quasi-static, which means that the characteristic time of the flow is assumed to be at least an order of magnitude lower than the natural period of the structural system. This assumption is debatable, because the unsteady frequency of the separation is in the order of 100 Hz, which could be similar to the structural natural frequency.

After a long derivation described in the literature survey [3], one arrives at the following equation for the change in natural frequency due to aeroelastic coupling

$$\Omega^2 = \omega^2 \left(1 - \frac{M_a(\theta, p_c)}{k\theta} \right) \quad (2.18)$$

and for a small angle θ

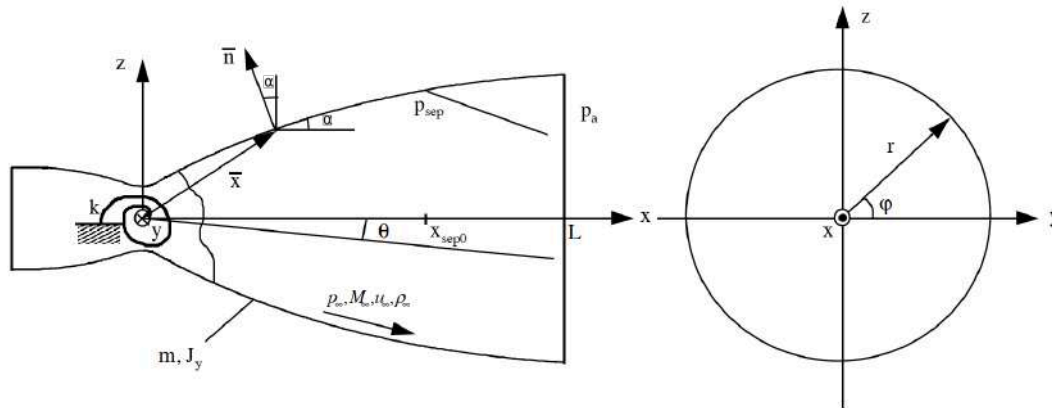


Figure 2.27: Nozzle configuration for the first bending mode model [11]

$$\Omega^2 = \omega^2 \left(1 - \frac{(p_{sep} - p_a)\pi r C (x \cos \alpha + r \sin \alpha)}{k} \Big|_{x=x_{sep,0}} \right) \quad (2.19)$$

where C is a constant depending on the nozzle contour and axial location of the separation point in the nozzle. It is obtained from 3D euler simulations. [11] From this result it can be concluded that three scenarios exist, namely:

1. $M_a < 0$: This means that the aerodynamic torque will be in the opposite to the direction of the wall deflection. Thus, the aerodynamic torque will restore the nozzle to the unloaded position. The natural frequency of the coupled system is higher than the natural frequency of the structural system, and is stiffer.
2. $0 < M_a < k\theta$: This means that the aerodynamic torque is acting in the same direction as the wall deflection. The natural frequency of the coupled system becomes lower than the natural frequency of the structural system, and is weaker.
3. $M_a > k\theta$: The aerodynamic torque is still acting in the direction of the wall deflection. However, in this case the the natural frequency of the coupled system becomes imaginary and so the system is statically unstable. The wall deflection will start to grow exponentially.

It can be concluded that low nozzle stiffness could favour instability. Moreover, from the derivation it can be observed that instability is more likely in locations with small pressure gradient, high free stream velocity and large displacement. All of these factors are present at the nozzle exit, which means that instability is likely when the separation point nears the nozzle exit.

Östlund et al. [95] obtained results shown Figure 2.28. It can be observed that for a setup with a low spring constant, designated as "super weak", the system becomes unstable as the separation point reaches close to the nozzle exit.

2.5.3. Stability of Higher Eigenmodes

The stability of higher eigenmodes has only been investigated numerically and requires much more sophisticated finite element models. Blades et al. [100] and Wang et al. [19] performed aeroelastic simulations of the RS-25 engine in the FSS regime. They found that a flexible nozzle tends to reduce the side loads and that the first two modes are most important. Zhao et al. [35] and Zhang et al. [101] performed simulations of the J-2S engine. They found that the side load increased by almost 50% for a flexible nozzle compared to a rigid one. Moreover, the frequency of the fluctuations in the direction of the side load also increases. Very asymmetric deformation is also observed. Bekka et al. [102, 103] and Garelli et al. [104] also used sophisticated models to determine the shift in eigenfrequencies. The

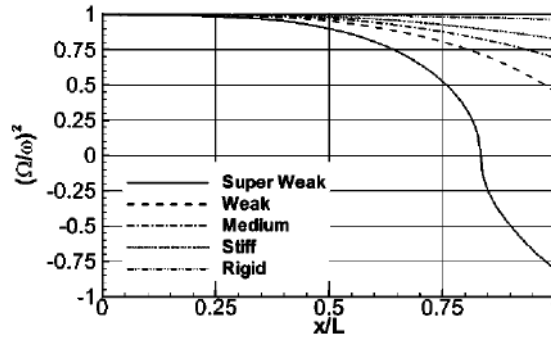


Figure 2.28: Aeroelastic stability of the first bending mode for nozzles with different stiffness [21]

results of Bekka et al. show that the coalescence of successive eigenmodes into a single eigenfrequency cases dynamic instability of the lower mode. Both find that the first mode becomes unstable for certain locations of the separation point.

The problem with the previously mentioned studies is that they only consider one nozzle, instead of investigating the effect of the structural properties of the nozzle on the aeroelastic stability. Zhang and Fuchiwaki [105] and Zhang et al. [22] are the only ones to have investigated this. Zhang et al. investigated deformation of a simplified J-2S structural model for different values of Young’s modulus and wall thickness, in order to determine the effect on the side loads and natural frequency of the first three eigenmodes. It was found that a decrease in Young’s Modulus also decreases the natural frequency of all modes. A consistent reduction of approximately 60% is achieved for a reduction in Young’s modulus of one order of magnitude. The norm of the displacement vector in the YZ plane of various points on the nozzle lip for each of the investigated nozzles is shown in Figure 2.29. [22]

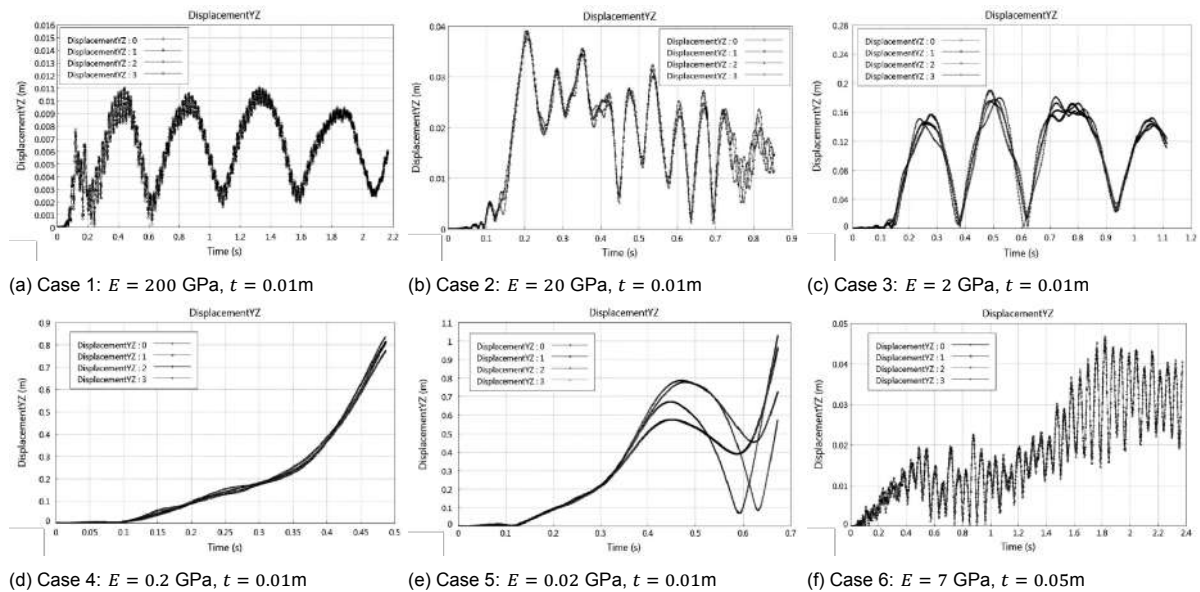


Figure 2.29: Wall displacement versus time for nozzles with different material properties [22]

From the first three figures it can be seen that the maximum deformation is increasing as the stiffness of the nozzle is lowered, but all cases still remain aeroelastically stable. The deformation in Figure 2.29d could indicate the static instability of the first bending mode, although this is not specifically stated by Zhang et al. The fifth case could indicate dynamic instability of the second mode, although again this is not stated directly in the paper.

Experiments on higher number mode shapes were performed by Tuovila and Land [106], Brown et al. [33] and Tinney et al. [25]. Brown et al. suggested that the nozzle vibrates mostly in the second eigenmode due to asymmetric separation. Finally, Tinney et al. performed tests on three flexible polyurethane nozzles with varying stiffness properties. They find that the transition from FSS to RSS and into EER occurs for lower NPR when the nozzle is more compliant. Moreover, for medium stiff nozzles it seems as if the side loads during transition are damped because of the compliance of the nozzle, since the sound power spectra indicate a lower power amplitude at transition. For very soft nozzles the vibrations become unsteady.

3

Setup Design

This chapter describes the design process and the final design parameters of the setup. First, the design requirements are presented, after which the design approach of all the specific components is discussed in detail.

3.1. Design Objective and Requirements

The main objective of the test setup is to provide the capabilities of performing measurements on the external flow in supersonic nozzles, mainly focusing on quantitative flow measurements such as particle image velocimetry (PIV). In the case of the current study, this specifically involves the investigation of separation of the internal nozzle flow at low upstream total pressure conditions which also warrants the inclusion of a 2D side load measurement capability. With this objective in mind, the following requirements have been set. Several requirements are determined by the safety requirements and constraints of the facility. Other requirements have been set based on the capability of other test facilities which were discussed in the literature survey. [3]

Table 3.1: Requirements

Identifier	Requirement
<i>System</i>	
SYS-01	The system shall measure side loads in 2 directions
SYS-02	The system shall visualize the flow field in the nozzle divergent section
SYS-03	The system shall visualize the flow field in the exhaust plume
SYS-04	The system shall run at a maximum NPR of at least 37
SYS-05	The system shall be able to control the NPR with an accuracy of 0.1
SYS-06	The system shall be able to accommodate a mass flow of at least 3 kg/s
SYS-07	The system shall be able to run continuously for at least 7 minutes
SYS-08	The system shall measure total thermodynamic conditions before the nozzle
SYS-09	The system shall be able to withstand pressures up to 100 bar including safety factor
SYS-10	The system shall be able to run on gas bottle supply
SYS-11	The system shall be able to connect to the high pressure storage tank at the High Speed Laboratory
<i>Nozzle</i>	
NOZ-01	The flexible nozzles shall be cheap to produce with a maximum price of €100 per piece
NOZ-02	It shall be able to produce a flexible nozzle within 2 days
NOZ-03	The flexible nozzle shall be supported up to a specific area ratio
NOZ-04	The nozzle wall shall be continuous from convergent section to exit
NOZ-05	The nozzle internal wall shall be as smooth as possible
<i>Flow</i>	

FLO-01	The working fluid shall be high pressure air or nitrogen
FLO-02	The flow shall be laminar when entering the nozzle
FLO-03	A plenum shall be used in front of the nozzle
FLO-04	No obstructions shall be present downstream of the nozzle that can affect the nozzle flow properties
<i>Structure</i>	
STRUC-01	The structure shall be able to withstand a thrust force including safety factor of 2
STRUC-02	The structure shall be able to withstand a lateral force equal to the thrust force
STRUC-03	The structure shall have a first natural frequency at least an order of magnitude higher than the highest natural frequency of the 4th mode shape of the flexible nozzles
STRUC-04	The structure shall be able to be firmly attached to the ground
STRUC-05	It shall be possible to easily swap out nozzles in the system
<i>Safety</i>	
SAFE-01	The system shall use remotely controlled valves to turn the main flow on and off
SAFE-02	People conducting the test shall be shielded from potential nozzle debris
SAFE-03	The system shall be safe in case of power loss
SAFE-04	The system shall be safe in case of loss of signal
<i>Testing</i>	
TEST-01	The system shall allow for the installation of a PIV seeder upstream of the nozzle
TEST-02	PIV shall be used to measure the velocity profile in the exhaust plume in at least 2D
TEST-03	Schlieren or Shadowgraphy shall be used to qualitatively visualise the exhaust plume
TEST-04	The camera capturing the Schlieren or Shadowgraphy images shall be able to record at 1000 fps
TEST-05	The side load shall be measured separately in y and z direction
TEST-06	The side load shall be measured at a frequency of 1000 Hz
TEST-07	The nozzle wall displacement shall be measured at a frequency of 1000 Hz
TEST-08	The total pressure upstream of the nozzle shall be measured at a rate of 500 Hz
TEST-09	The total temperature upstream of the nozzle shall be measured at a rate of 500 Hz
TEST-10	The ambient pressure shall be measured at a frequency of 500 Hz
TEST-11	The test shall be controlled using LabView
TEST-12	The NPR shall be visible directly on the screen of the operator

The design of the setup is based on these requirements, as explained in the following section.

3.2. The TU Delft High Speed Laboratory Facility

After the initial literature study, the first design choice to use the existing infrastructure at the TU Delft High Speed Laboratory (HSL) was made. This decision was taken to reduce the complexity of the design of the system, since the air supply system is already present at the HSL. The decision was made to place the setup in the same room as the already existing ST-15 wind tunnel¹, because in this room a pneumatically controlled start/shut-off valve and a hand operated flow control valve were already in place. This decision significantly limited the attainable maximum NPR, since the maximum pressure of the 300 m³ air tank is 40 bar. This means that the maximum possible NPR is 40, which is relatively low compared to other facilities and it is likely that it will not allow for the testing of EER because of the pressure losses that occur in the feed system between the main tank and the setup.

A major advantage of using the air supply system at the HSL is the massive volume of the tank. This means that it is very likely that active flow control is not required to maintain a constant NPR, because the variation in total pressure in the tank are minimal when running the tank. A quick analysis is performed to verify this is indeed the case. The total pressure in the tank is dependent on the density

¹<https://www.tudelft.nl/lr/organisatie/afdelingen/aerodynamics-wind-energy-flight-performance-and-propulsion/facilities/high-speed-wind-tunnels/st-15-supersonic-windtunnel>

and temperature through the equation of state.

$$p = \rho RT \quad (3.1)$$

If one assumes a starting point of 40 bar total pressure, 288 K total temperature and $R = 287 \text{ Jkg}^{-1}\text{K}^{-1}$, the initial density in the tank is 48.4 kg/m^3 . With a volume of 300m^3 this means that initially there is approximately 484 kg of air in the tank. The reduction in pressure is determined by the mass flow out of the tank. For a choked nozzle, the mass flow can be found using

$$\dot{m} = A^* p_c \gamma \sqrt{\frac{\left(\frac{2}{\gamma+1}\right)^{\frac{\gamma+1}{\gamma-1}}}{\sqrt{\gamma RT_c}}} \quad (3.2)$$

Where A^* is the throat area. The variation of total pressure with time can be determined by assuming the pressure in the tank is constant for a short amount of time Δt , in which time $m\Delta t$ kg of air flows out of the tank. The new pressure at $t + \Delta t$ is then determined by $p = mVRT$.

It is assumed that the thermal mass of the air in the tank is large enough such that the total temperature does not change. This analysis leads to the results for varying throat radius displayed in Figure 3.1. The throat radius is varied from 1 to 3 cm because this is the size range in which most of the nozzles in other experiments lie (as can be seen in Table 3.2). It can be seen that the variation in total pressure in the tank is negligible for nozzles with the throat radius of 1 cm or lower. Even for nozzles with a throat radius of 2 cm the reduction of pressure is relatively low. From experience, it is known that the pressure drop is approximately 8 bar. If this is included in the calculation, the total pressure change becomes even smaller. Thus it can be concluded that active flow control is not necessary. If the flow control valve is set such that a lower NPR is achieved, the change in pressure in the main tank will be even lower.

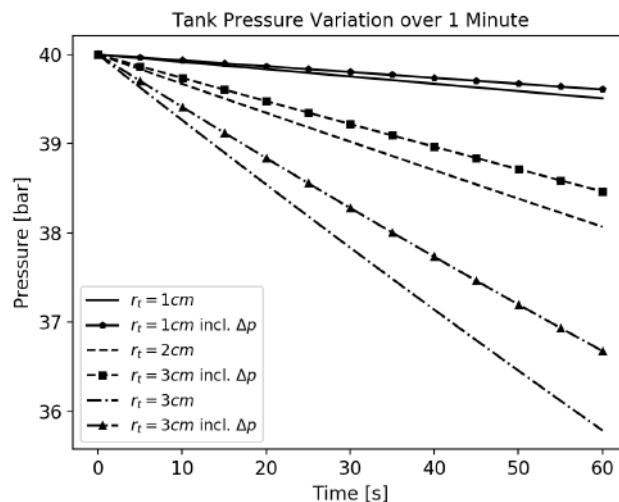


Figure 3.1: Tank total pressure variation over 1 minute for different throat radii

Nevertheless, it is possible to attach an alternative air supply to the setup if it is necessary to reach higher pressures in the system. This can also be combined with the main flow coming from the large air supply tank, if the required pressure is not more than 40 bar. It would be impossible to increase the pressure in the settling chamber above 40 bar if the main air tank is attached, because backflow would occur.

3.3. Design Overview

A render of the full design is shown in Figure 3.2. The most important components are indicated in the figure. The setup is placed in the location where normally the diffuser tube of the ST-15 wind tunnel

is sitting. The diffuser outlet connects to the outside wall of the building which means that the flow can exit the building through this hole. A noise reduction installation is present outside of the building. The setup is specifically designed to have its centre line at the same height as the centre line of the ST-15 wind tunnel. The design considerations of all the components in the setup are discussed in the following sections. The nozzle pressure ratio (NPR) is controlled using the hand operated control valve which is located 10m upstream of the nozzle and connected by a flexible hose. The flow is turned on and off by the pneumatically controlled main valve. Appendix D show the technical drawings for all of the parts.

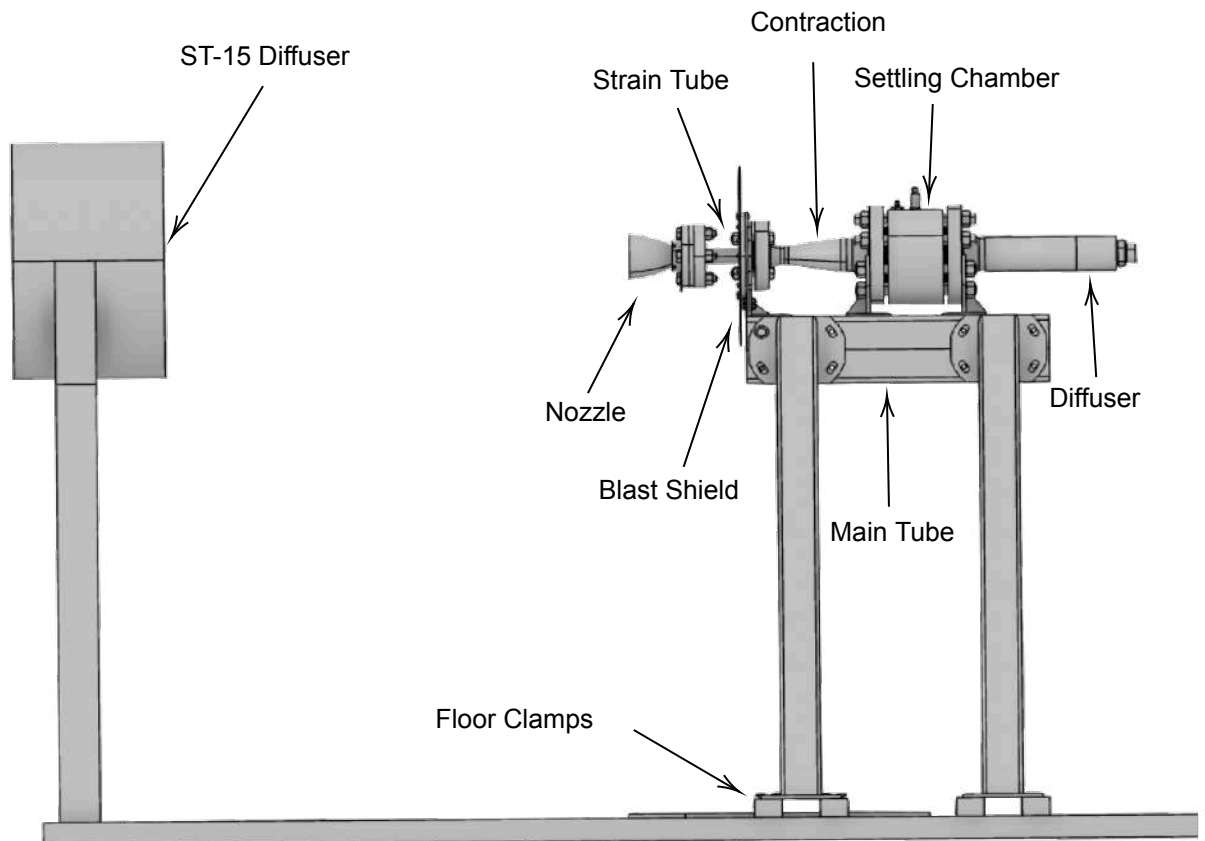


Figure 3.2: Design Overview Schematic

3.4. Nozzle Design

This section explains the design of both the stiff aluminium nozzle and the flexible nozzle. First, the selection of the nozzle contour is explained, after which the sizing of the nozzle is elaborated upon. For the flexible nozzle, the manufacturing method still had to be selected and so the reasoning behind this decision is explained. Finally, the structural design of the nozzle is highlighted.

3.4.1. Nozzle Contour Selection

The first parameter that needs to be considered in the design of the nozzle is the contour. To be able to compare the results to existing data from literature as well as to save time, it was decided to choose a contour found from literature. Table 3.2 shows an overview of the sub-scale overexpanded nozzles that have been used during studies about the start-up and shutdown transients of rocket engines. The scale of the nozzle is taken relative to the throat radius of the full scale engine on which the nozzle was based.

Table 3.2: Parameters of nozzles used in transient investigations

Number	r^* [mm]	ϵ	Scale	qRSS	FSS →RSS	EER	Unsteadiness Frequency [Hz]	Source
1	19.05	30.5	1:6.8	13	23.1-23.6	48	150-1500	[1, 34]
2	19.05	38	1:6.8	-	24.3	-	150-1500	[8]
3	10	30	1:13.1	9	31	36	-	[16, 18, 79]
4	33.54	20	1:3.9	-	15	28	100	[66, 95]
5	13.6	30.32	1:9.6	7	24	45	50-100	[107]
6	6.35	30.29	1:20.5	-	22	37-39	100-3000	[25, 108]
7	10	15.21	-	-	13.5	30	-	[109]
8	10.2	7.36	-	-	-	20	-	[82]

Nozzle numbers 1, 2 and 6 all use the same contour, which makes this contour the most widely used in the available literature. Moreover, the coordinates and pressure data of this contour were readily available through contact with Mr. Ruf. Therefore, the decision was made to use this contour for the current nozzle as well.

This contour is the PAR3 contour designed by Ruf et al. [34] for nozzle test campaigns at NASA Marshall Space Flight Center. The contour was designed using a skewed parabola with two-dimensional kinematics software (TDK). It is a thrust optimized contour, but the expansion angle at the throat was chosen to be 40° , much higher than normal TOP nozzles. This was done to ensure transition from FSS to RSS within the available NPR range. Ruf et al. estimate that FSS to RSS transition would occur at NPR around 24, which correlates very well to the experimental data presented in Table 3.2.

When comparing nozzle 1, 2 and 6, it can be observed that the number 6 nozzle, used by Rojo, Tinney and Ruf [108], is much smaller. This results in a lower NPR at transition and especially at the transition to EER, even though the nozzles have the same length. No good explanation for why this shift in the point of transition occurs is given by the authors. It could possibly be concluded that if the throat radius is selected between 6.35 and 19.05 mm, the FSS to RSS transition will occur somewhere between NPR 22 and 24, and EER between NPR 37 and 48. The high NPR at EER transition means that it will likely be impossible to achieve EER when using the air supply from the ST-15 wind tunnel. The pressure losses throughout the system will have to be lower than 2 bar, which seems unlikely. The lowest shock unsteadiness frequencies lie in the range of 100 Hz, while the highest frequencies go up to 3000 Hz. A nozzle with a vibrational modes in this range would be interesting to investigate, because resonance could potentially occur.

Since the separation point is only a function of incipient Mach number M_i , seen in the Schmucker and Stark criteria in Equations 3.3 and 3.4, shortening the nozzle should allow for the NPR at which EER occurs to be lowered. However, this has not been done by anyone in the past and so the real effects of shortening the nozzle are unknown. If the EER is to be investigated in the future, the tests could be started with a cheap baseline nozzle with the same length as the PAR3 contour, after which the nozzle is shortened in small increments until EER is achieved. Hysteresis effects should also be taken into account in this case, because the TOP nozzle can remain in the RSS state much longer during shutdown than during start-up. This means that one could shorten the nozzle so much such that no EER occurs during start-up, but that the prolonged RSS state during shutdown allows for EER to occur.

$$\text{Schmucker Criterion: } \frac{p_i}{p_a} = (1.88M_i - 1)^{-0.64} \quad (3.3)$$

$$\text{Stark Criterion: } \frac{p_i}{p_a} = \frac{1}{M_i} \quad (3.4)$$

The contour shape, pressure and Mach number distribution found from TDK simulations are shown in Figure 3.3.

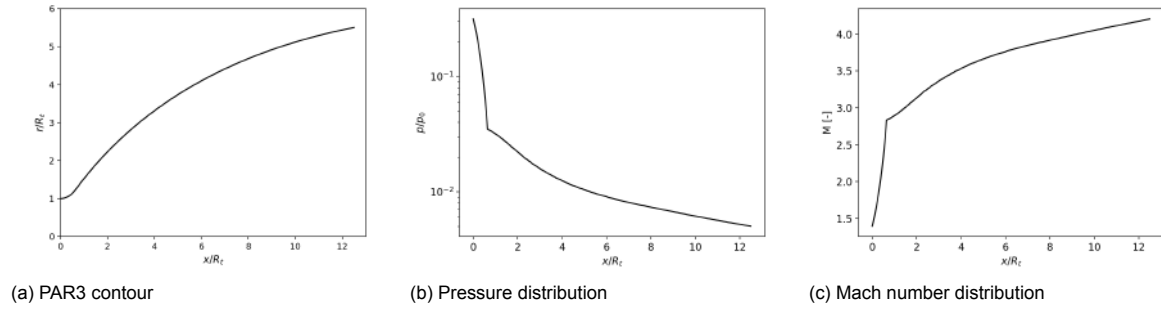


Figure 3.3: PAR3 contour properties

3.4.2. Nozzle Sizing

To determine the throat radius of the nozzle, the throat area of the nozzle was (arbitrarily) taken to be 20% of the area of the main valve. The main valve is a full bore DN40 valve, with a smallest diameter of 38mm. This means that the radius of the throat of the nozzle becomes 8.5mm. Later in the design process, this was changed to 8.175 mm such that the upstream chamber of the nozzle would have the same diameter as the standardized flange connection used for the contraction and strain tube. The wall thickness was selected to be 5mm, to ensure that no vibrations would be present for the baseline nozzle.

For the structural design of the rest of the setup as well as general safety, it is important to estimate the forces and noise produced by the nozzle. The thrust can be calculated using

$$T = \dot{m}v_e + (p_e - p_a)A_e \quad (3.5)$$

This is the ideal thrust force and therefore will always be an overestimation of the axial load on the setup. The side load can be estimated using the method presented by Östlund [11], using Equation 3.6.

$$F_{sl} = 2K_g K_{fl} \frac{r_i}{r_t} r_t^2 \frac{p_i}{p_a} \frac{p_a}{p_c} p_a \left(1 - \frac{p_i}{p_a}\right) \frac{1}{\frac{d(p_w/p_c)}{d(x/r_t)}} \frac{1}{1 - \frac{1 + \frac{\gamma-1}{2} M_i^2}{(1.88M_i - 1)M_i} \frac{1.2032}{\gamma}} \quad (3.6)$$

This equation is based on the unsymmetric separation line. In the last part of the equation it can be seen that the Schmucker separation criterion is used. The maximum distance between unsymmetrical separation locations is proportional to $(dp_w/dx)^{-1}$, which makes the wall pressure gradient the most important factor influencing the side load. K_{fl} was found to be 0.05 for the J2-D engine. [23] K_g is a geometric factor related to the area covered between the asymmetric separation points. This lies between 0.3 and 0.4. Since these are the only values for these constants available, they will also be used in the estimation of the side load for the current nozzle. To check the implementation of the model, it was compared to the side load data of the J-2S engine provided by Schmucker. The dimensionless pressure gradient, $d(p_w/p_c)/d(x/R_t)$ is found using a first order finite difference scheme. All the incipient conditions are taken from the TDK data at the separation point determined with the Schmucker criterion (see Figure 3.8a). The J-2S contour and pressure distribution are shown in Figure 3.4, the side loads are shown in Figure 3.5.

It can be seen that the estimated loads agree relatively well with the experimental data. The real value of K_g probably lies around 0.35. The estimation at least gives an idea about the order of magnitude of the side loads that can be expected for the current nozzle. The load estimation is shown in Figure 3.6. It can be seen that the maximum load is only around 15 N and occurs around NPR 35.

The overall sound power of a rocket nozzle can be estimated using equation Equation 3.7. [110]

$$W_{OA} = \eta N \left(\frac{T v_e}{2} \right) \quad (3.7)$$

where W_{OA} is the overall sound power, N is the number of nozzles and η is the radiation or acoustic efficiency. $\frac{1}{2}T v_e$ is the thrust power. NASA [24] gives some insight into the acoustic efficiency using data from solid- and liquid-propellant rockets with a thrust between 1.56 N and 31.1 MN, shown in

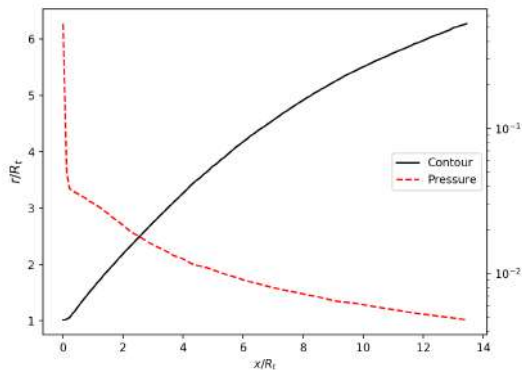


Figure 3.4: J-2S nozzle contour and pressure distribution

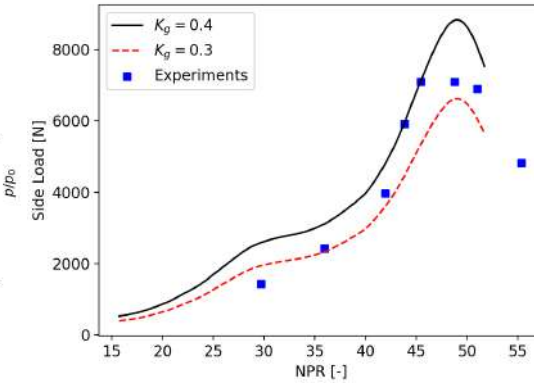


Figure 3.5: Comparison of Schmucker load model with experimental data of the J-2S engine [23]

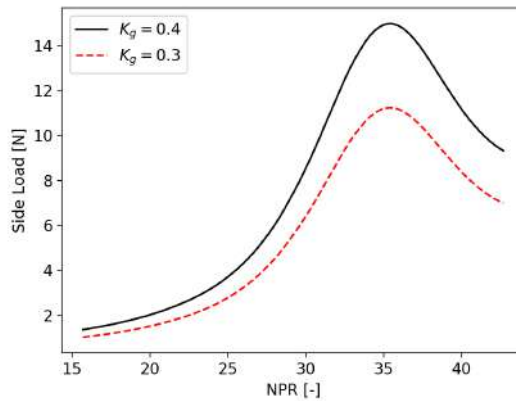


Figure 3.6: Average side loads for small-scale nozzle

Figure 3.7. It can be seen that most low-power rocket engines (power below 10^8 W) have an acoustic efficiency of 0.2-1%. Taking the worst-case scenario, where 1% of the thrust power is converted into sound, the overall sound power becomes 2084 W.

The sound power can be converted to dB using

$$SWL = 10 \log \left(\frac{W_{OA}}{W_{OA,ref}} \right) \tag{3.8}$$

where $W_{OA,ref}$ is the reference sound power of 10^{-12} W. The sound level experienced at a single observer location can then be determined using

$$SPL = SWL - \left| 10 \log \left(\frac{Q}{4\pi r^2} \right) \right| \tag{3.9}$$

where Q is the directivity factor and r is the distance from the source of the sound. Assuming the nozzle acts as a point source and radiates sound equally in all directions, the sound level varies between 142 and 122 dB from 1m to 10m distance from the nozzle. This assumption is obviously wrong, but this result still provides an order of magnitude estimation of the sound level that can be expected. This is extremely loud and operators will therefore always have to wear proper hearing protection when operating the system.

Aluminium is selected as the nozzle material to keep the mass of the nozzle relatively low. The large flange connection used to connect the nozzle to the strain tube would be very heavy in steel. The nozzle is connected to the setup using a DN25, PN100 threaded flange that is part of the aluminium

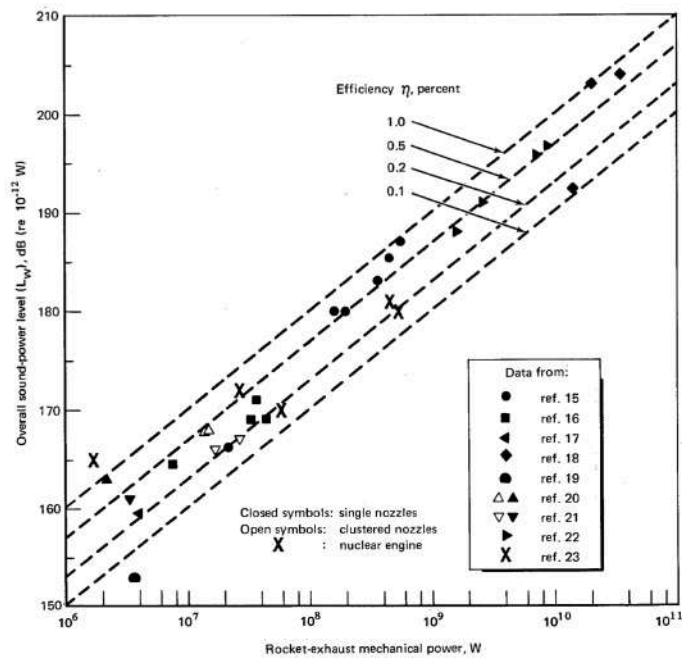


Figure 3.7: Sound power for various rocket engines [24]

nozzle. Two high tolerance, 4 mm holes which fit dowel pins are present in the flange as well as in the flange of the strain tube, such that the nozzle is always aligned with the centre of the strain tube.

Table 3.3: Nozzle properties

Property	Value	Unit
Throat radius	8.175	mm
Exit radius	44.99	mm
Wall thickness	5	mm
Length	102.2	mm
Exit expansion ratio	30.29	-
Mass flow	2	kg/s
Thrust	731.6	N
Ideal exit pressure	20.15	kPa
Ideal exit Mach number	4.2	-
Ideal exit velocity	623.9	m/s
NPR at optimal expansion	699.8	-

3.4.3. Pressure Ports

Three ScaniValve 3217² are available to perform wall pressure measurements on the nozzle. The pressure ports are located in rows at the -90, 0 and 90 degrees locations as seen in the front view of the nozzle drawing in Appendix D. This is done to be able to be able to measure asymmetries in the separation location between different quadrants of the nozzle.

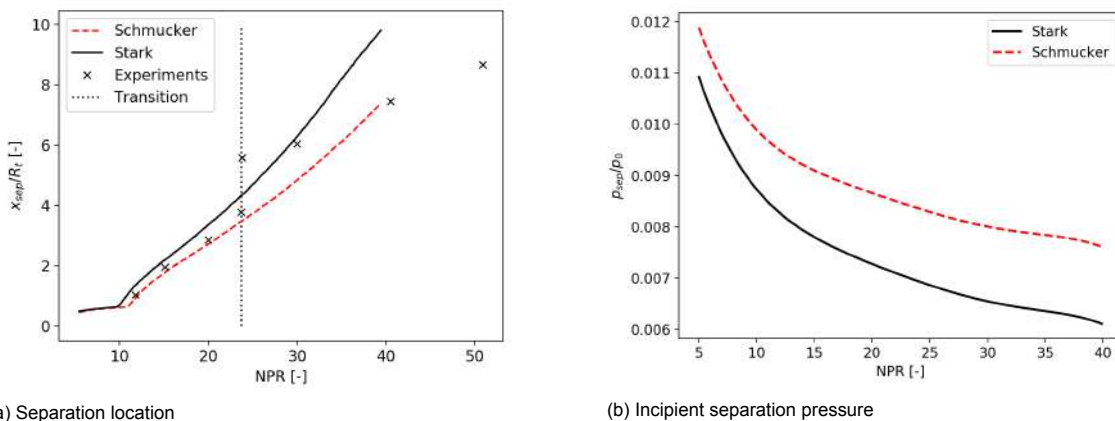
A total of 15 pressure ports are spaced evenly between the nozzle lip and the separation point at NPR 15. One of the pressure ports is left open to ambient conditions, such that the true NPR can be determined from the total pressure in the settling chamber and the ScaniValve measurement. NPR 15 was selected to allow for a relatively high spacial resolution in the pressure ports in the locations where FSS to RSS transition happens, while still being able to capture a large portion of the FSS phase (15

²<http://scanivalve.com/products/pressure-measurement/ethernet-intelligent-pressure-scanners/dsa3217-ptp-pressure-scanner/>

- 24 bar). Moreover, the location of the first pressure point has to be selected such that the measurement range of the ScaniValves is never exceeded. The minimum range of the ScaniValves is 15 psi, or 1.04 bar, gauge pressure, so a maximum absolute pressure of approximately 2 bar can be measured. Lastly, it should be taken into account that the flexible nozzle has to be supported up to a certain length downstream of the throat. After conversations with Charles Tinney, a research scientist working on nozzles at the University of Texas, this support was put at the location where the area ratio is five. The location of the first pressure port should not be too far upstream of this location, as not to compromise the support too much.

To determine the approximate separation location, both the Stark and Schmucker criterion were used. These criteria were used because the Stark criterion is the most recent, while the Schmucker criterion is still widely used in industry. These criteria are compared to experimental data of this contour provided by Ruf et al. [1] to decide which criterion should be used. The separation location is found by comparing the full flowing pressure distribution to the specific criterion for a range of NPR values. Since $p_i/p_c = p_i/p_a \cdot p_a/p_c = p_i/p_a \cdot 1/\text{NPR}$, the incipient separation pressure at a specific NPR can be determined. The location at which this pressure is higher than the full flowing pressure is the separation location. Figure 3.8 shows the location and incipient separation pressure for varying NPR. The NPR at which FSS to RSS transition occurs is indicated with the dotted line. After this point the criteria are not valid anymore.

It can be seen that the Schmucker criterion overestimates the separation location, while the Stark criterion underestimates the separation location. The Schmucker criterion also seems to correlate better with the experimental data for higher NPR. To make sure that the first pressure point lies as close to the nozzle exit as possible, but still captures FSS at low NPR, the Stark criterion is used to determine the location of the first pressure port. Thus, the first pressure port lies at $x/R_t = 2.1735$. The full flowing pressure at this location is approximately 2.1% of the total pressure in the settling chamber. At 40 bar, this would be 0.84 bar, which lies well within the measurement range of 2 bar.



(a) Separation location

(b) Incipient separation pressure

Figure 3.8: Separation location conditions with varying NPR according to Stark and Schmucker criteria

Figure 3.9 shows the dimensional contour and pressure distribution of the nozzle. The red dots in Figure 3.9a indicate the longitudinal location of the pressure taps. The dotted line in Figure 3.9b shows the 2 bar pressure level, which is the maximum measurement range of the ScaniValve pressure sensors. It can be seen that the location of the first pressure sensor is well downstream of the location at a 2 bar pressure level.

The pressure ports have a diameter of 0.2 mm to minimize the interference with the flow. The azimuthal position between each of the holes varies with 1 degree, such that an entire array spans 15 degrees. This ensures that the centers of two consecutive holes are separated by at least 2 hole diameters. This means that the turbulence generated by an upstream pressure port does not affect the flow of a downstream pressure port. Appendix B presents the internal wall coordinates and pressure

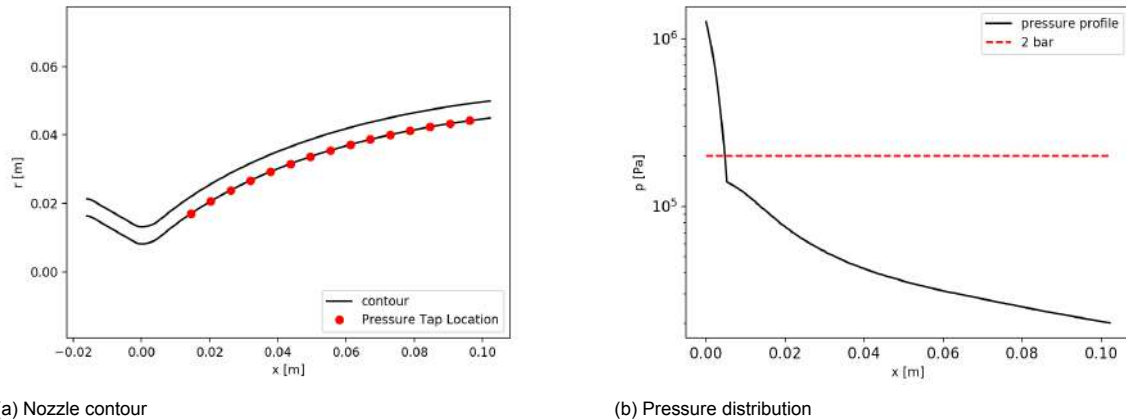


Figure 3.9: Dimensional nozzle contour and pressure distribution

port coordinates.

3.5. Flexible Nozzle Design

The flexible nozzles have the same geometric internal shape as the solid aluminium nozzle. In this section, several manufacturing methods are described and a preferred manufacturing technique is selected. Moreover, the nozzle material selection and structural design are explained.

3.5.1. Manufacturing

Little experience and literature is available about the production of flexible high area ratio nozzles. Only Tuovila and Land [106], Brown et al. [33] and Tinney et al. [25] have ever done tests on flexible nozzles. All three used different manufacturing methods for the production of their nozzles. The potential manufacturing techniques for the flexible nozzles are

- *Lathing/Milling*: A traditional way to manufacture the nozzle would be to use CNC lathing or milling. A disadvantage of this technique is the difficulty of machining the nozzles with extremely small wall thickness. For example, Either et al. [111] did modal analysis on a low-carbon steel nozzle with a wall thickness of 0.73 mm (0.03 in), which would be very difficult to machine. It is likely only possible with an internal mould supporting the nozzle wall. In general, this manufacturing method is labour intensive and also requires special machinery. It is therefore an exhaustive process to manufacture one nozzle, and so the number of iterations will be limited. This method is viable for the stiff nozzle since only one has to be made and no thin wall is required. The advantage of this manufacturing technique is that any wall thickness can be achieved. Because of the reasons described above, this production method is deemed infeasible and impractical for the flexible nozzles, and will not be researched further.
- *Forming*: Forming is common production method used for sheet metal. However, it requires precise pressing moulds and special pressing equipment. Moreover, the nozzle thickness is practically limited to standardised sheet thicknesses. The advantage of this manufacturing technique is that nozzles can be manufactured quickly and inexpensively, once the required machinery is in place. It would also be possible to use sheet metal of different materials to increase the number of different nozzles. The required specialised tools make this manufacturing technique unsuitable for this project.
- *Spin forming*: Spin forming is a technique that uses an internal mould and that forms sheet metal around the mould using rollers on a lathe. The same problems apply as for forming. Moreover, the process of making a nozzle is also labour intensive, which makes this manufacturing technique unsuitable for the project.

- Laminating:* Tuovila and Land used glass fiber laminates for their flexible nozzle. With this technique, the minimum wall thickness that can be achieved is the thickness of one fiber layer, which is normally in the order of several tenths of mm. Tuovila and Land used conical nozzle extensions with thicknesses of 0.241, and 0.356 mm. An internal mould can be used for layup such that the internal wall is smooth. A problem with this production technique is that the layup of double curved surfaces is very difficult. Moreover, the nozzle production process will be highly labour intensive. Furthermore, the number of different nozzles that can be made is limited, because the stiffness will increase significantly for each layer added and for more than a few layers the stiffness will be too high already. Also, it is difficult to achieve the exact same layup for each nozzle and it is likely that the anisotropy of the material will have an effect on the natural frequency. To achieve a smooth wall over the entire nozzle the convergent and divergent section will both have to be laminated. The stiffness at the convergent section and throat will have to be higher so this section would require more layers than the divergent section. An advantage is that production will be very cheap since only the mould has to be manufactured and glass fiber is generally not expensive. The fact that it is exceptionally difficult to produce consistent nozzles with homogeneous structural properties as well as the long manufacturing time makes this technique unsuitable for this project.
- Pouring:* This production method was used by Tinney et al. The advantage of this technique is that it is cheap and fast, because once a mould has been made, the nozzle itself is relatively inexpensive. The nozzle would be made out of a urethane-based material, for which it would be very easy to change the material properties by changing the mixture ratio of the individual components. Tinney et al. used the design as shown in Figure 3.10. [25]

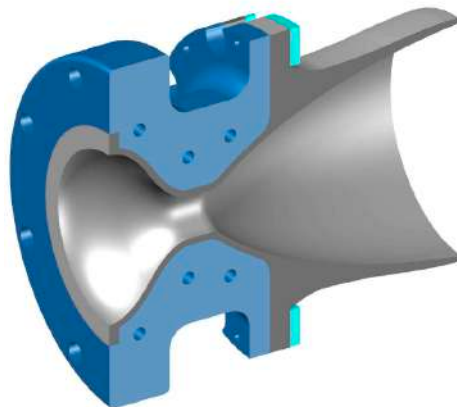


Figure 3.10: Render of the nozzle design used by Tinney et al. The gray section is the flexible urethane-based nozzle. The blue section is the metal reinforcement around the throat section [25]

The problem with this manufacturing technique is that there is not much experience with it for the production of nozzles. Moreover, the stress-strain curve of the material is non-linear, which makes it hard to predict how the nozzle will respond to an input force. This method will be investigated further.

- 3D printing:* 3D printing can be a quick and cheap method for the production of the nozzles. It is possible to quickly iterate the design if necessary. A potential problem could be that 3D printed structures are very anisotropic, and that generally their shear and tensile strength is much lower than their compressive strength. The implications of this are currently not clear, which is why this method will be investigated further. In reality, nozzles are obviously not isotropic because of the different materials and geometries used throughout the nozzle. However, for this research it is deemed beneficial to test an isotropic nozzle because it removes a variable. Moreover, the specific way in which real rocket nozzles are anisotropic is unknown.

Because of time constraints only pouring and 3D printing are considered as potential manufacturing options. To decide between these two options, meetings were organised with Charles Tinney about his

experience with pouring, as well as the Delft Aerospace Structures and Materials Laboratory (DASML), at the faculty. From the meeting with Charles Tinney I learned that the cost of a mould would be approximately €1000, and that the mould could be used for 10 to 15 nozzles before having to be replaced. Moreover, the cost of an individual nozzle would be around €100. Moreover, Charles Tinney indicated that Polyurethane with a shore A hardness of 80 - 90 was used in their experiments and had given them good initial results. To give an indication of how this relates to everyday objects, the shore hardness scale is shown in Figure 3.11.³ It can be seen that a shore A hardness of 80 - 90 lies between the consistency of a shoe heel and a shopping cart wheel. When pouring is used, the inner mould will have to be machined such that the inside of the nozzle is as smooth as possible. Moreover, the mould would have to be split into two parts for the converging and diverging sections in order to be able to remove the mould after hardening. The outer mould can be 3D printed because surface roughness is no issue on the outer nozzle wall. The advantage of this technique is that it is easy to change the material properties, and that these can be tuned very precisely.



Figure 3.11: Shore hardness scale

When initially considering 3D printing, only Fluid Deposition Modelling (FDM) printing was considered. This technique has the major disadvantage that the structure becomes extremely anisotropic because the shear strength of the part between printing layers is significantly lower than the tensile strength of the filament. Using this printing method, the infill and wall thickness of the nozzle could be varied to change its structural properties. However, during the meeting with DASML it was found that another, more suitable, technique is also available at the faculty, namely Stereolithography (SLA) printing. Until not long ago, this printing method was only possible in large industrial printers, but recently smaller desktop models have come onto the market. SLA printing allows for the use of a wide variety of printing materials, with vastly different properties. It is, for example, possible to print flexible materials with different material properties. SLA printing uses a UV laser to locally harden liquid resin from a cartridge on a build platform. Normally, the printer is inverted, which means that the build platform is upside down and the print is "pulled" out of the resin bath. This is shown in Figure 3.12⁴. Both a FormLabs Form 2 and Form 3 printer are available at the faculty.

Table 3.4 provides the specifications for the Formlabs Form 3 printer. The specified XY resolution is extremely high, potentially even better than for machined parts, while the minimum layer thickness also allows for extremely smooth prints. It must be noted that the tolerances provided by the manufacturer are often not met because these were obtained in a very controlled environment. Varying shrinkage on each individual nozzle could cause much larger dimensional fluctuations than the tolerances of the printer itself. One disadvantage is the relatively small build volume. Even though the entire nozzle bell fits, a similar flange design to the aluminium nozzle would be too big to print. This means that the design for the clamping of the flexible nozzle has to be different from the one used by Tinney et al. as shown in Figure 3.10. Another drawback of using a 3D printer is that only specific materials are available, contrary to the almost unlimited number of materials that can be used with pouring. However, the structural properties of the nozzle can also be changed by varying the nozzle wall thickness.

³<https://www.smooth-on.com/page/durometer-shore-hardness-scale/>, accessed on 27 Nov. 2020

⁴<https://formlabs.com/3d-printers/form-3/>



Figure 3.12: Formlabs form 3 printer

Table 3.4: Formlabs Form 3 printer specifications

Property	Value	Unit
XY resolution	25	μm
Layer thickness	25 - 300	μm
Build volume	14.5 x 14.5 x 18.5	cm

A decision between pouring and 3D printing was made using a pugh chart, shown in Table 3.5. The selected criteria are

1. *Nozzle quality*: How smooth the inside wall of the nozzle is and how much variation exists between different instances;
2. *Design flexibility*: How easy it would be to change the design of the nozzle if necessary;
3. *Material flexibility*: How easy it is to change the material properties of the nozzle;
4. *Ease of use*: How easy it would be to manufacture the nozzle in-house;
5. *Cost*: Cost of manufacturing one nozzle, including necessary equipment;
6. *Manufacturing time*: Time to manufacture one nozzle.

Pouring gets a +1 score for nozzle quality because the inner nozzle wall will be as smooth as the machined mould. Moreover, the nozzle shape will always be the same and will be minimally affected by atmospheric conditions. 3D printing gets a score of 0 because even though ideally the shape of the nozzle only differs from the model by 25 microns, in reality this is often much more depending on the amount of shrinkage.

In the case that the nozzle design needs to be significantly changed, a new mould would have to be manufactured, which would be relatively expensive and take a lot of time. This is why pouring gets a -1 score in design flexibility. On the other hand, 3D printing allows for the design to be changed very easily. This means it gets a score of +1.

Since the material properties of polyurethane can be tweaked very precisely, pouring gets +1 score for material flexibility. Since the materials used available for 3D printing are limited to the ones available at Formlabs, 3D printing get a -1 score.

Pouring gets a score of 0 for ease of use because no one at the faculty has experience with it. Even though the process should be relatively straightforward, it would likely take a few attempts before good quality nozzles can be manufactured. The 3D printers are very easy to use and require no specialised knowledge to operate, which is why 3D printing gets a score of +1.

The fact that a €1000 mould has to be made for every 10 nozzles, combined with €100 per nozzle, makes pouring a relatively expensive technique, which is why it gets a score of -1 for cost. On the

website of Formlabs it can be found that the price of a 1L cartridge of printing resin costs €180. From the nozzle design it is estimated that 4-5 nozzles can be printed from one cartridge, which would result in a cost of approximately €45 per nozzle. This results in a score of +1 for 3D printing.

Finally, the manufacturing time for both pouring and 3D printing would be around 24 hours. This is sufficiently fast which is why they both receive a score of +1.

Table 3.5: Pugh chart to choose nozzle manufacturing option

Criterion	Pouring	3D printing
Nozzle quality	+1	0
Design Flexibility	-1	+1
Material Flexibility	+1	-1
Ease of use	0	+1
Cost	-1	+1
Manufacturing time	+1	+1
Total	1	3

From the pugh chart it becomes evident that 3D printing is the best manufacturing technique for the current study. However, once the design is better defined, pouring could still potentially be a better alternative because the structural properties of the nozzle can be changed in a much more controlled way.

3.5.2. Material Selection

After selecting the manufacturing technique, the nozzle material has to be selected. A starting point is given by Tinney et al. [25], who give the materials used in their flexible nozzle experiments. It must be noted that the materials used by Tinney et al. are all polyurethane polymers, while the materials available for the Formlabs printer are photopolymers, which are polystyrene polymers. The material properties shown in Table 3.6 can nevertheless give an idea about in what order of magnitude the properties of the 3D printing material should lie.

Table 3.6: Urethane properties used in experiments by Tinney et al. [25]

Material	Shore Hardness	Tensile Strength [MPa]	Tensile Modulus [MPa]	Flexural Modulus [MPa]	% Elongation at Break
Hard (AFP3200) [112]	D70	25	530	500	100
Medium (E1095AB) [113]	A95	28.88	33.26	-	595
Soft (E1090AB) [114]	A90	21.46	20.65	-	776

Tinney et al. concluded that the hard and medium materials show little to no deflection during their tests, while the soft material showed very large deflections, especially during FSS to RSS transition and the end-effect regime. The significant difference in deflection between the medium and soft nozzles is quite surprising, as the material properties of both of these nozzles are fairly similar. This might indicate that the magnitude of the deflections in the nozzle could be very sensitive to the structural properties (i.e. material choice or geometric design). It is unknown whether the natural frequency of the nozzle-fluid system lies close to the unsteadiness frequency of the separation shock, but this could be an explanation for the large difference between the medium and soft nozzles.

The material properties of a selection of materials available from Formlabs is shown in Table 3.7.

Table 3.7: Formlabs printing materials

Material	Shore Hardness	Tensile Strength [MPa]	Tensile Modulus [MPa]	Flexural Modulus [MPa]	% Elongation at Break
Standard	-	38	1600	1350	12
Grey Pro	-	35	1400	940	32.5
Elastic 50A	A50	3.23	-	-	100
Flexible 80A	A80	8.9	-	-	100

The Standard and Grey Pro materials are included because they are the most common. It can be seen that there is no real overlap in material properties exists between the Formlabs materials and the materials used by Tinney et al. After testing some samples with the Standard and Grey Pro materials these could be ruled out because they were way too stiff. The elastic 50A and flexible 80A materials are specifically designed for compliant parts. Formlabs states that the flexible 80A is most suitable for cushioning, damping and shock absorption. This material has a shore hardness that lies in the range indicated by Charles Tinney. Elastic 50A is also an option, but it is questionable whether this material is stiff enough to hold the pressure forces when separation occurs on the inside of the nozzle. Flexible 80A is selected because the shore hardness is similar to the soft material used by Tinney et al.

3.5.3. Structural Design

During the preliminary design an attempt is made to estimate the stresses in the nozzle as well as the natural frequency of its first mode, i.e. the horizontal and vertical bending deflection. To determine the natural frequency of the nozzle it is assumed that the nozzle can be modelled as a cantilever beam with a cross section of a hollow cylinder. The natural frequency of a cantilever beam modelled as a mass-spring system is given by

$$f_n = \frac{1}{2\pi} \sqrt{\frac{k_{\text{eff}}}{m}} \quad (3.10)$$

if the entire beam is considered to be a spring where Hooke's law applies, $F = kx$, then the effective stiffness of the beam can be determined by

$$k_{\text{eff}} = \frac{F}{w} \quad (3.11)$$

where w replaces x as the deflection because of naming conventions. Here F is a load applied at the end of the beam. To determine the deflection of a beam, the bending equation can be used

$$\frac{d^2w}{dx^2} = \frac{M}{EI} \quad (3.12)$$

where M is the local moment, E is the Young's modulus and I is the local cross-sectional moment of inertia. The maximum beam deflection can be found by integrating this equation twice. Since in the case of the nozzle, the cross-sectional moment of inertia and the moment are changing with x , numerical integration using the trapezoidal rule is used to calculate the maximum deflection. The points along the length of the nozzle x_i are defined by the contour. The local cross-sectional moment of inertia can then be defined using

$$I_i = \frac{\pi}{4} (r_{i,\text{out}}^2 - r_{i,\text{in}}^2) \quad (3.13)$$

where $r_{i,\text{out}}$ is the local outer diameter and $r_{i,\text{in}}$ is the local inner diameter. The shear stress distribution V_x and the deflection distribution w_x can then be calculated using

$$V_L = \left(\frac{dw}{dx} \right)_i = \sum_{i=1}^L \left(\frac{\left(\frac{d^2w}{dx^2} \right)_{i+1} + \left(\frac{d^2w}{dx^2} \right)_i}{2} \right) (x_{i+1} - x_i) \quad (3.14)$$

$$w_L = \sum_{i=1}^L \left(\frac{(V)_{i+1} + (V)_i}{2} \right) (x_{i+1} - x_i) \quad (3.15)$$

Since the nozzle will be supported up to an area ratio of 5, it will be assumed that the deflection is zero until this point. To verify the model, it is compared to data provided by Zhang et al. [22] on the J2S engine. They used a model of the J2S engine with varying Young's modulus and wall thickness to determine the first mode natural frequency. This is shown in Table 3.8.

Table 3.8: Validation of first natural frequency with data by Zhang et al. [22]

Nozzle Case	Young's Modulus [MPa]	Wall Thickness [mm]	f_n from Zhang et al.	f_n estimate
1	$2 \cdot 10^{11}$	10	25.08	21.84
2	$2 \cdot 10^{10}$	10	7.93	6.91
3	$2 \cdot 10^9$	10	2.51	2.18
4	$7 \cdot 10^9$	50	9.03	7.3

It can be concluded that the estimation results in a slightly lower natural frequency than the far more involved method of Zhang et al. but that the order of magnitude is correct. The error is between 10 and 15%. It must however be noted that damping is not taken into account in the simplified model. Damping significantly influences the natural frequency, especially when the damping ratio with a nozzle of a specific material is very high. It could be that the model is moderately accurate for metal nozzles, that have relatively low damping capacity, but for the nozzles made out of flexible polymers, with high damping capacity, is very inaccurate.

The mechanical natural frequencies of flat plates and shells are generally non-dimensionalized using Equation 3.16. [115]

$$\Omega_{nd} = \omega L_{ref} \sqrt{\frac{\rho}{E}} \quad (3.16)$$

This relation holds for shells with equal poisson ratio and that are geometrically similar. It is unlikely that this will hold when scaling down from full scale engines, because the wall thickness would have to be extremely small to keep the relative thickness equal. However, it provides a good approximation of the natural frequency of nozzles with the same geometry but with different material properties. This is proven by the change in natural frequency for different material properties as shown in Table 3.8, where a 10 times lower Young's modulus causes a reduction by a factor of $\sqrt{10}$ in natural frequencies almost exactly. This relation could make it easier to estimate the natural frequencies of different versions of the flexible nozzle, once the natural frequency of the baseline nozzle is known.

Not only is the natural frequency of the nozzle important to consider, but the nozzle should also be able to withstand the stresses induced by the side-loads. To determine the stresses in the nozzle wall, the nozzle is modelled as a thick walled pressure vessel with a vertical load applied as shown in Figure 3.13. The vertical load represent the resultant force of an asymmetric flow structure and internal pressure distribution.

In this case, the hoop stress can be calculated using

$$\sigma_h = \frac{p_i r_i^2 - p_o r_o^2}{r_o^2 - r_i^2} - \frac{r_i^2 r_o^2 (p_o - p_i)}{r^2 (r_o^2 - r_i^2)} \quad (3.17)$$

$$(3.18)$$

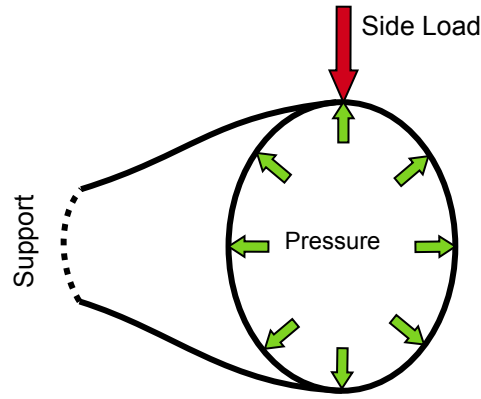


Figure 3.13: Nozzle load case

where i indicates the inner surface and o the outer surface. It can be seen that the hoop stress is maximum when $r = r_o$. To make the computation easier, all loads are calculated at the average radius $(r_i + r_o)/2$. The maximum load is achieved when the difference between the pressure on the inside and the outside of the pressure vessel is maximum. This means that the loads will always be highest when the flow is attached. An estimation of the pressure loads can thus be made by using the ideal pressure distribution to determine p_i . r_i and r_o are taken directly from the nozzle contour.

Additionally, when asymmetric separation occurs, the side load causes a shear stress and a bending stress. These can be calculated using the shear and flexure formula.

$$\tau_V = \frac{VQ}{It} \quad (3.19)$$

$$\sigma_M = \frac{Mr}{I} = \frac{F(L-x)r}{I} \quad (3.20)$$

Where V is the shear force, Q is the first moment of area. In the case of a thick cylinder, the maximum shear stress occurs on the centerline, where the first moment of area is found using

$$Q = \frac{2}{3} (r_o^3 - r_i^3) \quad (3.21)$$

This means that the maximum shear stress can be calculated using

$$\tau_{V,\max} = \frac{4V}{3\pi} \frac{r_2^2 + r_2 r_1 + r_1^2}{r_2^4 - r_1^4} \quad (3.22)$$

Mohr's circle can be used to calculate the maximum principal stresses from

$$\sigma_1 = \frac{\sigma_h + \sigma_M}{2} + \sqrt{\left(\frac{\sigma_h - \sigma_M}{2}\right)^2 + (\tau_{V,\max})^2} \quad (3.23)$$

$$\sigma_2 = \frac{\sigma_h + \sigma_M}{2} - \sqrt{\left(\frac{\sigma_h - \sigma_M}{2}\right)^2 + (\tau_{V,\max})^2} \quad (3.24)$$

When one of the principal stresses exceeds the ultimate tensile strength of the material including a safety factor, the nozzle wall thickness will have to be increased. Figure 3.14 shows the load distribution for a nozzle with a 5mm wall thickness. It can be seen that the expected loads easily stay within the ultimate tensile strength of both materials. However, it must be noted that these are static loads, which means that according to subsection 2.4.1, the dynamic loads can be up to twice as high.

The aforementioned stress calculation method also allows for varying wall thickness along the nozzle length, which is convenient because the wall thickness can be kept constant for the supported

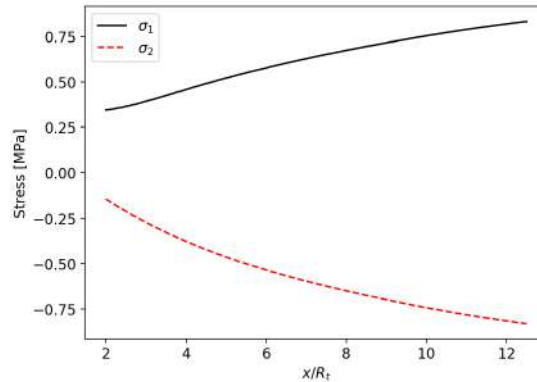


Figure 3.14: Nozzle stresses for 5mm wall thickness

section, where the loads are highest, and can be gradually decreased to the design wall thickness. The first nozzle to be tested will be a nozzle out of the flexible 80A material with a 5mm thickness. The dynamic response of this nozzle will be evaluated and design changes will be made according to its performance. The nozzle can be made stiffer or weaker to change the structural natural frequency such that it will lie closer to the unsteadiness frequency of the flow, to determine if resonance could occur. Moreover, a trend can then be established which relates the structural properties of the nozzle to the magnitude of the side loads.

To clamp the flexible nozzle to the setup, a flange similar to the one in the aluminium nozzle is designed. The base of the flexible nozzle is extended to a diameter of 70 mm with a thickness of 10 mm. The internal shape of the clamp follows the same contour as the external shape of the flexible nozzle up to the point where the area ratio is equal to 5. The clamp is made out of two halves, in order to be able to insert the flexible nozzle. Two M4x20 mm bolts are used to connect the two halves. The same 4 mm dowel pin holes as in the aluminium nozzle are used, but in this case two holes per clamp half are present. Figure 3.15 shows the assembly of the flexible nozzle in the clamp.



Figure 3.15: Assembly of flexible nozzle in nozzle clamp

3.6. Fluid component design

This section explains the approach to the design of all other fluid components in the system. These are the strain tube, the contraction, the settling chamber and the diffuser. In order to achieve a required safety factor of two on all pressure loads, the entire system will have to be designed for a pressure of 80 bar. Since mostly standardised components are used, the closest pressure standard is selected, which is PN100. For all components, the design lateral load is taken to be equal to the thrust load. This is mainly important for the design of the strain tube. For overview, a cut view of the assembly of fluid

components is shown in Figure 3.16.

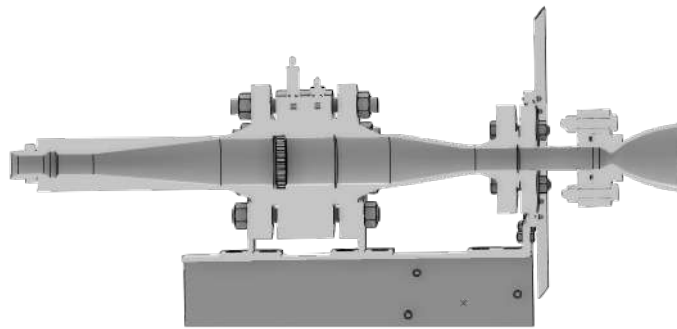


Figure 3.16: Cut view of fluid components

3.6.1. Strain Tube

The strain tube is a thin tube that is installed directly upstream of the nozzle convergent section. This tube is kept as thin as possible in order to be able to measure the small deflection of the tube as a result of lateral loads with strain gauges. The strain tube can be considered thin walled and therefore the pressure loads can be calculated using

$$\sigma_h = \frac{\Delta p r}{t} \quad (3.25)$$

$$\sigma_a = \frac{\Delta p r}{2t} \quad (3.26)$$

where σ_h is the hoop stress and σ_a is the axial stress. In this case it is assumed that the strain tube is a closed pressure vessel. Additionally, the side load causes a shear stress and flexure stress. The flexure stress, calculated using Equation 3.20, is the most important of these two and largest at the point furthest upstream. This stress is in the same direction as the axial pressure stress, and therefore these have to be added in the calculation.

The strain tube is made out of aluminium 6082-T6, just as the one used at DLR. [26] This decision is made because the lower stiffness of aluminium causes the strain tube to deflect more, which makes it easier to measure the strain. The yield strength of aluminium 6082-T6 is 240 MPa⁵, and taking the inner diameter of the strain tube to be equal to the maximum diameter of the convergent section of the nozzle, 32.7 mm, results in a minimum thickness of 0.653 mm. For a length of 6 cm, which is estimated from the DLR design, and a thickness of 0.653, and a conservative magnitude of the side load equal to the maximum thrust, the bending stress would be approximately 63 MPa. Thus, the maximum axial stress will be 183 MPa, which shows that the hoop load is the critical load. To allow for a machining tolerance of 0.05 mm, the thickness of the strain tube is increased to 0.7 mm.

In each quadrant of the strain tube, two strain gauges are placed to measure the forces in both lateral directions. The signal obtained from the strain gauge is proportional to the deformation of the strain tube which is determined by the bending torque around the position of the strain gauges. To make sure that the strain tube is still sensitive to lateral forces it should therefore be relatively thin. The stiffness of the strain tube should therefore also be considered in the total natural frequency of the system. For static problems, the relation between the deformation and the applied torque is easy, but for dynamic systems it required knowledge about the transfer function of the system. A schematic of the strain tube setup is shown in Figure 3.17. [26]

The torque about any point of interest, such as a cardan joint about which the nozzle gimbals, can then be determined using

$$T_{pi} = T_{sg} \frac{l_{pi}}{l_{sg}} \quad (3.27)$$

⁵http://www.matweb.com/search/datasheet_print.aspx?matguid=fad29be6e64d4e95a241690f1f6e1eb7

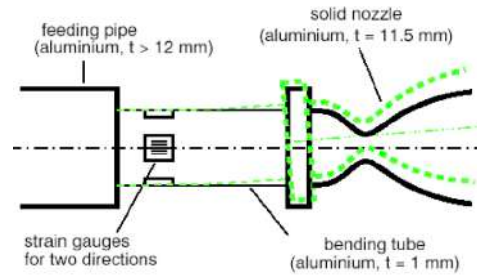


Figure 3.17: Schematic of strain tube setup [26]

where T_{pi} is the torque about the point of interest, T_{sg} is the measured torque and l_{pi} and l_{sg} are the locations of the point of interest and the strain gauge relative to an arbitrary datum. One has to assume the location of application of the resultant lateral force, e.g. the average separation location or the nozzle exit, to be able to calculate the lateral force at the point of interest.

The transfer function of the system is most easily retrieved by structural testing using a vibration table with a sinusoidal load at several frequencies. If the system is isotropic, so that the transfer function in the first displacement plane is the same as in second, and the higher mode natural frequencies are much higher than the fundamental one, f_0 , the system can be approximated fairly well as a single degree of freedom (SDOF) system. [11] The transfer function of the damped SDOF system with an external force is given by

$$H(f) = \frac{1}{k} \left(1 - \left(\frac{f}{f_0} \right)^2 + \left(2\zeta \frac{f}{f_0} \right) i \right)^{-1} \quad (3.28)$$

where ζ is the damping ratio, which, together with f_0 and k will have to be determined experimentally. The stiffness k can be determined from static calibration. The fundamental natural frequency and damping ratio can be found from dynamic calibration by measuring the free vibration response to a pulse load. In these tests one can measure the damped natural frequency f_d and the rate of exponential decay of the system α , from which the damping ratio and fundamental natural frequency can be obtained using

$$\zeta = \frac{1}{\sqrt{1 + \left(\frac{2\pi f_d}{\alpha} \right)^2}} \quad (3.29)$$

$$f_0 = \frac{f_d}{\sqrt{1 - \zeta^2}} \quad (3.30)$$

This method of side load determination is the one used most commonly in cold flow tests. The spectrum of side load torques can then be determined from the spectrum of the strain using the inverse transfer function

$$\hat{T}(f) = H^{-1}(f)\hat{S}(f) \quad (3.31)$$

The strain tube is connected to the nozzle and the contraction using two standardised flanges. To keep the mass low, it is decided to select a DN25, PN100 flange on the nozzle side, while a DN32, PN100 flange is selected on the contraction side. In order to protect the rest of the setup downstream of the nozzle, a metal plate is attached to the upstream side of the strain tube. For this, an additional ring with 16 holes is added to the flange. The length of the strain tube is determined by the length of the aluminium nozzle bolts, since these have to be screwed in from the upstream side of the flange. Standardised M16x60mm bolts are selected, and so the strain tube is 70mm long. A 50mm internal diameter by 5mm thickness o-ring is used as a seal between the strain tube and the nozzle. Standardised dimensions for Nitrile Butadiene Rubber (NBR) o-rings are used to dimension the o-ring groove⁶.

⁶<https://radaseals.nl/index.php/groefafmetingen-o-ringen/>

3.6.2. Settling chamber

The purpose of the settling chamber is to measure the total pressure and temperature right before the nozzle. Pope and Gain [116] mention that the flow velocity in a settling chamber should be between 3 and 30 m/s. Because a lot of space is available, it is decided that the velocity should not exceed 15 m/s. The velocity in the settling chamber can be calculated using continuity

$$d_{sc} = 2 \sqrt{\frac{\dot{m}RT_0}{\pi p_0 v}} \quad (3.32)$$

Since the settling chamber is connected to the diffuser and contraction with standardised flanges, the first standard diameter flange that results in a velocity lower than 15 m/s is selected as the settling chamber diameter. The smallest diameter to satisfy this requirement, for $p_0 = 40$ bar and $T_0 = 288$ K is DN65. Ho and Emanuel [117] state that to achieve a uniform Mach number distribution in the nozzle, the length of the settling chamber should be at least 6 times the radius at the exit of the contraction. It is decided to keep the diameter of the settling chamber constant along its length and equal to the diameter of the standard DN65, PN100 flange⁷. This way, the diffuser, settling chamber and contraction can be connected with M22 threaded rods, and the machining will be significantly easier. ERIKS DN65, PN100 spiral wound gaskets are used as a seal⁸. The total pressure sensor is placed upstream of the temperature sensor, in order to minimise the effect of the turbulent wake of the temperature sensor on the pressure measurement. The total pressure sensor is also placed as far downstream as possible to make sure the flow is as developed as possible before reaching it.

The settling chamber also houses a honeycomb flow straightener at its entry. The thickness is designed to be more than 6 times the cell diameter, which should always be the case according to Mehta and Bradshaw. [27] The honeycomb is obtained from Holland Shielding Systems and is normally used in ventilation systems. The flow straightener is press fit into a recess in the settling chamber. The settling chamber is made out of aluminium 6082-T6 to minimise the weight such that it is still possible to carry the settling chamber with one person. The settling chamber properties are provided in Table 3.9.

Table 3.9: Settling chamber properties

Property	Value	Unit
Internal Diameter	DN65	-
Length	97	mm
Flow velocity	12.45	m/s
Flange connection	8 x M22	-
Pressure sensor connection	1/4" BSP	-
Temperature sensor connection	1/2" BSP	-
Material	ALU 6082-T6	-
Honeycomb thickness	12	mm
Honeycomb cell size	1.6	mm

3.6.3. Contraction and Diffuser

A diffuser is used to reduce the flow velocity upstream of the settling chamber in order to correctly measure total pressure and temperature. Mehta and Bradshaw provide an indication of the maximum rate of expansion of the flow before separation in the diffuser occurs. The maximum diffuser full angle as a function of expansion ratio is given in Figure 3.18. [27] The expansion ratio of the diffuser is equal to 4.7. Since no screens are present in the diffuser, the line furthest to the left in Figure 3.18 should be used.

It can be seen that for an expansion ratio of 4.7 the full diffuser angle 2θ should be less than 15° . A safety factor of 1.25 is used and so the chosen diffuser angle becomes 12° . To keep the design as simple as possible, a constant wall slope is used, and so the length of the diffuser can be calculated

⁷<https://www.arcuseurope.com/product/voorlasflens-en#tab-id-7>

⁸<https://shop.eriks.nl/nl/afdichtingen-vlakke-dichtingen-spiraalgewonden-pakkingen/spiraalgewonden-afdichting-sri-316l-316l-c-316l-pn100-160-dn65-10002681/>

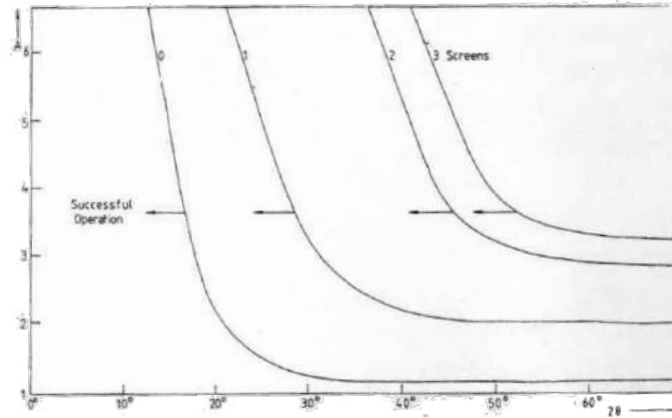


Figure 3.18: Design boundaries for diffusers [27]

using $L = (d_o - d_i) / \sin(\theta)$. The diameter at the entry of the diffuser is kept constant for a short distance such that a PIV seeder connection can be placed upstream of the settling chamber.

Mehta and Bradshaw mention that the wall contour of the contraction does not really matter if at least the contour is smooth at the edges. such that the first and second derivative of the contour are as close as possible to zero. [27] What makes this specific contraction special is that the test section is not directly downstream of the contraction. Obviously, the nozzle converging section acts as an additional contraction. Therefore, the specific shape of this contraction is not very important. The length of the contraction is defined by other constraints, mainly the bolt length to connect the contraction to the strain tube. The edges of the contour are smooth and a constant area section is added upstream and downstream of the contraction. A hydrostatic test was performed on the entire system in order to validate the design. This showed that the system could hold pressures of at least 60 bar. The properties of the diffuser and the contraction are provided in Table 3.10.

Table 3.10: Diffuser and contraction properties

Property	Value	Unit
Flexible hose type ⁹	DN31 PN140	-
Flexible hose length	10	m
<i>Diffuser</i>		
Entry connection ¹⁰	1-1/4" BSP	-
Exit flange	DN65 PN100	-
PIV seeder connection	1/4" BSP	-
Expansion ratio	4.7	-
Diffuser angle	12	deg
Material	SS-316	-
<i>Contraction</i>		
Entry flange	DN65 PN100	-
Exit flange	DN32 PN100 80sch	-
Length	123	mm
Wall thickness	4.35	mm
Material	SS-316	-

⁹<https://www.fluiconnecto.nl/en/p/rockmaster-2sc---hydraulic-hose-2-wire-braid---manuli-hydraulics/A11001>

¹⁰<https://www.landefeld.com/artikel/en/hydraulic-double-nipple-g-1-14-g-1-14-zinc-plated-steel/DN%20114114%20HD>

3.6.4. PIV tube

The final flow component to be designed is the so-called PIV tube, shown in Figure 3.19. This tube encloses the space between the nozzle and the ST-15 wall outlet, such that when small seeding particles are used, they do not fill up the wind tunnel room. The design of the PIV tube is relatively straightforward. A rectangular tube that is normally used for air vents is used as the main structure. A rectangular shape is selected because this makes it much easier to install transparent polycarbonate panels in the tube in order to keep optical access to the flow. On the nozzle side, this tube connects directly to the steel protection plate connected to the strain tube. On the other side it is connected to a circular steel sheet which fits tightly into the ST-15 diffuser outlet. The circular sheet houses an o-ring of 470mm inner diameter and 6mm thickness in order to seal between the diffuser outlet and the PIV tube. The connections on either side of the PIV tube are sealed with polyurethane tape. The width and height of the cross section of the PIV tube are entirely determined by the maximum size achievable to still fit within the diffuser outlet. This results in a cross section of 300mmx300mm, which means that there are around 1.5 diameters between the nozzle lip and the wall. This could cause interference between the flow and the wall resulting in varying flow properties between cases without and with PIV tube. Four transparent polycarbonate sheets are placed in the PIV tube, one on each side. These are 800mmx250mm size and are connected using M5 bolts at 10mm intervals.

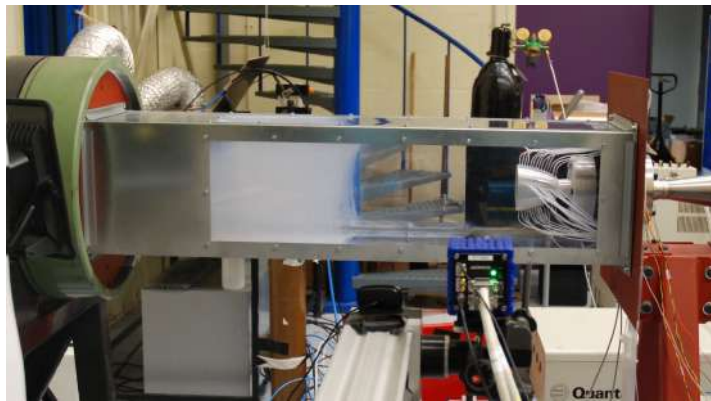


Figure 3.19: PIV tube on the setup

3.6.5. Feed System

A diagram of the feed system is provided in Appendix E. The main valve is a pneumatic ball valve that requires pressurised air to operate. The control valve is a manually operated globe valve. A DN25, PN40 threaded flange is used to connect to the control valve. This flange has an internal thread of 1-1/4" BSP. A straight nipple with 60 degree internal cone is used in order to connect the female end of the flexible hose to the flange. The same is used to connect the hose to the setup.

3.7. Structural Component Design

Structural components are used to secure the setup to the floor of the wind tunnel facility, and to raise the setup to a height that will make it easier to work on, and to allow the exhaust to exit the building. A frame with four legs, two front legs and two aft legs, is chosen. The legs angle outward at an angle of 20 degrees, such that they can carry the lateral loads. All of the legs are made out of standardised rectangular steel tube of 80 x 50 x 5 mm. They are attached to the main tube on which the setup is mounted. The main tube is a rectangular steel tube of 150 x 150 x 6 mm. The height of the setup was chosen to be 1250 mm, which is equal to the centre line of the ST-15 wind tunnel.

The flow contains a rail track in which the diffuser of the wind tunnel normally sits. On the inside of both rail tracks a guide plate is installed, in order to guide the wheels of the diffuser when it is driven across the tracks. These guide plates can be used to clamp the setup onto. Clamp blocks have been designed to sit in the rail track and using 2 M10 bolts per block, these blocks can be clamped onto the guide plates, similar in operation to a vice. These blocks are installed on the front legs, while the

hind legs only connect to blocks that sit loosely in the rail track. An 8mm thick steel plate is welded at the bottom of the feet, which is directly connected to the clamp blocks with 2 M12x30mm bolts per block. A 5mm thick plate is used to attach the leg to the main tube. The attachment to the main tube is achieved by 4 M12x30 bolts threaded into the main tube, while slots in the attachment plate of the leg allow for the rotation of the main tube relative to the front legs, such that the setup can be placed exactly horizontal. The floor clamp blocks are shown in Figure 3.20.



Figure 3.20: Floor clamp block mechanism

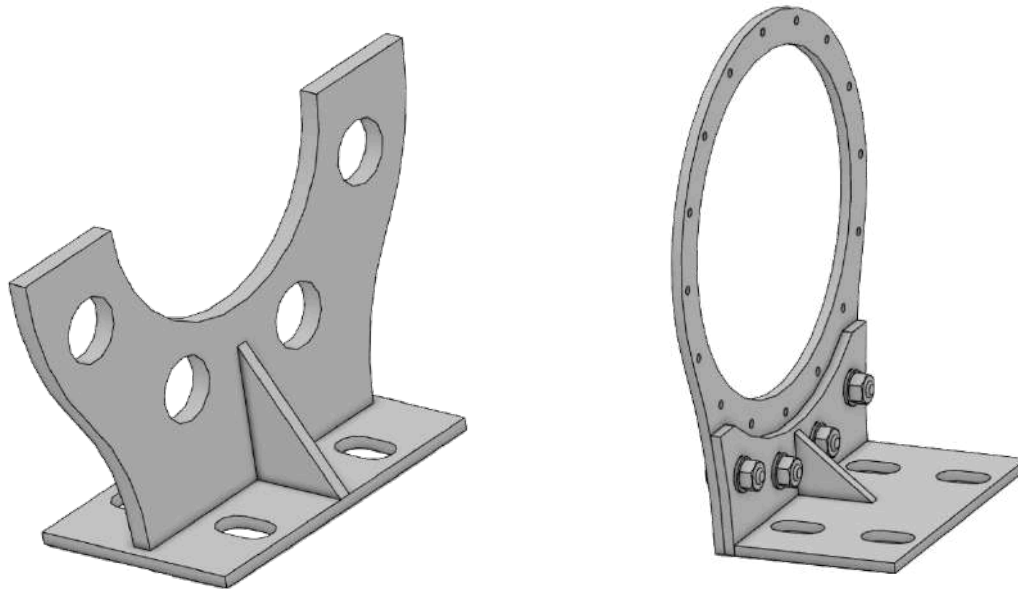
In the relatively unrealistic scenario that all of the load would be carried by only one leg, the leg is basically a cantilever beam. The deflection of a cantilever beam with a load at its end is given by

$$\delta = \frac{PL^3}{3EI} \quad (3.33)$$

for a load of 1463 N, double the thrust load, in the axial direction and a length of 1.25 m the deflection of the beam would only be 5mm. For a side load equal to the thrust load (731 N), the deflection would be 5.8 mm. This shows that the structure will easily be able to handle the thrust loads acting on it.

The fluid components are mounted to the setup using several clamps. Two clamps attach to the same threaded rods that are used to attach the diffuser, settling chamber and contraction together. 4 of the 8 M20 threaded rods are used. The clamps are made out of 5mm thick laser cut steel, and the parts are welded together. A triangular support makes sure that the angle between the base plate and the connector plate is very close to 90 degrees. The connector plate is made slightly wider than the maximum radius of the neck of the flange, to prevent interference.

A third clamp is used at the flange connection of the strain tube to the contraction, to make sure that the components only start deflecting downstream of this point. A similar base plate is used to the other clamps. However, in this case it is opted to use a full ring around the flange connection of the strain tube that uses 16 M5x20 bolts. This plate is connected to the base plate assembly by 4 M8 bolts which allow for some up and downward motion before tightening, such that the clamp itself is not straining the fluid components. This plate makes sure that the entirety of the strain tube is constrained. This same ring also allows for the connection of the blast plate which has to be used when PIV is performed. This clamp is also made out of 5mm thick laser cut steel. These are shown in Figure 3.21.



(a) Settling chamber clamp

(b) Strain tube clamp

Figure 3.21: Structural clamps in the setup

3.8. Electronic Component Design

The electrical components of the setup consists of two parts: (1) the electronics required to perform measurements and (2) the electronics required to start and stop the flow. One electronic box with power supply, terminal blocks and a relay switch. The power supply is a Mean Well 68W Embedded Switch Mode Power Supply, which outputs three signals at 5V, 12V and 24V. This power supply was selected because this way the valve, which requires 24V has its own power supply, and the pressure sensor can run on a separate supply. As explained in subsection 4.1.4, the National Instruments modules used to read out the temperature sensor and the strain gauges have an internal voltage excitation source. In the case that this is not available, the strain gauges can be connected to the 5V supply, while the temperature sensor can be connected to the 12V supply in parallel.

Figure 3.22 shows a schematic of the electrical layout of the system. Most of the electronic components are housed in a plastic box for safety reasons. A 24V relay is used as a switch which is itself switched by the NI9481 relay module. This is done in order to protect the NI9481 relay module from induced current when the main valve is closed because of the high valve power. The relay in the NI9481 module can be controlled using the NI LabView software. An emergency button is installed in the main valve circuit, in order to be able to close the main valve even when the connection to the relay module is lost, or when a dangerous situation occurs.

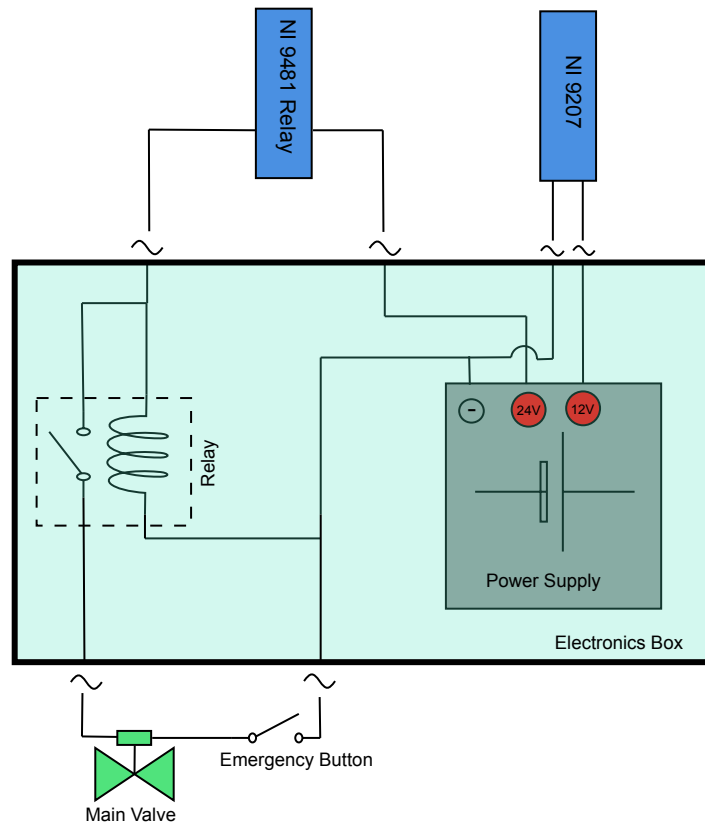


Figure 3.22: Schematic of electrical layout

3.9. Software Design

A specific NI LabView program has been written to use the test setup. The graphical user interface is shown in Figure 3.23. Several features are explained below.

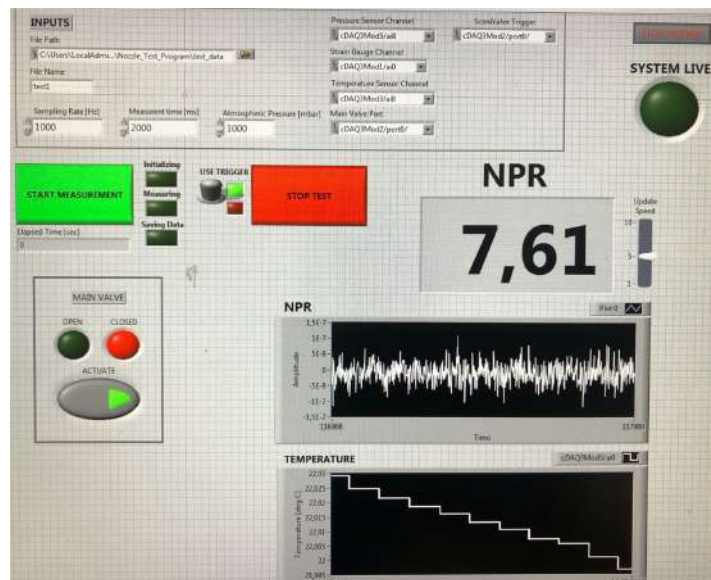


Figure 3.23: NI LabView interface

Inputs:

- File path: Folder where the test data should be stored

- File name: Name of the file with the test data (the name will also be formatted with the time at which the measurement is performed, such that a new file is created for each measurement)
- Sampling rate in Hz: Rate at which data is acquired
- Measurement time in ms: duration of time for which measurements are taken and saved
- Atmospheric pressure in mbar: To calculate the NPR, the atmospheric pressure should be given, division of the total pressure and the atmospheric pressure then gives the NPR.
- Pressure sensor channel: Channel in the NI DAQ module corresponding to the total pressure sensor.
- Strain Gauge Channel: Channel in the NI DAQ module corresponding to the total strain gauges (should always be 2 channels).
- Temperature sensor channel: Channel in the NI DAQ module corresponding to the total temperature sensor.
- Main Valve port: Channel in the relay module connected to the main valve.
- ScaniValve Trigger: channel in the relay module connected to the ScaniValve trigger line.

Commands:

- Start measurement: Once the start measurement button is clicked, the data acquisition program will initialize, and the computer will take measurements for the duration of “measurement time” ms at a rate of “sampling rate”. The elapsed time is displayed below the button.
- Use trigger: This command can only be changed while not taking measurements. It changes whether the ScaniValve trigger relay will actuate or not.
- Stop Test: Stops all loops and can also be used when taking measurements. The stop test command should be used when the test is done or in case of an emergency. It will automatically close the main valve if it is still open and stop all data acquisition.
- Close Program: shuts off the program correctly, this should be used rather than just clicking the abort execution button in LabView.
- Main valve actuate: Opens or closes the main valve (open when pressed). At the start of the program the main valve state will always reinitialize to the closed position, such that the main valve is not accidentally opened when starting the program.
- Update speed: Changes the speed at which the NPR numeric value will update. The value of the update speed corresponds to the number of times per second the value will update. I.e. 1 means an update rate of once per second, while 10 means the value is updated 10 times per second.

4

Measurement and Data Processing Methodology

This chapter describes the setup and data analysis of all measurement systems used during the test campaigns, as well as the specific tests that were performed. It is decided to use total pressure and total temperature, strain and nozzle wall pressure measurements, in combination with schlieren imaging, digital image correlation and particle image velocimetry to obtain data about the flow field in the nozzle. Moreover, the accuracy of measurement of the separation location by means of wall pressure measurements is deemed sufficient in order to compare the data of this study with existing literature. The test procedures are provided in Appendix E.

4.1. Pressure, Temperature and Strain Measurements

This section describes the setup used to measure the total pressure, total temperature, nozzle wall pressure and strain.

4.1.1. Total Conditions

The IFM PT5402 pressure transmitter ¹, shown in Figure 4.1a, is used to measure the total pressure in the settling chamber. It is a threaded sensor with a 1/4" BSP external thread that can be directly screwed into the settling chamber. The measurement range reaches to 100 bar, the design pressure of the setup. It is a current sensor that outputs an analogue current signal between 4 and 20 mA that is practically linearly proportional to the pressure on the membrane (with an offset of 0.1 bar over the entire measurement range). The precision of the sensor between different measurement campaigns lies within 0.05 bar. A Mensor 8100 pressure calibrator available at the faculty was used to perform sensor calibration, the data of which is provided in Appendix C. This resulted in the following equation to convert the measured current to pressure

$$p[\text{bar}] = 6269.83I[A] - 24.02 \quad (4.1)$$

The IFM TM4431 Pt100 temperature sensor, shown in Figure 4.1b, is used to measure the total temperature in the settling chamber. It is a 4-wire, resistance temperature detector (RTD) type sensor with an external thread such that it can be directly screwed into the 1/2" BSP hole in the settling chamber (see Figure 4.1b), with a temperature range of -40 to 150 °C. This means it is easily capable of measuring the expected temperature of around 0 °C in the settling chamber. The sensor is specifically designed to operate in high-pressure environments, and as such it can handle pressures of up to 160 bar. The accuracy of the sensor is dependent on the temperature according the DIN-EN 60751 standard class A, which means the sensor adheres to Equation 4.2.

$$\delta T = 0.15 + 0.002|T| \quad (4.2)$$

¹<https://www.ifm.com/nl/nl/product/PT5402>

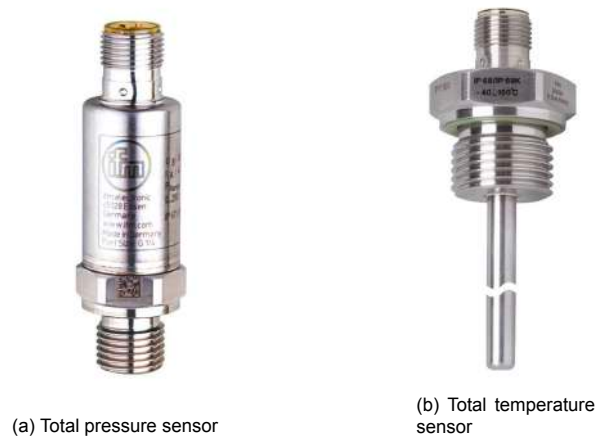


Figure 4.1: Total condition sensors

Pt100 sensors work with a resistance that varies with temperature. A known current excitation is sent by the NI9219 module, and the resulting voltage is measured. From this measurement the resistance of the sensor can be determined. The 100 in Pt100 corresponds to the resistance of the sensor at 0 °C, namely 100 Ω. The temperature can be computed from the measured resistance using the Callendar-Van Dusen equation

$$R = R_0 (1 + AT + BT^2 + C(T - 100)T^3) \quad (4.3)$$

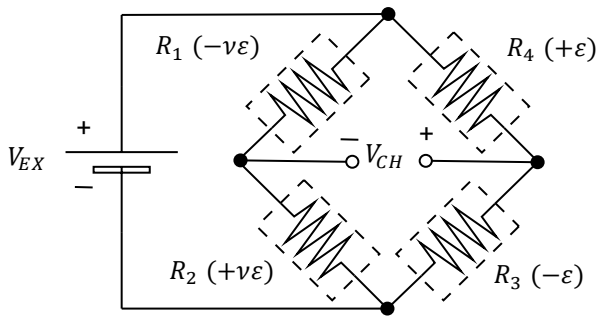
where R_0 is the resistance at 0 °C. The constants in this equation are standardised for Pt100 sensors according to the DIN-EN 60751² standard, where $A = 3.908 \cdot 10^{-3} \text{ } ^\circ\text{C}^{-1}$, $B = -5.775 \cdot 10^{-7} \text{ } ^\circ\text{C}^{-2}$ and $C = -4.183 \cdot 10^{-12} \text{ } ^\circ\text{C}^{-4}$.

4.1.2. Strain Gauges

Two full strain gauge bridges are installed on the strain tube in order to measure the side loads on the nozzle. The full bridges are of Type II configuration, as shown in Figure 4.2a. In this configuration, two strain-gauges are mounted in the direction of the bending strain, on opposite sides of the strain tube. Another pair of strain gauges are placed perpendicular to the direction of the bending strain on opposite sides of the strain tube and as such act as Poisson gauges. The advantage of this configuration is that it automatically corrects for expansion and contraction of the strain tube, which can occur due to temperature fluctuations or pressure loads when running the system. One full bridge is placed in the vertical direction to measure vertical bending stress, and the other is placed in horizontal direction. The full bridge measures the voltage between the two sides of the full bridge. Since the strain gauges have varying resistance when strained, one side of the bridge will be in compression and the other in tension, the measured voltage can be related to the strain, and subsequently to the applied moment.

Eight Kyowa KFGS-5-120-C1-23 strain gauges coming from the same batch are used in the full bridges. They are applied by hand, with the gauges in the bending strain direction positioned with their centre line at 12 mm from the upstream flange of the strain tube, and the Poisson gauges positioned with their centre line 24 mm from the upstream flange of the strain tube. These positions were used for practical reasons when gluing the strain gauges. The longitudinal gauges are positioned further upstream to improve the sensitivity of the full bridge. This is shown in Figure 4.2b. The properties of these strain gauges are presented in Table 4.1.

²<https://www.nen.nl/nen-en-iec-60751-2008-en-127819>



(a) Schematic of Type II full bridge. V_{EX} is the excitation voltage, while V_{CH} is the measured voltage. R_1 and R_2 are the poisson gauges, R_3 and R_4 are the bending gauges.



(b) Strain gauges attached to strain tube

Figure 4.2: Strain gauges

Table 4.1: Kyowa Strain gauge properties

Property	Value	Unit
Gauge factor	$2.13 \pm 1\%$	-
Gauge length	5	mm
Gauge resistance	$120.2 \pm 0.2\%$	Ω
Transverse sensitivity ratio	0.4	-

Since no integral module of longitudinal and transverse gauges was available, individual strain gauges were glued to the strain tube by hand. The strain gauges are calibrated using known weights with the load applied at the aluminium nozzle throat at a distance of 121 mm from the longitudinal gauges' centre line. This way, the variation in output voltage for a known moment around the bending strain gauges can be determined, such that the moment generated by the side load can be measured. For vertical load calibration, the weights are hung directly from the throat of the nozzle, while for the horizontal load calibration, a pulley is used in order to change the direction of the load from vertical to horizontal. The coordinate system shown in Figure 4.11 is used, with vertical loads being positive upwards, and horizontal loads being positive to the right when viewed from downstream of the nozzle. The calibration data is provided in Appendix C, and results in the following conversion from voltage to load if the load (in gram) is applied at the throat

$$\text{Horizontal: Weight}[g] = 6.4296 \cdot 10^7 [\epsilon] + 1.1013 \cdot 10^4 \tag{4.4}$$

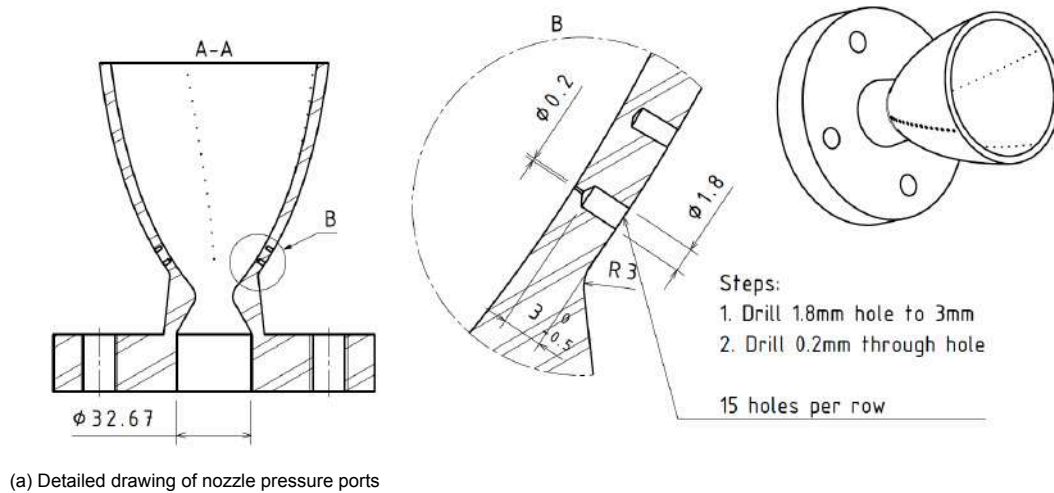
$$\text{Vertical: Weight}[g] = -5.4039 \cdot 10^7 [\epsilon] - 6.4786 \cdot 10^3 \tag{4.5}$$

$$\tag{4.6}$$

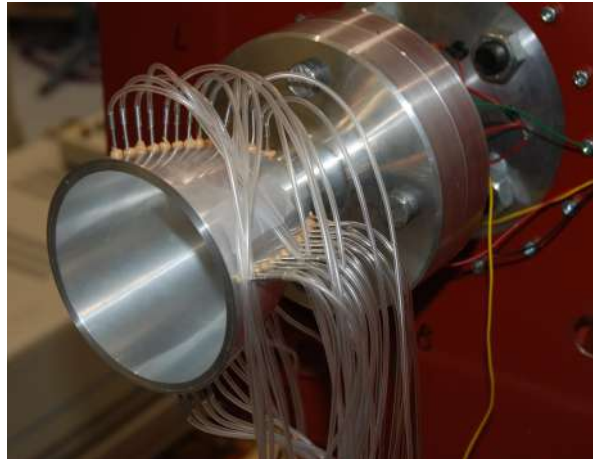
4.1.3. Wall Pressure Measurements

As stated in subsection 3.4.3, the nozzle contains 45 0.2 mm holes in the nozzle wall in three longitudinal arrays spaced 90° along the nozzle circumference. Figure 4.3a shows a detailed section of one of the pressure ports. It can be seen that the hole can be divided in two sections, one with a diameter of 0.2 mm which is 1.5 mm deep, and the other with a diameter of 1.8 mm diameter and with a depth of 3 mm. The 1.8 mm diameter section is used to glue a short steel tube into the hole. Two component epoxy glue is used to glue 1.6 mm stainless steel tubes of approximately 2 cm length into the pressure ports. 1.6 mm inner diameter rubber tubing can be connected to these, while the other end can be connected

to the Scanivalve pressure scanners. A close up of these is shown in Figure 4.3b.



(a) Detailed drawing of nozzle pressure ports



(b) Close up of plastic tubing connected to nozzle pressure ports

Figure 4.3: Nozzle pressure ports

Three Scanivalve DSA3217-PSP pressure scanners are used to measure the local wall pressure in the nozzle. These sensors are differential pressure sensors, meaning that the atmospheric pressure needs to be recorded in order to convert the data to actual pressure values. Each day the sensors are zero-calibrated against the daily atmospheric pressure in order to measure the gauge pressure correctly. One pressure scanner contains 16 pressure sensor ports which can measure gauge pressure at a maximum rate of 500 Hz. In all of the pressure scanners, one of the ports is left unconnected to measure the local atmospheric pressure during operation. This might be different from the stationary atmospheric pressure, because the nozzle flow attracts a significant amount of air from the surroundings, especially at high NPR when the jet is extremely overexpanded. This causes the local atmospheric pressure to drop below the stationary atmospheric pressure, which changes the NPR. A pressure scanner is shown in Figure 4.4.

The software to operate the pressure scanners, ScanTel, is supplied by the Scanivalve company as well. Several settings of the scanner can be changed using this interface. The settings used during the tests are provided in the procedures presented in Appendix E. The data is written to a data file with a timestamp in microseconds. This is important for the combination of the data with the total pressure, total temperature and strain measurements. Through this interface, the pressure scanners can be triggered to start measuring manually, or can be set into a trigger mode such that they only start measuring when a trigger signal is received. In the current experiments, it is required to synchronise the measurements of the total quantities, strain and local wall pressure in order to be able to combine them.



Figure 4.4: ScaniValve 3217 pressure scanner (courtesy of Scanivalve)

A disadvantage of using the remote trigger, is that the pressure scanners only take one measurement when a voltage ramp in the trigger signal input is detected. Thus, if only one trigger signal would be sent, only one pressure measurement would be taken. Therefore, it is required to use a square wave signal generator to generate a ramp at the required measurement rate of 500 Hz. The scanner automatically stops taking measurements when the set number of measurements is reached, which means that this can also be synchronised with the time of stopping measurement of total quantities and strain.

4.1.4. National Instruments Modules

In order to read out the outputs from the total pressure, total temperature sensor and the strain gauges, A/D data acquisition modules built by National Instruments are used. These modules are specialised in reading analogue or digital output sensors, and have the capability of extremely high sampling rates. However, this is not required for the current experiments. The total pressure is read out using a NI9207³. This is a general purpose module which is capable of measuring analogue voltage or current input sources. This module does not have an internal power supply, which means that an external power supply is used to power the pressure sensor as discussed in section 3.8. The total temperature is measured using the NI9219 module⁴. This module is specifically made for temperature sensors and strain gauges. It has an internal current excitation source, which can be used to determine the change in voltage from the temperature variable resistance in the temperature sensor.

The voltage from the strain gauges is measured using an NI9237 module⁵. This is a module specifically made for strain gauge measurements. This module has an internal excitation voltage source which can supply variable voltage depending on the resistance of the strain gauges. In this case, an excitation voltage of 5V is selected in order to keep the current running through the strain gauges within their operation limits. With an input range of ± 25 mV/V this means that the maximum voltage over the full bridge that can be measured is 150 mV. In order to improve the measurement sensitivity and increase the SNR, the full bridge can be balanced with an additional resistance on either side of the bridge in order to make sure that the measured voltage when no strain is applied is very close to zero. Due to lack of time this could not be done for these experiments. An NI9481 relay module is used to switch the main valve and the trigger signal on and off. The LabView software, also developed by National Instruments, is used to interact with the modules. The data is stored in a single text file for each run.

³<https://www.ni.com/pdf/manuals/375206d.pdf>

⁴<https://www.ni.com/pdf/manuals/374473f.pdf>

⁵https://www.ni.com/pdf/manuals/374186a_02.pdf

4.1.5. Data Post-Processing

Since the data of the total pressure, total temperature and strain is not measured at the exact same time as the wall pressures from the Scanivalves, some post-processing is required in order to assign total conditions and strain from the LabView measurements to a specific wall pressure distribution from the Scanivalves. When the data rate of the total conditions is different from the Scanivalves, the same procedure can be used to combine the data. This processing makes sure that the data from the total pressure and total temperature sensors and the strain gauges is exactly synchronised with the data from the Scanivalves. Linear interpolation of the total conditions is used to determine their value at the timestamps of the Scanivalve measurements. The calculated total pressure is then divided by the average pressure measured by the ambient port on each of the three Scanivalve pressure scanners to determine the NPR. The moving average of the data is taken with a period of 50 data points in order to reduce potential errors.

Since the spacial resolution of the wall pressure sensors is low, the free interaction theory described in subsection 2.3.2, is used to improve the resolution. Instead of just taking the location of the last pressure sensor with a pressure well below the plateau pressure as the separation point, the free interaction theory allows for the relatively accurate determination of the location of the separation, also when this locations lies between pressure ports. Recall the main equation in free interaction theory

$$F(s, p') = \sqrt{\frac{p(x) - p_i}{q_i} \frac{\bar{v}(x) - v(x)}{C_{fi}}}, \quad s = \frac{x - x_i}{x_s - x_i} \quad (4.7)$$

where F is the correlation function taken from experimental data provided by Östlund. [11] Östlund defines the separation point at the location where the correlation function is equal to 4.22, while the plateau point is defined as the location where the correlation function is equal to 6. The generalised correlation function is defined for $s \in [0, 3.6]$, such that a pressure curve can be drawn with $x \in [0, 3.6(x_s - x_i)]$. There are two independent variables that are unknown in this case: the incipient separation point x_i , the real separation point x_s and one dependent variable: the local pressure at location x , $p(x)$. All the other terms in the equations are a function of the incipient separation point and the x -coordinate. The Prandtl-Meyer angle v is defined as

$$v = \sqrt{\frac{\gamma + 1}{\gamma - 1}} \tan^{-1} \sqrt{\frac{\gamma - 1}{\gamma + 1} (M^2(x) - 1)} - \tan^{-1} \sqrt{M^2(x) - 1} \quad (4.8)$$

The Mach number can be calculated from the isentropic flow equations for a known static to total pressure ratio. $\bar{v}(x)$ is the Prandtl-Meyer angle at location x if separation had not occurred. The pressure ratio at location x can in this case be determined from linearly interpolating the TDK data for this nozzle contour. $v(x)$ is the Prandtl-Meyer angle in the case where separation does occur and so the pressure at location x is unknown in this case. However, this does not add an additional unknown to the problem since $p(x)$ already was an unknown dependent variable. Finally, the skin friction coefficient at the incipient separation location can be estimated using Prandtl's 1/5th power law [118]

$$C_f = 0.058 Re_x^{(-1/5)} \quad (4.9)$$

The Reynolds number is determined by taking the ideal flow conditions at the incipient separation point x_i from the TDK simulations. The viscosity is determined using Sutherland's law

$$\frac{\mu}{\mu_0} = \left(\frac{T}{T_0}\right)^{\frac{3}{2}} \frac{T_0 + 111}{T + 111} \quad (4.10)$$

For air $\mu_0 = 1.716 \cdot 10^{-5}$ Pa s and $T_0 = 273$ K. For a specific x_i and x_s , Equation 4.7 can then be numerically solved to determine $p(x)$ for each x , which can then be used to draw a pressure distribution on top of the experimental pressure data. When iterating over many potential values of x_i and x_s , it is possible to find a pressure distribution that has the lowest squared residual and thus fits the data best. Taking this curve and determining at which x location the correlation curve has a value of 4.22 results in the actual separation location.

It was found that the direct use of the $1/5^{\text{th}}$ power law did not yield pressure distributions that fit the data well, because the pressure curve is relatively sensitive to changes in the skin friction coefficient. Thus, the skin friction coefficient was lowered for all cases by a constant factor of 0.75, which resulted in a much better fit of the curve to the experimental data. There are several reasons why this is justified.

- The $1/5^{\text{th}}$ power law was derived for flat plate boundary layers, while in the current study an adverse pressure gradient is present at the incipient separation location. Since the flow starts separating, the skin friction will be lower than the one estimated by the $1/5^{\text{th}}$ power law.
- There is no information about the upstream development of the boundary layer properties, while the derivation of the $1/5^{\text{th}}$ power law relies on the predictable development of the boundary layer in flat plate flows. Moreover, the presence of the internal shock just downstream of the throat means that the boundary layer thickness at the throat is even unknown and definitely not zero.
- A smooth wall is assumed, while it is likely that the nozzle is better modelled as a rough wall, which would increase the skin friction coefficient. However, this factor is deemed much less influential than the first argument of this list.

An example of a fit of the correlation curve to the measurement data is shown in Figure 4.5. It can be seen that the curve fits the data very well, and that the separation point lies somewhere between the 5th and 6th pressure port.

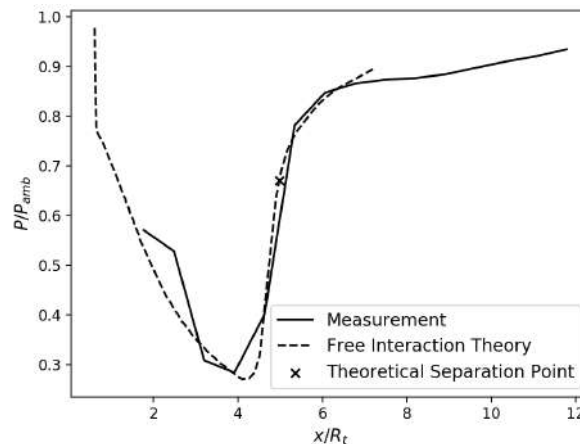


Figure 4.5: Free interaction correlation curve fit to data obtained at NPR 24.03

4.2. Schlieren Imaging Setup

Schlieren imaging is one of the most important imaging techniques used in compressible flow experiments. Schlieren imaging is a non-intrusive full-field flow visualisation technique that provides insight into the density variations in the flow. In the case of schlieren, the pixel intensity in an image is proportional to the spatial derivative of density, $\nabla\rho$. This means that locations with rapid density variations, such as shocks, will be clearly visible on schlieren images. Schlieren imaging is a qualitative visualisation method. This visualisation technique was selected for the test campaign because schlieren imaging can give a good idea about the flow state (i.e. FSS or RSS), such that the transition point can easily be determined. Moreover, a high speed camera allows for the visualisation of pseudo-instantaneous flow, which can be used during transition to determine whether asymmetric transition is present. Finally, the system is relatively easy to set up, while it can provide great insight into the flow structure.

4.2.1. Working Principle

Schlieren imaging relies on the fact that the refractive index of a compressible medium, such as air, is a function of its density. The change in refractive index, n , is captured in the Gladstone-Dale relation. [30]

$$n = 1 + K\rho \quad (4.11)$$

where K is the Gladstone-Dale constant ($2 \cdot 10^{-4} \text{ m}^3/\text{kg}$ for air). From Snell's law $n_1 \sin \theta_1 = n_2 \sin \theta_2$, it is known that light rays bend at the boundary between two substances with different refractive index. This fact is exploited by the schlieren imaging technique. When a light is shone through a flow with density gradients, and so gradients in refractive index, light rays are bent in the direction of this gradient. This light is focused using a parabolic mirror and part of the light is blocked by a schlieren knife before it reaches the camera CCD. In a flow with density gradients, part of the light that would normally be blocked passes through the schlieren knife because it was bent due to the density gradients in the flow. On the other hand, light that would have normally passed can now be blocked. This causes a change in light intensity at the camera CCD, which results in the visualisation of density gradients. The change in intensity of a hypothetical square light source at a horizontal schlieren knife can be calculated using Equation 4.12.

$$\frac{\Delta I}{I} = \frac{f}{a} KW \frac{\partial \rho}{\partial y} \quad (4.12)$$

where f is the focal length of the camera, a is the fraction of light passing the knife edge and W is the width of the light source. [30] It can be seen that the intensity when using a horizontal schlieren knife is only proportional to the density gradient in vertical direction. In similar fashion, the intensity when using a vertical schlieren knife is only proportional to density variations in horizontal direction. This means that the flow should always be visualised with the schlieren knife in both directions because important features might not be visible in either one. It can also be seen that as more light is blocked, the fraction of light getting through, a , is reduced and so the sensitivity of the intensity to density variations increases.

4.2.2. Setup

The schlieren setup used in the experiment is positioned in a Z-configuration because of space constraints. A schematic is shown in Figure 4.6. A continuous light source shines through a lens which focuses the light into a pinhole. The pinhole ensures that the light is emitted from something very close to a point source, which makes sure that parallel light rays enter the flow. The pinhole is located at the focal point of a 1500mm parabolic mirror. The light then passes in parallel rays through the nozzle flow. The PIV tube is intentionally excluded from the setup, in order to prevent interference from the polycarbonate plates with the incoming light. An equal parabolic mirror is placed after the light has passed through the flow. The schlieren knife is placed in the focal point of the mirror. It was found that a large portion of the light had to be blocked because the images would become overexposed otherwise.

A photron fastcam SA1.1 at 1000 fps with a shutter speed of $1/12,000$ s was used as the camera⁶. A single measurement at 12,000 fps was also performed during the transition. The camera has a square aspect ratio CMOS sensor of 1024x1024 pixels with a pixel size of $20 \mu\text{m}$. The image size has to be reduced to 512x512 pixels for the 12,000 fps measurement. 8 GB of internal storage allow for a filming time of approximately 5 seconds at 1000 fps. 300 images are obtained per test case.

⁶<https://photron.com/fastcam-sa1-1/>

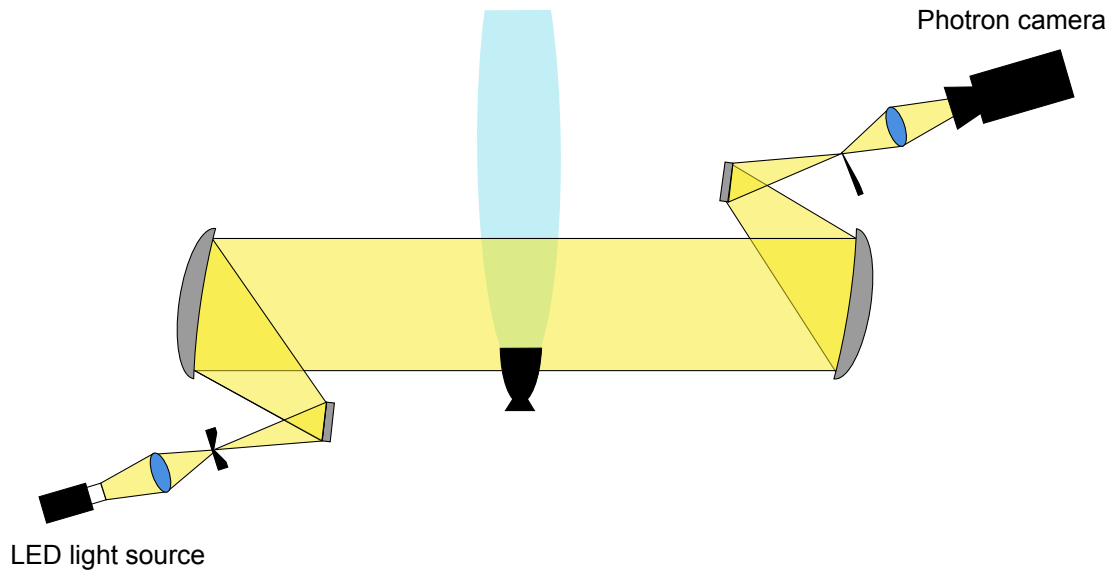


Figure 4.6: Schematic of schlieren imaging setup

In order to synchronise the pressure and schlieren measurements, the signal that triggers the start of the pressure measurements is also used to trigger the start of the recording.

4.2.3. Data Processing

To be able to identify any features on the images, their brightness has to be increased. This is done by raising the intensity of each pixel value through the following equation

$$I_{\text{new}} = \frac{I_{\text{old}} - \min(I)}{\max(I)} \cdot BF \quad (4.13)$$

where $\min(I)$ and $\max(I)$ are the minimum and maximum pixel intensity in the entire image respectively. BF is the brightness factor which should be selected by trial and error until the required brightness is achieved. The average intensity of each pixel is then obtained by adding all intensities of a single pixel in each image and dividing by the number of images. The standard deviation can be calculated using

$$\sigma = \sqrt{\frac{\sum_{i=0}^n (I_i - \bar{I})^2}{n - 1}} \quad (4.14)$$

Both the average intensity field and its standard deviation can be normalised with respect to their highest value, such that $I \in [0, 1]$. These results can be converted back to real images or a contour plots can to analyse the data.

4.3. Digital Image Correlation

Digital image correlation (DIC) is a measurement technique that is used to determine the full-field deformation and strain of solid components. Similarly to PIV, one can determine the deformation of a component by comparing an image of the component in the deformed state to an image in the undeformed state. Tracking dots are placed on the component which can be used to construct a correlation map between the calibration and instantaneous image. This allows for the determination of 2D or 3D displacement depending on the number of cameras used. Because of time constraints, it is decided to only measure the deformation of the nozzle lip. Despite the limited scope, this data does allow for the determination of the modal frequencies of the azimuthal nozzle shapes at the lip as well as the displacement energy per mode. In future research this data could for instance be used to dampen a specific mode that has the highest energy. In this research, only the radial displacement of the nozzle wall is of interest. Therefore, tracking dots are not required and the lip can be detected using solely the pixel intensity if the contrast between the nozzle lip and the rest of the image is large enough.

4.3.1. Setup

The same photron fastcam SA1.1 that is used in the schlieren setup is also used in the DIC setup. Because the vibrations of the nozzle lip are expected to occur in the same order of magnitude as the shock unsteadiness frequency in the nozzle, the frame rate of the camera is set to 1000 fps. With this frame rate, vibrational frequencies of up to the Nyquist frequency of 500 Hz can be resolved. To make sure enough light hits the CCD, two large LED spot lights are used to illuminate the nozzle lip.

The camera cannot be positioned directly downstream of the nozzle because it would be damaged by the nozzle flow. Therefore, it is placed as far downstream as possible at a slight horizontal offset relative to the nozzle flow. If the lens would be put directly on the camera, a large aperture, and thus a low depth-of-field, would result in part of the image being out of focus because one side of the nozzle is closer to the camera than the other. This is why a scheimpflug is required. A scheimpflug allows for the rotation of the plane of focus of the image, such that this can be put parallel to the nozzle lip even though the camera is at an angle. This way, the entire nozzle lip can be in focus. The plane of focus corresponds to the plane which intersects the lens plane and the image plane at a single point. This is shown in Figure 4.7. [28] The lens can be rotated until the plane of focus overlaps with the nozzle lip.

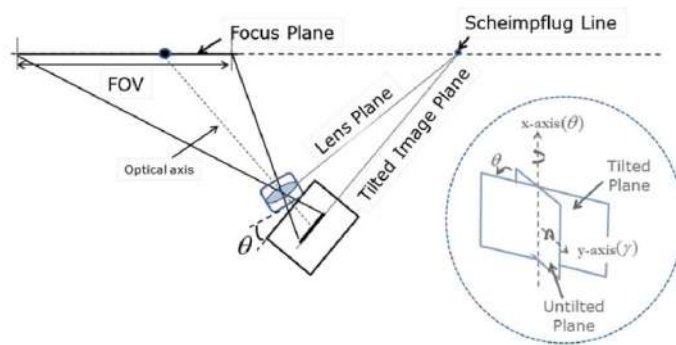


Figure 4.7: Schematic of the scheimpflug principle [28]

A schematic of the DIC setup is shown in Figure 4.8. A polycarbonate shield is used to protect the camera from the flow. The DIC setup can also be used with the PIV tube installed, such that the differences in vibrations can be measured between PIV tube on and off configurations. The diffuser outlet is the main limitation with regards to how large the offset between the camera and the nozzle lip has to be. The nozzle lip is painted white in order to maximise the contrast between the nozzle lip and the rest of the image.

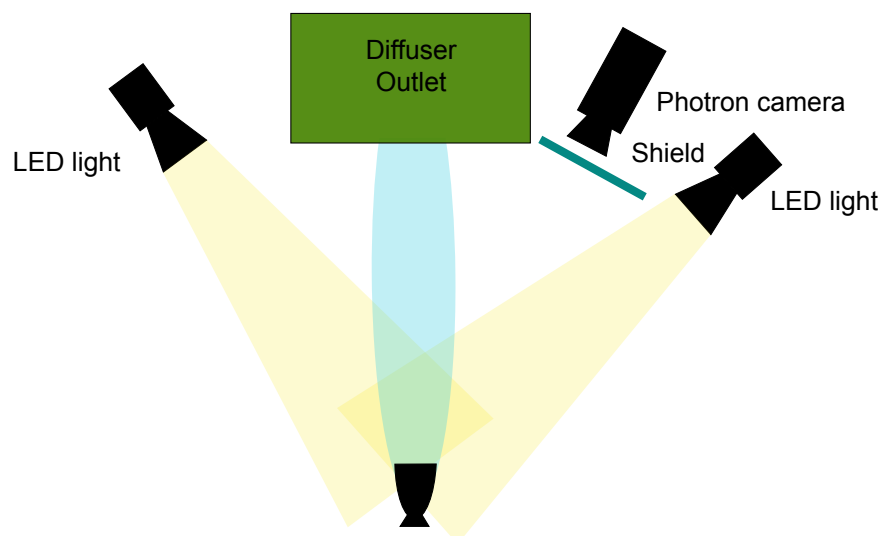


Figure 4.8: Schematic of DIC setup

4.3.2. Data Processing

The schiefpflug does not automatically correct for the perspective distortion that is a result from the offset of the camera. This distortion will have to be digitally removed during post-processing. The same brightness change as for the schlieren images is performed on the DIC images to make sure the nozzle lip brightness is constant for each image. Afterwards the image has to be corrected for the perspective warping caused by the offset of the camera. Because the camera is positioned at the same height as the nozzle, the image is only warped in horizontal direction. Criminisi et al. [29] describe a method for the perspective transform. This method maps points from the image plane onto the world plane. The advantage of this type of transform is that it maps straight lines on the image planes to straight lines on the world plane, unlike other transforms that can introduce image distortions. The transform is shown in Figure 4.9.

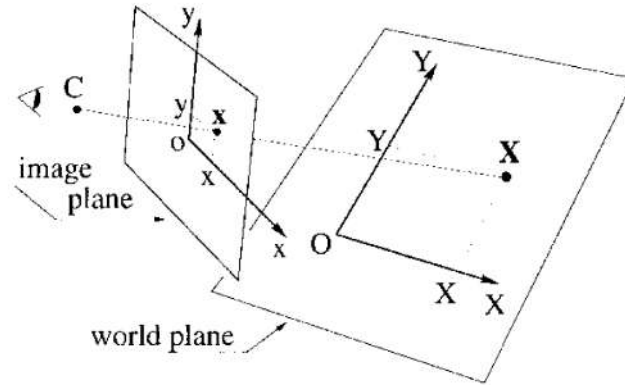


Figure 4.9: Schematic of the plane camera model [29]

It can be seen that the coordinates on the image plane x, y are mapped onto the world plane coordinates X, Y . The premise of this transform is that this mapping of coordinates can be written as $\mathbf{X} = H\mathbf{x}$, where \mathbf{X} is the vector of world plane coordinates, \mathbf{x} is the vector of image plane coordinates, and H is a transformation matrix. This equation can be expanded to

$$\begin{bmatrix} X \\ Y \\ W \end{bmatrix} = \begin{bmatrix} a & b & c \\ d & e & f \\ g & h & 1 \end{bmatrix} \begin{bmatrix} x \\ y \\ 1 \end{bmatrix} \quad (4.15)$$

which results in the following transformation equations

$$X = \frac{ax + by + c}{gx + hy + 1} \quad (4.16)$$

$$Y = \frac{dx + ey + f}{gx + hy + 1} \quad (4.17)$$

which can be rewritten to the following system of linear equations

$$\begin{bmatrix} x_1 & y_1 & 1 & 0 & 0 & 0 & -X_1x_1 & -X_1y_1 \\ 0 & 0 & 0 & x_1 & y_1 & 1 & -Y_1x_1 & -Y_1y_1 \\ x_2 & y_2 & 1 & 0 & 0 & 0 & -X_2x_2 & -X_2y_2 \\ 0 & 0 & 0 & x_2 & y_2 & 1 & -Y_2x_2 & -Y_2y_2 \\ \vdots & \vdots & \vdots & \vdots & \vdots & \vdots & \vdots & \vdots \\ x_n & y_n & 1 & 0 & 0 & 0 & -X_nx_n & -X_ny_n \\ 0 & 0 & 0 & x_n & y_n & 1 & -Y_nx_n & -Y_ny_n \end{bmatrix} \begin{bmatrix} a \\ b \\ c \\ d \\ e \\ f \\ g \\ h \end{bmatrix} = \begin{bmatrix} X_1 \\ Y_1 \\ X_2 \\ Y_2 \\ \vdots \\ X_n \\ Y_n \end{bmatrix} \quad (4.18)$$

which is a system of linear equations of the form $A\boldsymbol{\lambda} = \mathbf{b}$ and it is solved using the pseudo-inverse by Criminisi et al.

$$\boldsymbol{\lambda} = (A^T A)^{-1} A^T b \quad (4.19)$$

where, in this case, $\boldsymbol{\lambda}$ is the vector of transformation coefficients. Because eight transformation coefficients are unknown, eight equations are required to solve, and so four calibration points on the image plane of which the location on the world plane is known are required to find the transformation coefficients. An image of the nozzle without flow including fiducial markers can be used to determine the magnification factor. Once the transformation coefficients are known, Equation 4.16 and Equation 4.17 can be used to transform all coordinates from the image plane to the world plane.

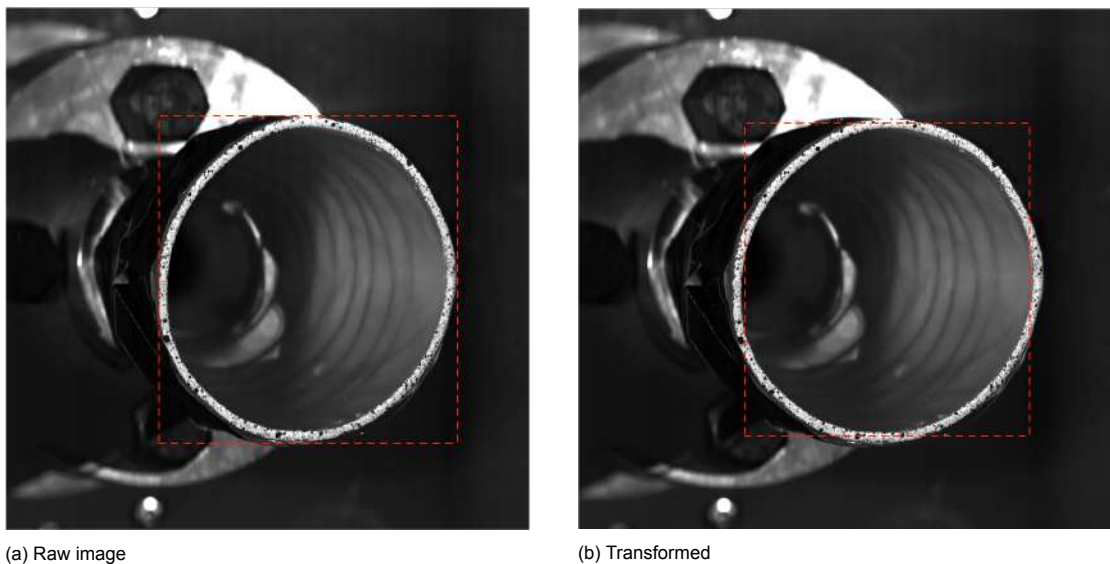


Figure 4.10: Perspective Transform on DIC images at NPR 2

Figure 4.10 shows the same DIC image before and after the transformation. It is clearly visible that in the raw image the nozzle is slightly ovalised in vertical direction, while in the transformed image the nozzle is almost round. What can also be concluded from these images is that there is not sufficient contrast in the image such that the pixels that make up the nozzle lip are the only ones above a certain high intensity level. This means that a more complicated algorithm has to be used in order to determine the location of the nozzle edge.

In this case, a centre point is manually selected in the first image of a test case. This centre does not have to be extremely precise, because it is only used to determine the relative x, y position of points on the nozzle lip, and the real centre is mathematically determined. The relative centre then defines the coordinate system for its specific test case. The coordinate system is shown in Figure 4.11.

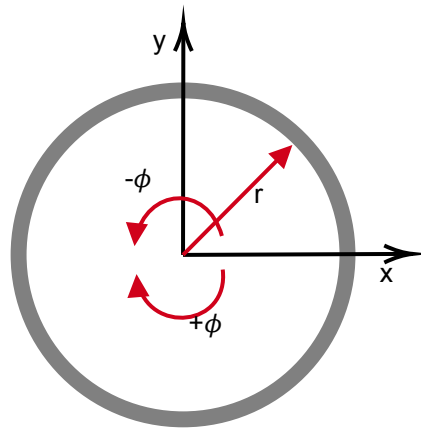


Figure 4.11: Nozzle coordinate system

Each pixel is given a pixel number relative to the image centre. These are then converted to the x, y -coordinates in mm using the known number of pixels per mm taken from the calibration images. These are then converted to polar coordinates using $r = \sqrt{x^2 + y^2}$ and $\phi = \tan^{-1}(y/x)$. This results in $\phi \in [-\pi, \pi]$ rad, with the zero point on the positive x -axis.

Once the coordinates have been determined, the image can be divided in a number of sections n such that $\Delta\phi = 360/n$. The pixel intensity is then calculated as the average of the colour intensity as described by Equation 4.20 of all the pixels within the range $r < r_{\text{pixels}} < r + \Delta r$, where Δr is selected to be equal to the number of pixels per mm and iterated from $r = 0$ until the image edge.

$$I = \frac{1}{n_{\text{pixels}}} \sum_r^{r+\Delta r} \frac{1}{3} (I_R + I_G + I_B) \quad (4.20)$$

Normally, the image centre is not exactly in the centre of the image (i.e. pixel 512x512). In this case the shortest distance to an image edge is taken as the maximum radius of the iteration and it is assumed that the lip lies within this maximum r for all ϕ . An example plot of the intensity normalised with a maximum average intensity of 255 as a function of radius is shown in Figure 4.12.

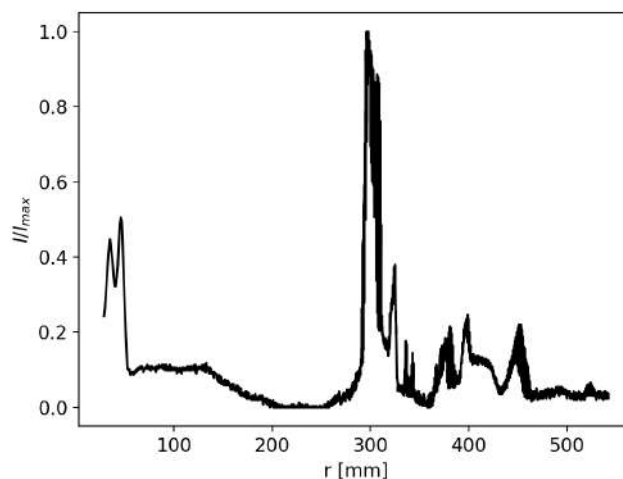


Figure 4.12: Intensity variation with radius from image centre

It can be seen that in this section of the nozzle the intensity is relatively low everywhere apart from the large peak around a radius of 300mm. This peak indicates the lip. The first pixel that reaches a

value above a certain threshold, which in this case was set to 0.75, is designated as the inner wall of the nozzle lip. The centre of the nozzle lip can then be determined by adding half the wall thickness to the radius of the inner wall. This approach could result in problems if high intensity reflections are present inside the nozzle, since the intensity can show two or more peaks before reaching the actual peak of the nozzle lip. Luckily, the amount of reflections in the nozzle is fairly minimal and normally lie close to the centre. Therefore, an easy fix of only detecting peaks when present at a minimum radius of 250mm can be used to filter out the reflections. For reflections close to the nozzle lip, a condition of a maximum variation of the radial position of the lip of 5 pixels is set. The detected point on the nozzle lip is then translated to lie on the centre line of its specific section. Choosing a section size of 2° , this analysis results in image detection such as displayed in Figure 4.13.



Figure 4.13: Lip detection for a section size of 2°

In the case that the centre of the nozzle moves too much over the duration of the test, the peak detection boundaries presented above might result in the fact that no peak is found at all, because the selected image centre is not at all close to the approximate centre of the nozzle in a specific image some time later. In this case, an adaptive image centre is used, where the centre point is varied in the case that no peaks are detected. After analysing all images of a test case, the real centre position of the nozzle is defined as follows

$$\Delta x, \Delta y = \min \left(\sum_{i=1}^n (\bar{r}_i - \bar{r})^2 \right) \quad (4.21)$$

where \bar{r}_i is the average radial coordinate of the nozzle lip in section i , and \bar{r} is the average radial coordinate of all sections combined. Iterating over the shift in x and y position, Δx and Δy , relative to the initially selected centre point and calculating the sum of squared residuals makes it possible to find the least squares centre shift. The real centre position then becomes $x = x_{in} + \Delta x$ and $y = y_{in} + \Delta y$. This centre can also be related to a common centre, which is the centre of the calibration image, using a simple coordinate transformation. This means that the constant offset of the nozzle relative to the no-flow condition can also be visualised.

4.3.3. Modal Decomposition

The aforementioned data analysis method results in a list of lip section radial coordinates in time, $r(\phi, t)$. Additional insight into the specific vibrations of the nozzle can be gained by Fourier transforming the data both in time as well as in azimuth. When Fourier transforming along the azimuth for a given instant in time, we obtain

$$\rho(m, t) = \mathcal{F}(r(\phi, t))$$

The Fourier transform in azimuth provides a list of complex mode coefficients, with mode numbers running from the negative to positive azimuthal Nyquist wave number, $m \in [-k_n, k_n]$. The coefficients are ordered according to mode number in the following way: $m = [0, 1, 2, \dots, k_n, -k_n, \dots, -2, -1]$. Because of the circular shape of the nozzle the signal is perfectly periodic and the first and last point in $r(\phi, t)$ are the same. This means that in the case of 180 sections of 2 degrees, the azimuthal Nyquist wavenumber is 90 m^{-1} resulting in 181 Fourier coefficients. The coefficients of positive and negative mode numbers with the same magnitude form conjugate pairs, such that

$$\rho(m, t) = \rho^*(-m, t)$$

The imaginary component of the 0th mode is equal to zero because it represents the mean radius over all sections. This is why the 0th mode defines the breathing mode, in which the circular shape of the nozzle only changes in radius, as can be seen in Figure 4.14a. The individual nozzle vibrational modes can be determined from performing the inverse Fourier transform on the list of Fourier coefficients with all but the required mode number coefficients set to zero. For example, in case one only wants to know the first mode, all coefficients but 1 and -1 would be set to zero, and the inverse Fourier transform would be calculated with just the 1 and -1 mode number coefficients.

The designation of the mode numbers also give insight into the nozzle lip shape of each mode. Since mode 1 coefficients represent a single cosine and sine wave around the lip circumference, it can be easily visualised that the first mode should be directly connected to displacement of the entire nozzle lip in the same direction, as is shown in Figure 4.14b. This makes the first mode the only asymmetric mode which means it could be directly correlated to the measured side loads. The mode 2 coefficients represent two cosine and sine waves around the circumference, which means it is connected to the ovalisation of the nozzle (Figure 4.14c) and mode 3 coefficients represent three sine and cosine waves along the circumference (Figure 4.14d) etc.

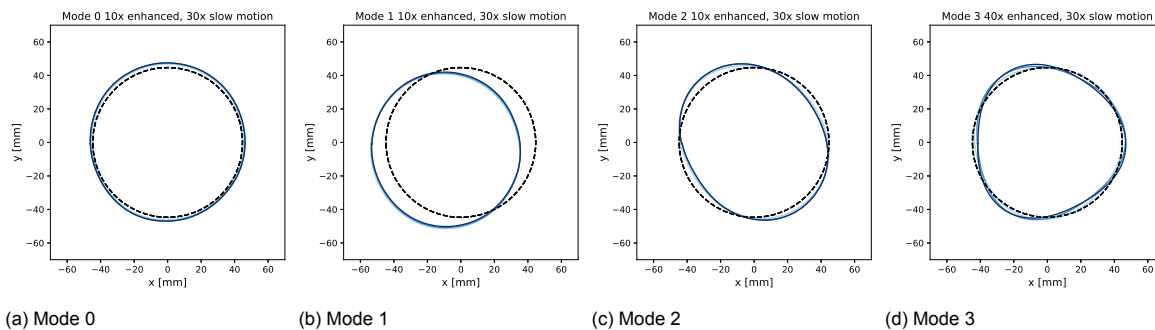


Figure 4.14: Mode shapes of different mode numbers

More information about each vibrational mode can be extracted when treating the Fourier coefficients as a time series. The energy embedded in a single mode can be defined as the variance of the time-dependent mode coefficients, analogous to the turbulence kinetic energy in turbulent flow. The energy in positive mode numbers represents the variance of the real part of the Fourier coefficient, while the energy in the negative mode numbers represents the variance in the imaginary part. In the case of the first mode shape this means that mode number 1 captures energy of the deflections from the mean in horizontal direction, while the energy of the deflections from the mean in vertical direction are captured in mode number -1. The same is true for mode 2, where horizontal ovalisation is captured by mode number 2, and vertical ovalisation is captured by mode number -2. The total energy in all modes combined can then be calculated using

$$E = \sum_m \overline{(\rho'_m)^2} \quad (4.22)$$

The energy in each mode as a fraction of the total energy can then be determined. Furthermore, if the Fourier coefficients, $\rho(m, t)$, are once again Fourier transformed but in time, where $P(m, f) = \mathcal{F}(\rho(m, t))$, the frequency spectra of individual modes can be determined. By means of Parseval's theorem, shown in Equation 4.23, the variance of the Fourier coefficients $\rho(m, t)$ is equal to the integral over all frequencies of the magnitude of its transform if the transform is normalised with the number of samples. The magnitude of the transform is written as the product of the transform and its complex conjugate. Because the spectrum is symmetric, the boundaries of integration can be changed from $[-f_n, f_n]$ to $[0, f_n]$ if the magnitude is multiplied by 2.

$$\overline{(\rho'_m)^2} = 2 \int_0^{f_n} P(f)P^*(f)df \quad (4.23)$$

It is common practice to plot the frequency interval on a logarithmic axis, which deduces from the intuitive visualisation of the amount of energy in a specific frequency range. Namely, in a linear plot the energy in a certain frequency range is directly proportional to the area under the frequency spectrum curve. However, this proportionality is removed when plotting the frequency with a logarithmic scale. In order to restore the proportionality, instead of directly plotting the magnitude of $P(m, f)$, the coefficients can be multiplied by the frequency interval, such that $fP(m, f)$, with f being the frequency vector, is plotted instead. This is a result of the property

$$\int_0^{f_n} P(f)P^*(f)df = \int_0^{f_n} P(f)P^*(f)f d \log f$$

A 5% bandwidth moving filter is used to smooth the data.

4.4. Particle Image Velocimetry

Particle Image Velocimetry (PIV) is a full field, non-intrusive measurement technique that can be used to generate velocity vector fields. A laser sheet is used to illuminate seeding particles present in the flow, which are tracked by a camera in order to deduce the velocity. In planar PIV, which is used in this study, a single camera is used to obtain a 2D velocity field with two velocity components, u and v . Stereographic PIV allows for the determination of the third velocity component in the 2D flow field as well. With tomographic PIV the entire 3D flow field can be measured. Planar PIV is selected for this study because no previous PIV experiments known to the author have ever been performed. Additionally, the setup of a planar PIV system is relatively simple, whereas the setup of stereographic or tomographic PIV is much more intricate. Trying these PIV techniques could result in no data being obtained at all if problems with the setup arise, due to limited time in the wind tunnel. Proof of concept is therefore a large part of the PIV measurement campaign as well. PIV is performed because it will provide a better understanding of the velocity magnitude in the exhaust of the nozzle, which so far has only been simulated in CFD cases [18, 59, 119]. The PIV data can also provide validation data for these simulations. Compared to measurement techniques such as hot-wire anemometry (HWA) and laser doppler velocimetry (LDV), the main benefit of PIV is that it measures the entire flow field, instead of the velocity in a single location. The main drawback is that the temporal resolution of the PIV measurements is relatively low, which means that long measurement times are required. Moreover, visualisation of the instantaneous flow field is difficult because of the limited spatial resolution and spurious vectors.

4.4.1. Working Principle

A high power laser beam is passed through a series of mirrors and lenses in order to create a thin, but wide laser sheet that can illuminate a large amount of particles in a plane parallel to the imaging plane. The particles are illuminated twice by a laser pulse with a small time separation δt . When these two images are compared it can be seen that the particles have moved in the time δt . The velocity can then be determined from a known displacement and time difference. Figure 4.15 shows a schematic of a planar PIV setup.

Normally, the concentration of tracer particles ranges between 10^9 and 10^{12} particles/m³. Ideally, a tracer particle has good light reflective properties and moves with the exact same velocity as the flow. In reality, because the particles are very small, their dynamics are governed by the Stokes drag, i.e.

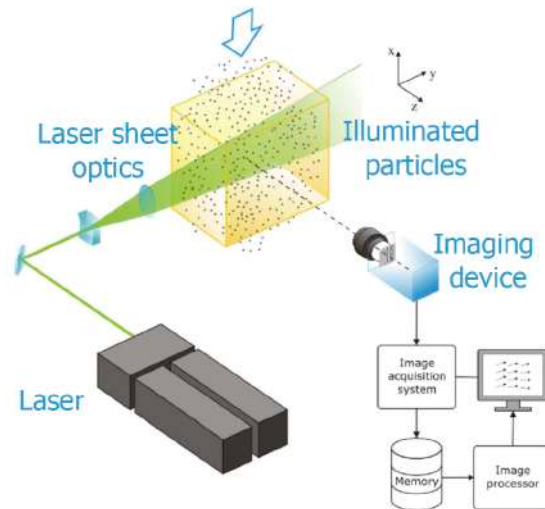


Figure 4.15: Schematic of planar PIV setup [30]

the viscous force on the particles. The difference in velocity between the particle and the flow can be estimated using [30]

$$\mathbf{V} - \mathbf{U} = \frac{2}{9} \frac{r_p^2 (\rho_p - \rho_{\text{fluid}})}{\mu} \frac{d\mathbf{V}}{dt} \quad (4.24)$$

From this equation, it can be concluded that particles with very high buoyancy, $(\rho_p - \rho_f)/\rho_f \ll 1$, are most suitable to follow the fluid flow. Assuming that the density of the solid particles in the flow is much larger than the density of the fluid, Equation 4.24 has a solution of the form

$$\mathbf{V}(t) = C_1 + C_2 e^{-\frac{t}{\tau_p}} \quad (4.25)$$

from which it can be concluded that the difference between the particle and flow velocity follows an exponential decay over time. How fast the velocity difference decays depends on the response time of the particle, τ_p , defined as

$$\tau_p = d_p^2 \frac{\rho_p}{18\mu} \quad (4.26)$$

A step change in the flow velocity, such as when passing through a shock, can thus never be tracked exactly by particles. The velocity of the particle will have changed 63% of the step change velocity of the flow ΔU in one particle response time. From this equation it can be concluded that in air flows with rapid velocity changes, the particle diameter and density should be as small as possible. This is quantified by the Stokes number, defined as

$$S_k = \frac{\tau_p}{\tau_f} \quad (4.27)$$

Scarano [30] states that a Stokes number of less than 0.1 should return good flow tracing with errors of less than 1%. In order to select an appropriate tracer particle material, an order of magnitude analysis is performed to estimate the Stokes number.

The flow characteristic time τ_f can be estimated using dimensional analysis, such that $\tau_f = L_f/\Delta U$, where L_f is a flow length scale and ΔU is the velocity change over this length. An important flow length scale in the current experiment is the separation length, the distance between the incipient separation point and the actual separation point. Östlund [11] mentions that during flat plate boundary layer studies, the separation length is of the same order as the boundary layer displacement thickness, i.e. $L_s/\delta_{99} = 1$. The velocity change over the distance of the separation length is caused mainly by

the oblique separation shock. The change in velocity can be estimated using the Rankine-Hugoniot relations.

$$\frac{v_1}{v_2} = \frac{(\gamma + 1)M_1^2 \sin^2 \beta}{(\gamma - 1)M_1^2 \sin^2 \beta + 2} \quad (4.28)$$

However, estimating the properties of the oblique shock such as the shock angle is difficult. To take a conservative estimate, it is assumed that the shock is normal ($\beta = \pi/2$), such that the maximum velocity change is achieved. Because the strongest shock occurs when the incoming Mach number, M_1 , is highest, the location of the shock will be taken at the nozzle lip. From the ideal nozzle theory, it can be found that the maximum velocity ratio is approximately 4.7, which means the velocity change would be 490 m/s.

The displacement thickness of the boundary layer in the nozzle is hard to estimate, because there is almost no literature available. However, an estimation can be made based on flat plate turbulent boundary layers, similar to the estimation for the free interaction theory. The Reynolds number based on the boundary layer displacement thickness is given as a function of the lengthwise Reynolds number using the Prandtl estimation [118]

$$Re_\delta = 0.16Re_x^{6/7} \quad (4.29)$$

where the Reynolds number is taken at the nozzle lip because the Reynolds number is highest there. The boundary layer displacement thickness can then be determined from the definition of the Reynolds number

$$\delta = \frac{Re_\delta \nu}{U_\infty} \quad (4.30)$$

Using these equations, the characteristic time of the flow is estimated to be around 4 μs . Since the velocity change is relatively sensitive to the shock angle, the characteristic time of the flow will increase quite rapidly with decreasing shock angle. Therefore, the assumption of a normal shock might have a disproportionate effect on the characteristic time, which could rule out many of the potential seeding particle types.

Several materials for seeding particles are considered for the experiments. They are presented in Table 4.2, with data taken from Scarano. [30]

Table 4.2: Properties of various common seeding particle types [30]

Material	Particle Diameter [μm]	Density [kg/m^3]	τ_p [μs]	S_k
DEHS	1-3	1000	3.1 - 27.6	1.3 - 11.5
Vegetable Oil	1-3	1000	3.1 - 27.6	1.3 - 11.5
TiO ₂	0.2-0.5	1000-4000	0.12 - 3.1	0.031 - 0.77

From this analysis it can be concluded that the only feasible seeding particle materials for this experiment is TiO₂. It can be seen that for the worst conditions with a particle size of 0.5 μm and a density of 4000 kg/m^3 , the stokes number is still too high. However, it must be noted that this is for the lowest possible characteristic time encountered in the entire flow field, which means that the vast majority of the flow field will still be properly traced by these particles. In order to remain conservative TiO₂ was selected, but future tests could also be performed with other seeding particle types in order to observe their performance. Since these other types are generally easier to handle and will allow for PIV runs to be performed without the PIV tube, this is definitely worthwhile looking into.

After the images have been taken, the following process is used to extract the velocity field from the images. First, the image is divided in so-called interrogation windows, which is just a small portion of the image. The size of the interrogation window is determined by the motion of the particles. Namely, the particles should not move more than 1/4 of the length of width of the interrogation window. If particles move more, a lot of particles that are in the interrogation window in the first image will have moved

out of the window, which makes it impossible to track them. On the other hand, if the interrogation window is too large, the velocity field becomes very coarse, because one velocity vector is calculated per interrogation window. Moreover, the maximum in-plane variation in particle displacement within the interrogation window should be less than the particle image diameter, because otherwise it could become hard to track the particle motion within an individual window. [30]

Second, a cross-correlation analysis between the images taken at time t and $t + \Delta t$ is performed for each interrogation window. The position of the peak in the cross correlation function then corresponds to the average displacement of the particles in the interrogation window. This will give the displacement of the particles in pixels on the CCD sensor of the camera. The real displacement in meters can be calculated when the magnification factor, M , between the real object and the image is known. The magnification factor is defined as

$$M = \frac{d_i}{d_o} = \frac{d_{\text{pix}} n_{\text{pixels}}}{\text{FOV}} \quad (4.31)$$

where d_i is the image size of an object of known dimensions and d_o is the size of the same object in reality. d_{pix} is the size of a pixel on the CCD, n_{pixels} number of pixels in one axis on the CCD and the FOV is the field of view of the image in m. Normally the magnification factor is smaller than 1, because the imaged region is larger than the size of the CCD.

Third, the sub-pixel displacement can be determined by interpolating the points in the cross-correlation using a gaussian fit.

$$f = \phi_0 e^{-\frac{(x-x_0)^2}{\sigma^2}} \quad (4.32)$$

For the best sub-pixel accuracy, the tracer particle diameter should be around two to three pixels.

Finally, the average velocity components in the interrogation window can be determined by dividing the displacement by the pulse separation time using

$$u = \frac{\Delta x}{M \delta t} \quad (4.33)$$

$$v = \frac{\Delta y}{M \delta t} \quad (4.34)$$

4.4.2. Setup

A schematic of the PIV setup is shown in Figure 4.16. A Spectra Physics, Quanta Ray Neodymium doped: Yttrium Aluminium Garnet laser (Nd: YAG)⁷ is used to create the laser sheet. This laser is capable of producing light at a wavelength of 532 nm, which corresponds to the green part of the visible spectrum, with a pulse energy of 200 mJ. The main drawback of this laser is that the maximum measurement rate is 10 Hz, which means that time resolved flow measurements are not possible when using this laser. The laser is positioned on the next to the setup, and the laser beam is deflected and stretched to a sheet by a series of mirrors and lenses. The laser sheet enters the PIV tube from the bottom, as shown in Figure 4.17.

In order to obtain proper PIV data, it is required that the particle displacement between the two images in an image pair is approximately 1/4th of the interrogation window size. The minimum window size for this experiment was selected to be 32x32 pixels, which means that the displacement of a particle between the two images should be around 8 pixels. The extreme velocity differences between the supersonic regions in the flow where the flow velocity can reach up to 400 m/s, and the recirculation region just downstream of the normal shock where the flow is almost stationary makes it quite difficult to select a proper time difference between the two images. After some initial testing, it was found that a time separation of 3 μs worked best. This still allows for the tracking of particles in the high speed flow even when the interrogation window is 64x64 pixels and overall most particles in the flow can be tracked properly.

⁷http://publish.illinois.edu/ae-lambros/files/2017/07/Lab-Series-Users-Manual_Nd_YAG.pdf

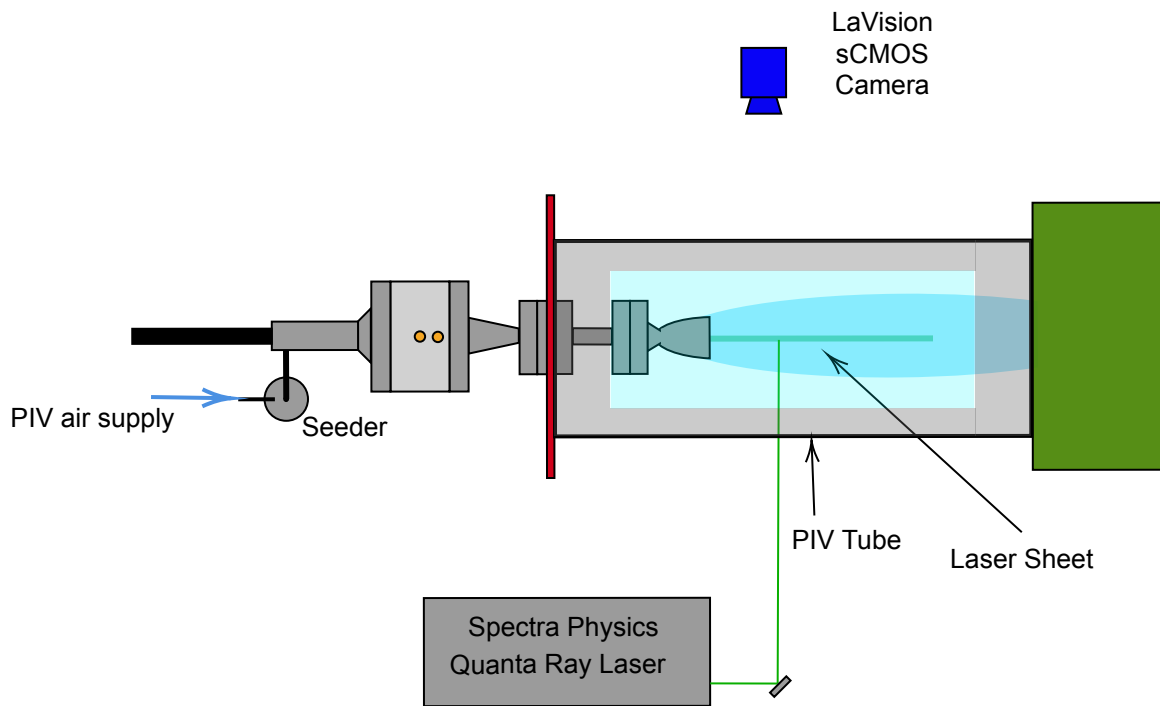


Figure 4.16: Schematic of PIV setup (top view)

The camera used is a Lavision sCMOS Imager⁸. This camera has a CCD of 2560x2160 pixels with a pixel size of $6 \mu\text{m}$. The standard frame rate of the camera is 50Hz, but due to the limitations of the laser, this has to be reduced to 10Hz. This camera is optimised to work with light with a wavelength around 500 nm, which is perfect in combination with the laser. The camera is positioned on the left side of the setup at about one meter distance. This is shown in Figure 4.18. A 60mm focal length lens is installed on the camera. The field of view (FOV) of the camera should at least include 1 nozzle radius downstream of the nozzle because this region is commonly simulated in CFD simulations such as by Hagemann and Frey and in the single physical experiment that obtained quantitative velocity field data using hydroxyl tagging velocimetry by Yoon et al. [82, 119] Because the entire flow field has never been measured before, it is decided to increase the FOV to include at least 2 nozzle diameters downstream of the nozzle. The result of this is that the detailed shock patterns in the supersonic flow regions can likely not be visualised because the image resolution is too small.

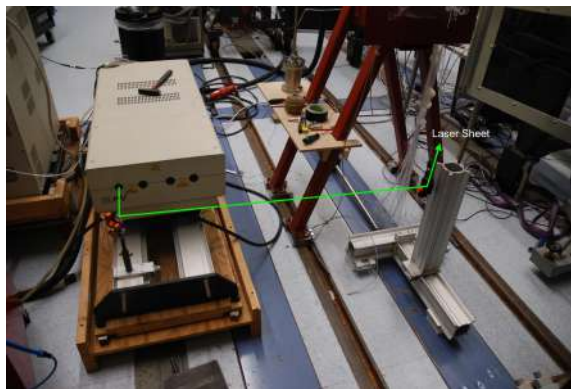


Figure 4.17: Laser beam path

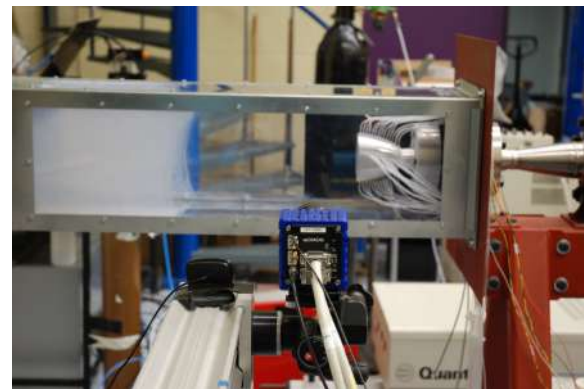


Figure 4.18: Lavision sCMOS imager looking at nozzle

In order to capture proper images, the aperture of the lens should be set to the correct setting. Instead of setting the aperture directly, it is commonplace to instead refer to the so-called f-stop, $f_{\#}$,

⁸<https://www.lavision.de/en/products/cameras/cameras-for-piv/>

which is defined as

$$f_{\#} = \frac{f}{D} \quad (4.35)$$

where f is the lens' focal length and D is the diameter of the aperture. The setting of the f-stop is a balancing act between the depth of field of the image, and the diffraction of the particle image on the CCD. As stated before, ideally the particle diameter is 2-3 pixels to allow for the best possible sub-pixel interpolation. The effective particle diameter on the CCD, d_{τ} can be determined using [30]

$$d_{\tau} = \sqrt{(Md_p)^2 + (d_{\text{diff}})^2} = \sqrt{(Md_p)^2 + (2.44\lambda(1+M)f_{\#})^2} \quad (4.36)$$

The depth of field of the image is also a function of $f_{\#}$, and the depth of field should always be larger than the laser sheet thickness. The depth of field δz can be determined using

$$\delta z = 4.88\lambda f_{\#}^2 \left(\frac{M+1}{M} \right)^2 \quad (4.37)$$

It can be seen that increasing the $f_{\#}$ will result in an increase of effective particle diameter, but also depth of field. From the calibration images it is found that the magnification factor in the experiment was 0.078. Using a particle diameter of the TiO_2 particles of $0.3 \mu\text{m}$, which is in the middle of the range as presented in Table 4.2, it is found that for an $f_{\#}$ of 11, the effective particle diameter will be 2.6 pixels, and the depth of field will be 6 mm. With a laser sheet thickness of approximately 2 mm these figures meet the requirements for proper PIV images. The PIV setup parameters are summarised in Table 4.3.

Table 4.3: PIV camera setup properties

Property	Value	Unit
Pixel size	6.4	μm
FOV	213x180	mm
Magnification factor	0.078	-
$f_{\#}$	11	-
Laser sheet thickness	2	mm
λ	532	nm
d_{τ}	15.4	μm
d_p	0.3	μm
d_{diff}	15.4	μm
δz	6	mm

A cyclone type seeder, shown in Figure 4.19 is used to seed the flow with the TiO_2 particles. As can be seen in the image, the flow is seeded before reaching the settling chamber, which means that the particles will be homogeneously distributed in the flow by the time they enter the nozzle. Air is supplied to the cyclone seeder by two large pressurised air bottles at 250 bar. A pressure regulator valve is used between the pressurised air bottles and the seeder in order to reduce the bottle pressure to a suitable air pressure for seeding. Because a pressure regulator is used, it is very easy to change the flow rate entering the cyclone seeder, which in turn can change the particle density in the flow. By means of trial and error, it was found that an over pressure of 2 bar in the cyclone seeder compared to the total pressure in the settling chamber resulted in the correct particle density. The air is supplied through a 5mm inner diameter stainless steel tube in which an additional hand-operated shut-off valve is placed with which the flow of seeding particles can be started and stopped quickly. A 10mm inner diameter stainless steel tube runs from the cyclone seeder to the entrance of the diffuser. A wooden board that can be connected to the legs of the setup at adjustable height was made in order to support the cyclone seeder. Since the mass flow of the nozzle is relatively high, a large amount of seeding material is required to obtain acceptable particle density. This means that after every run, the seeder needs to be refilled with TiO_2 particles, which results in a relatively long setup time for each run. Moreover, after a full run, the polycarbonate panels are covered in seeding particles, and become slightly opaque. These

need to be cleaned before every run, adding to the setup time as well. These two factors severely limit the number of runs that can be performed each day of testing.

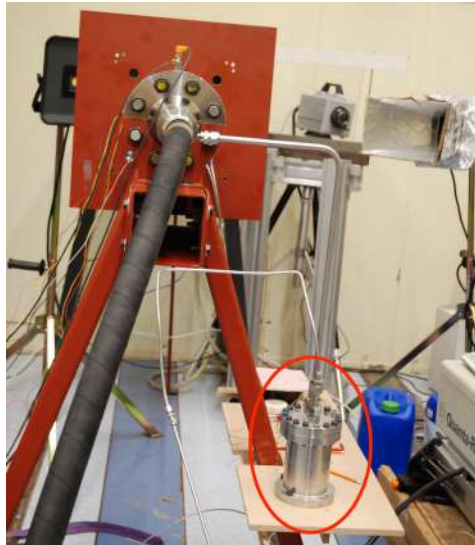


Figure 4.19: Cyclone Seeder

Finally, a section of the polycarbonate panel on the opposite side of the camera was covered with black, non-reflective tape in order to reduce the laser reflections as much as possible. In images where this tape was not applied a reflection of the nozzle in the panel was clearly visible, but this reflection is completely removed by the tape.

4.4.3. Data Processing

The PIV data was analysed with the Lavisision DaVis 8.4 software. This is software written specifically for the analysis of PIV data, which means a lot of settings can be optimised in order to extract the most data possible from the images. This subsection describes the settings that were used in the processing of the PIV images.

Improving Image Quality

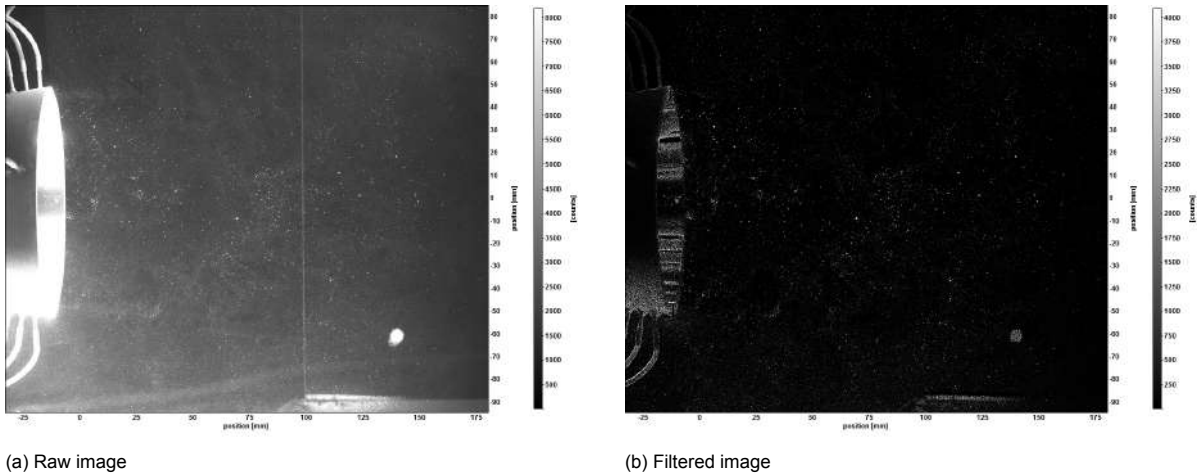
In order to improve the quality of the images, i.e. increasing the contrast between the particles and the image background and to remove potential reflection, a Butterworth high pass filter is used to remove low frequency components from the images. A filter length of 10 images is used, such that the Butterworth filter removes all of the pixels from the image that change very little between those 10 images. The result of this operation can be seen in Figure 4.20.

Masking

A geometric mask is put over the nozzle such that it is not taken into account in the image analysis. This is done because the nozzle is relatively reflective, but the exposure changes quite significantly between individual images, such that the Butterworth filter does not remove all of the reflections of the nozzle. The mask is placed over the entire visible portion of the nozzle. Initially, it was tried if velocity data could be extracted from inside the nozzle by only masking the part of the nozzle closest to the camera, and leaving the aft part exposed. This however did not results in any acceptable data, likely due to the reflectivity of the internal nozzle surface, and so it was decided to mask the entire nozzle.

Velocity Field Generation

Because of the large difference in flow velocity throughout the flow field, it was decided to use multiple passes with variable interrogation window size to generate the velocity fields. In the first pass, the images are cross-correlated using a square 64x64 pixel interrogation window, with an overlap of 75%. For the second pass, the shape and size of the interrogation window is changed in order to improve the concentration of obtained velocity vectors. This pass, which is repeated twice, uses a circular



(a) Raw image

(b) Filtered image

Figure 4.20: Butterworth filtering of PIV images

32x32 pixel interrogation window with again an overlap of 75%. The final pass uses a 6th order B-spline interpolation instead of linear interpolation to improve the accuracy of the data. An example of an instantaneous velocity field is shown in Figure 4.21.

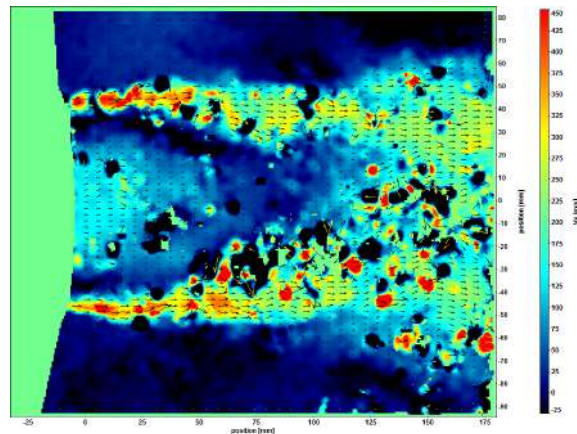


Figure 4.21: Example of an instantaneous velocity field

Statistical Analysis

The previously described process results in an instantaneous velocity field of one image pair. In order to reduce the error percentage of the data, the velocity field of 900 images is used to determine the statistical properties of the velocity field. These are the average, standard deviation and Reynolds stress tensor components. The Reynolds stress is determined from the images using

$$Re_{ij} = \frac{1}{n_{img}} \sum_{k=1}^n (v_k - \bar{v})_i (v_k - \bar{v})_j \quad \text{for} \quad i, j = 1, 2 \quad (4.38)$$

where i, j are the spatial coordinates. These results are only computed when 100 source vectors that lie within 3σ of the mean are present at a specific position.

Post processing

The velocity fields will be normalised with the ideal jet velocity of the nozzle. Moreover, the Mach number field can be determined because the total temperature of the flow is measured in the settling chamber. By using the energy equation

$$c_p T_0 = c_p T + \frac{1}{2} v^2 \quad (4.39)$$

the local temperature can be determined because the total temperature and local velocity are known and the flow can be assumed to be adiabatic. The local speed of sound can then easily be calculated with $a = \sqrt{\gamma RT}$, which can then be used to determine the Mach number. For the low temperatures involved, γ can be assumed to be independent of temperature.

4.5. Test Cases

The test campaign is divided into two parts: in the first part, the main purpose of the tests is to gain experience with the operation of the system, and to obtain calibration data about the nozzle that is similar to data already available in literature, such that the data can be compared. Moreover, in this part, initial tests with the flexible nozzle are performed in order to observe its behaviour, such that potentially required design changes can be made for the second phase. In the second part, the main focus lies on obtaining PIV data on the aluminium nozzle, in order to obtain quantitative flow field data, and on taking measurements of the vibrations in flexible nozzles of varying stiffness.

To obtain data already available in literature, several tests are performed in the first part of the measurement campaign. These are

1. *Set up tests*: In these tests, the system is initially run at relatively low NPR in order to check if everything works the way it is supposed to. It is made sure that the sensors are working correctly, that data is measured and stored correctly, and that the test procedures are complete and allow for safe operation of the system.
2. *5 minute ramp tests*: One test run will be performed where the NPR is increased from 10 to 30 in approximately 5 minutes. In another five minute run the NPR is decreased from 30 to 10 in approximately 5 minutes. Both the start-up and shutdown ramp is tested because of the significant hysteresis effect present in the flow, as discussed in subsection 2.3.5. This means the NPR on average changes about 0.067 per second, such that the flow can still be considered steady for all conditions. Due to a delay in the delivery of the parts, these runs could not be performed with the strain gauges attached to the strain tube. The total pressure, total temperature and nozzle wall pressures are all recorded at 500 Hz for the entire duration of the ramp. The ramp study will provide insight into when separation occurs in the nozzle, and if this is comparable to existing data about this contour. Moreover, it can be determined at which NPR transition occurs, which is the main area of interest of this study because the side loads are highest and so it is expected that the vibrational loads are also highest in this NPR region. Lastly, it will tell the difference between the transition point during start-up and shutdown.
3. *Constant NPR runs*: After the ramp studies, the nozzle is run at constant NPR for a measurement time of two seconds for several NPRs in the vicinity of the transition point. During these tests, schlieren images can be taken of the flow during FSS and RSS state. This is only done for the start-up case. These runs were done at NPR 24 to 25.2, with 0.2 increments in NPR between cases.
4. *Transition runs*: Several runs were performed in which the NPR is put very close to the transition point in the start-up phase, and the NPR is increased quickly in order to measure the flow properties during transition. High speed schlieren imaging at 12000 fps is used to determine if asymmetric separation is present, and if so, for how long. This is done with a horizontal, as well as a vertical schlieren knife in order to obtain horizontally and vertically oriented features in the flow. Moreover, it might be possible to measure the asymmetry in the separation line in the nozzle due to the different azimuthal position of the wall pressure port arrays.
5. *Flexible nozzle tests*: Finally, the first flexible nozzle is tested. This nozzle is a flexible 80A nozzle with a 5 mm wall thickness. In this case, the NPR will be slowly increased incrementally in order to observe the nozzle behaviour. Initially no DIC is used because of lack of time and because these tests are just performed to observe whether the nozzle shows the required vibrations at all.

The results of these tests, as discussed in chapter 5, warranted a redesign of the flexible nozzle as the nozzle did not vibrate, but just statically deformed.

Due to unavailability of the wind tunnel, a three week gap was present between the first and second part of the measurement campaign. This time allowed for the redesign of the flexible nozzle, as well as making some improvements to the test setup, such as the addition of the strain gauges. In the second part, the PIV system was set up and the following tests are performed:

1. *Set up tests*: After the PIV system is set up, several tests are performed in order to optimise the parameters such as laser power, pulse separation time, removing reflections and overpressure in the cyclone seeder. Moreover, these tests are used to determine how long the supply of seeding material in the cyclone seeder lasts, which was found to be around 900 images at 10 Hz. Several calibration runs are done in order to make sure that the illuminated particles are in focus of the camera.
2. *PIV tests*: Because of the relatively long setup time and the time to optimise the operation of the PIV system, it was only possible to take 6 PIV measurements at a total pressure of 10, 15, 20, 21, 23 and 24 bar. In this case, the NPR is not immediately known since the atmospheric pressure in the PIV tube can be significantly lower than the ambient pressure in the room. From this data velocity fields in the FSS and RSS phase can be determined. Because it was unknown how far the seeding particles would travel up the pressure tubes connecting to the Scanivalves, they were not used during the PIV runs. 900 image pairs were taken at 10 fps, which means that one PIV run takes approximately 90 seconds to complete. During this time, the total conditions and strain were measured at a rate of 100 Hz.
3. *Flexible Nozzle tests*: Unfortunately, the flexible nozzle tests were not successful after implementing the design changes based on the knowledge gained in the first part of the test campaign. This is discussed in more detail in chapter 5. The conclusion was that the new flexible nozzle is too weak to withstand the atmospheric pressure forces when the flow is attached to the wall, and therefore completely collapses. At this point, due to lack of time, it was decided to reinforce the nozzle with steel wire and duct tape, which makes the experiment unrepeatably, but it does allow for the proof of concept of the DIC system. Moreover, it is likely still possible to extract some useful information about the most energetic modes in the nozzle vibration, and how these evolve with NPR. The reinforcements caused the nozzle to vibrate acceptably. Still, the nozzle could only handle NPRs of up to 10 before the nozzle would start deforming too much and risk of failure became very high. Moreover, the nozzle is tested with and without the PIV tube on the setup, to determine the difference in vibrations and schlieren images are taken during tests without the PIV tube. Without the PIV tube, runs are performed at a total pressure of 2, 8, 8.8, 9.8 and 10 bar. With the PIV tube, runs are performed at a total pressure of 4, 5, 8, 8.8, 9.8 and 10 bar. The DIC images are taken at 1000 fps, and the total conditions and strain were measured at 500 Hz.

5

Results

This chapter presents the results of the tests outlined in the previous chapter. The results are divided into results of the tests with the aluminium nozzle, which focus on pressure, schlieren and PIV measurements, and tests on the flexible nozzle, which focus mainly on DIC.

5.1. Aluminium Nozzle

5.1.1. Flow Development Analysis

Most of the information about the flow in the aluminium nozzle is obtained from the 5 minute sweep runs, since data at practically all NPR values is available. Plots of the wall pressure normalised to ambient pressure as a function of NPR and distance from the throat x are shown in Figure 5.1. The separation point according to free interaction theory is indicated with the solid black line, and a second degree polynomial fit through these points is shown in the dotted line. The dashed white line shows the predicted separation point using the Stark criterion. The FSS separation point could only be obtained for the increasing ramp with $d(\text{NPR})/dt > 0$ because, as can be seen in the images for decreasing ramp, the FSS separation point lies very close to the first pressure port. The pressure port locations are indicated on the y-axis.

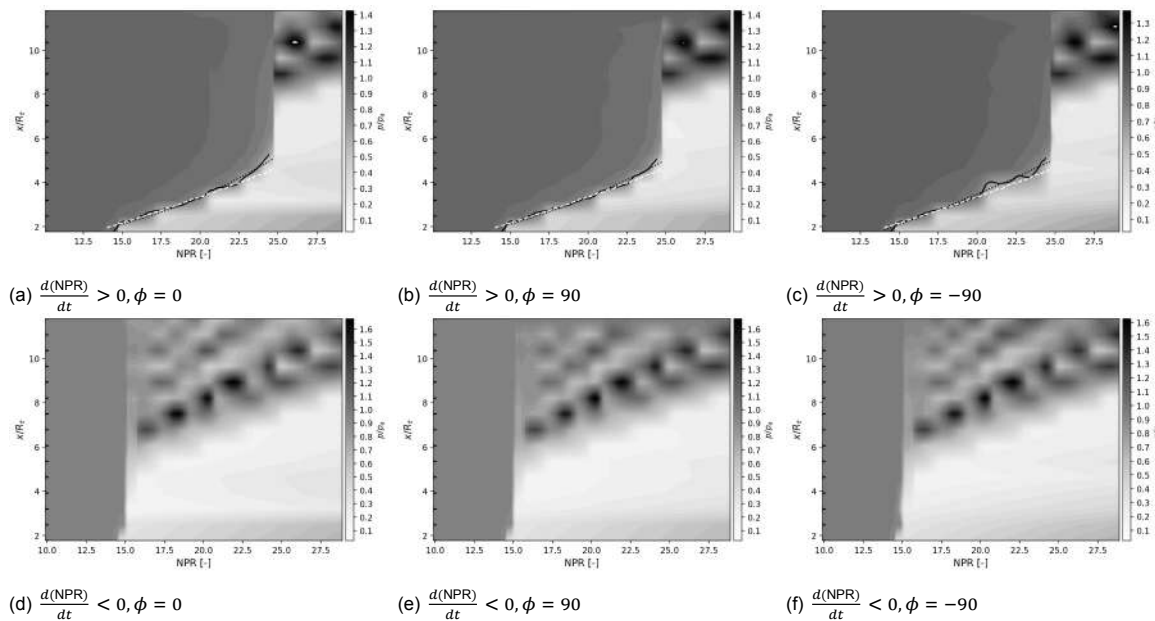


Figure 5.1: Wall pressure contours for 5 minute ramp cases. The solid black line shows the separation point according to free interaction theory. The dotted black line shows the second degree polynomial fit and the dashed white line shows the separation point according to the Stark criterion

This data is very similar to the data obtained in literature, such as by Baars and Tinney. [120] For the increasing ramp, a very distinctive FSS to RSS transition point is observed for NPR 24.75, which is in the expected range of NPRs for which transition should occur. Nevertheless, it is slightly higher than expected when comparing to the data presented in Table 3.2, which showed a decreasing trend for the transition point with decreasing size of the nozzle. As such, it was expected that the transition point would lie at a lower NPR than the one obtained by Ruf et al. and Baars and Tinney [1, 120], who used a nozzle with a throat twice the diameter of the current nozzle and found the transition point to lie at NPR 23.1-23.6. For the decreasing ramp, the separation point is not so clear. It can be observed that there exist a region between NPR 15.1 and 16 where the pressure seems to rise gradually from ideal to ambient, unlike during FSS or RSS when the pressure rises rapidly after separation. This could be a result of how the data is averaged. If the flow is constantly transitioning between FSS and RSS, this effect could be averaged out such that it seems that the pressure is rising slowly.

For the increasing ramp, two clear pressure peaks are visible in the RSS regime, which are both moving downstream at a rate of $\frac{dx}{d(\text{NPR})} \approx 4.15 \text{ mm/NPR}$, with a maximum pressure of 1.4 times ambient. During the decreasing ramp, four distinct pressure peaks are distinguishable. The first two separation bubbles that exist at high NPR seem to merge when the NPR is decreased at around NPR 21. It is also interesting to note that the velocity of recession is different for each of the separation bubbles. It can be seen that the first separation bubble has the lowest recession rate, and that the other separation bubbles obtain increasing recession rate for increasing longitudinal position.

From the separation point line it can be observed that the downstream motion of the separation point for increasing NPR is not at all steady. Instead, the separation point seems to move downstream relatively fast for some parts of the sweep, while it stays relatively constant for others. This could be related to the position and resolution of the pressure ports, as the separation point seems to jump from one pressure port location to the next. The separation line from free interaction already shows a much more constant downstream movement of the separation location. This shows that the fitting of the free interaction correlation curve can improve the sensor resolution significantly. Likely, the polynomial fit is an even better representation of the actual position of the separation line, since according to the Stark criterion the separation location is inversely proportional to M_t , which follows a parabolic shape for the largest part of the nozzle as can be seen in Figure 3.3c. The white dashed line in the plot shows the separation position according to the Stark criterion. It can be seen that initially, the Stark criterion estimates the separation point very well, but the separation point starts deviating when moving closer to transition. Another effect that is caused by the low resolution of the pressure ports is the apparent pulsation of the highest pressure peak in RSS regime between 1.4 and 1.1. It can be observed that the highest pressure peaks are observed at the same longitudinal position as the pressure ports. This occurs when the position of the maximum value of the pressure peak overlaps with the position of the pressure port.

Figure 5.2 shows the location of the separation point as a function of NPR, including a second degree polynomial fit. The data shows relatively little asymmetry between the pressure port arrays at different azimuthal locations. It can be seen that as the NPR moves closer to transition, the rate at which the separation point moves downstream also increases. This is likely due to the fact that partial reattachment of the flow already occurs due to the unsteadiness of the flow in this regime, which makes the adverse pressure gradient less steep.

Figure 5.3 and Figure 5.4 show the pressure distribution at various NPR at $\phi = 90$ for the increasing and decreasing ramp respectively. It can be seen that during the FSS the plateau pressure is decreasing as the separation point moves downstream. Moreover, the first NPR at which the flow is still attached at the first pressure port is NPR 15.51, which again shows that the Stark criterion, which was used to determine the position of the first pressure port at the separation location at NPR 15, can definitely be used as a design guideline. A clear shift in the separation point is visible between NPR 24.5, where separation occurs, which is expected because of the lower adverse pressure gradient between the attached flow and the separation bubble. The most interesting part of the decreasing ramp plot is the line at NPR 15.51, which does not show the distinctive rapid pressure rise seen in both FSS and RSS, but instead the pressure is increasing slowly from the attached value at $x/R_t = 3.3$ to a sub-atmospheric plateau pressure at $x/R_t = 6.7$. However, the pressure at $x/R_t = 6.7$ can not

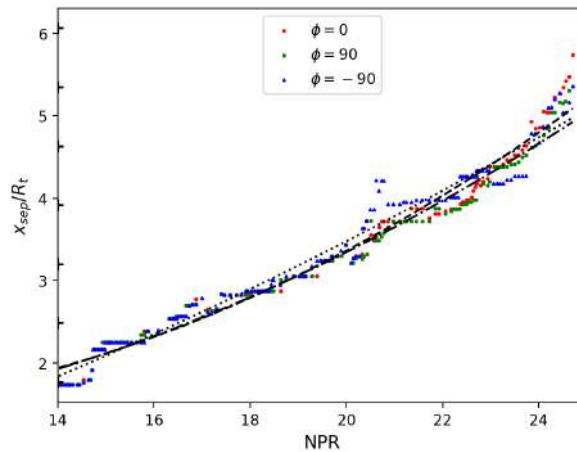


Figure 5.2: Separation location according to generalised free interaction correlation function fit, including second degree polynomial fit

really be considered a plateau pressure as the pressure still increases significantly when moving further downstream. This seems to be a steady effect, since no significant fluctuations in the pressure measurements around NPR 15.5 are observed. Moreover, the effect is visible in the data of all three of the Scanivalve pressure scanners.

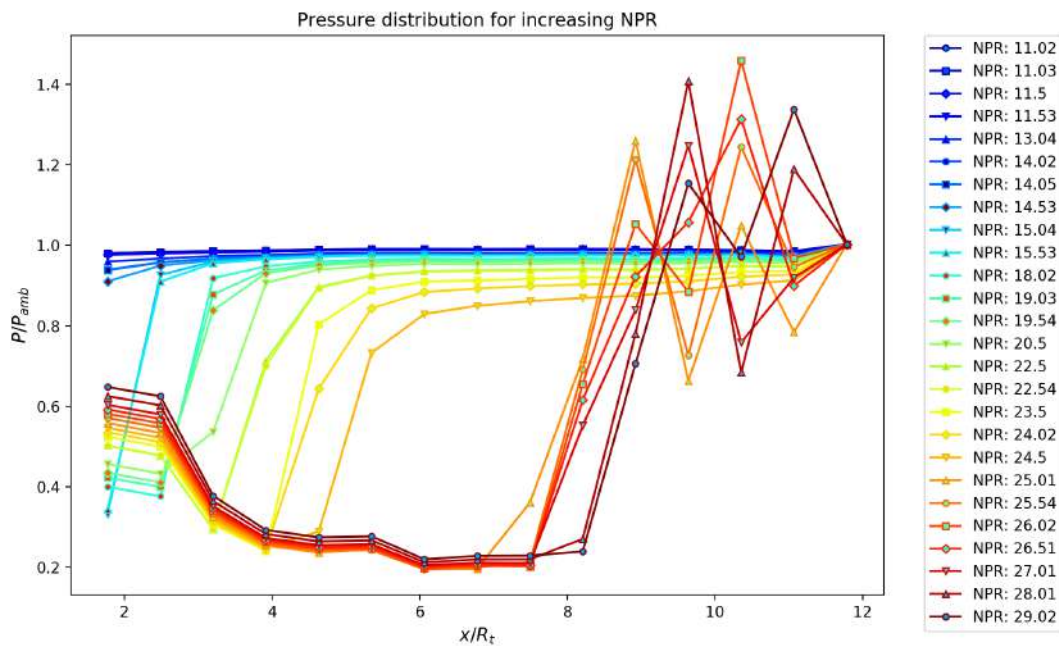


Figure 5.3: Pressure distribution for varying NPR during increasing ramp at $\phi = 90$

The pressure distribution around the transition point at $\phi = 90$ for start-up is shown in Figure 5.5. These results are obtained from two seconds of data averaged for each NPR. Finally, to get an idea about the level of asymmetry in the flow, the measurements from all three Scanivalve pressure scanners are combined for several NPR values. These are shown in Figure 5.6. Some asymmetry exists between the $\phi = 0$ and other pressure ports, but what is mainly interesting is the relatively large asymmetry at the last pressure port between $\phi = 90$ and the other azimuthal locations. As seen later in this chapter, this is also visible in the schlieren data. The asymmetry is mainly striking in the RSS phase shown in Figure 5.6c. It seems as if the flow remains attached at $\phi = -90$ and $\phi = 0$, but separates at $\phi = 90$

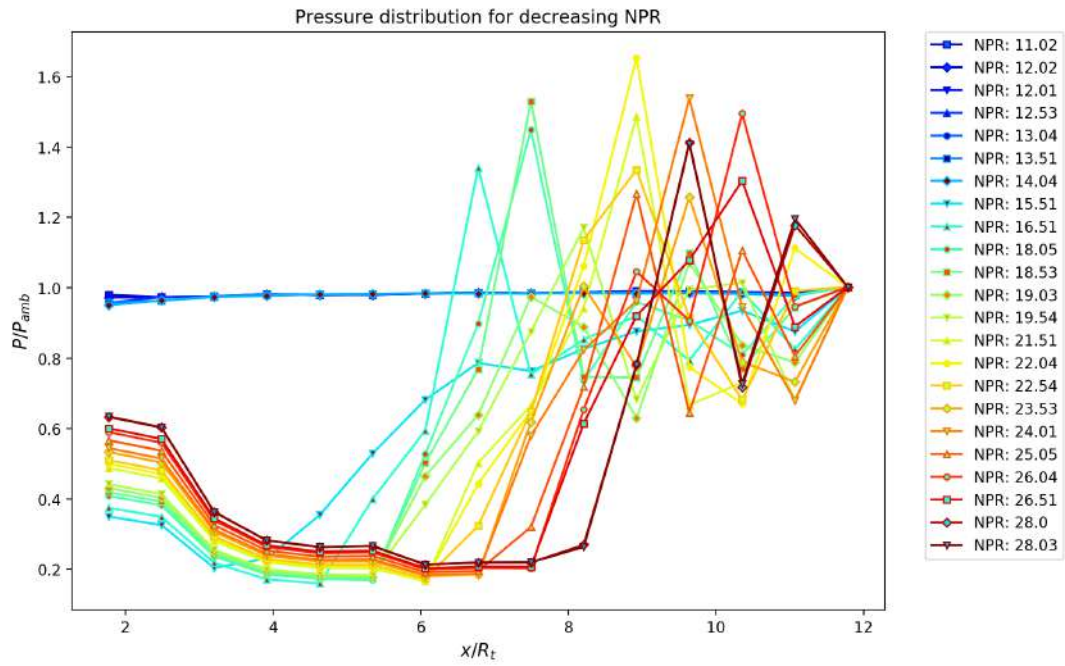


Figure 5.4: Pressure distribution for varying NPR during decreasing NPR at $\phi = 90$

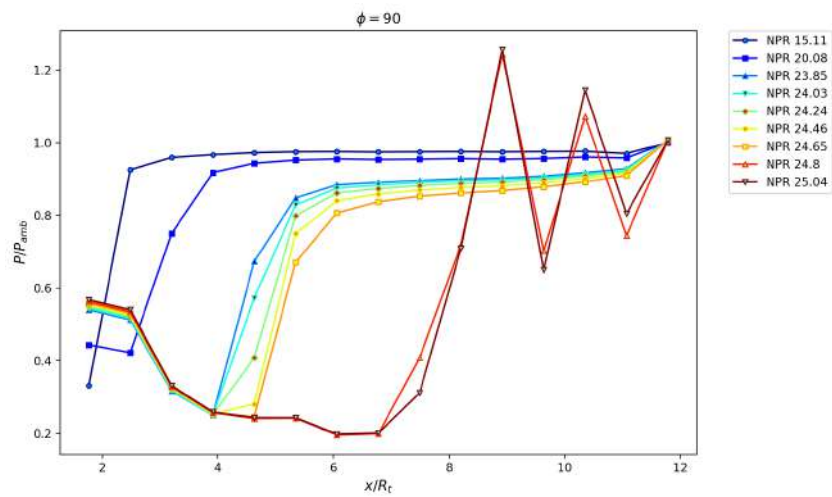


Figure 5.5: Pressure distribution for varying NPR close to FSS to RSS transition

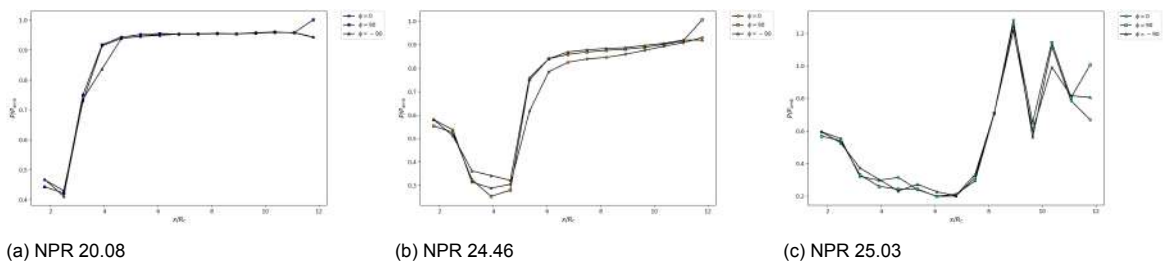


Figure 5.6: Wall pressure contours at various azimuthal locations for different NPR values

5.1.2. Schlieren analysis

The schlieren images show the same flow development and the pressure plots. The schlieren images for several NPR values are presented in Figures 5.7 to 5.9. Note that the contour levels run from 0 to 1, which represents the fraction of maximum pixel intensity in the actual schlieren images.

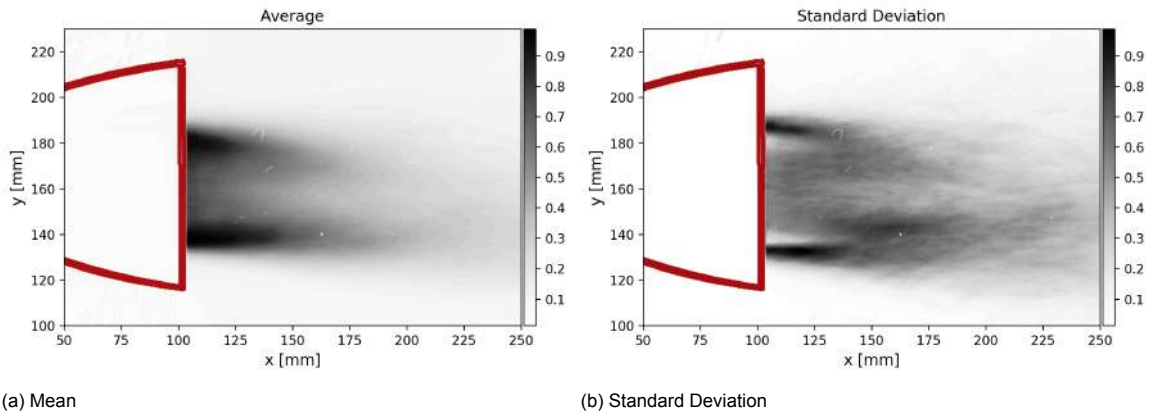


Figure 5.7: Mean flow and fluctuations at NPR 23.84

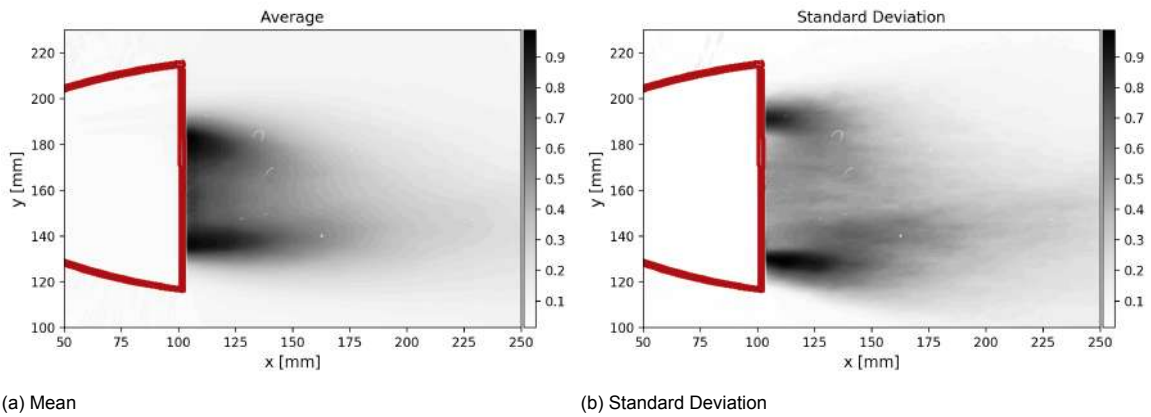


Figure 5.8: Mean flow and fluctuations at NPR 24.65

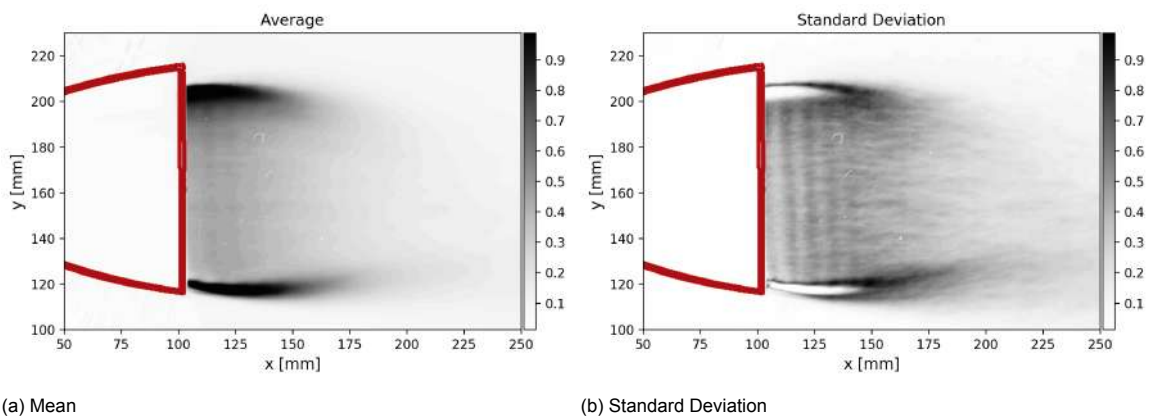


Figure 5.9: Mean flow and fluctuations at NPR 25.03

The mean flow can be seen to widen for increasing NPR, also in the case of FSS, which is expected because the separation point moves downstream and thus also moves to a larger radial position in

the nozzle. The supersonic flow regions in the FSS phase are clearly visible in the mean flow and fluctuations. What can be noted is that the flow is slightly angled downwards relative to the nozzle. This might be caused by upstream asymmetries in the nozzle geometry and is also the cause of the difference between the pressure measurements at the final pressure port. In the case where the NPR is very close to transition, 24.65, it can be seen that the fluctuations are significantly spread out, indicating an increased vertical flapping motion of the flow. The flapping motion is also favoured toward the bottom of the nozzle. In the instantaneous schlieren images, the flow seems to attach to the bottom wall for a very short time, only to separate immediately again. This partial RSS mode, where the flow is extremely asymmetric, is the main contributor to the side load generation. During the high speed schlieren tests during FSS to RSS transition, the flow was seen to attach to the bottom first, separating and reattaching several times, before attaching to the top.

This is shown in Figure 5.10. It can be seen that the flow initially transitions to RSS in the bottom of the nozzle as shown in Figure 5.10a, but transitions back to FSS after approximately 35 frames in Figure 5.10b. since the video was taken at 12,000 fps, this means the flow is attached for approximately 2.9 ms. Afterwards, the flow at the bottom of the nozzle transitions again to RSS and stays attached as in Figure 5.10c. It takes 110 frames for the flow at the top of the nozzle to transition as well as shown in Figure 5.10d, which means that the flow structure is extremely asymmetric for approximately 9 ms. This is faster than the time between two measurements of the Scanivalve pressure, scanners (recording at 500 Hz), which is likely why no extreme asymmetry is observed between the pressure port arrays during transition.

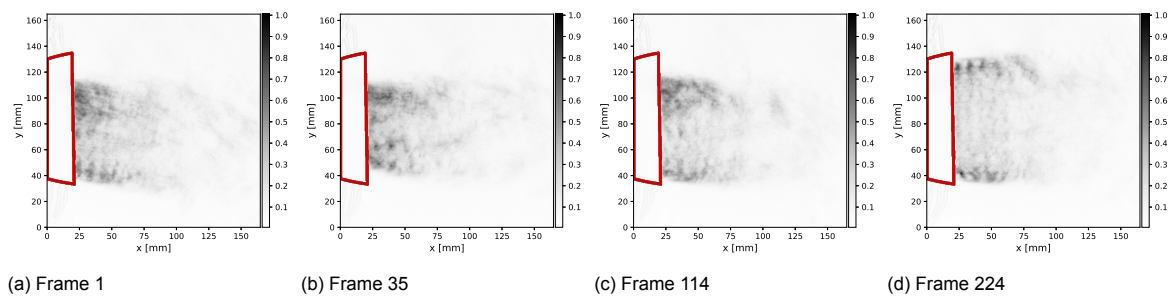


Figure 5.10: Different flow conditions during FSS to RSS transition

It is interesting to note that the only other source with visual data of asymmetric separation by Terhardt et al.[15], namely of the full scale Vulcain engine, show the flow attaching at the top of the nozzle before the bottom in a similar horizontal test stand. This rules out the possibility that gravity could have a significant effect on the flow.

The flow is still observed to be asymmetric after transition to RSS in Figure 5.9. There is a stark difference between the width of the supersonic region at the top and bottom of the nozzle. This indicates that the position of the second separation bubble is different between the top and the bottom of the nozzle, something which is also observed in Figure 5.6c. It is likely that a third separation bubble is present at the bottom of the nozzle, with the reattachment point very close to the nozzle lip. On the top, the second separation bubble lies further downstream, meaning that there is not enough space for the formation of a third separation bubble. Therefore, a flow similar to the flow seen during EER is seen at the top of the nozzle. Vertical streaks are visible in Figure 5.9b, but much less visible in the mean flow, which indicates an unsteady shock train is present in the supersonic region of the flow. Because the flow is annular around the circumference of the nozzle, these streaks can be seen along the entire height of the nozzle. The streaks with high pixel intensity (black) indicate the location of the normal shock in the shock train. Spectral analysis of the pixel intensity of the centerline reveals the wavelength of the unsteady standing wave is around 8.55 mm, and that the shocks seem to move over a distance of about 2 mm.

5.1.3. Velocity Fields

Using PIV, the velocity fields and Mach number contours of the flow can be drawn. The velocity is normalised to the ideal expansion exhaust velocity, which is 623.85 m/s. The mean flow and fluctuations

of several, but not all NPR values are shown below. The data from the other runs can be found in Appendix A. These are omitted from the main report because the flow fields look relatively similar and they would not contribute to the discussion.

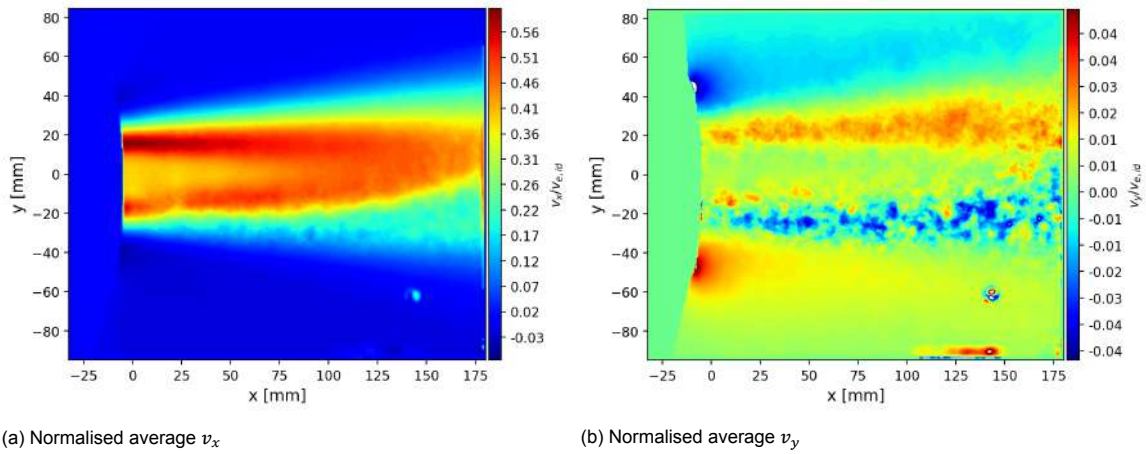


Figure 5.11: Mean flow velocity components at NPR 16.42

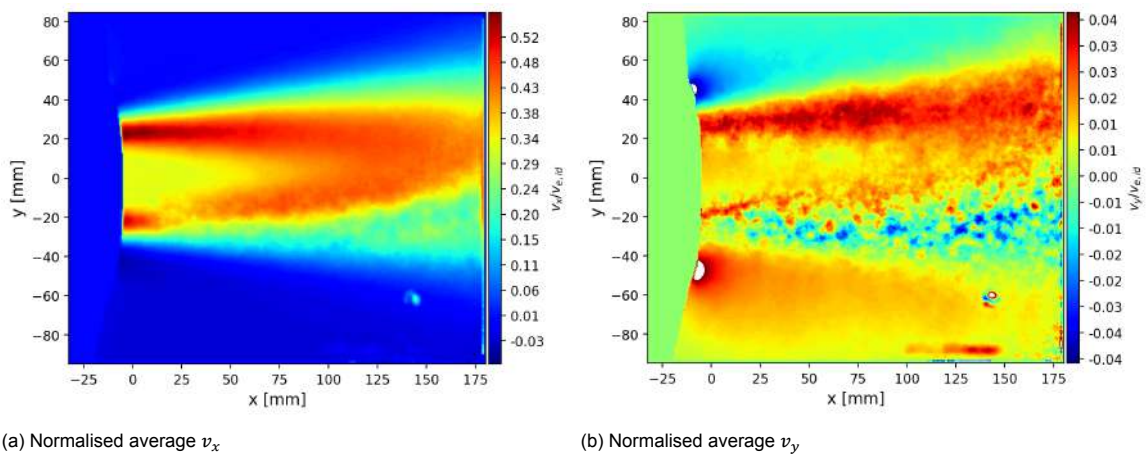


Figure 5.12: Mean flow velocity components at NPR 22.21

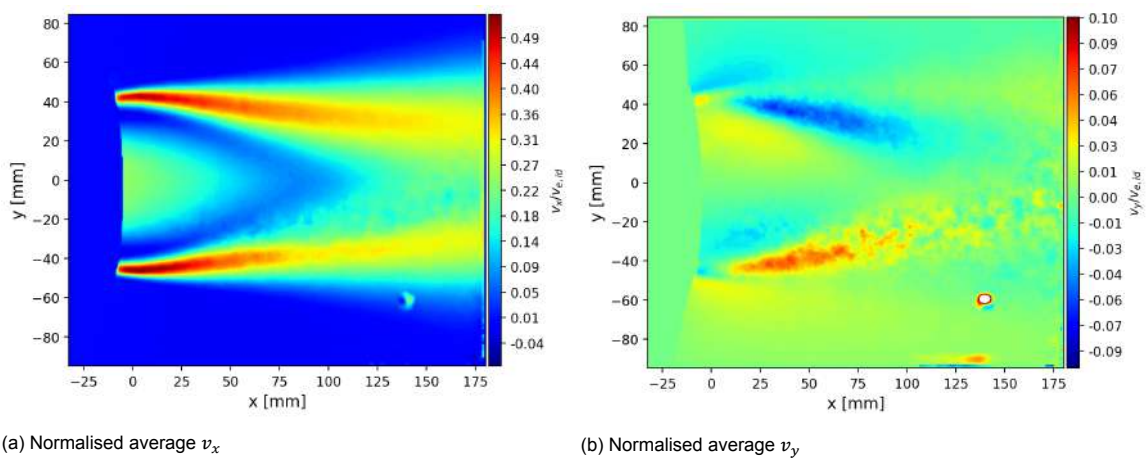


Figure 5.13: Mean flow velocity components at NPR 24.48

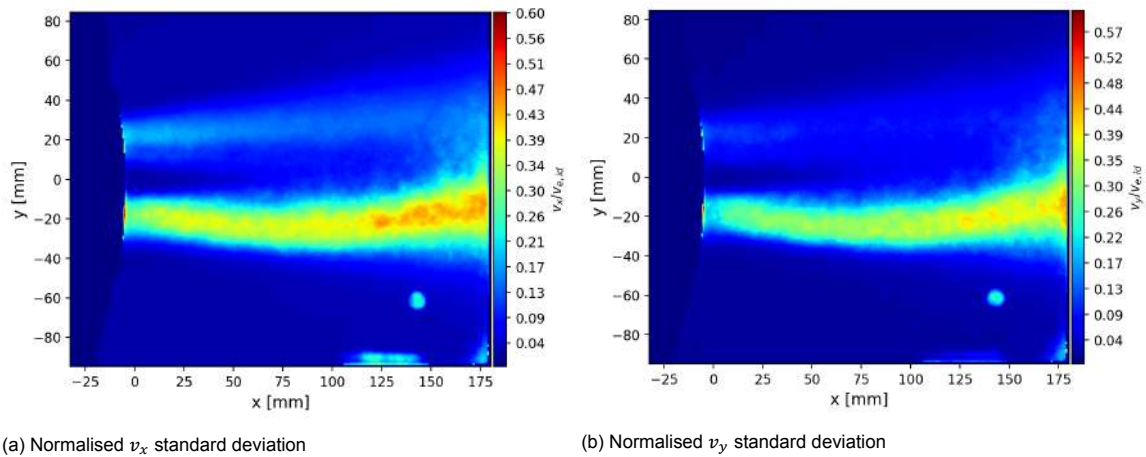


Figure 5.14: Standard deviation of velocity components at NPR 16.42

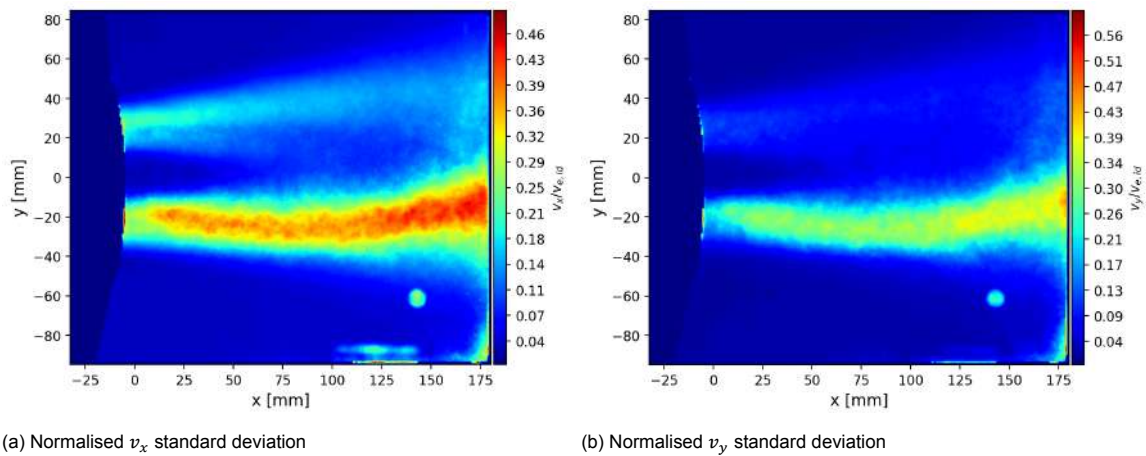


Figure 5.15: Standard deviation of velocity components at NPR 22.21

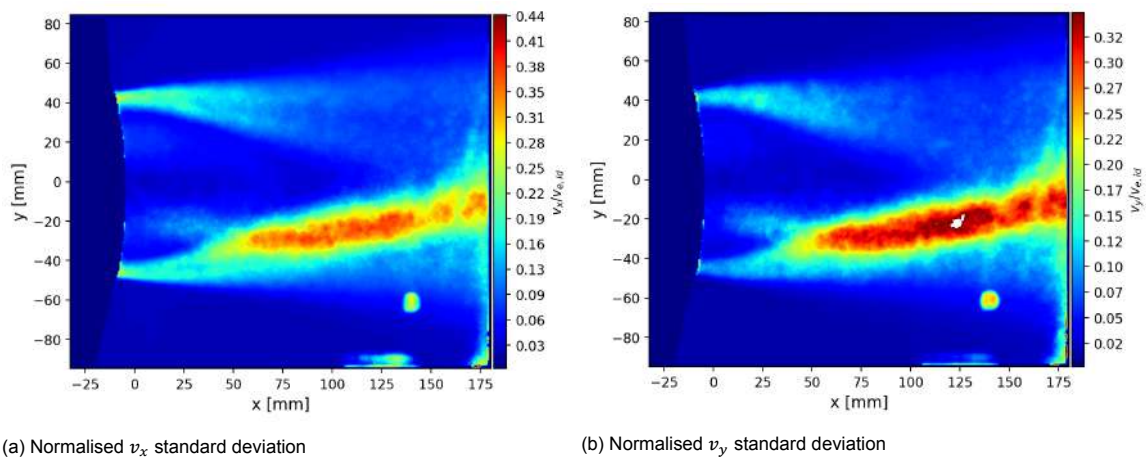


Figure 5.16: Standard deviation of velocity components at NPR 24.48

The first thing to note is that the transition from FSS to RSS occurs for a lower NPR when the PIV tube is installed, even when corrected for the lower ambient pressure in the PIV tube. It can thus be concluded that the PIV tube does have an effect on the flow development and causes the tests to

be less representative. The reason for this might be that the placement of the air holes in the nozzle back plate cause unsteady fluctuations in the ambient pressure in the PIV tube. From the Scanivalve measurements, it is found that the standard deviation in the ambient pressure is around 500 Pa. This means that almost all fluctuations lie within 1.5 kPa of the mean. The largest fluctuations can alter the NPR by a few tenths. This means that the flow could have transitioned at NPR 24.75 because of the ambient pressure fluctuation, even though the mean ambient pressure resulted in NPR 24.4. Because of the hysteresis effect, it would be unlikely that once the flow has entered the RSS state it transitions back to FSS even when the mean NPR is lower than the transition NPR.

In the axial velocity profiles, the annular supersonic jet is clearly visible, just as in the average flow from the schlieren measurements. When comparing the two FSS cases, the height of the subsonic region at the nozzle exit increases and the jets become more distinct because of the limited time the flow spends inside the nozzle, where mixing could occur. Turbulent mixing of the two jets causes the flow to become subsonic. In the RSS flow case shown in Figure 5.13, the two supersonic jets attached to the wall are very clearly visible. In the case of RSS, back-flow with a velocity around 4% of the ideal exhaust velocity is also observed very close to the nozzle lip, which indicates the presence of a recirculation zone. A large region with very low velocity of around 10 m/s is observed on the inside of the supersonic jet, while the kernel flow is still relatively high velocity. Thus, the recirculation zone has to be at least partially inside the nozzle, which is to be expected since the separation point is still far upstream in the nozzle. From the contours of velocity fluctuations, it is again observed that the fluctuations in the bottom half of the nozzle are much more severe than the fluctuations in the top half. This is congruent with the observations from the Schlieren measurements. It can be seen that the flapping of the flow in the bottom half of the nozzle increases as the NPR moves closer towards the NPR at transition. However, when the flow has transitioned, severe fluctuations are observed, especially in the vertical flow direction, which seem to become worse as the NPR is increased further.

The Mach number distribution for the same NPR values is shown in Figure 5.17, such that it is possible to clearly distinguish between supersonic and subsonic regions. It can be seen that as the NPR increases, the maximum Mach number decreases. This likely happens because of the increasing flow area when the separation point moves downstream. In the FSS regime, the height of the annular shock seems to remain relatively constant, but at larger radius this causes a drop in velocity. Even though the shock in the RSS regime becomes much thinner, the flow area becomes so large that the Mach number reaches barely above 1.

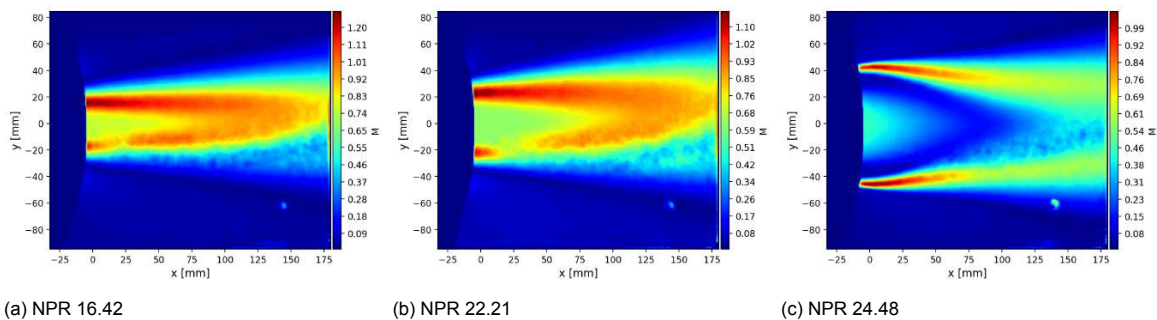


Figure 5.17: Mach number contours at various NPR

The existence of the recirculation region is further confirmed by the vertical velocity profile, which shows a large negative velocity region on the bottom of the nozzle and a positive velocity region at the top. This indicates that the recirculation region is rotating clockwise in the bottom half of the nozzle and counterclockwise in the top. The z-vorticity, shown in Figure 5.18b, also indicates rotational flow just downstream of the nozzle lip, with a large region of negative vorticity at the bottom of the nozzle and positive vorticity at the top. The streamlines in Figure 5.18a suggest the same. It must be noted however, that experimental observations by Yoon et al. [82] and Ramsey et al. [17], who both used Hydroxyl Tagging Velocimetry (HTV) on hot gas flows, find no indications of a recirculation zone. CFD simulations by Hagemann and Frey [119] do show a similar flow structure with a high velocity flow around the nozzle centre line, and lower velocity flow further removed. According to common theory

[18], the recirculation zone forms because of the radial flow component and vorticity introduced by the non-uniform shock strength of the Mach stem on the inside of the nozzle. Additionally, the low momentum flow downstream of the shock experiences an adverse pressure gradient to the ambient pressure at the nozzle exit, which causes the flow velocity in the negative x direction. The streamlines provide an even better picture of the flow field in the recirculation region and also allow for better explanation of the existence of the low velocity area right after the nozzle lip.

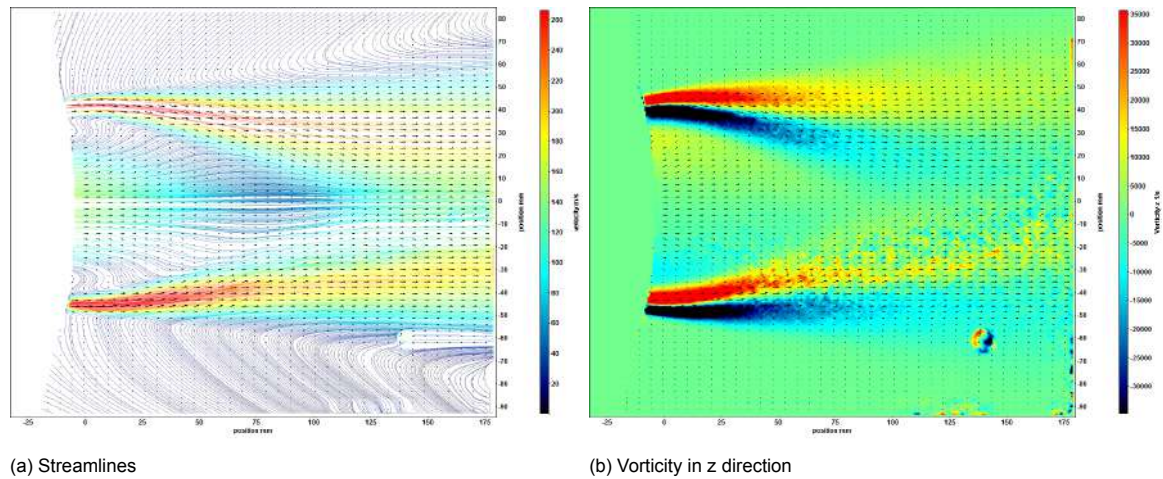


Figure 5.18: Visualisation of nozzle flow at NPR 24.48

From continuity, it is known that three factors play a role in the mass flow through a stream tube, namely the density, velocity and streamtube area. From the streamlines it is clearly visible that the area of the stream tubes in the low velocity region is significantly increasing, especially when moving away from the nozzle centre line. The reason for this is likely the flow blockage by the recirculation zone, which leads to a zone with lower pressure than the kernel flow downstream of the recirculation zone. This leads to streamline curvature in the radially outward direction, until the flow is met by the surrounding supersonic jets which are at higher pressure and cause the streamlines to curve back. The increase in total flow area means that the velocity has to decrease in a region where the flow is relatively incompressible. Useful insight into the flow structure can be gained by assuming an isobaric region at ambient pressure downstream of the nozzle lip at $x = 0$. Even though this does not fully represent reality, the pressure is not expected to vary with respect to ambient pressure significantly as can be judged by the final pressure measured by the Scanivalves, which even in the RSS flow case is close to atmospheric. The density in this plane is then obtained through the equation of state, and the mass flux J_m can then be determined from $J = \rho V$. The mass flow can be estimated by assuming a constant annular stream tube area determined by the vertical resolution of the data

$$A = \pi(y_{i+1}^2 - y_i^2) \quad \text{for} \quad y \in [0, r_e] \quad (5.1)$$

with r_e being the exit radius of the nozzle. This results in the contours shown in Figure 5.19. The integrated mass flow of this analysis results to 1.25 kg/s, which is an underestimation likely caused by the assumption of constant pressure and stream tube area. Nevertheless, the trend shows that by far the majority of the flow is carried through the supersonic jets, which means that the minimal amount of flow through the kernel has an extremely large area to expand into, resulting in an area with very low flow velocity.

Because the pressure in the supersonic jets is slightly sub-atmospheric, they are bent towards the nozzle centre line, which decreases the flow area available for the kernel flow, which causes it to speed up.

5.2. Flexible Nozzle Analysis

The first nozzle tested was the flexible 80A with a wall thickness of 5mm. This nozzle was only tested to determine in which direction the stiffness of the nozzle should move in order to obtain relevant data

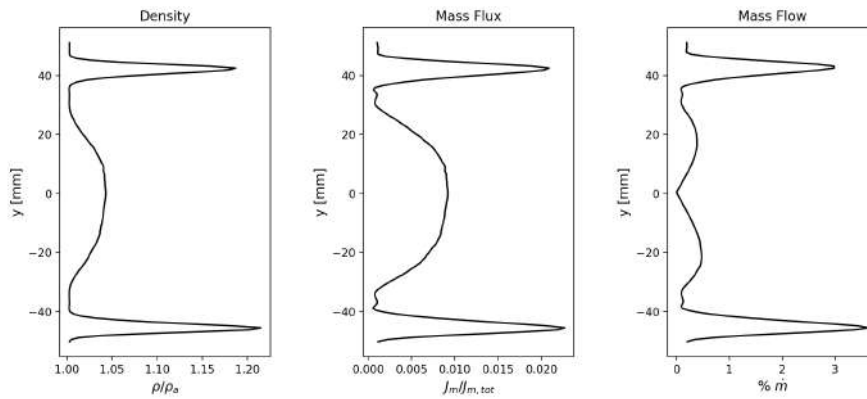


Figure 5.19: Estimated density, mass flux and mass flow distribution for a vertical plane at $x = 0$

about the vibrational modes of the nozzle. It is found that this nozzle could be tested to an NPR of approximately 15, before it would collapse. A collapse of the nozzle is defined here as a rapid deviation from a previously existing quasi-steady state, to a condition where two opposite walls at any point on the nozzle are touching or close to touching. This results in severe distortion of the internal nozzle shape and flow blockage in the part where the walls meet.

In the case of the flexible 80A nozzle, the nozzle shows a steady deformation towards the bottom left when seen from downstream straight onto the nozzle lip. The nozzle deformation increases with NPR, which can be explained by the fact that the separation point moves downstream. Moreover, as stated by Génin et al. [20], a deformation of the nozzle during FSS will be unsteady, because the separation point will move further downstream on the side where less flow expansion is warranted by the contour and thus, assuming that the side load acts at the separation point, the moment lever arm of the side load will increase. A slight ovalization in the same direction as the deformation is observed, which causes the side load to act in the same direction as the deformation. The ovalisation is also amplified as the NPR is increased. The progression of the nozzle deflection is shown in Figure 5.20. The first image shows the no flow condition. The second image shows the deformation of the nozzle at low NPR around 5, with slight ovalisation and deformation towards the bottom left. Figure 5.20c shows the deformation of the nozzle right before the collapse and Figure 5.20d shows the deformation of the nozzle right before the main valve was closed. It must be noted that the deformation took approximately one minute to reach the third image, and only one second to move from the third to the fourth state. Thus, there exists a point where the structural integrity of the nozzle suddenly deteriorates quickly, similar to a yield point in a metals, even though the deformation is not plastic. Fan and Chen show that this point exists in the stress strain curve of polyurethane for dynamic loading. [121]

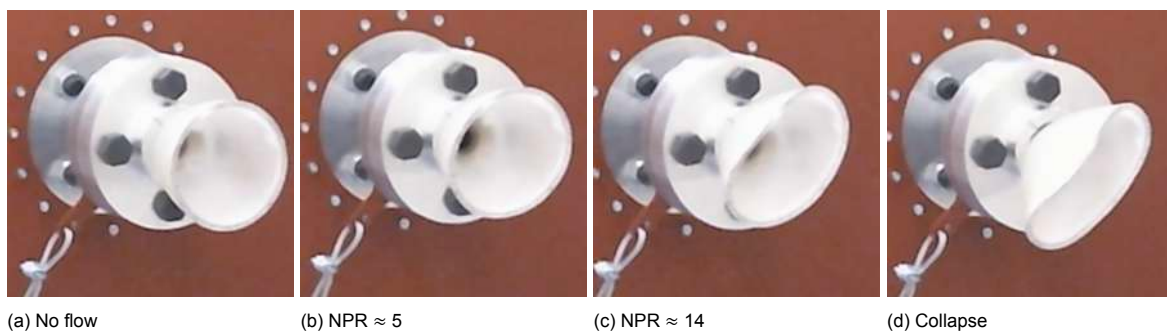


Figure 5.20: Deformation over NPR ramp of flexible 80A 5 mm wall nozzle

The lack of vibrations is likely caused by the slow spring-back of the flexible 80A material. Moreover, the large wall thickness makes the nozzle very stiff, such that a relatively large force is required to deform the nozzle. The damping capacity, which was not taken into account in the material selec-

tion of the nozzle, seems to be too high for this material to be suitable for the achieving a somewhat representative FSI. Two other nozzles with a wall thickness of 1.5 mm and 2 mm respectively were printed, but the prints were of low quality and so they were not tested. These findings resulted in the switch to the elastic 50A material, even though it was known that the low tensile modulus could pose a problem. It was decided to start with a nozzle with 3 mm wall thickness. Unfortunately, during testing it was found that as soon as the flow would become supersonic, at an NPR of approximately 2, the nozzle would start to collapse, which is shown in Figure 5.21.

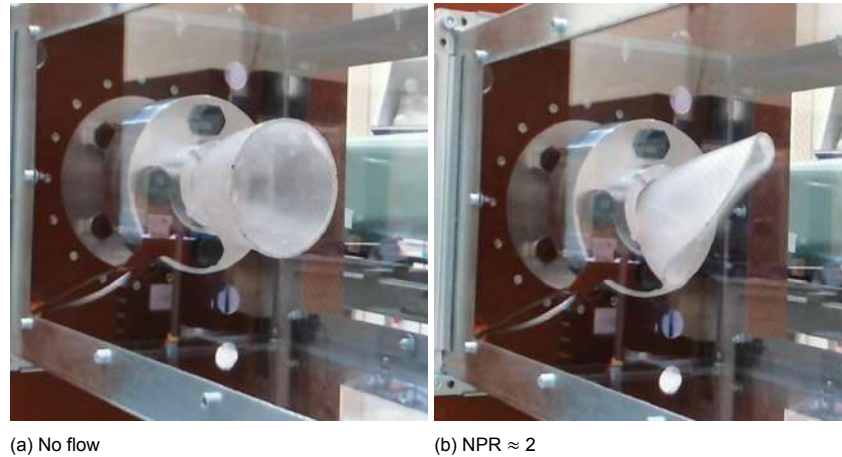


Figure 5.21: Collapse of 3 mm elastic 50A nozzle

This shows that in order to design a Elastic 50A nozzle such that it is strong enough to take the pressure loads, it would have to be extremely thick. No time was left in the project to switch to polyurethane pouring, and as such the nozzle was stiffened using steel wire. This was done in order to achieve some vibration in the nozzle, even though the structural properties of the nozzle are now unknown. It is still possible to show the capabilities of DIC for this type of research, and the image processing tools could be developed. The addition of the steel wire allowed the nozzle to be tested up to NPR 10 before the deflections would become too severe, and allowed for some vibrations to be measured.

Figure 5.22 shows the progression of the average flow from the schlieren measurements. The mach diamonds in the flow exhaust are clearly visible, which indicates that the flow is separating very close to the throat. A steady deflection towards the downside is observed, and the flow seems to attach to the top of the nozzle.

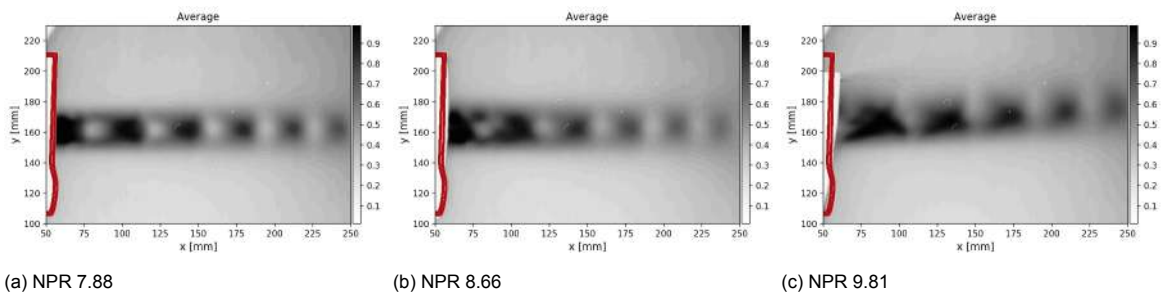


Figure 5.22: Collapse of 3 mm elastic 50A nozzle

Figure 5.23 and Figure 5.24 show examples of the energy spectrum and power spectral density (PSD) of the vibrations that can be extracted from the DIC images. The energy spectrum shows the energy in a specific mode relative to the total energy in the vibrations. It can be seen that by far the largest amount of energy is present in the 0th and 1st modes for all tests. It is interesting to see that a small shift in NPR from 7.88 to 8.66 increases the energy in the 1st mode significantly, while this is not maintained for higher NPR. This could suggest that around NPR 8.66 some coupling exists between

the shock wave unsteadiness frequency and the eigenfrequency of the first mode of the structure.

In the case of purely random vibrations, the energy spectrum should be symmetric about the 0th mode, because for example mode 1 and mode -1 represent the nozzle deflection from the mean in the horizontal and vertical direction respectively. It can be seen that this is the case for all modes but the 1st. This indicates that the first mode favours horizontal deflection over vertical. This could be caused by the fact that the nozzle was already slightly horizontally displaced, which means that it has less support in the horizontal direction than the vertical. Another explanation could be that the measurement time of one second is too short to cover enough statistically independent states of the nozzle's first mode deformation. It can be seen that with increasing NPR, the relative energy in the 0th mode decreases, and that the energy in higher mode numbers - especially mode 1 and 2 - is increasing. From the PSD plots it can be seen that the frequency of the 0th mode is approximately 100 Hz, and very narrow-band. The first mode shows a much more broad-band spectrum, with frequencies ranging mainly from 10 to 30 Hz. The second and third modes are not clearly visible in these spectra, because they lie in the same frequency range as the 0th mode. It must be noted that this data was obtained without PIV tube installed. In tests where the PIV tube was installed, the vibrations became so excessive for NPR values higher than 5 that it became impossible to track the nozzle lip.

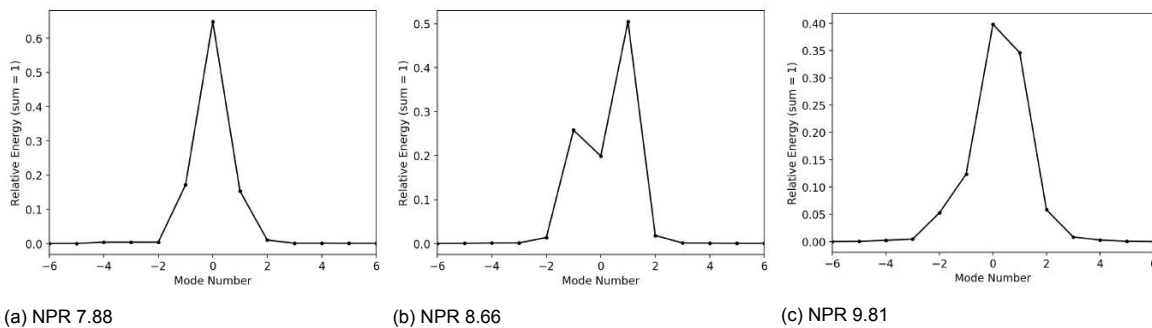


Figure 5.23: Energy spectrum for 3 mm elastic 50A nozzle at various NPR

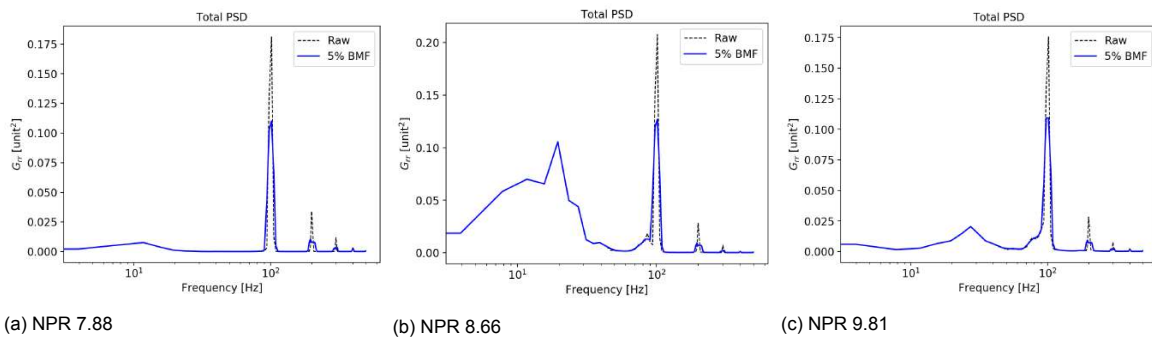


Figure 5.24: PSD for 3 mm elastic 50A nozzle at various NPR

6

Conclusion and Recommendations

The conclusion is divided into two parts. Since a large part of the thesis assignment was the design of the setup, conclusions and recommendations about the design process are discussed separately from the conclusions and recommendations obtained from the test data. The conclusions are presented as answers to the research questions posed in chapter 1.

6.1. Design

One of the main purposes of this MSc thesis was the development of the setup in order to obtain the capability within the faculty to perform nozzle research. The success of the design is initially judged by reviewing if requirements are met.

Table 6.1: Requirements

Identifier	Requirement	Met?
<i>System</i>		
SYS-01	The system shall measure side loads in 2 directions	Yes
SYS-02	The system shall visualise the flow field in the nozzle divergent section	Yes
SYS-03	The system shall visualise the flow field in the exhaust plume	Yes
SYS-04	The system shall run at a maximum NPR of at least 37	Yes
SYS-05	The system shall be able to control the NPR with an accuracy of 0.1	Maybe
SYS-06	The system shall be able to accommodate a mass flow of at least 3 kg/s	Yes
SYS-07	The system shall be able to run continuously for at least 7 minutes	Yes
SYS-08	The system shall measure total thermodynamic conditions before the nozzle	Yes
SYS-09	The system shall be able to withstand pressures up to 100 bar including safety factor	Yes
SYS-10	The system shall be able to run on gas bottle supply	Yes
SYS-11	The system shall be able to connect to the high pressure storage tank at the High Speed Laboratory	Yes
<i>Nozzle</i>		
NOZ-01	The flexible nozzles shall be cheap to produce with a maximum price of €100 per piece	Yes
NOZ-02	It shall be able to produce a flexible nozzle within 2 days	Yes
NOZ-03	The flexible nozzle shall be supported up to a specific area ratio	Yes
NOZ-04	The nozzle wall shall be continuous from convergent section to exit	Yes
NOZ-05	The nozzle internal wall shall be as smooth as possible	Yes
<i>Flow</i>		
FLO-01	The working fluid shall be high pressure air or nitrogen	Yes
FLO-02	The flow shall be laminar when entering the nozzle	Yes

FLO-03	A plenum shall be used in front of the nozzle	Yes
FLO-04	No obstructions shall be present downstream of the nozzle that can affect the nozzle flow properties	Partially
<i>Structure</i>		
STRUC-01	The structure shall be able to withstand a thrust force including safety factor of 2	Yes
STRUC-02	The structure shall be able to withstand a lateral force equal to the thrust force	Yes
STRUC-03	The structure shall have a first natural frequency at least an order of magnitude higher than the highest natural frequency of the 4th mode shape of the flexible nozzles	Probably
STRUC-04	The structure shall be able to be firmly attached to the ground	Yes
STRUC-05	It shall be possible to easily swap out nozzles in the system	Yes
<i>Safety</i>		
SAFE-01	The system shall use remotely controlled valves to turn the main flow on and off	Yes
SAFE-02	People conducting the test shall be shielded from potential nozzle debris	Yes
SAFE-03	The system shall be safe in case of power loss	Yes
SAFE-04	The system shall be safe in case of loss of signal	Yes
<i>Testing</i>		
TEST-01	The system shall allow for the installation of a PIV seeder upstream of the nozzle	Yes
TEST-02	PIV shall be used to measure the velocity profile in the exhaust plume in at least 2D	Yes
TEST-03	Schlieren or Shadowgraphy shall be used to qualitatively visualise the exhaust plume	Yes
TEST-04	The camera capturing the Schlieren or Shadowgraphy images shall be able to record at 1000 fps	Yes
TEST-05	The side load shall be measured separately in y and z direction	Yes
TEST-06	The side load shall be measured at a frequency of 1000 Hz	Yes
TEST-07	The nozzle wall displacement shall be measured at a frequency of 1000 Hz	Yes
TEST-08	The total pressure upstream of the nozzle shall be measured at a rate of 500 Hz	Yes
TEST-09	The total temperature upstream of the nozzle shall be measured at a rate of 500 Hz	Yes
TEST-10	The ambient pressure shall be measured at a frequency of 500 Hz	Yes
TEST-11	The test shall be controlled using LabView	Yes
TEST-12	The NPR shall be visible directly on the screen of the operator	Yes

It can be concluded that almost all requirements that were set at the start of the design process are fully met. The requirement that the NPR shall be controllable with an accuracy of 0.1, is questionably met, because the fluctuations in NPR at constant NPR tests probably has fluctuations around ± 0.05 . It is definitely possible to control the NPR with an accuracy with 0.2, which is sufficient for the current study. In the case that more accurate control is required, an electronic valve control system can be designed to fit on the existing hand actuated valve.

The requirement that no obstruction should be present downstream of the nozzle that affects the flow properties is only partially met because it is observed that the addition of the PIV tube does significantly affect the flow conditions in the nozzle. This could be solved by making a tapered PIV tube, with a very large diameter close to the nozzle, which tapers down to the diameter of the diffuser outlet. Moreover, a square to circular shape would allow for the size of the PIV at the exit to be much larger.

Finally, the natural frequency of the structure has not been measured, but since the structure is extremely overdesigned, it is likely that the natural frequency of the structure is much higher than several hundred Hz.

The setup provides the faculty with the capability of safely measuring external nozzle flows of various types, using various measurement techniques, which means that the overall conclusion can be drawn that the design of the setup was successful. It is unfortunate that no representative vibrations could be observed in the flexible nozzle, but useful knowledge about the design of flexible nozzles is obtained nonetheless.

A few recommendations about how to improve the design of the setup and nozzles are given below.

- Future research should put more focus on the design of the flexible nozzles. This can initially be done by performing more advanced simulations to determine the structural properties, such as finite element modelling (FEM) simulations. Furthermore, the optimal manufacturing method should be reassessed. If more time is available, and staff and students involved have more affinity with structural design, the design and manufacturing of the nozzle can definitely be improved.
- The dynamic response of the system should be measured in order to better determine the side loads. Moreover, the strain gauges should be balanced with additional resistors in order to improve the signal to noise ratio at low levels of side load.
- The design of an electronic control system for the control valve would improve the operation of the system. In the current system, the operators have to be present in the same room as the setup, which means that the operators have to deal with a lot of noise. Moreover, hand control of the NPR might not be sufficient for more detailed studies into the flow phenomena inside nozzles. An electronic control system would allow for the test setup to be controlled from a control room, separate from the wind tunnel room and would result in better NPR control.
- Currently, no edge fillet is included in the connection of the strain tube to the connection flange. This potentially causes large stress concentrations at the interface. Therefore, it is recommended that edge fillets are added to both sides of the strain tube.
- An already available cyclone seeder was used in the setup, but it ran out of seeding particles after about 1.5 minutes. Since refilling the seeder takes some time, a bigger cyclone seeder specifically designed for this setup would allow for longer run times or higher seeding concentration for longer periods of time, such that more tests can be performed sequentially.
- To improve the spacial resolution of the pressure measurements, it could be decided to put all of the 45 pressure ports in a single array, because no significant asymmetry is observed from the data, likely because the measurement frequency of the Scanivalves is not high enough to measure significant instabilities.
- The effect of the PIV tube is significant on the nozzle behaviour. Therefore, the design of the PIV tube could be changed to be wider in order to decrease the degree of interference.

One of the research questions posed in chapter 1 should be answered in this section, namely

What is the best manufacturing method for flexible nozzles?

In the initial design phase it was decided to use SLA 3D printing in order to save time and money on the production of the flexible nozzles. This turned out not to be the best manufacturing method for the nozzles. Firstly, it is uncertain whether the material properties of the commercial resin are equal to those given on the data sheet. From experience within the 3D printing group at the faculty, this seems not to be the case. This can result in theoretically similar nozzles having different behaviour. Moreover, fine adjustments to the structural properties of the nozzle by a change in geometry can be completely negated by the variance in material properties. This makes 3D printing unsuitable for fine adjustment of structural properties which could be useful in future research. Moreover, the types of materials available are very limited, which means that the only way to change the structural properties of the nozzle

is through changing the geometry, i.e. the wall thickness. This severely limits the amount of nozzle variations that can be tested, which is exacerbated by the previous statement that small changes in the geometry can be negated by changes in material properties. Most importantly, it was found during this research that it is unlikely that the materials available from Formlabs are suitable. The flexible 80A material has a too large damping capacity and much too slow spring back to allow for any fluid structure interaction. On the other hand, the flexible 50A material likely has a quick enough spring back, but the material is much too weak to hold the pressure loads even at very low NPR. This likely cannot be solved by increasing the nozzle wall thickness, as this will make the nozzle unreasonably thick, which in turn will increase the damping capacity but also will increase print time significantly. For both materials the nozzles were shown to collapse well before the FSS to RSS transition point.

For these reasons, it is recommended that for future research, either polyurethane pouring or sheet metal forming is used to manufacture the nozzles. Of these two options, likely polyurethane pouring is the most viable because it does not require special tooling apart from the mould. Once the mould is produced, the production time per nozzle should be similar to 3D printing. The benefit of polyurethane pouring is that the material properties can be varied relatively easily, while nozzles with theoretically similar properties should also be very similar in practice, because the mixture ratio of different components and the cure cycle are very easy to control. The design of the test setup and the nozzle likely does not have to be changed, because the clamping mechanism used for the 3D printed nozzles is equally suitable for poured nozzles. Furthermore, if a stiffer material is used, it might be possible to include pressure ports in the flexible nozzle, to allow measurement of the pressure distribution in a deformed nozzle. Before pursuing metal forming, experts should be consulted on the viability.

6.2. Conclusions from Experimental Results

This section describes the conclusions that can be drawn from the data presented in chapter 5. An attempt is made to answer the research questions posed in chapter 1.

1. *How does the flow development for a fixed shape nozzle compare to literature?*

From the data it can be concluded that the behaviour of the nozzle is very similar to experiments performed previously. A very clear transition from the FSS to RSS regime is present during both start-up and shutdown. Moreover, the extreme hysteresis behaviour between start-up and shutdown is also observed in these experiments. The longitudinal pressure distribution along the nozzle is similar during both the FSS and RSS regime. During the FSS regime, a fast increase from the ideal pressure to the plateau pressure is observed, which fits the generalised free interaction theory very well, which is why this theory can be used to achieve sub-sensor resolution on the separation point. During the RSS regime, super-atmospheric pressures are observed at reattachment locations and several bubbles can be observed in some situations. This data is very similar to the data presented by Ruf et al. [34] Moreover, the pressure contours presented in Figure 5.1 are very similar to the ones presented by Baars et al. [8] The separation point also follows the Stark criterion relatively well.

2. *At what NPR does FSS to RSS transition occur for this nozzle?*

During start-up, FSS to RSS transition is observed at an NPR of 24.75. This is slightly higher than expected compared to other experiments, with the expected NPR lying between 23.1-23.6. For shutdown, the separation point at transition lies very close to the first pressure port, which makes it hard to determine the exact transition point.

3. *To what extent are the separation and transition asymmetric?*

From the pressure distribution plots it can be concluded that the separation is relatively axisymmetric, at least to the extent that can be resolved by the resolution of the pressure ports. From the separation points determined using generalised free interaction theory, it can also be concluded that the longitudinal position of the separation location is relatively consistent along the azimuth. From the schlieren images it becomes clear that the separation is extremely asymmetric. It is observed that the transition occurs at the bottom of the nozzle occurs approximately 9 ms before the transition at the top. This means that during this time a large side load is present which explains the peak in side loads observed during transition for example by Hagemann et al. [18] It

was even observed that the flow at the bottom of the nozzle transitions to RSS for a short period of time, only to transition back to FSS before the real transition occurs.

4. **What does the velocity field look like during FSS?**

The PIV images provide good insight in the flow structure during FSS. Two supersonic jets away from the centre line are clearly visible in the images. A region of lower velocity is observed in the kernel, but this region still achieves a relatively high Mach number, especially compared to the low velocity region that is visible in the RSS regime. This confirms that there is no trapped vortex present in the FSS regime. As the NPR is increased, the Mach number in the supersonic jets is found to decrease, likely because of the larger flow area available due to the separation point lying further downstream.

5. **What does the velocity field look like during RSS?**

Again, the PIV images provide good insight into the flow structure present during the RSS regime. The two supersonic jets are visible, but at a much lower Mach number than in the case of FSS. The supersonic jets are also much thinner than in the FSS regime. A large zone of extremely low velocity is present around the centre line of the nozzle, with reverse flow with a velocity of up to 4% of the ideal exhaust velocity in some locations. This fact, together with the streamline and vorticity plots, could indicate the presence of a trapped vortex inside the nozzle, but this can not be stated for certain.

6. **How do PIV velocity fields compare to CFD simulations and other experimental data?**

Since only experimental data on the RSS regime is available, it is only relevant to compare this. Moreover, the resolution of the FSS images is not good enough to effectively compare these images to CFD simulations. Unfortunately, the only experimental data provided by Yoon et al. [82] and Ramsey et al. [17] is not normalised, which makes it impossible to compare the quantitative velocity fields. The comparison is shown in Figure 6.1. It can be concluded that the region of higher velocity at the exit of the nozzle is not observed by Ramsey et al. This could be because of the much lower expansion ratio of the nozzle in their research. However, the area of extremely low velocity is present in both experiments as well as in the simulation.

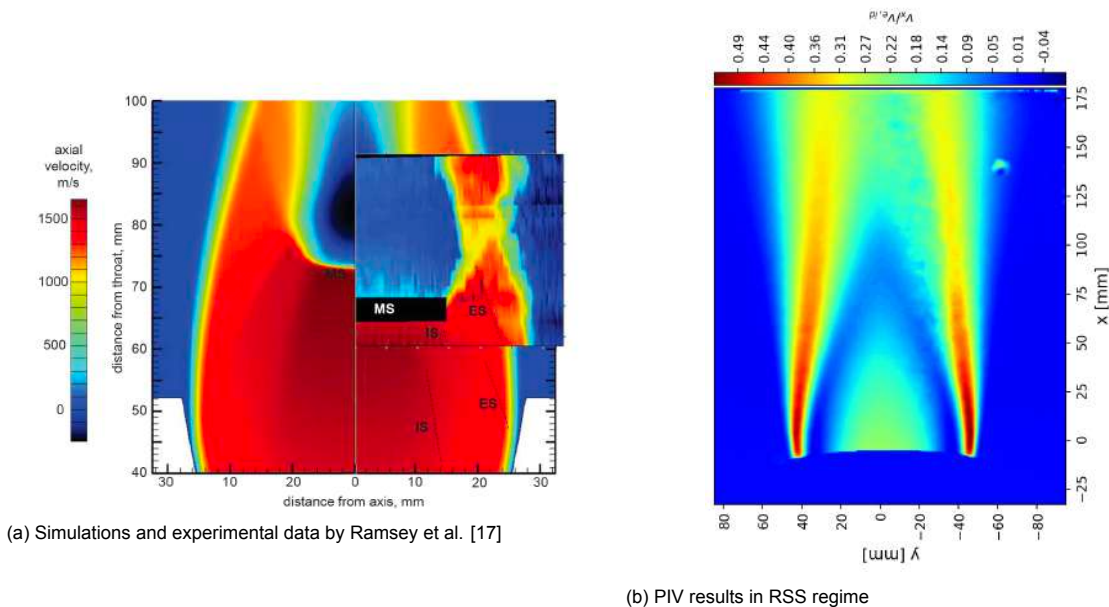


Figure 6.1: Comparison between experiments from literature and current research data

Because the flexible nozzle did not perform as expected, the questions posed at the start of the project can only partially be answered.

1. **At what NPR are vibrations present?**

Vibrations of varying severity were present at all values of NPR.

2. At what NPR are vibrations most prevalent?

From the flexible nozzle tests with the steel wire it could not be determined at which NPR the vibrations were most prevalent. In the small range of NPR that were tested, the largest vibrations were observed at an NPR of 2, likely because of some increased degree of coupling between the flow and the nozzle structure.

3. What modes are dominant in nozzle vibrations?

From the modal analysis it can be concluded that the 0th and 1st modes are most important for low NPR values. Which of these two contains the most energy is not consistent for the NPR range, since for some of the NPR values tested the first mode contained more energy than the zeroth mode. It can also be concluded that the relative energy of higher modes increases as the NPR is increased, at least for the range of NPR values that were tested.

4. How does the frequency of dominant modes vary with NPR?

Not enough data was obtained to be able to answer this question.

5. How does the PIV tube affect nozzle vibrations?

It is very clear that the PIV tube significantly affects the vibrational behaviour of the nozzle. The vibrations in the nozzle for NPR values larger than 5 became so excessive that it became impossible to track the lip of the nozzle. After several tests, the nozzle even failed, the divergent section being torn off at the throat, as shown in Figure 6.2. Likely this is the case because of a combination of impingement of the nozzle flow in the PIV tube windows as well as an asymmetric pressure distribution around the nozzle.



Figure 6.2: Failure of the nozzle at NPR 10

6. How does nozzle stiffness affect dominant mode frequencies?

Not enough data was obtained to be able to answer this question.

6.3. Research Objective

At the start of the research, the following objective was formulated:

The objective of this research is to build a nozzle test setup to be able to determine the effect of the stiffness of a rocket engine nozzle on the amplification of aerodynamic side loads due to fluid-structure interaction, while also providing critical validation data for numerical flow simulations on flexible rocket engine nozzles. This will be done by performing experiments on several flexible nozzles.

The first part of this objective, to build a nozzle test setup, has definitely been achieved. The work resulted in a test setup that can be used to tests a variety of different nozzles, stiff or flexible that has similar capabilities to other nozzle test facilities around the world. The addition of quantitative velocity

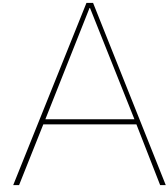
field measurement capability through the use of PIV makes this setup unique and will allow future studies to obtain high fidelity validation data for CFD simulations. Moreover, the research has proven that DIC can be used very effectively to track the nozzle lip and to extract modal data in order to determine mode shapes, frequencies and relative energy. Moreover, the setup is relatively easy to use and can be operated safely. The strain gauges on the setup have to be calibrated and balanced better in order to obtain better quality data.

However, the second part of the objective could not be achieved. Due to time constraints, the flexible nozzle design could not be iterated enough in order to obtain relevant vibrational data. The decision to manufacture the nozzles using 3D printing at an early stage of the project has severely limited the possibilities for design changes in the nozzle. It is however believed by the author that if the only other viable option, polyurethane pouring, was chosen as a manufacturing technique, it would still be very doubtful whether or not this objective could have been reached. Since little to no literature on the behaviour of flexible supersonic nozzle exits, and the modelling of FSI of such a nozzle would have been a completely separate thesis, it would have been equally hard to make a representative nozzle in the first few tries. This risk was identified at the start of the project, and the current outcome was deemed acceptable. Future research should investigate the vibrations and side loads at much higher NPR than in the current research, at the FSS to RSS transition point.

Other recommendations for future research are given below

- For the flexible nozzle tests to result in relevant data, more work needs to be done on defining the requirements for the flexible nozzle, especially regarding natural frequency. Moreover, the parameters of the nozzle that have the greatest effect on the dynamic structural properties, such as geometry and material choice should be understood better. An FSI simulation of the nozzle can be performed in order to provide better insight into the requirements of the flexible nozzle. Afterwards, the experimental data can also be used for validation of the simulation. This can then be used for more research into various topics such as side load minimisation, mass optimisation, foldable nozzles and unconventional nozzle geometries.
- The current research only performed high speed schlieren measurements on the start-up transition. However, it would be interesting to see the flow structure during the shutdown transition as well. This should be relatively easy to obtain. Moreover, multiple transitions can be visualised in order to obtain statistical data about the transition time and whether there is a preference to attach to one side of the nozzle first, or if it is random.
- The setup can be adapted such that higher NPR can be achieved. High pressure gas bottles can be connected to the PIV inlet in order to increase the total pressure in the settling chamber. This can be done up to the point that the pressure in the settling chamber is just below the pressure in the main supply tank, which should make it possible to increase the NPR to approximately 40, which would potentially allow for capturing of the EER. If this is not possible, high pressure nitrogen can be connected to the main inlet instead, but in this case a control valve will have to be installed because the storage volume is likely limited. The flow rate is also limited by the pressure regulator valves on the gas bottles, and these are normally not made for high flow rate. Measurements at a higher NPR will allow for better visualisation of the trapped vortex as well.
- More measurements should be performed zoomed in on the location of the supersonic jet in order to achieve better resolution of the velocity field in this region. Furthermore, the flow structure during RSS at low NPR close to the transition point during shutdown can be measured in order to compare it to the flow structure just after transition during start-up which could provide more insight into the reason behind the hysteresis behaviour.
- Tomographic PIV on the setup would allow for visualisation of the flow inside the nozzle, which would obviously provide great insight into the flow structure during the FSS and RSS phase.
- In future research, vibration tests of the nozzle can be performed in order to determine the natural frequencies of the nozzle, such that it can be determined how these change in the presence of airflow. If the unsteadiness frequencies of the flow in the nozzle are known, one could also

design a nozzle with the same natural frequency in the first or second mode as the unsteadiness frequency, in order to determine the degree of resonance.



Additional Test Data

A.1. Pressure Data

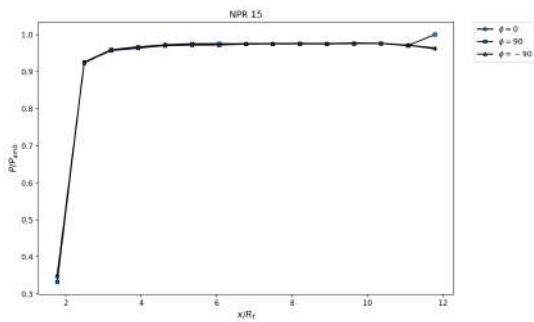


Figure A.1: NPR 14.83

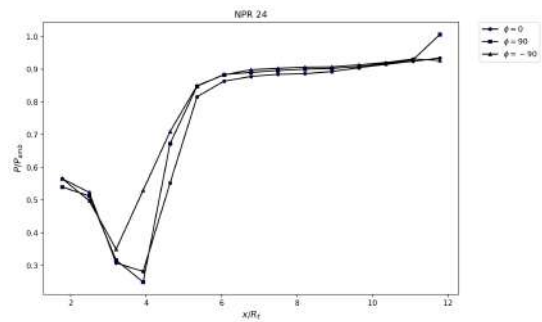


Figure A.2: NPR 23.84

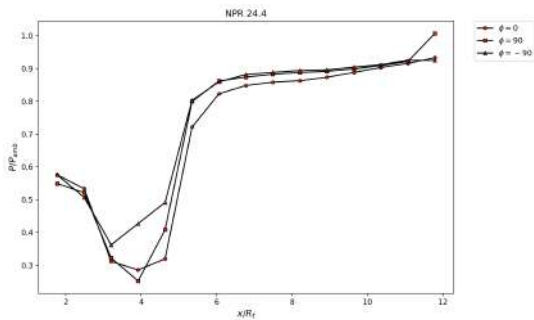


Figure A.3: NPR 24.23

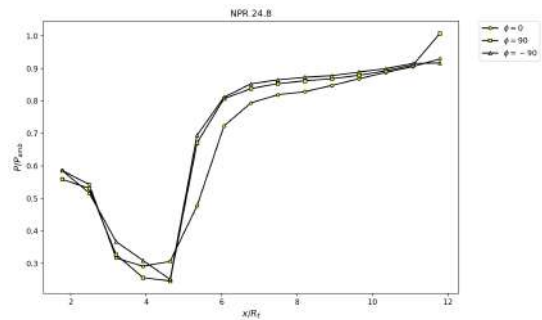


Figure A.4: NPR 24.65

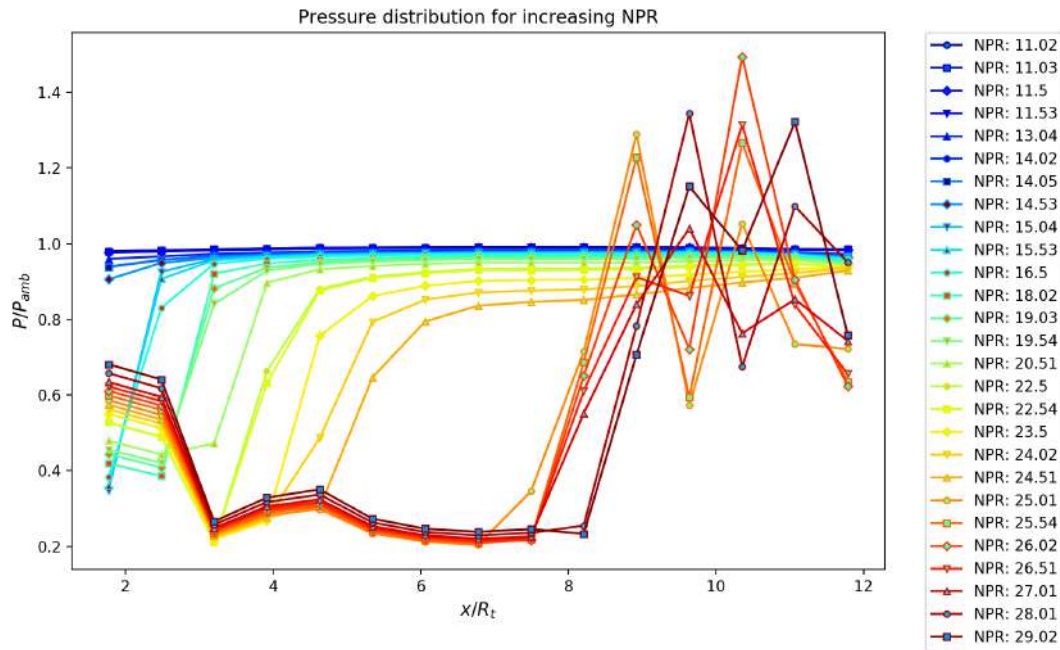


Figure A.5: Pressure distribution for varying NPR during increasing NPR for $\phi = 0$

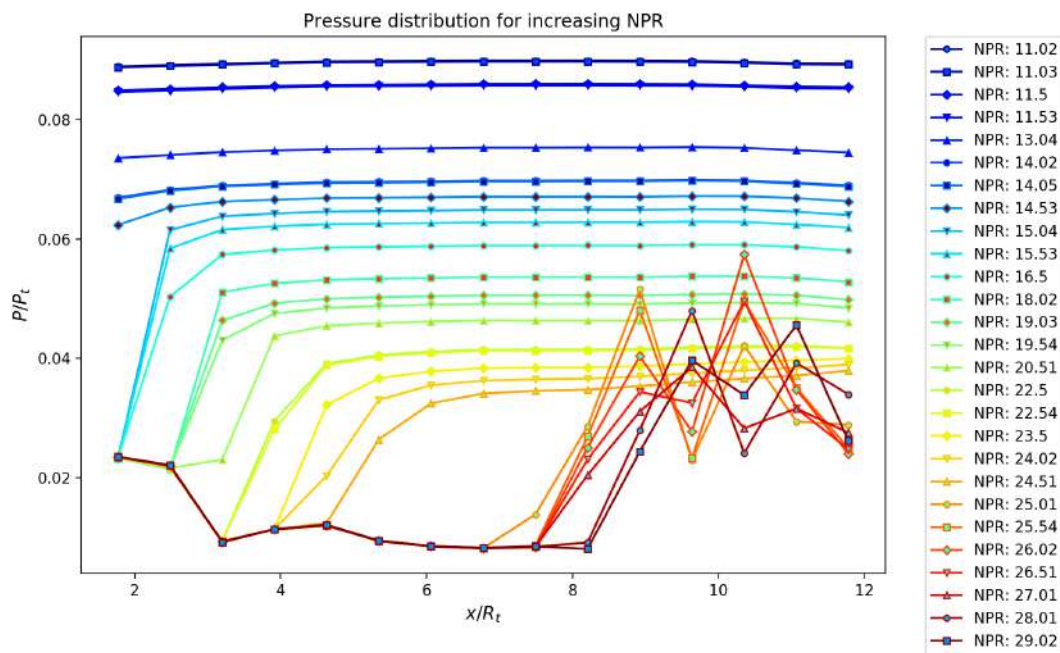


Figure A.6: Pressure distribution for varying NPR during increasing NPR for $\phi = 0$ compared to total pressure

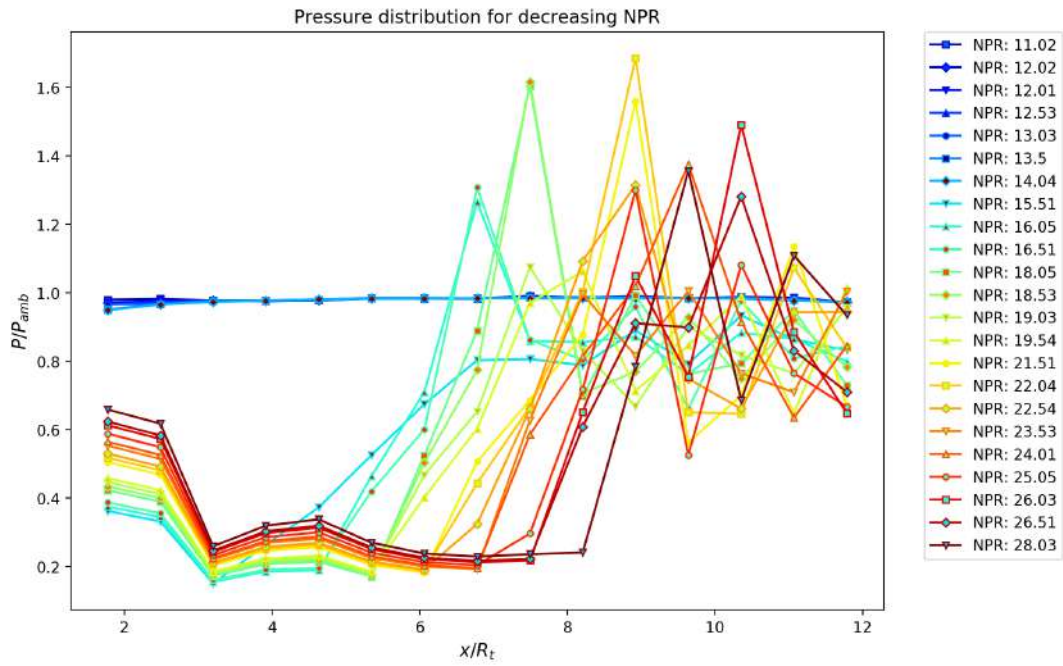


Figure A.7: Pressure distribution for varying NPR during decreasing NPR for $\phi = 0$

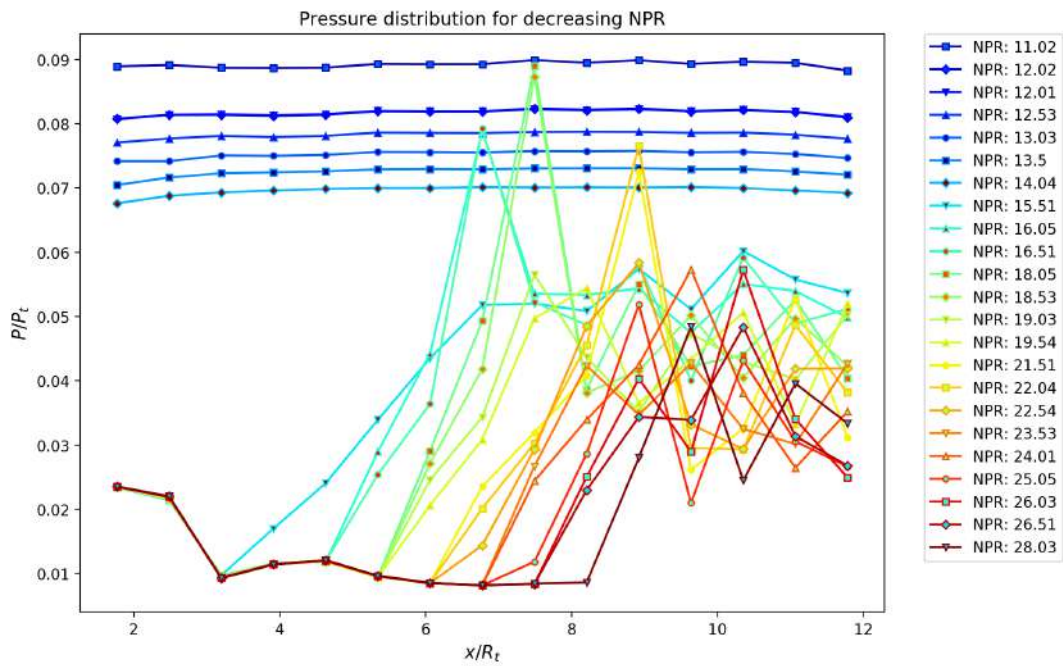


Figure A.8: Pressure distribution for varying NPR during decreasing NPR for $\phi = 0$ compared to total pressure

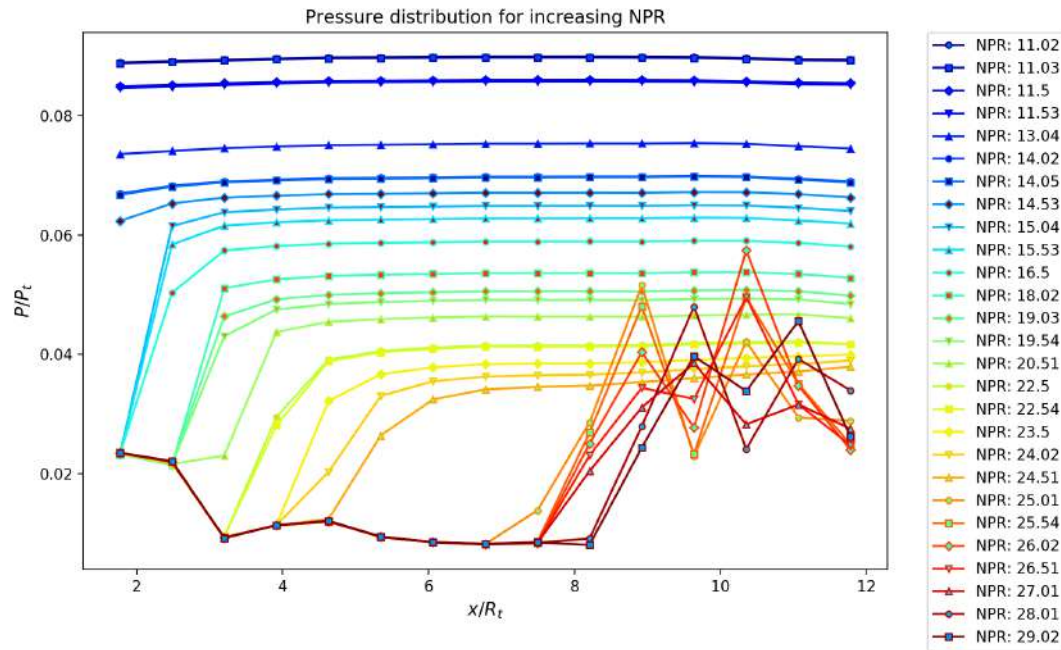


Figure A.9: Pressure distribution for varying NPR during increasing NPR for $\phi = 90$ compared to total pressure

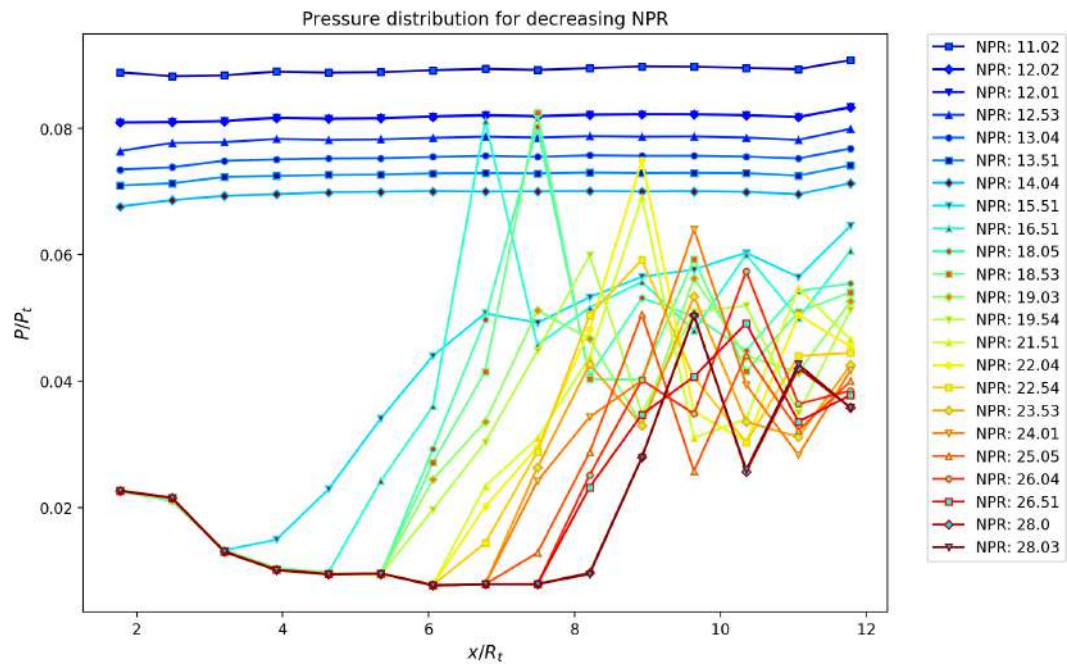


Figure A.10: Pressure distribution for varying NPR during decreasing NPR for $\phi = 90$ compared to total pressure

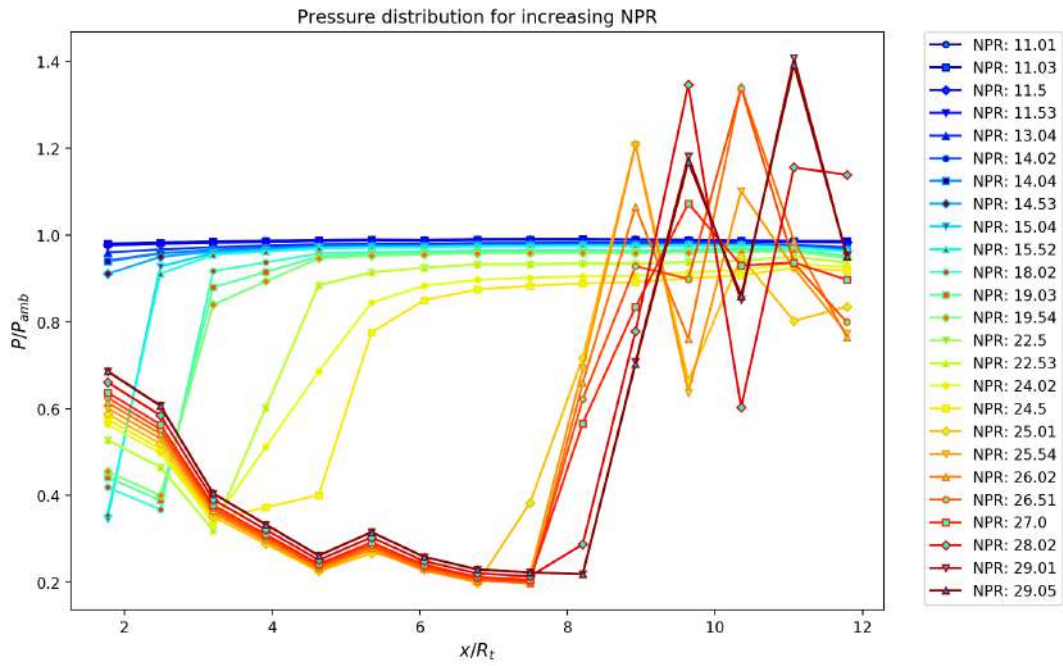


Figure A.11: Pressure distribution for varying NPR during increasing NPR for $\phi = -90$

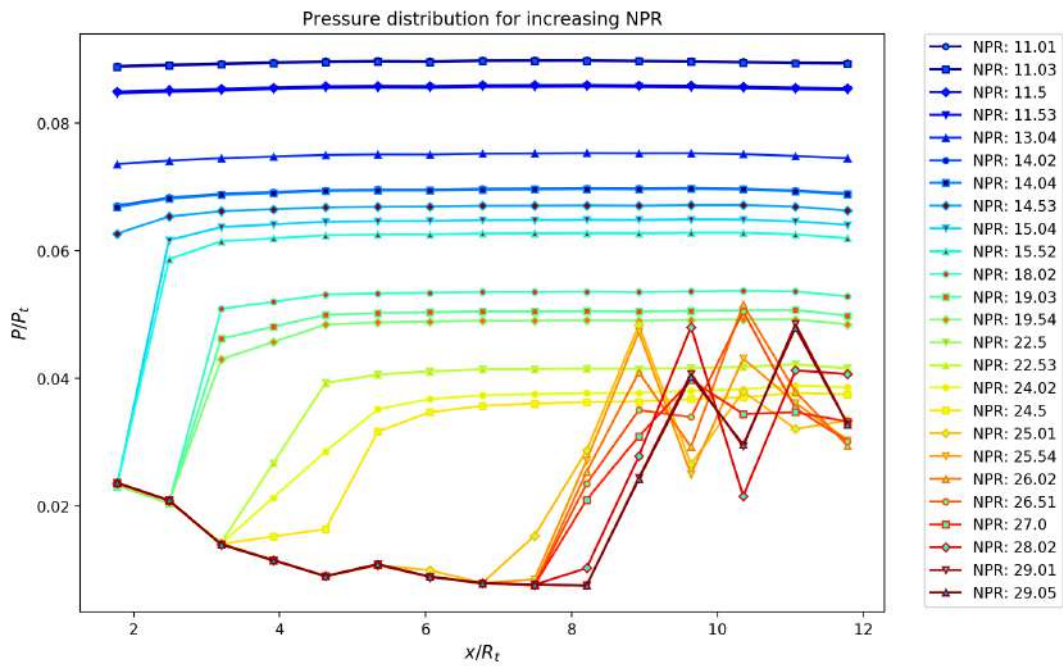
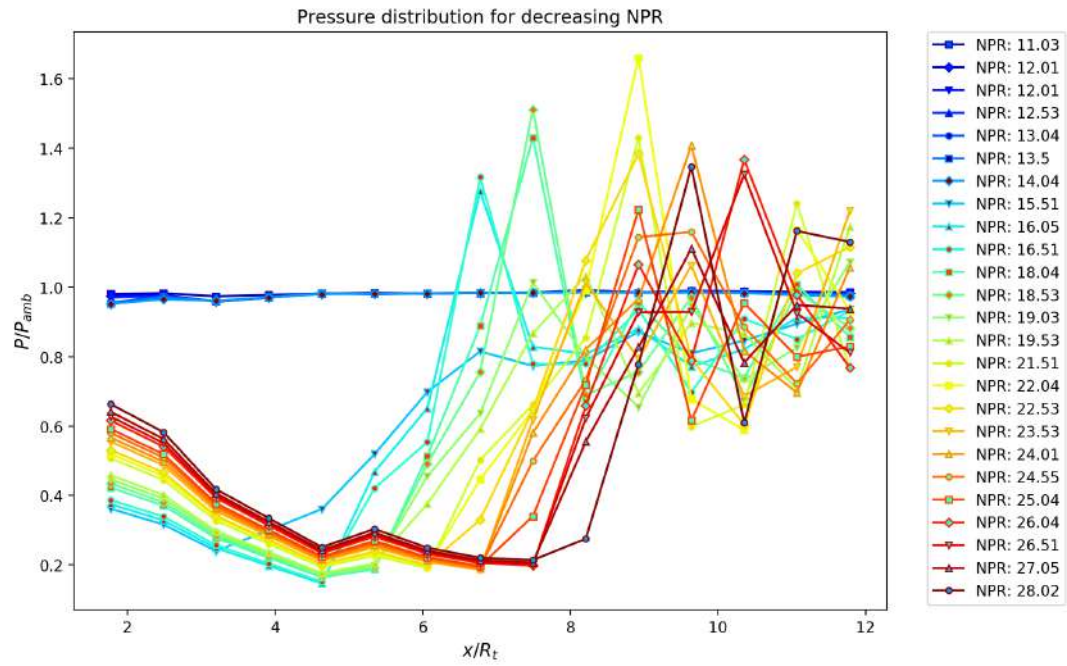
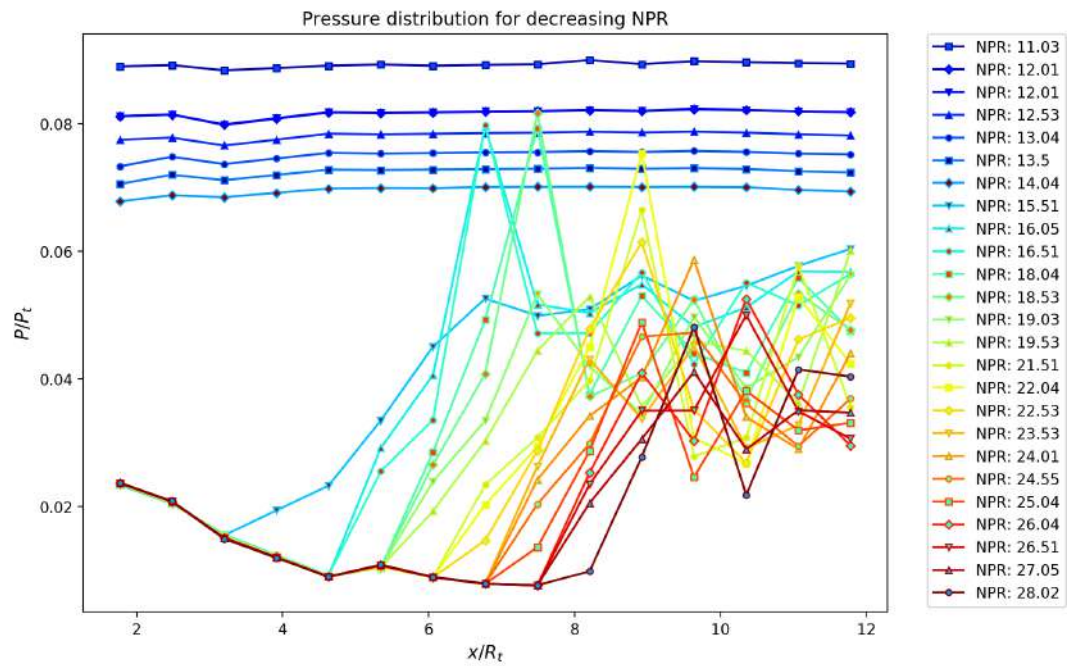
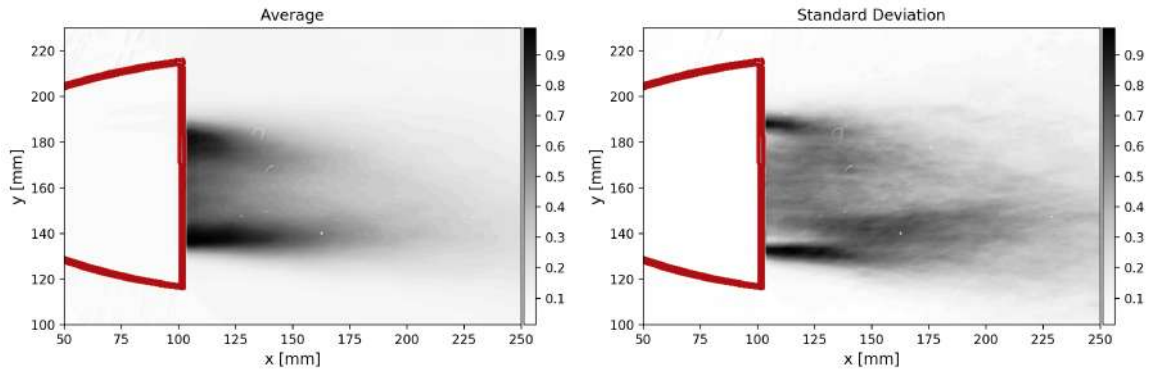


Figure A.12: Pressure distribution for varying NPR during increasing NPR for $\phi = -90$ compared to total pressure

Figure A.13: Pressure distribution for varying NPR during decreasing NPR for $\phi = -90$ Figure A.14: Pressure distribution for varying NPR during decreasing NPR for $\phi = -90$ compared to total pressure

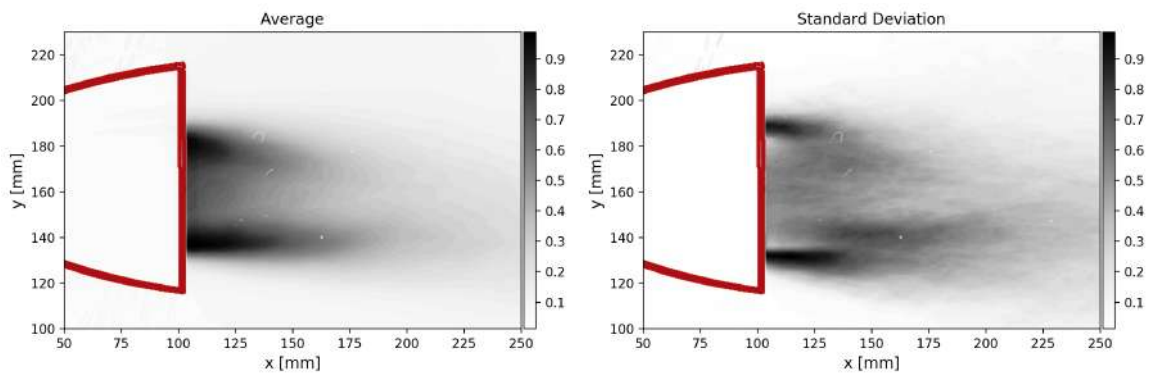
A.2. Schlieren Data



(a) Mean

(b) Standard Deviation

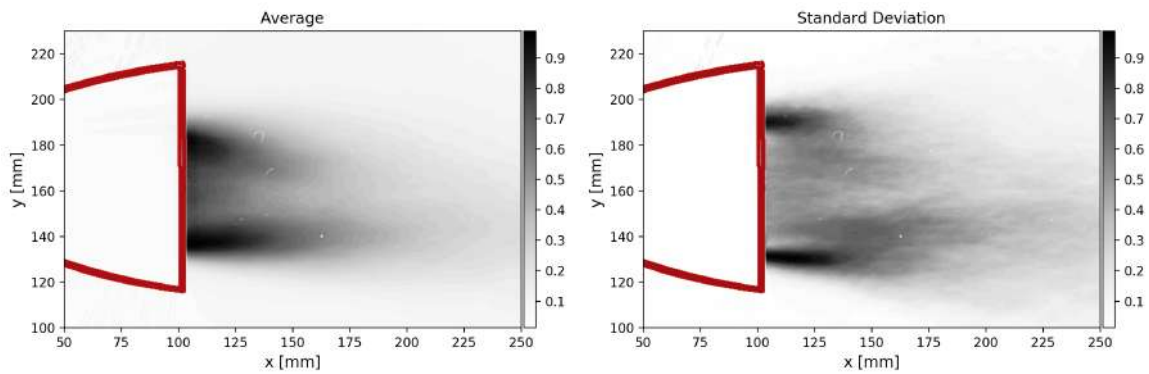
Figure A.15: Mean flow and fluctuations at NPR 24.03



(a) Mean

(b) Standard Deviation

Figure A.16: Mean flow and fluctuations at NPR 24.23



(a) Mean

(b) Standard Deviation

Figure A.17: Mean flow and fluctuations at NPR 24.45

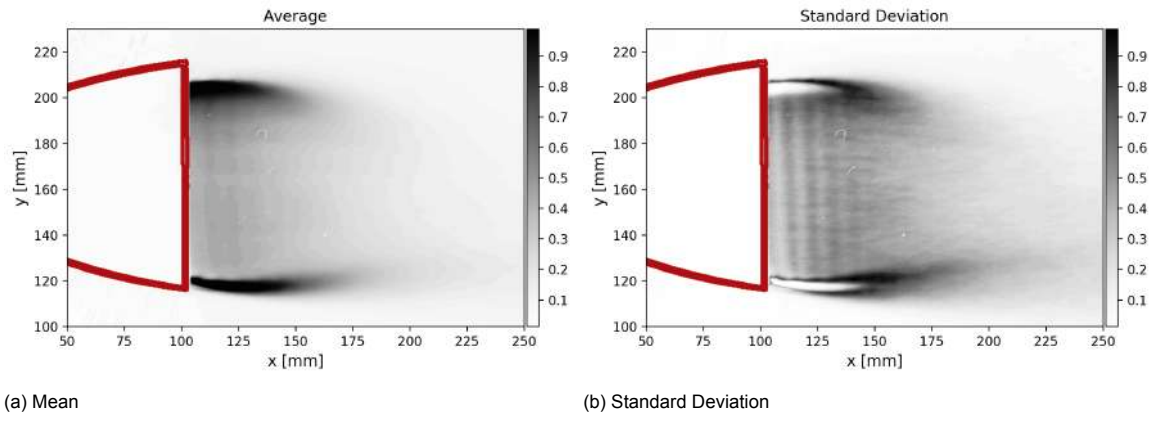


Figure A.18: Mean flow and fluctuations at NPR 24.80

A.3. PIV Data

A.3.1. NPR 10.52

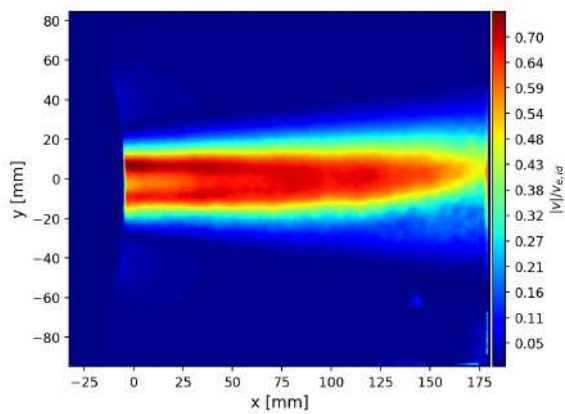


Figure A.19: Normalised average velocity magnitude

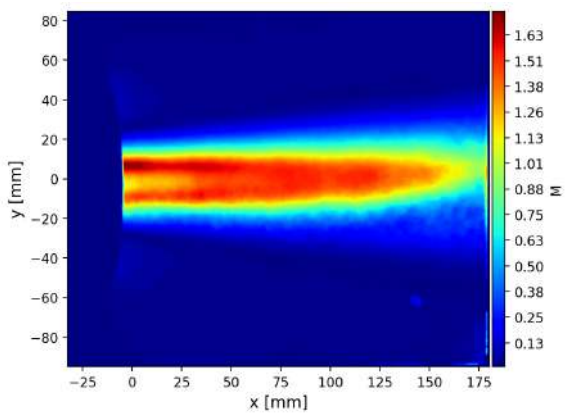


Figure A.20: Average Mach number

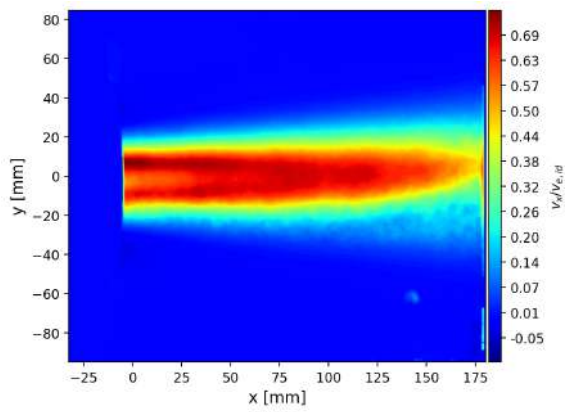


Figure A.21: Normalised average horizontal velocity

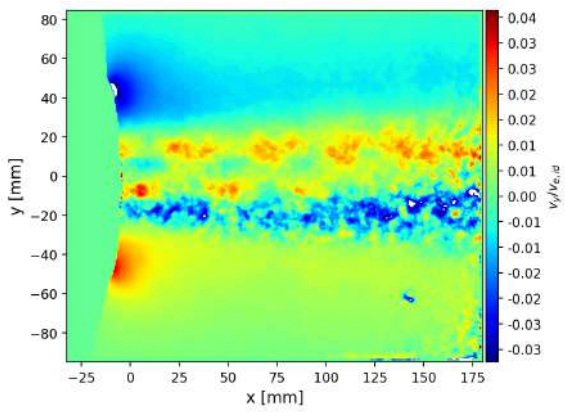


Figure A.22: Normalised average vertical velocity

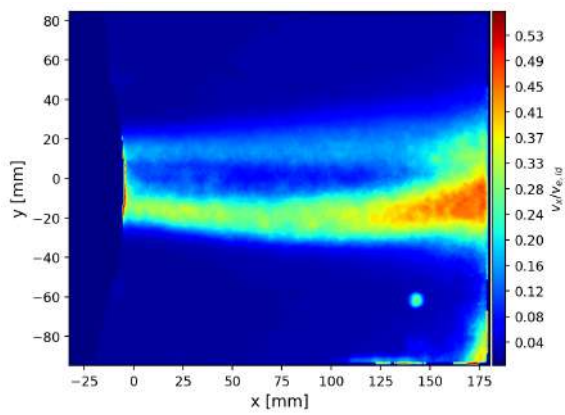


Figure A.23: Normalised standard deviation horizontal velocity

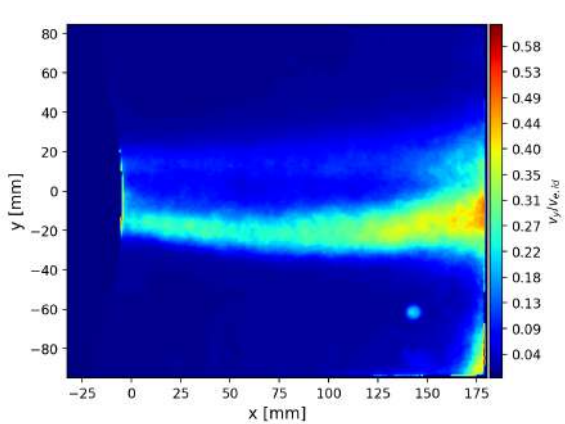


Figure A.24: Normalised standard deviation vertical velocity

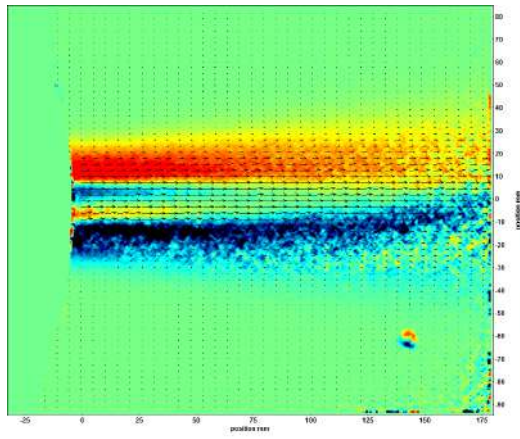


Figure A.25: Vorticity in z direction

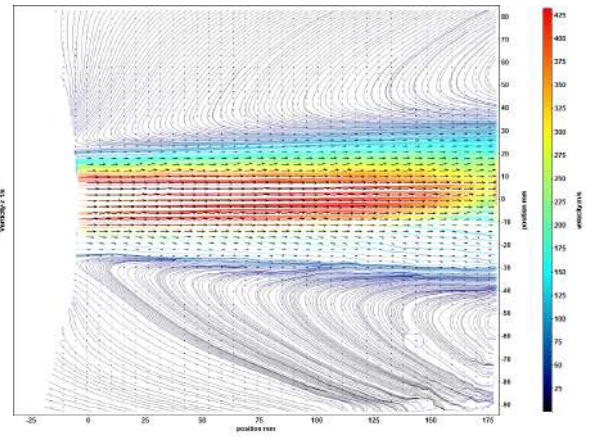


Figure A.26: Streamlines

A.3.2. NPR 16.42

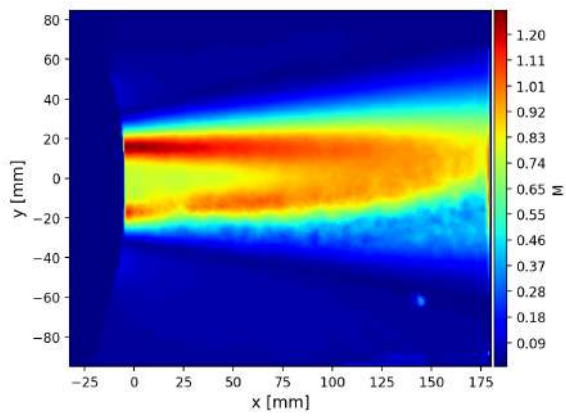


Figure A.27: Normalised average velocity magnitude

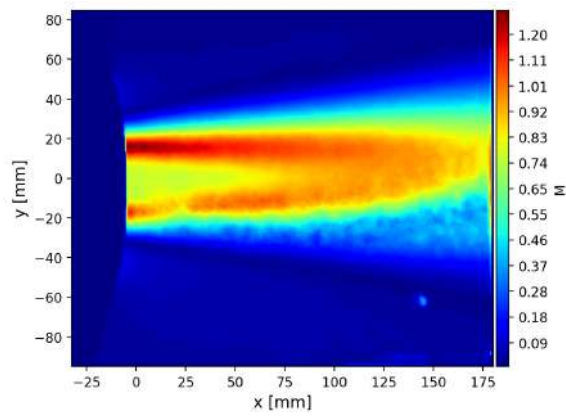


Figure A.28: Average Mach number

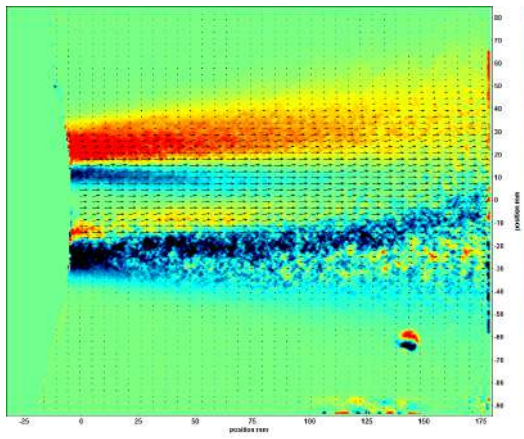


Figure A.29: Vorticity in z direction

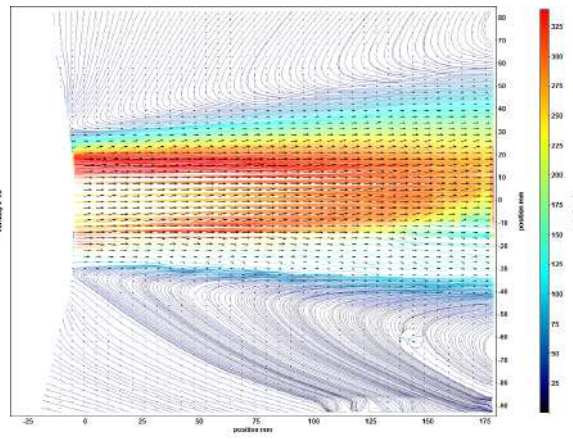


Figure A.30: Streamlines

A.3.3. NPR 22.21

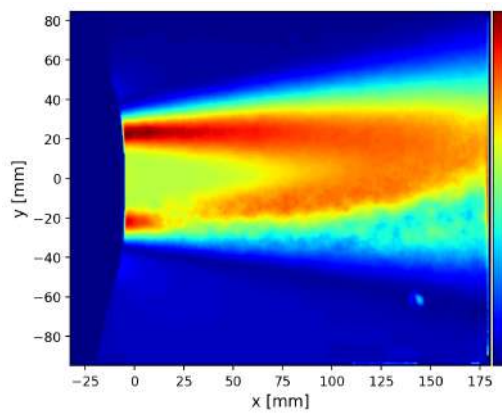


Figure A.31: Normalised average velocity magnitude

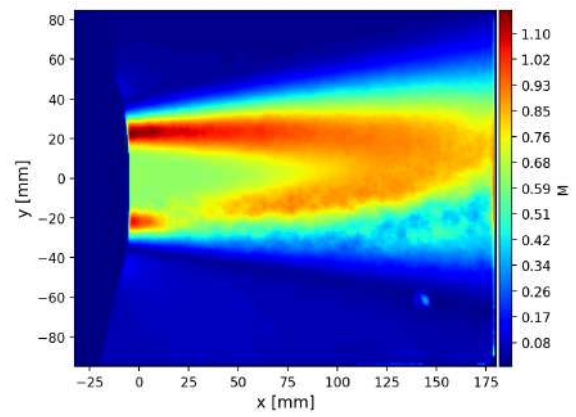


Figure A.32: Average Mach number

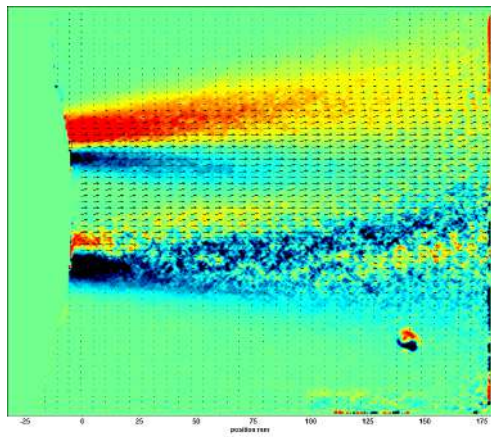


Figure A.33: Vorticity in z direction

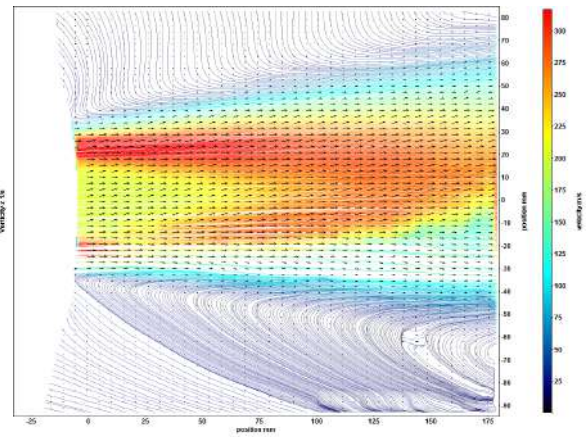


Figure A.34: Streamlines

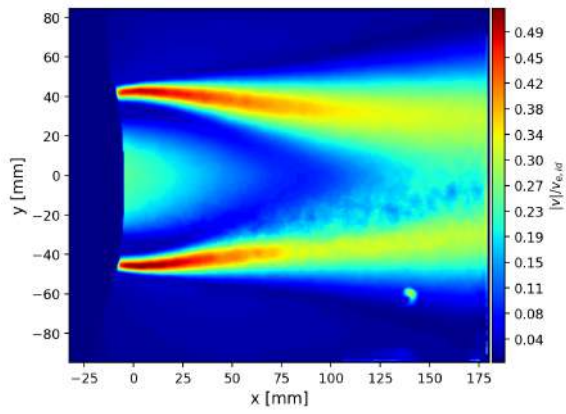
A.3.4. NPR 24.48

Figure A.35: Normalised average velocity magnitude

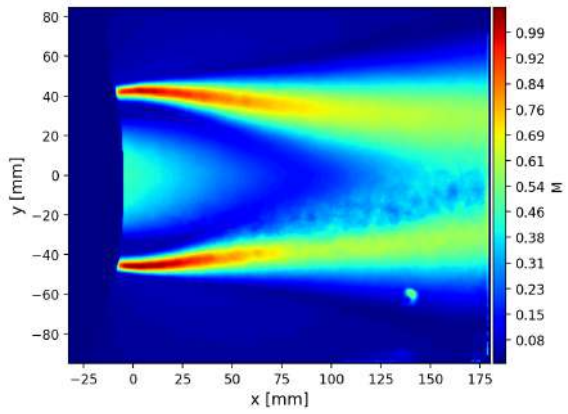


Figure A.36: Average Mach number

A.3.5. NPR 25.98

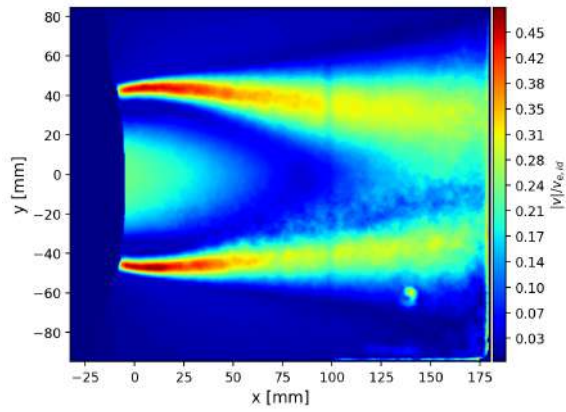


Figure A.37: Normalised average velocity magnitude

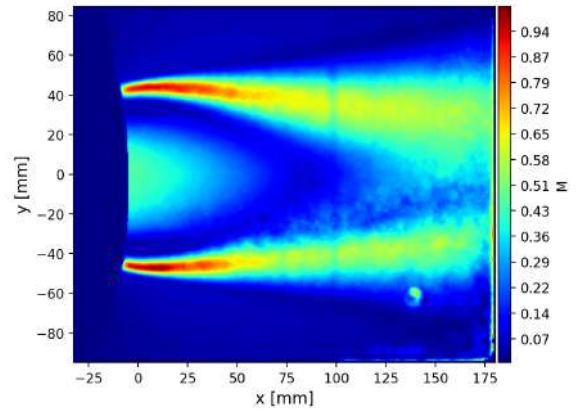


Figure A.38: Average Mach number

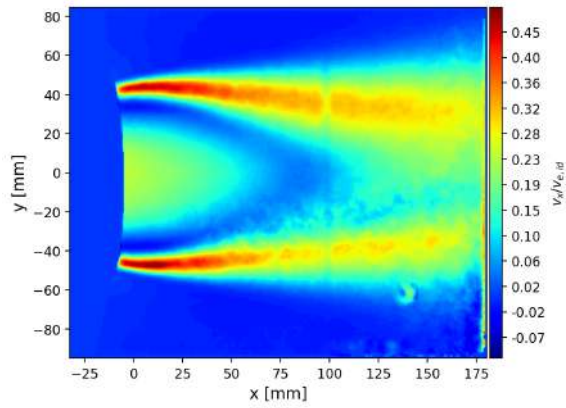


Figure A.39: Normalised average horizontal velocity

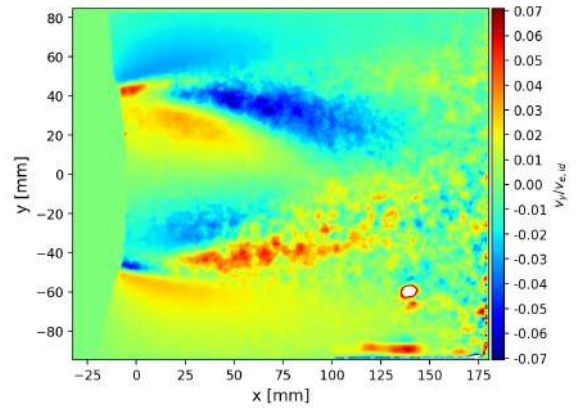


Figure A.40: Normalised average vertical velocity

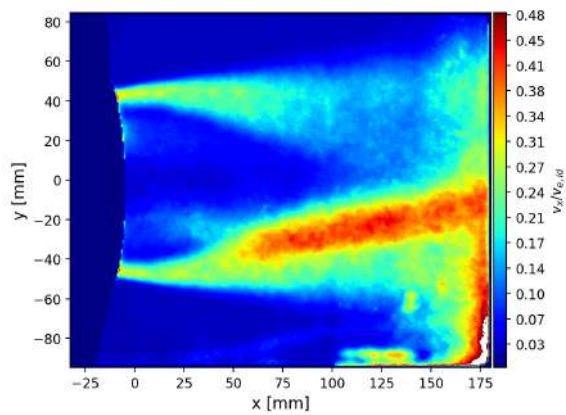


Figure A.41: Normalised standard deviation horizontal velocity

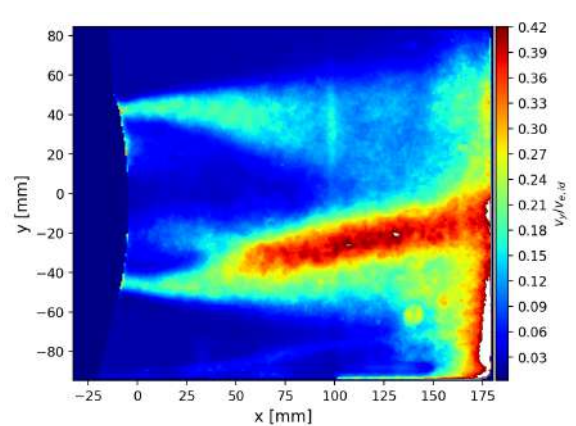


Figure A.42: Normalised standard deviation vertical velocity

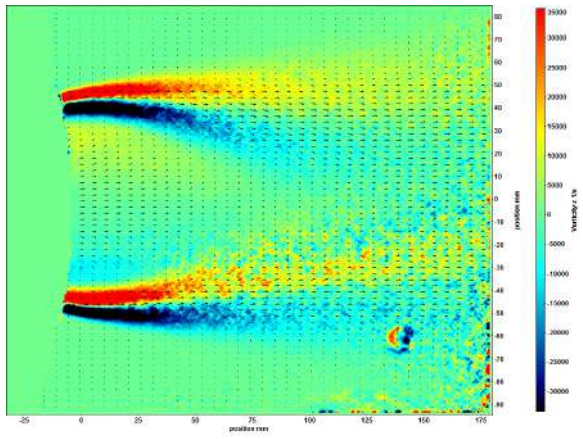


Figure A.43: Vorticity in z direction

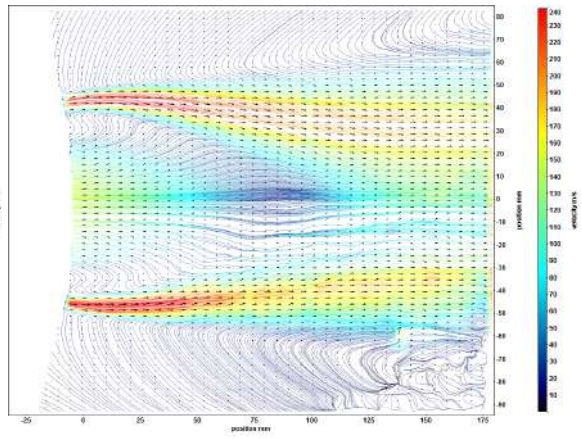


Figure A.44: Streamlines

A.4. DIC

A.4.1. NPR 2.07

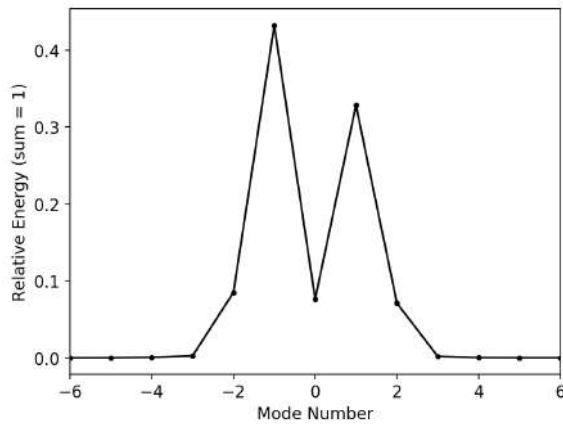


Figure A.45: Energy Spectrum

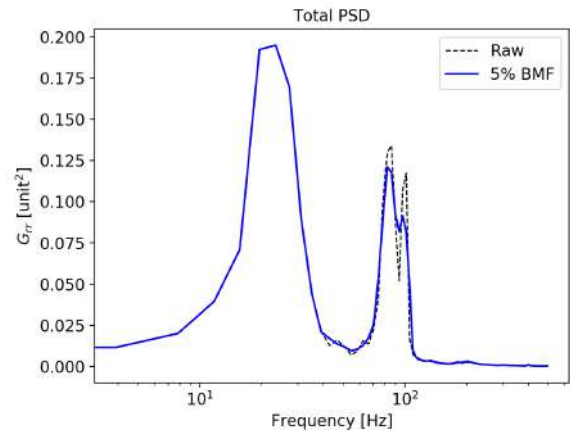


Figure A.46: Full PSD

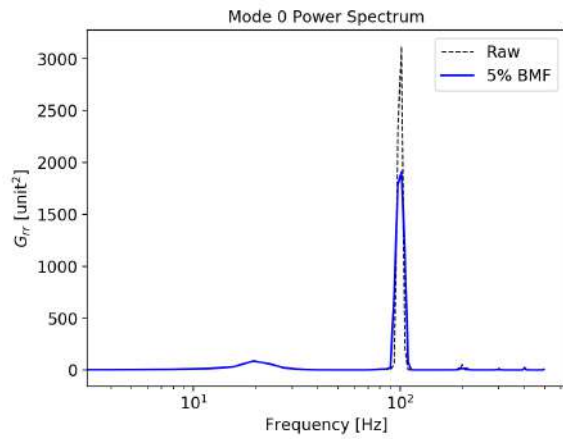


Figure A.47: Mode 0 PSD

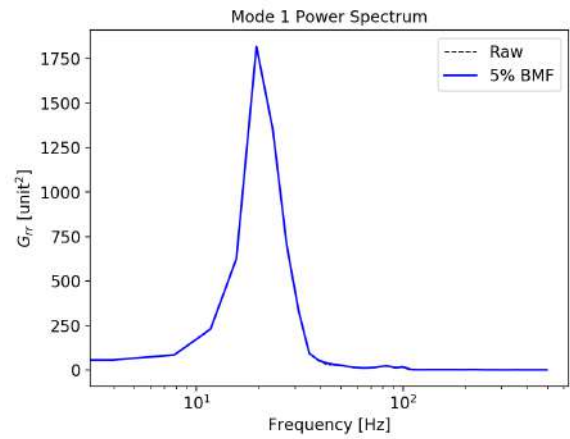


Figure A.48: Mode 1 PSD

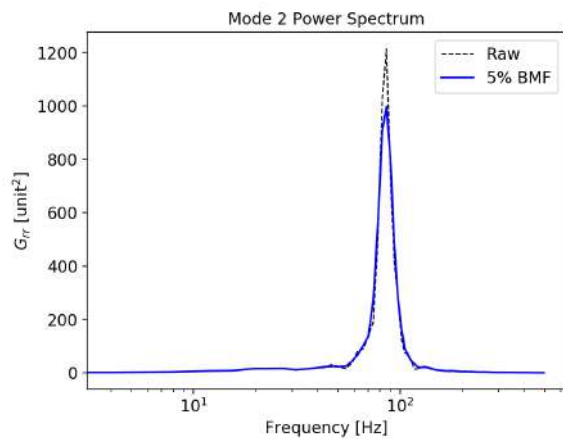


Figure A.49: Mode 2 PSD

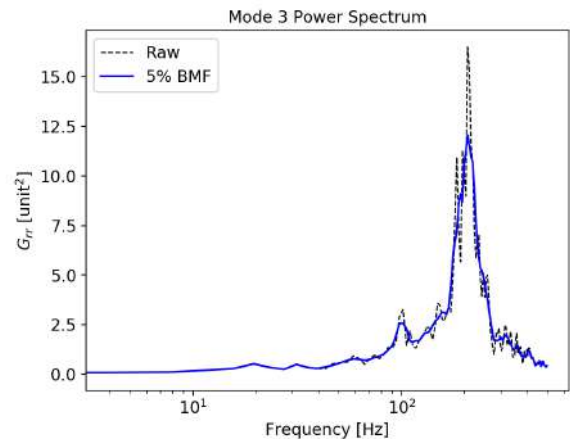


Figure A.50: Mode 3 PSD

A.4.2. NPR 7.88

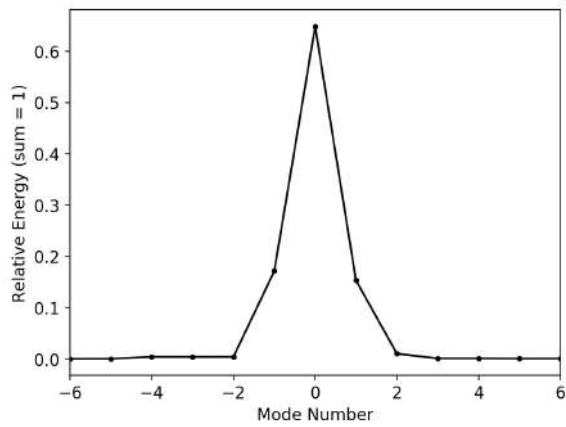


Figure A.51: Energy Spectrum

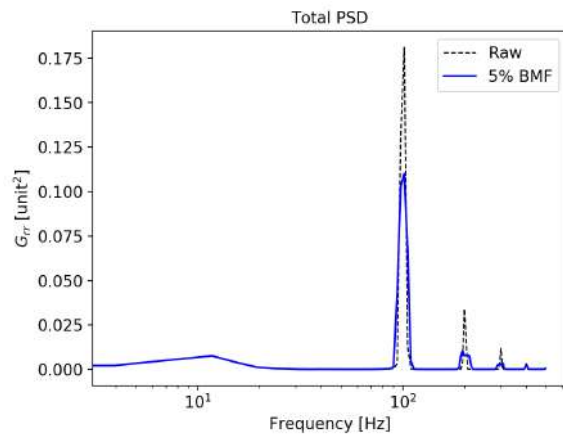


Figure A.52: Full PSD

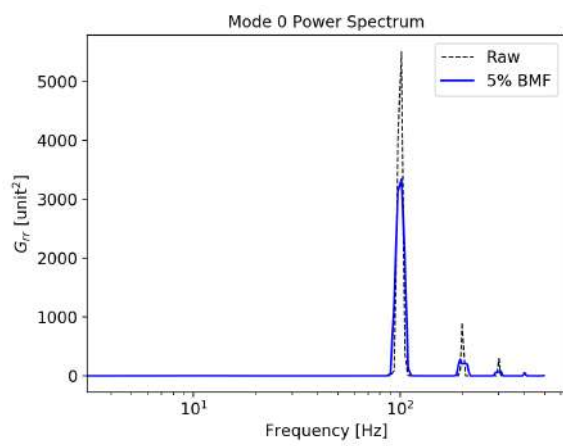


Figure A.53: Mode 0 PSD

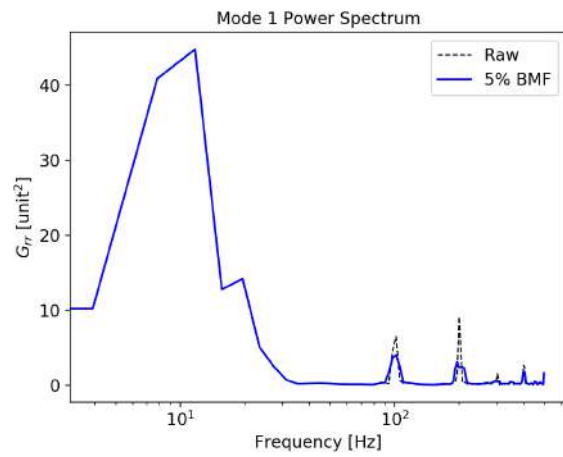


Figure A.54: Mode 1 PSD

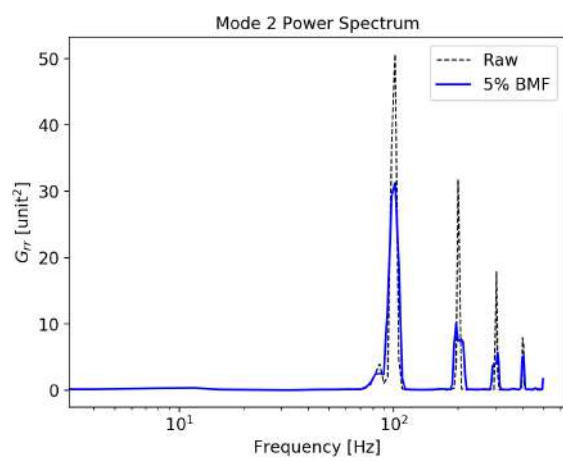


Figure A.55: Mode 2 PSD

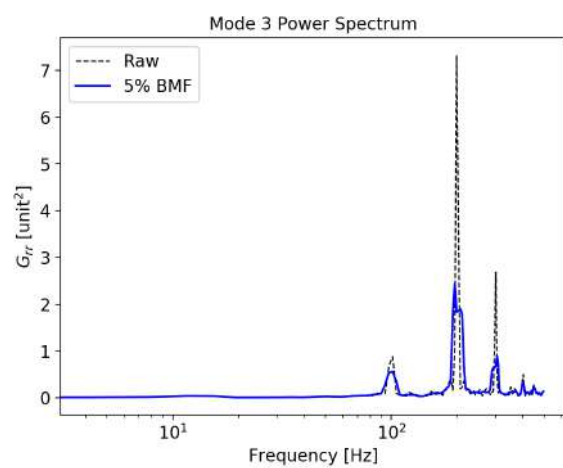


Figure A.56: Mode 3 PSD

A.4.3. NPR 8.66

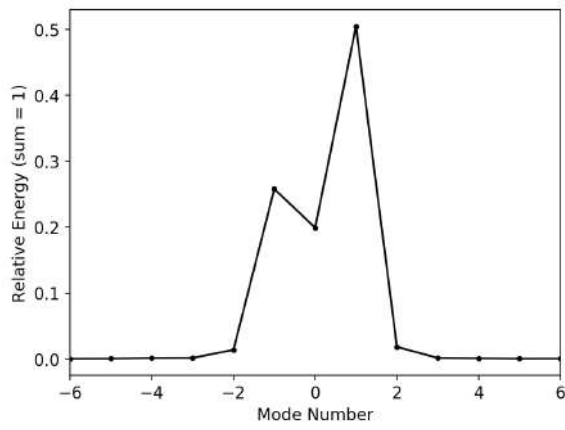


Figure A.57: Energy Spectrum

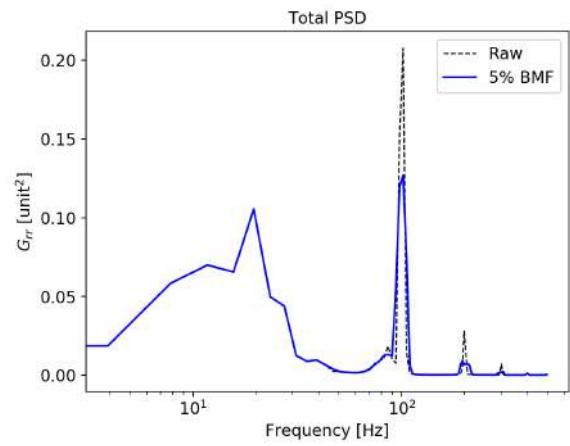


Figure A.58: Full PSD

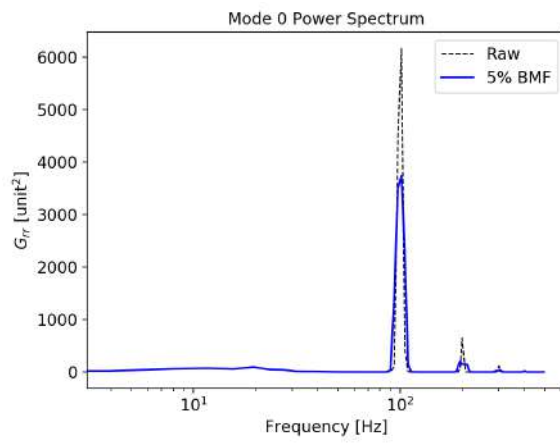


Figure A.59: Mode 0 PSD

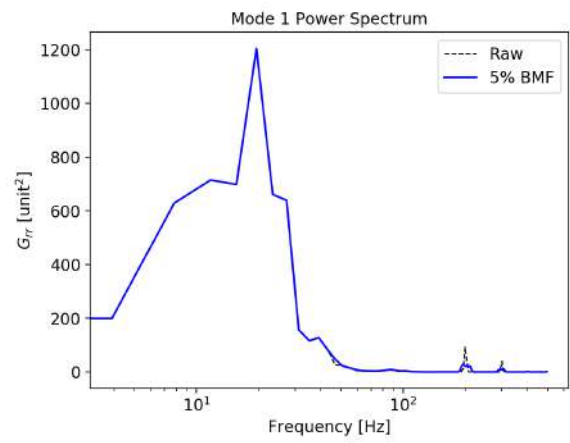


Figure A.60: Mode 1 PSD

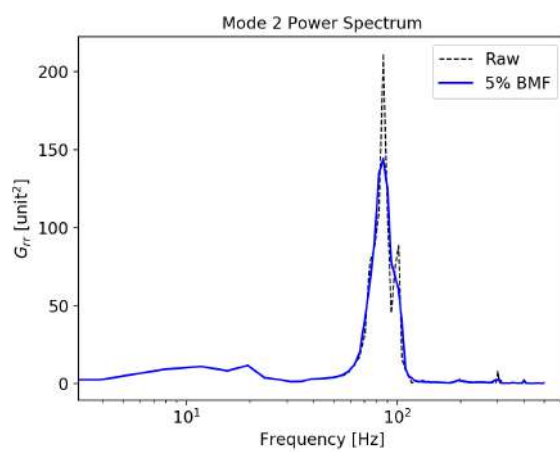


Figure A.61: Mode 2 PSD

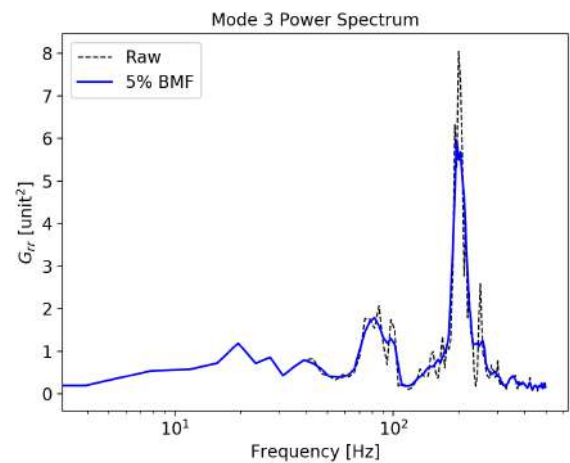


Figure A.62: Mode 3 PSD

A.4.4. NPR 9.55

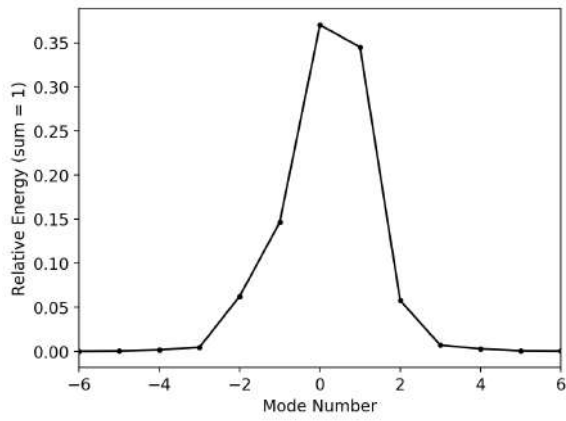


Figure A.63: Energy Spectrum

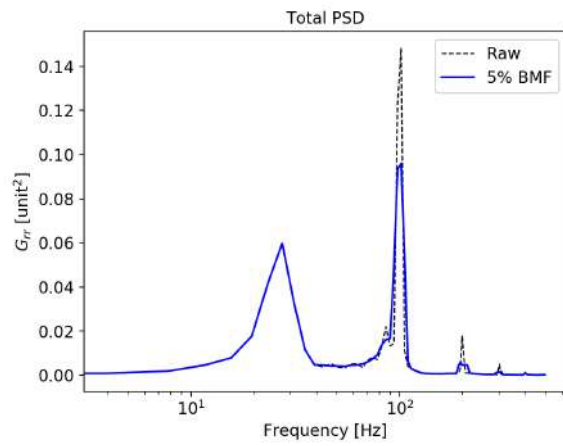


Figure A.64: Full PSD

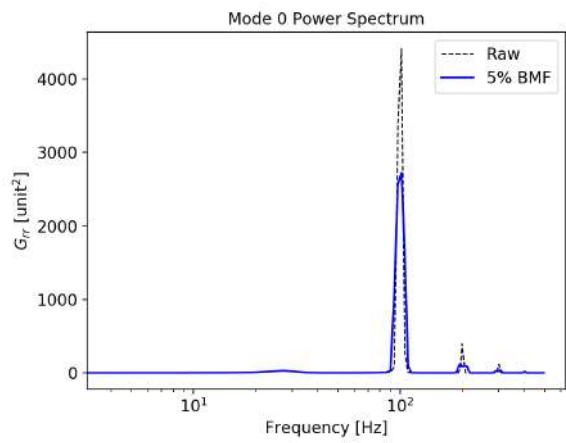


Figure A.65: Mode 0 PSD

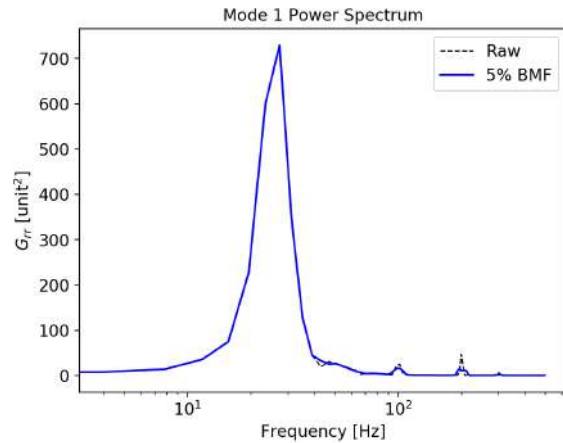


Figure A.66: Mode 1 PSD

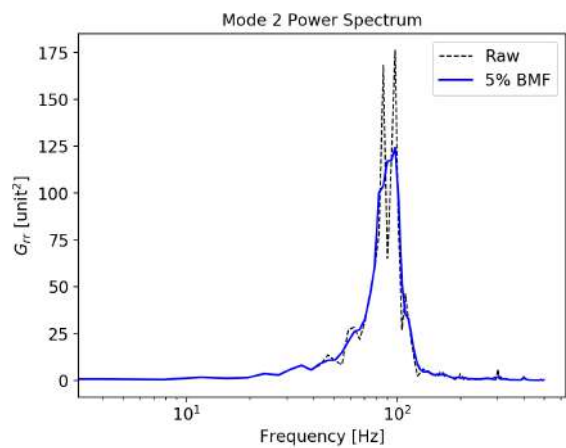


Figure A.67: Mode 2 PSD

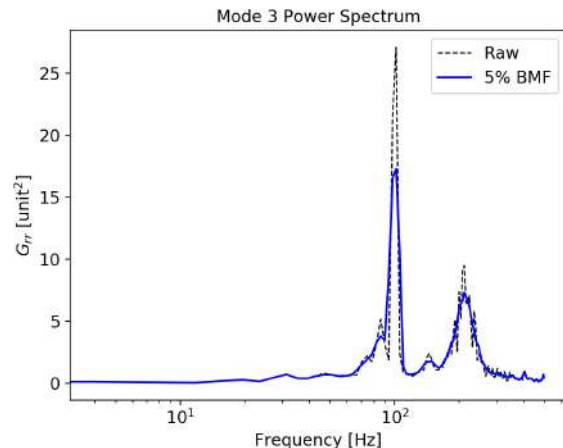


Figure A.68: Mode 3 PSD

A.4.5. NPR 9.81

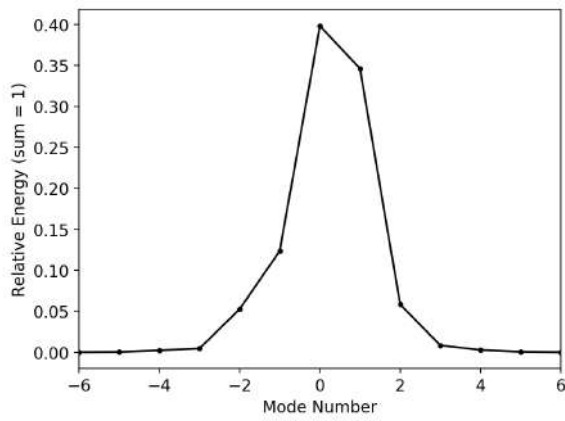


Figure A.69: Energy Spectrum

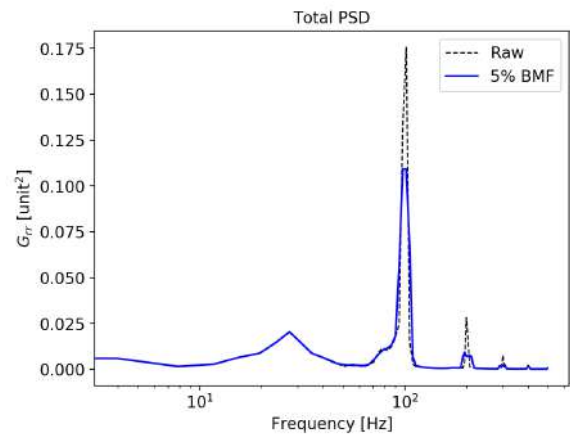


Figure A.70: Full PSD

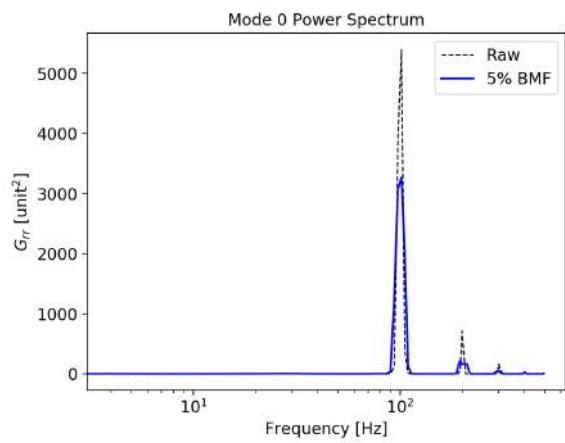


Figure A.71: Mode 0 PSD

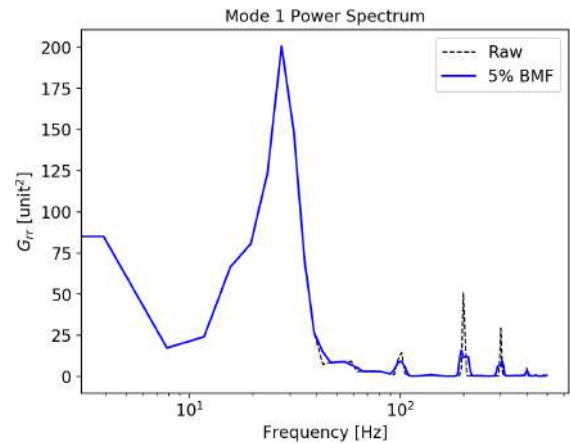


Figure A.72: Mode 1 PSD

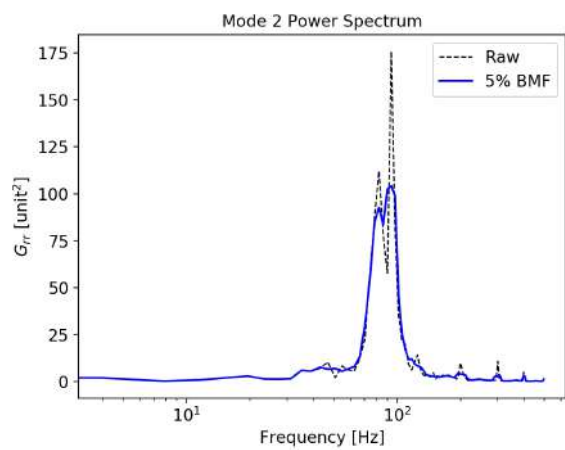


Figure A.73: Mode 2 PSD

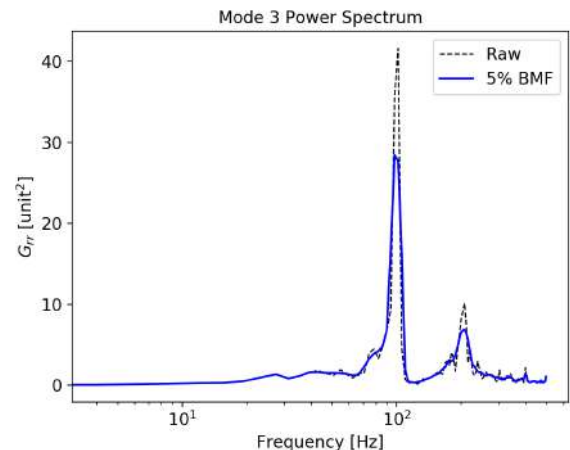


Figure A.74: Mode 3 PSD

B

Nozzle Parameters

B.1. Nozzle Wall Coordinates

x/R_t	y/R_t	x/R_t	y/R_t
-1.9590727836	1.998324799	-0.5266022106	1.226688491
-1.9181407673	1.993248797	-0.4856749943	1.203048481
-1.8772207509	1.984692794	-0.4447465779	1.179424072
-1.8362887345	1.972440789	-0.4038193615	1.155794862
-1.7953567181	1.956204782	-0.3628909452	1.132165653
-1.7544367018	1.935540774	-0.1991808797	1.041386817
-1.7135046854	1.911948765	-0.1582524633	1.025705210
-1.6725726690	1.888308755	-0.1173248869	1.013960806
-1.6316526527	1.864680746	-0.0763970706	1.005871602
-1.5907206363	1.841052736	-0.0354693742	1.001260001
-1.5498006199	1.817424727	0.00000E+00	1.00000E+00
-1.5088686035	1.793796718	7.67170E-03	1.00003E+00
-1.4679365872	1.770168708	1.53430E-02	1.00012E+00
-1.4270165708	1.746540699	2.30133E-02	1.00026E+00
-1.3860845544	1.722900689	3.06823E-02	1.00047E+00
-1.3451525381	1.699272680	3.83495E-02	1.00074E+00
-1.3042325217	1.675644670	4.60144E-02	1.00106E+00
-1.2633005053	1.652016661	5.36766E-02	1.00144E+00
-1.2223684889	1.628388651	6.13357E-02	1.00188E+00
-1.1814460726	1.604760642	6.89911E-02	1.00238E+00
-1.1405188562	1.581132632	7.66425E-02	1.00294E+00
-1.0995904398	1.557504623	8.42894E-02	1.00356E+00
-1.0586620235	1.533864614	9.19313E-02	1.00423E+00
-1.0177360071	1.510236604	9.95678E-02	1.00497E+00
-0.9768075907	1.486608595	1.07198E-01	1.00576E+00
-0.9358791744	1.462980585	1.14823E-01	1.00661E+00
-0.8949519580	1.439352576	1.22440E-01	1.00752E+00
-0.8540235416	1.415724566	1.30051E-01	1.00849E+00
-0.8130963252	1.392096557	1.37654E-01	1.00952E+00
-0.7721691089	1.368456547	1.45248E-01	1.01060E+00
-0.7312406925	1.344828538	1.52834E-01	1.01175E+00
-0.6903134761	1.321200528	1.60411E-01	1.01295E+00
-0.6493850598	1.297572519	1.67979E-01	1.01421E+00
-0.6084578434	1.273944510	1.75537E-01	1.01553E+00
-0.5675294270	1.250316500	1.83084E-01	1.01690E+00

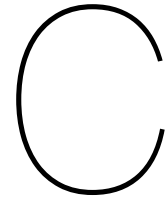
x/R_t	y/R_t	x/R_t	y/R_t
1.90621E-01	1.01834E+00	5.69642E-01	1.17811E+00
1.98146E-01	1.01983E+00	5.75931E-01	1.18250E+00
2.05660E-01	1.02138E+00	5.82185E-01	1.18694E+00
2.13162E-01	1.02298E+00	5.88406E-01	1.19143E+00
2.20651E-01	1.02465E+00	5.94591E-01	1.19597E+00
2.28127E-01	1.02637E+00	6.00742E-01	1.20056E+00
2.35589E-01	1.02815E+00	6.06858E-01	1.20519E+00
2.43038E-01	1.02998E+00	6.12937E-01	1.20987E+00
2.50473E-01	1.03188E+00	6.18981E-01	1.21459E+00
2.57893E-01	1.03383E+00	6.24988E-01	1.21937E+00
2.65297E-01	1.03583E+00	6.30959E-01	1.22418E+00
2.72686E-01	1.03790E+00	6.36892E-01	1.22905E+00
2.80059E-01	1.04002E+00	6.42479E-01	1.23370E+00
2.87416E-01	1.04219E+00	6.48341E-01	1.26788E+00
2.94755E-01	1.04443E+00	7.52730E-01	1.32510E+00
3.02077E-01	1.04672E+00	8.23735E-01	1.38283E+00
3.09382E-01	1.04906E+00	8.96621E-01	1.44120E+00
3.16668E-01	1.05146E+00	9.26364E-01	1.46476E+00
3.23936E-01	1.05392E+00	9.71628E-01	1.50034E+00
3.31184E-01	1.05643E+00	1.01775E+00	1.53623E+00
3.38413E-01	1.05900E+00	1.06478E+00	1.57249E+00
3.45622E-01	1.06163E+00	1.11279E+00	1.60915E+00
3.52811E-01	1.06431E+00	1.16185E+00	1.64624E+00
3.59979E-01	1.06704E+00	1.22899E+00	1.69640E+00
3.67126E-01	1.06983E+00	1.28076E+00	1.73462E+00
3.74251E-01	1.07267E+00	1.33382E+00	1.77340E+00
3.81354E-01	1.07557E+00	1.35178E+00	1.78642E+00
3.88435E-01	1.07852E+00	1.40664E+00	1.82593E+00
3.95493E-01	1.08153E+00	1.44397E+00	1.85258E+00
4.02527E-01	1.08459E+00	1.48199E+00	1.87952E+00
4.09538E-01	1.08771E+00	1.52069E+00	1.90675E+00
4.16525E-01	1.09088E+00	1.54026E+00	1.92043E+00
4.23487E-01	1.09410E+00	1.57999E+00	1.94806E+00
4.30425E-01	1.09737E+00	1.62046E+00	1.97598E+00
4.37337E-01	1.10070E+00	1.66164E+00	2.00419E+00
4.44223E-01	1.10408E+00	1.68247E+00	2.01838E+00
4.51083E-01	1.10752E+00	1.72478E+00	2.04700E+00
4.57917E-01	1.11100E+00	1.76786E+00	2.07592E+00
4.64723E-01	1.11454E+00	1.81172E+00	2.10511E+00
4.71502E-01	1.11814E+00	1.85636E+00	2.13460E+00
4.78254E-01	1.12178E+00	1.90180E+00	2.16434E+00
4.84977E-01	1.12547E+00	1.94803E+00	2.19437E+00
4.91672E-01	1.12922E+00	1.99507E+00	2.22464E+00
4.98338E-01	1.13302E+00	2.04292E+00	2.25518E+00
5.04975E-01	1.13687E+00	2.09156E+00	2.28595E+00
5.11582E-01	1.14077E+00	2.14103E+00	2.31696E+00
5.18158E-01	1.14472E+00	2.19127E+00	2.34820E+00
5.24704E-01	1.14872E+00	2.24234E+00	2.37964E+00
5.31220E-01	1.15277E+00	2.29418E+00	2.41127E+00
5.37704E-01	1.15687E+00	2.32039E+00	2.42716E+00
5.44156E-01	1.16102E+00	2.34679E+00	2.44308E+00
5.50577E-01	1.16522E+00	2.40018E+00	2.47505E+00
5.56965E-01	1.16946E+00	2.42713E+00	2.49107E+00
5.63320E-01	1.17376E+00	2.45425E+00	2.50712E+00

x/R_t	y/R_t	x/R_t	y/R_t
2.48154E+00	2.52320E+00	5.56427E+00	3.94681E+00
2.50901E+00	2.53931E+00	5.65294E+00	3.97855E+00
2.56448E+00	2.57160E+00	5.74241E+00	4.01017E+00
2.59243E+00	2.58774E+00	5.83266E+00	4.04165E+00
2.62054E+00	2.60390E+00	5.92364E+00	4.07294E+00
2.64878E+00	2.62007E+00	6.01530E+00	4.10406E+00
2.67719E+00	2.63624E+00	6.06131E+00	4.11952E+00
2.73442E+00	2.66860E+00	6.15373E+00	4.15026E+00
2.76320E+00	2.68475E+00	6.24667E+00	4.18075E+00
2.79210E+00	2.70089E+00	6.34008E+00	4.21098E+00
2.85025E+00	2.73312E+00	6.43388E+00	4.24092E+00
2.87945E+00	2.74919E+00	6.52802E+00	4.27057E+00
2.90874E+00	2.76522E+00	6.62246E+00	4.29989E+00
2.93810E+00	2.78123E+00	6.71712E+00	4.32888E+00
2.99705E+00	2.81309E+00	6.81196E+00	4.35752E+00
3.02657E+00	2.82894E+00	6.90694E+00	4.38582E+00
3.05612E+00	2.84473E+00	7.00204E+00	4.41376E+00
3.11531E+00	2.87611E+00	7.09724E+00	4.44133E+00
3.14488E+00	2.89168E+00	7.19258E+00	4.46857E+00
3.20396E+00	2.92254E+00	7.28809E+00	4.49548E+00
3.26279E+00	2.95298E+00	7.38383E+00	4.52207E+00
3.32125E+00	2.98295E+00	7.47990E+00	4.54840E+00
3.37915E+00	3.01234E+00	7.57644E+00	4.57446E+00
3.46451E+00	3.05516E+00	7.67365E+00	4.60036E+00
3.51997E+00	3.08267E+00	7.77170E+00	4.62608E+00
3.57389E+00	3.10919E+00	7.87076E+00	4.65172E+00
3.65066E+00	3.14653E+00	7.97102E+00	4.67728E+00
3.69769E+00	3.16919E+00	8.07272E+00	4.70282E+00
3.71924E+00	3.17952E+00	8.17619E+00	4.72842E+00
3.78428E+00	3.21046E+00	8.28155E+00	4.75409E+00
3.84631E+00	3.23968E+00	8.38906E+00	4.77988E+00
3.90966E+00	3.26922E+00	8.49886E+00	4.80580E+00
3.97429E+00	3.29905E+00	8.61115E+00	4.83186E+00
4.04021E+00	3.32917E+00	8.72606E+00	4.85809E+00
4.10741E+00	3.35956E+00	8.84372E+00	4.88448E+00
4.14149E+00	3.37484E+00	8.96419E+00	4.91102E+00
4.21062E+00	3.40561E+00	9.08750E+00	4.93770E+00
4.28102E+00	3.43661E+00	9.15024E+00	4.95109E+00
4.35265E+00	3.46778E+00	9.21372E+00	4.96451E+00
4.42554E+00	3.49916E+00	9.27791E+00	4.97794E+00
4.49964E+00	3.53071E+00	9.34284E+00	4.99140E+00
4.57495E+00	3.56240E+00	9.40849E+00	5.00486E+00
4.61303E+00	3.57829E+00	9.47488E+00	5.01835E+00
4.69014E+00	3.61018E+00	9.54202E+00	5.03185E+00
4.72909E+00	3.62615E+00	9.60985E+00	5.04536E+00
4.80790E+00	3.65816E+00	9.67842E+00	5.05886E+00
4.88780E+00	3.69023E+00	9.74771E+00	5.07236E+00
4.96883E+00	3.72235E+00	9.81773E+00	5.08586E+00
5.05091E+00	3.75450E+00	9.88847E+00	5.09936E+00
5.13406E+00	3.78666E+00	9.95994E+00	5.11284E+00
5.21820E+00	3.81880E+00	1.00321E+01	5.12630E+00
5.30335E+00	3.85091E+00	1.01050E+01	5.13974E+00
5.38938E+00	3.88295E+00	1.01786E+01	5.15317E+00
5.47638E+00	3.91493E+00	1.02530E+01	5.16656E+00

x/R_t	y/R_t	x/R_t	y/R_t
1.03280E+01	5.17993E+00	1.14551E+01	5.36245E+00
1.04038E+01	5.19328E+00	1.15411E+01	5.37505E+00
1.04802E+01	5.20657E+00	1.16281E+01	5.38759E+00
1.05575E+01	5.21984E+00	1.17158E+01	5.40005E+00
1.06354E+01	5.23306E+00	1.18042E+01	5.41243E+00
1.07140E+01	5.24624E+00	1.18935E+01	5.42473E+00
1.07934E+01	5.25937E+00	1.19836E+01	5.43696E+00
1.08735E+01	5.27245E+00	1.20745E+01	5.44910E+00
1.09543E+01	5.28548E+00	1.21662E+01	5.46115E+00
1.10359E+01	5.29847E+00	1.22587E+01	5.47312E+00
1.11182E+01	5.31138E+00	1.23521E+01	5.48500E+00
1.12013E+01	5.32424E+00	1.24463E+01	5.49678E+00
1.12851E+01	5.33705E+00	1.25000E+01	5.50340E+00
1.13697E+01	5.34978E+00		

B.2. Pressure Port Coordinates

x/R_t	y/R_t	z/R_t
1.768	2.076	0.000
2.483	2.524	0.047
3.199	2.918	0.109
3.914	3.266	0.183
4.630	3.575	0.268
5.345	3.850	0.361
6.061	4.093	0.461
6.776	4.310	0.567
7.492	4.501	0.678
8.207	4.669	0.793
8.923	4.816	0.911
9.638	4.944	1.032
10.354	5.054	1.154
11.069	5.148	1.277
11.785	5.225	1.400



Sensor Calibration Data

pressure and temperature sensor and strain gauge calibration data

C.1. Pressure Sensor

Table C.1: Pressure sensor calibration data

Current [A]	Pressure [bar]
0.003991091	1.02045
0.004151847	2
0.004311302	3
0.004469822	4
0.004630356	5
0.00478883	6
0.004948612	7
0.005107771	8
0.005266791	9
0.005425935	10
0.005585294	11

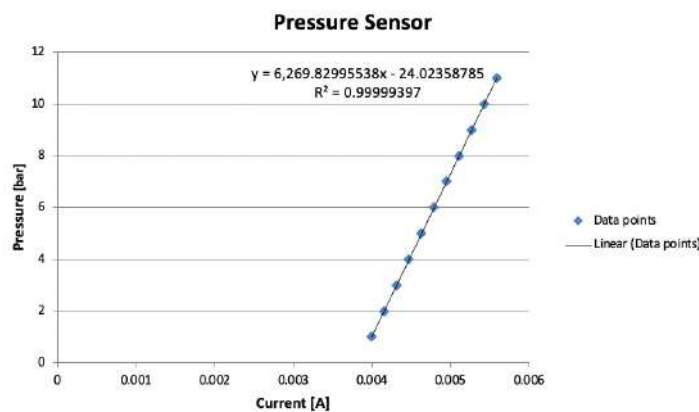


Figure C.1: Pressure sensor calibration curve

C.2. Strain Gauges

Table C.2: Strain gauge calibration data

<i>Horizontal Bridge</i>		<i>Vertical Bridge</i>	
Weight [g]	Strain	Weight [g]	Strain
0	-0.000119443	0	-0.000170367
-463	-0.000111734	-364	-0.000177995
-770	-0.000104942	-599	-0.000180114
-1154	-9.98915E-05	-916	-0.00018592
-1634	-8.8928E-05	-1300	-0.000190681
-1869	-8.50417E-05	-1800	-0.000201279
-2088	-8.18641E-05	-2393	-0.000209075
-2682	-6.9831E-05	-2909	-0.000214863
-3182	-6.11638E-05	-3936	-0.000224665
-3730	-5.18746E-05		

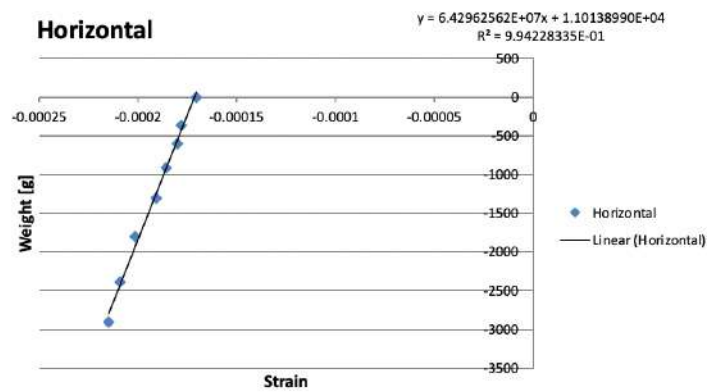


Figure C.2: Horizontal strain calibration curve

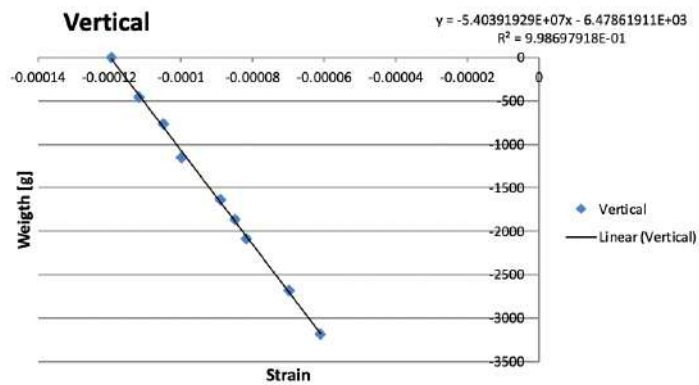
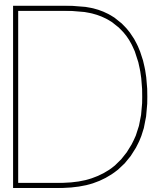
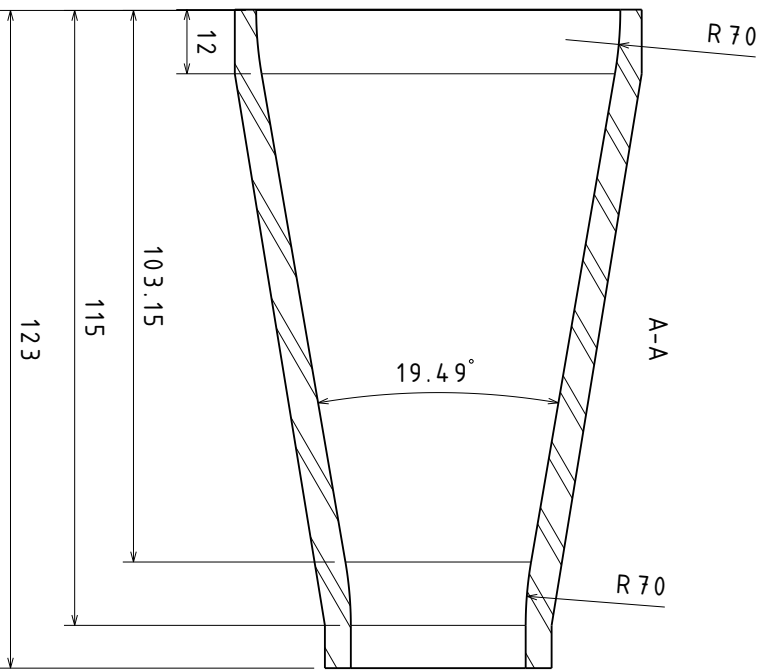
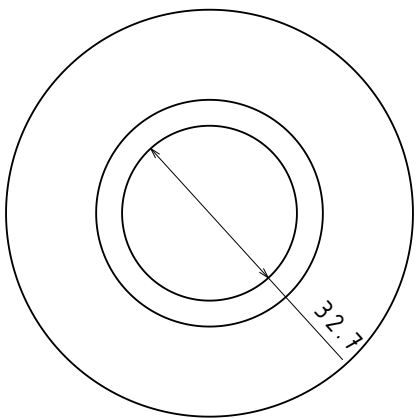
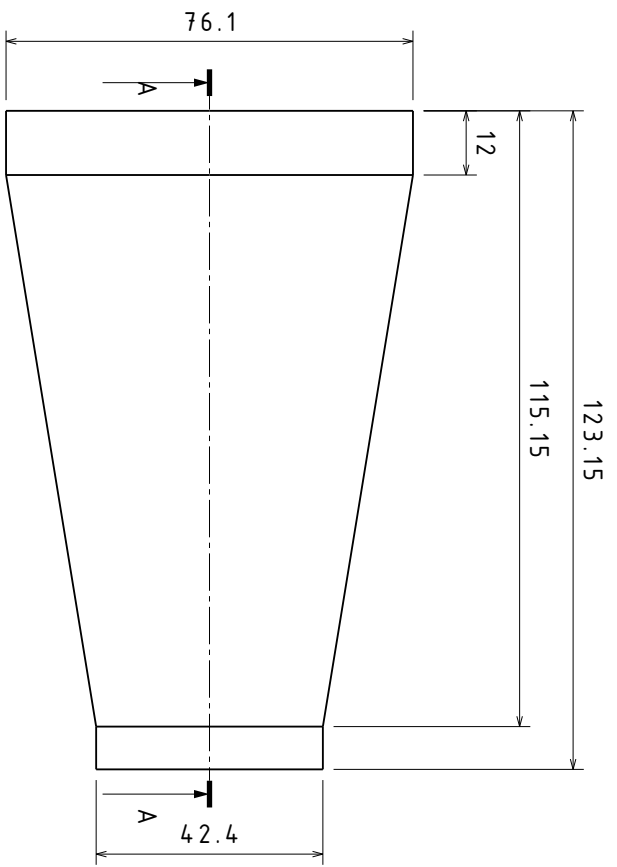
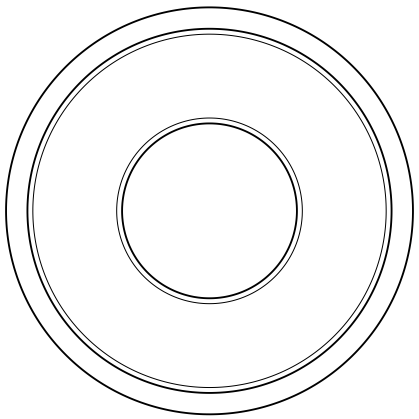


Figure C.3: Vertical strain calibration curve



Technical Drawings

This appendix presents technical drawings of unique parts in the setup.



DESIGNED BY: Krijn de Kievit		DRAWING NUMBER FLD-01		SHEET 1/1	
DATE: 06/01/2021		DRAWING NUMBER FLD-01		SHEET 1/1	
MATERIAL: Stainless Steel 316		DRAWING NUMBER FLD-01		SHEET 1/1	
SIZE: A3	AMOUNT: 1	DRAWING NUMBER FLD-01		SHEET 1/1	
SCALE: 1:1	AMOUNT: 1	DRAWING NUMBER FLD-01		SHEET 1/1	
This drawing is our property; it can't be reproduced or communicated without our written agreement.					

Fluid Contraction

Thesis TU Delft

I	—
H	—
G	—
F	—
E	—
D	—
C	—
B	—
A	—

1

2

3

4

1

2

3

4

H

G

F

E

D

C

B

A

H

G

F

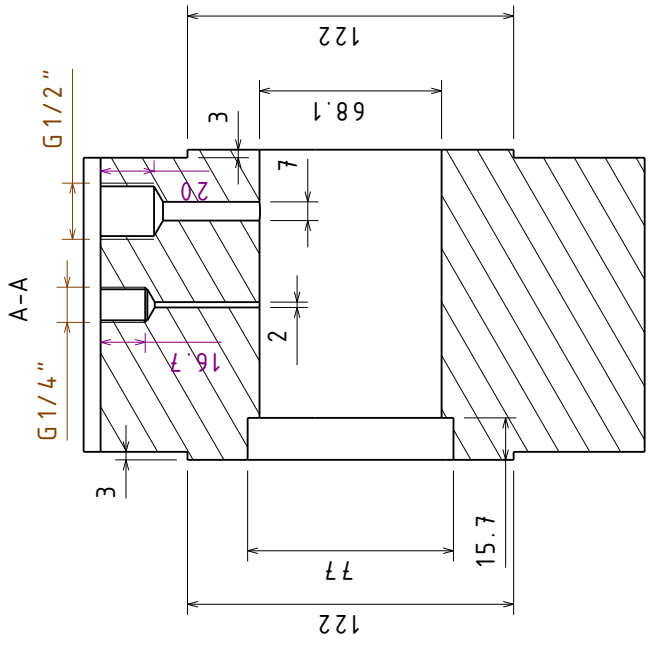
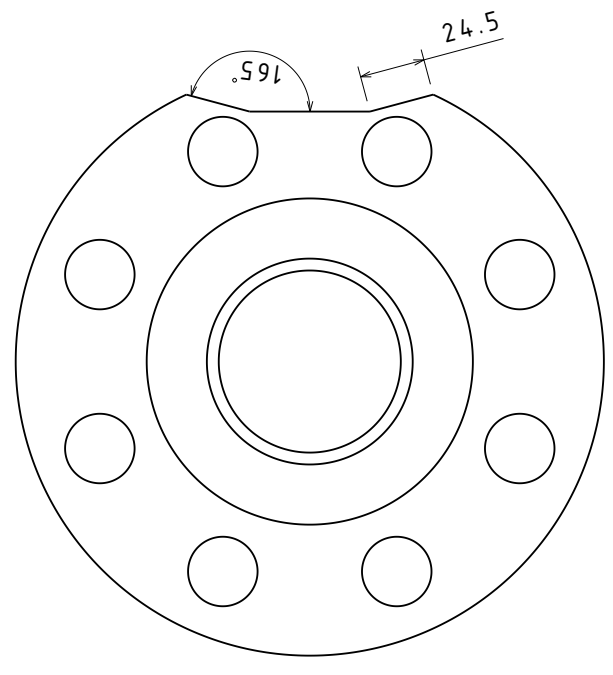
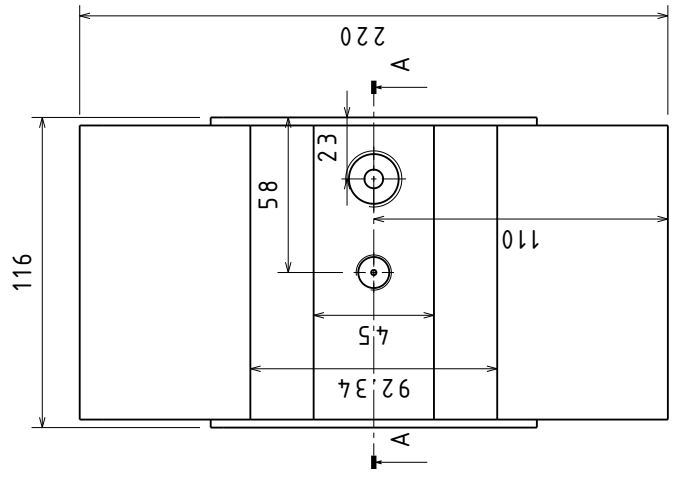
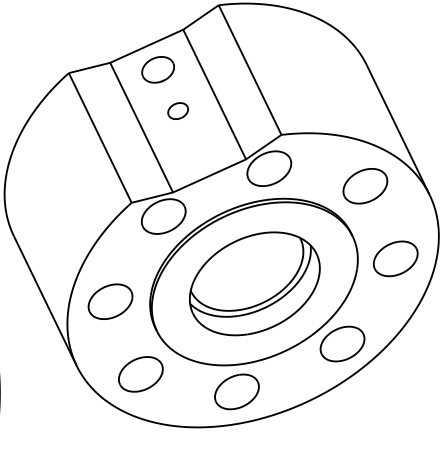
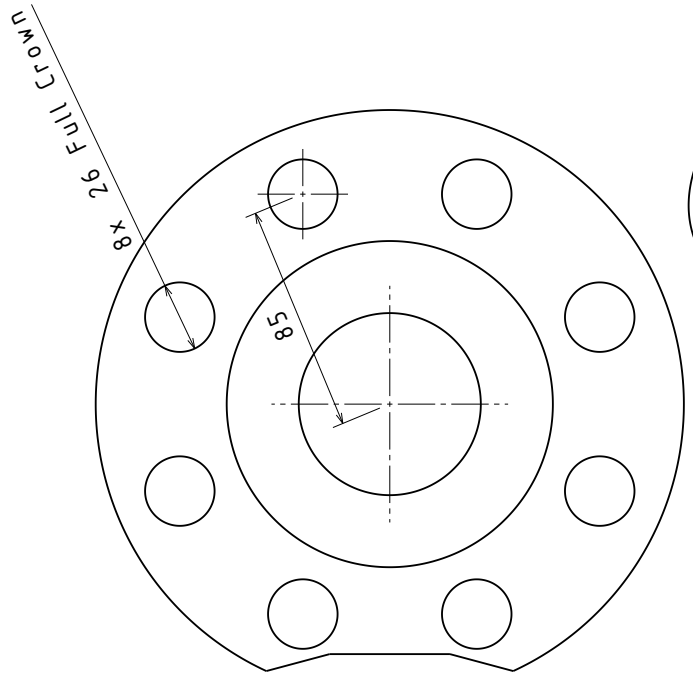
E

D

C

B

A



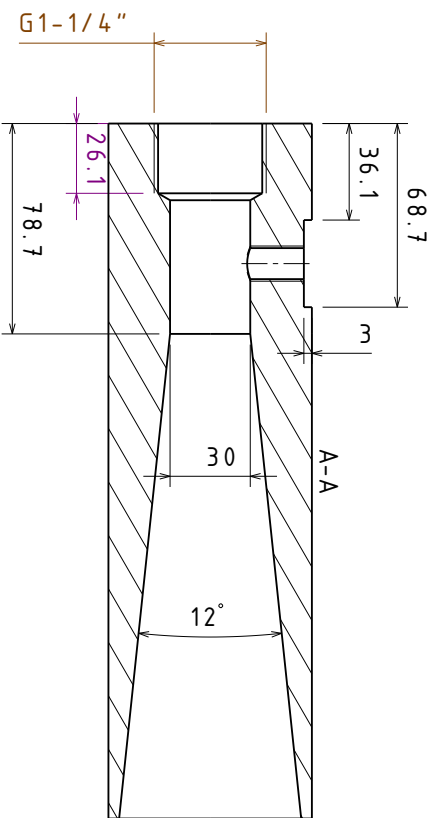
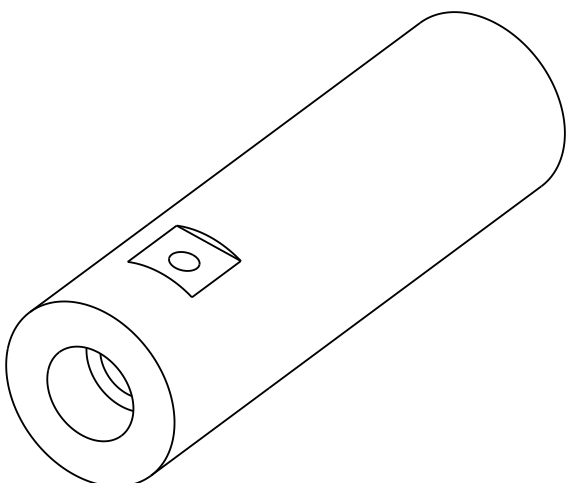
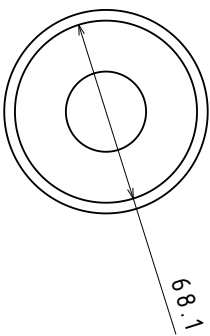
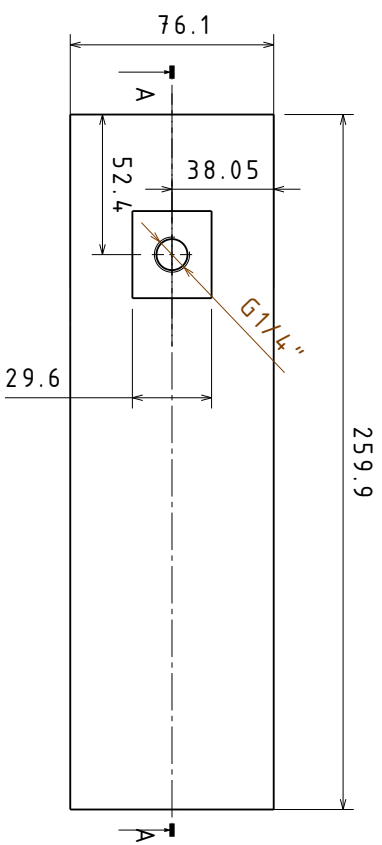
Notes:
 G1/4" (BSPP) thread predrill diameter: 11.8mm
 G1/2" (BSPP) thread predrill diameter: 19 mm

DESIGNED BY:	Krijn de Kievit
DATE:	06/01/2021
MATERIAL:	ALU-6082T6
SIZE:	A3
SCALE:	1:2
DRAWING NUMBER:	FLD-02
SHEET:	1/1

Fluid Setting Chamber

Thesis TU Delft

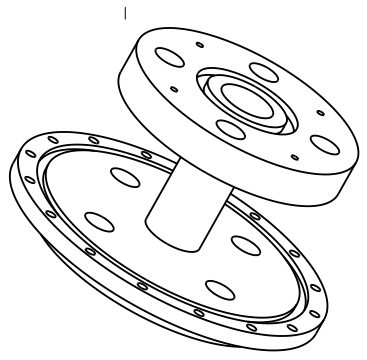
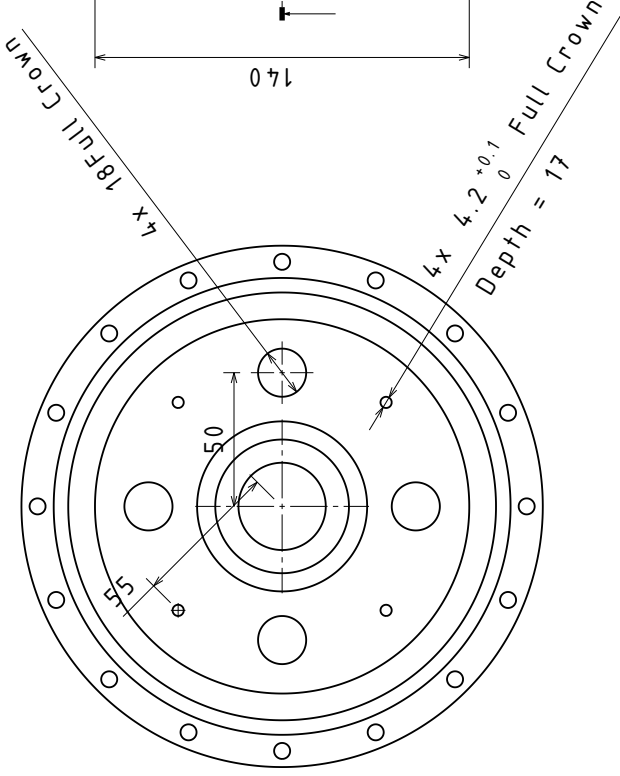
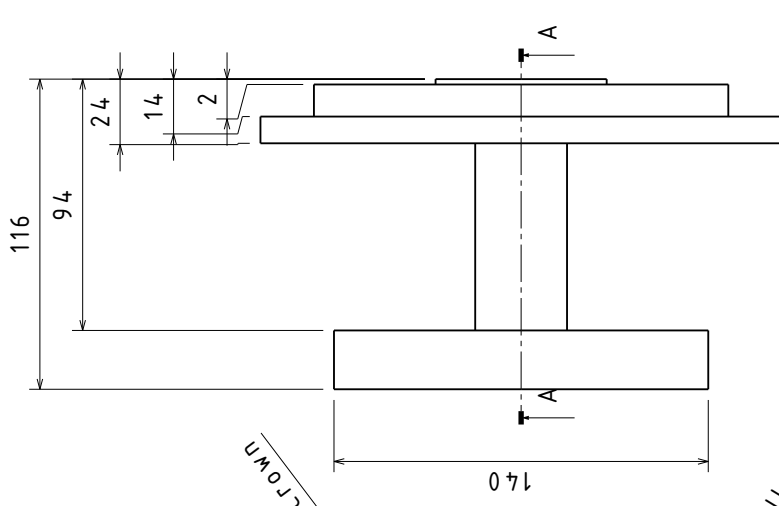
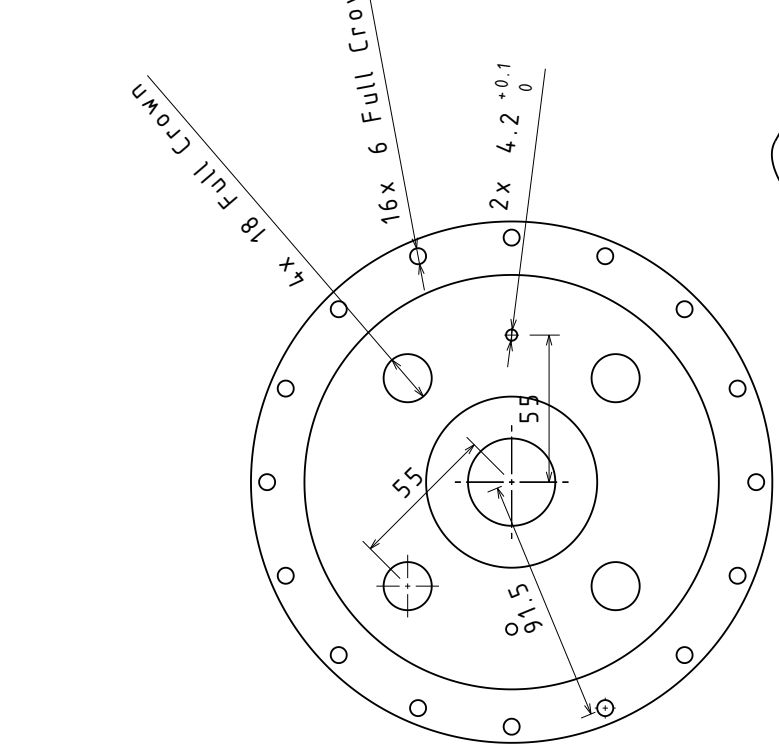
This drawing is our property; it can't be reproduced or communicated without our written agreement.



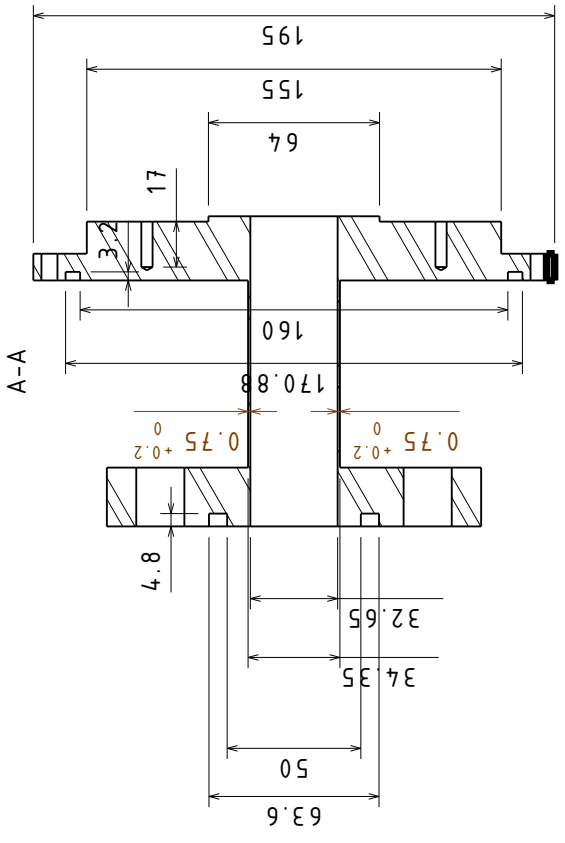
G1/4" predrill diameter: 11.8mm

DESIGNED BY: Krijn de Kievit	FLUID DIFFUSER		
DATE: 06/01/2021	Thesis TU Delft		
MATERIAL: Stainless Steel 316	FLD-03		
SIZE: A3	AMOUNT: 1	DRAWING NUMBER: FLD-03	SHEET: 1/1
SCALE: 1:2	This drawing is our property; it can't be reproduced or communicated without our written agreement.		

I	—
H	—
G	—
F	—
E	—
D	—
C	—
B	—
A	—



Notes:
The center tube is very thin.
It is extremely important that the thickness is not less than 0.75mm at any point.

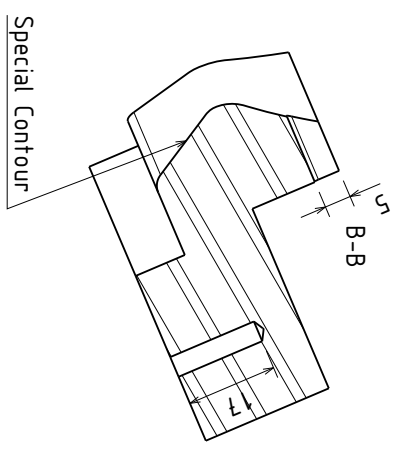
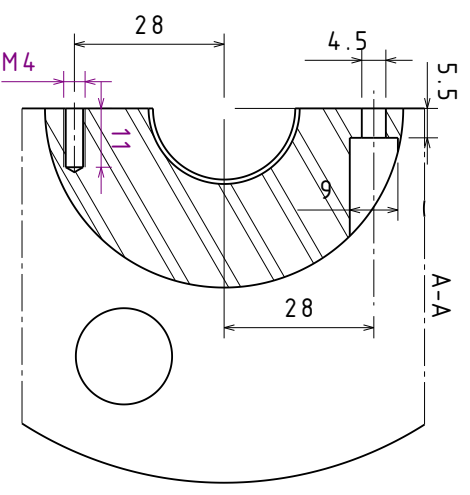
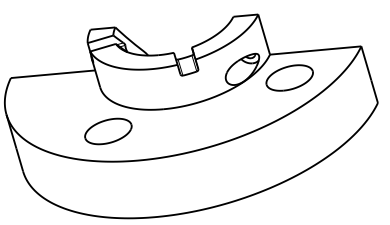
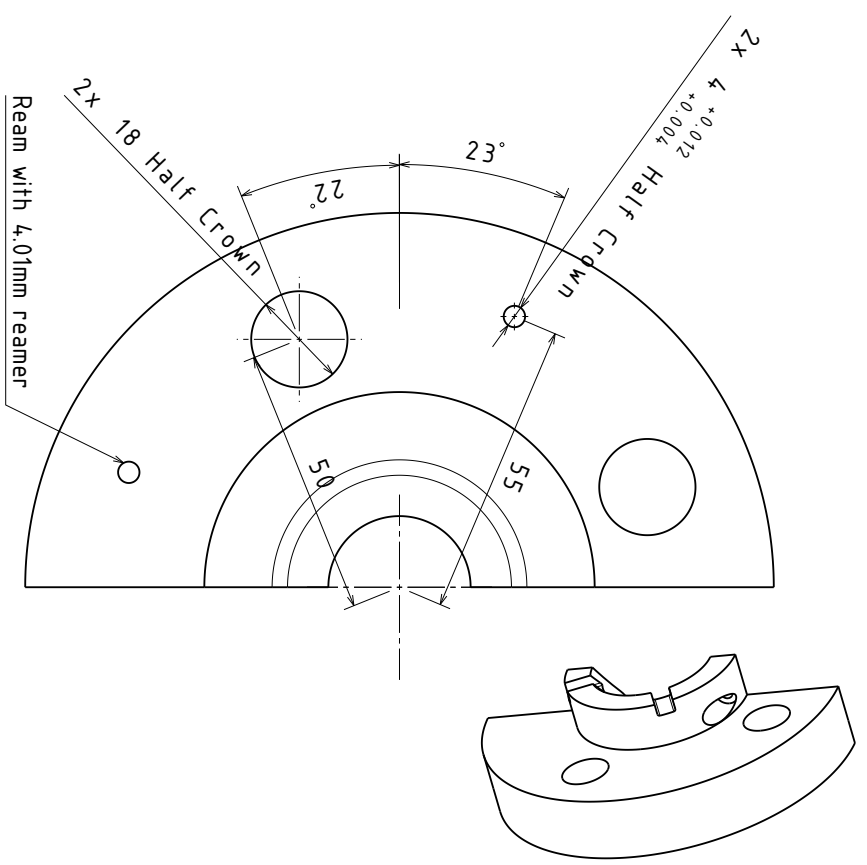
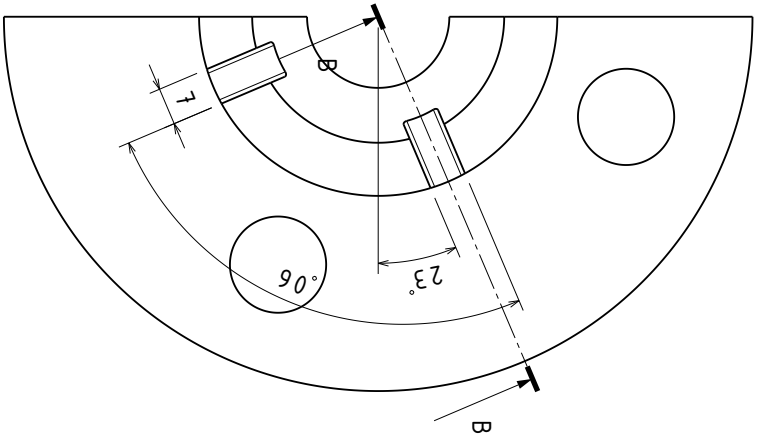
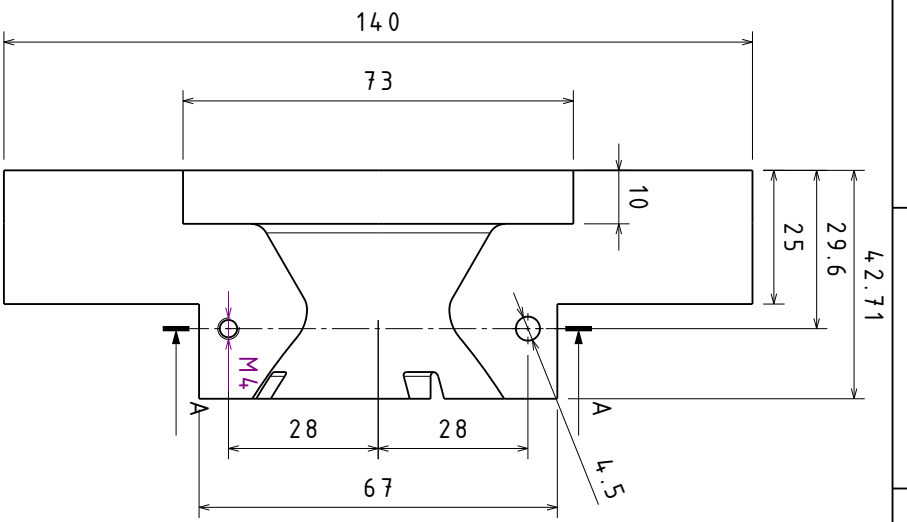


DESIGNED BY:	Krijn de Kievit		
DATE:	05/01/2021		
MATERIAL:	ALU 6082-T6		
SIZE:	A3	AMOUNT:	1
SCALE:	1:2	DRAWING NUMBER:	NOZ-02
		SHEET:	1/1

Nozzle Strain Tube

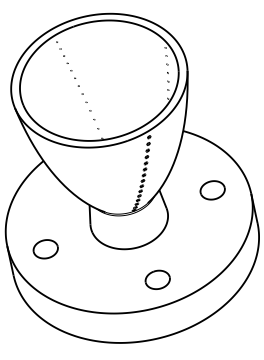
Thesis TU Delft

This drawing is our property; it can't be reproduced or communicated without our written agreement.

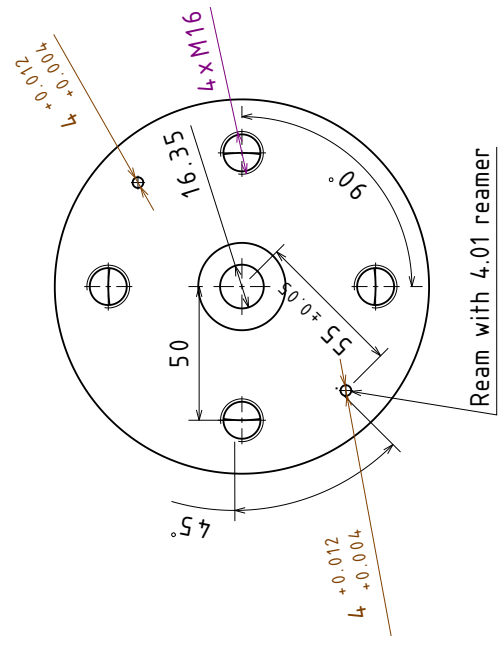
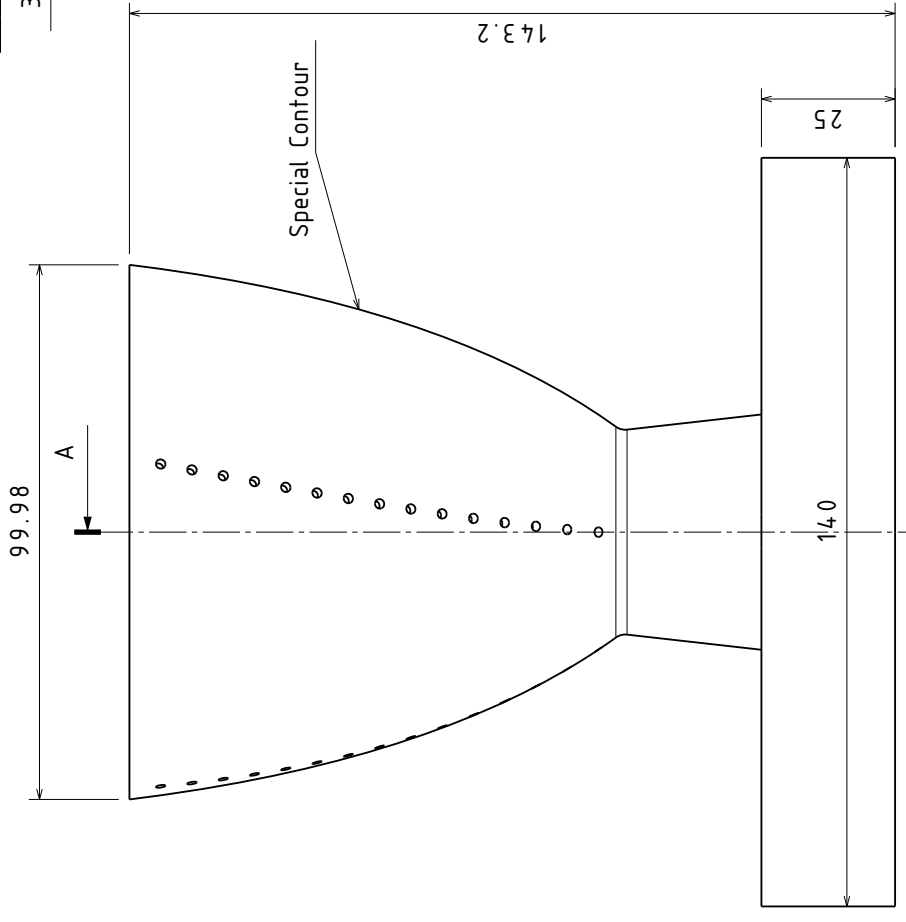
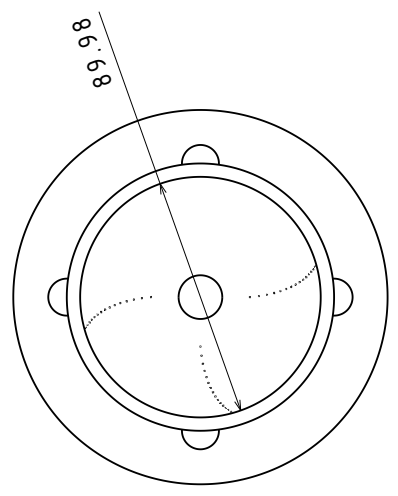
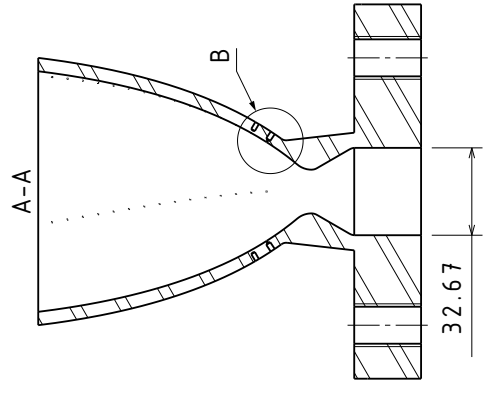
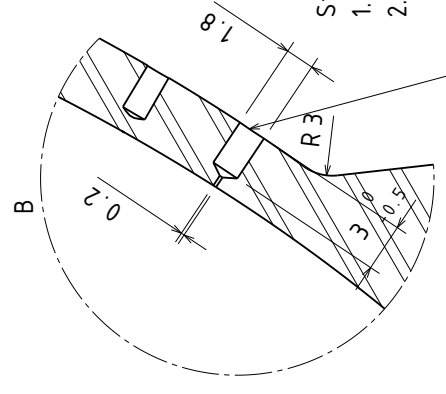


DESIGNED BY: Krijn de Kievit	DATE: 08/01/2021		MATERIAL: ALU 6082-T6		SIZE: A3		SCALE: 1:1		WEIGHT (kg): XXX		DRAWING NUMBER: NOZ-03		SHEET: 1/1				
Nozzle Clamp					Thesis TU Delft												
I	—	H	—	G	—	F	—	E	—	D	—	C	—	B	—	A	—

This drawing is our property; it can't be reproduced or communicated without our written agreement.

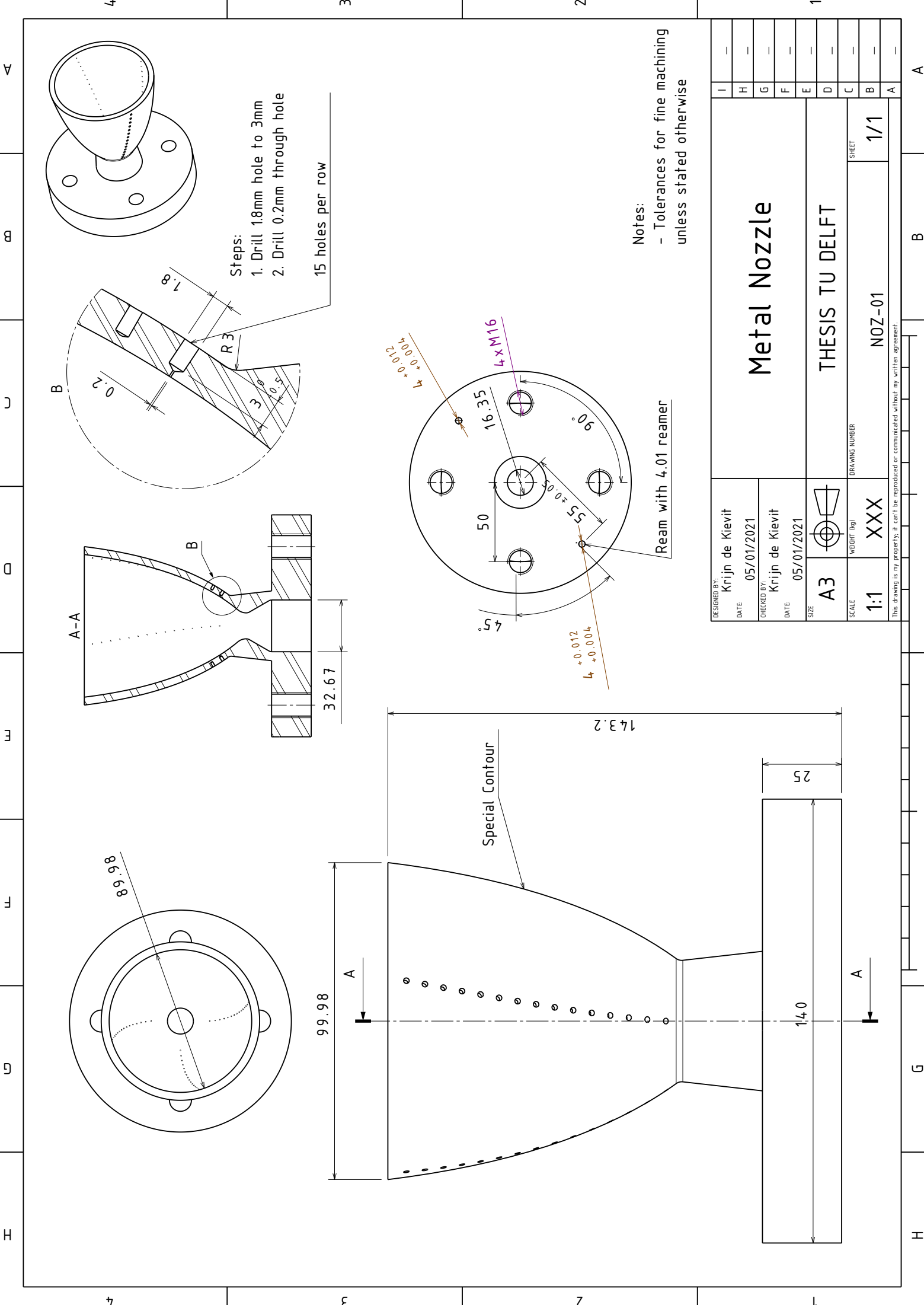


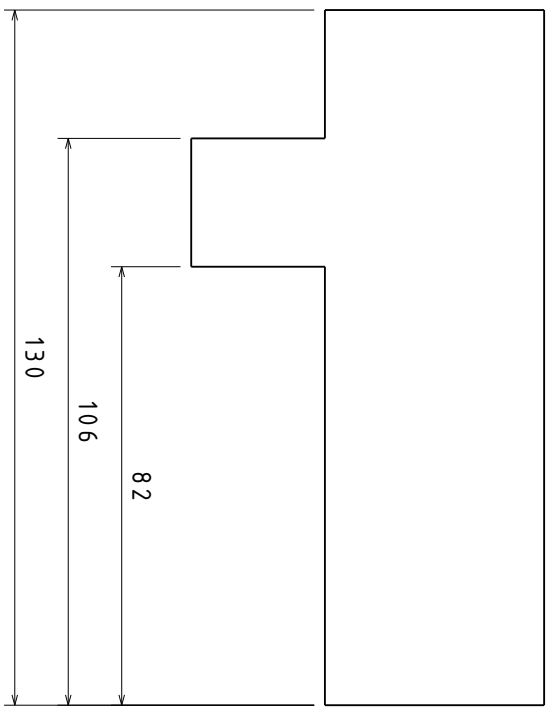
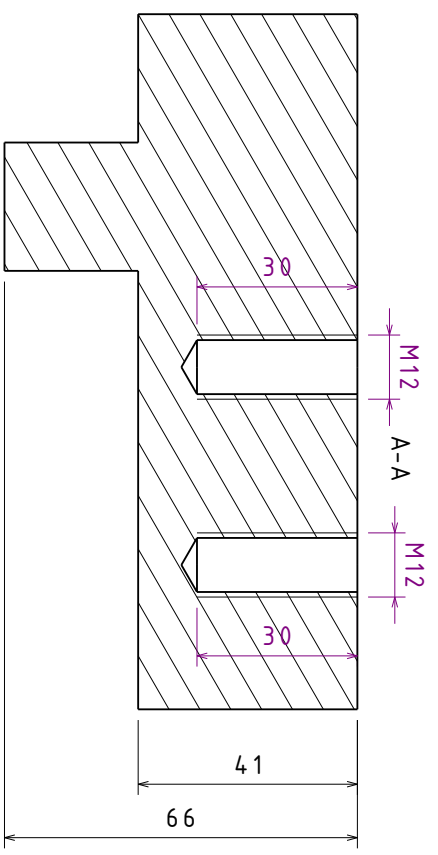
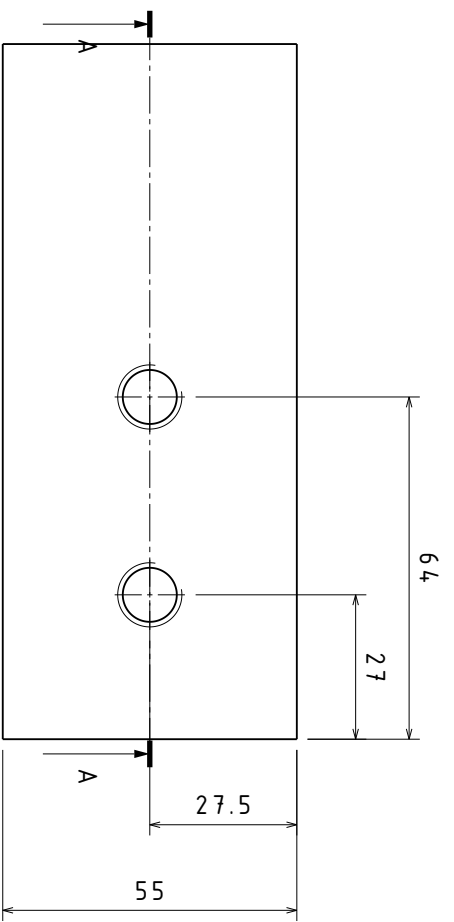
- Steps:
1. Drill 1.8mm hole to 3mm
 2. Drill 0.2mm through hole
- 15 holes per row



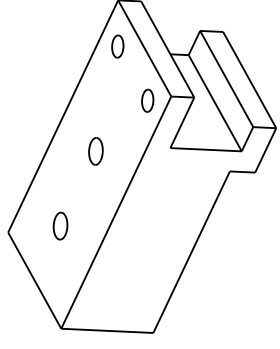
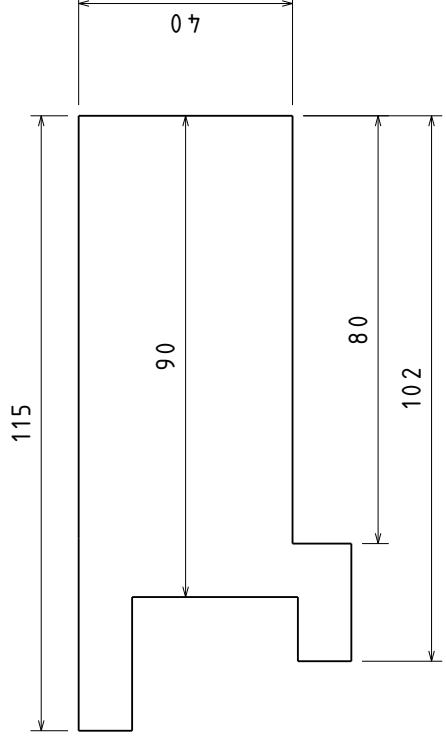
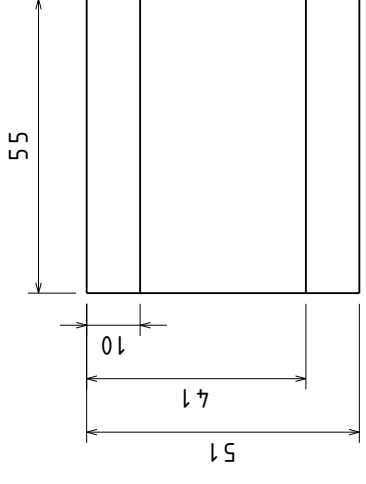
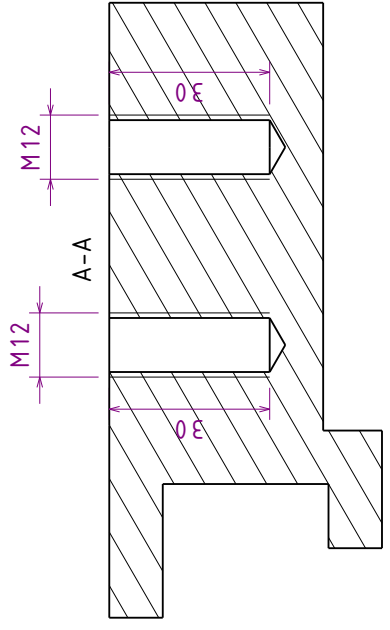
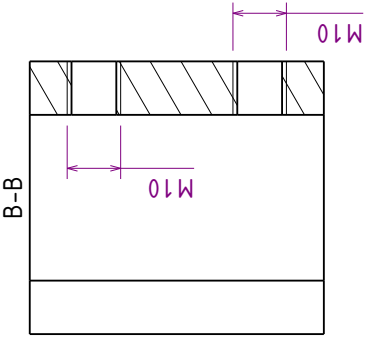
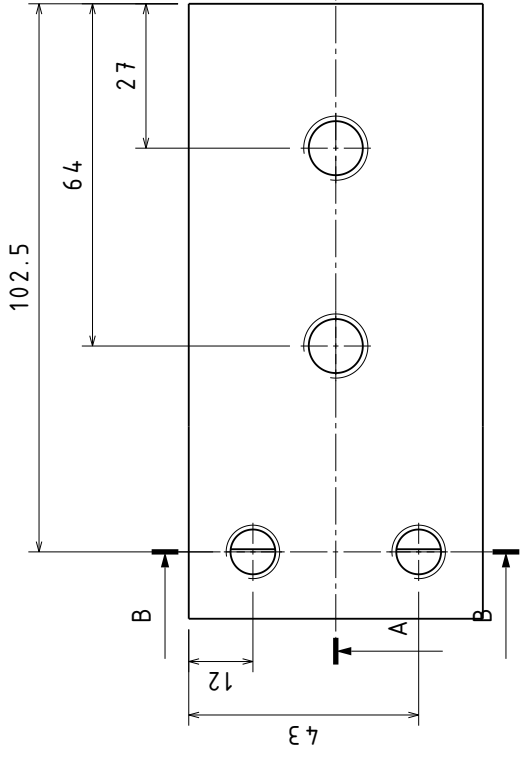
Notes:
 - Tolerances for fine machining unless stated otherwise

DESIGNED BY: Krijn de Kievit	DATE: 05/01/2021		DRAWING NUMBER NOZ-01	SHEET 1/1
CHECKED BY: Krijn de Kievit	DATE: 05/01/2021			
SIZE A3	SCALE 1:1			
<h1>Metal Nozzle</h1>			<h2>THESIS TU DELFT</h2>	
<small>This drawing is my property. It can't be reproduced or communicated without my written agreement.</small>				





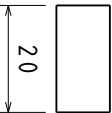
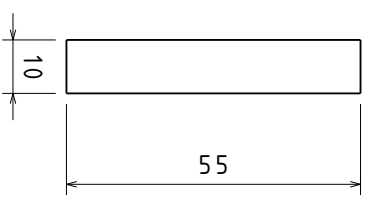
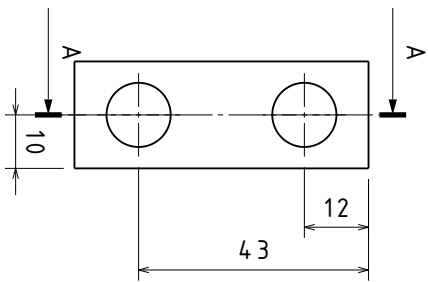
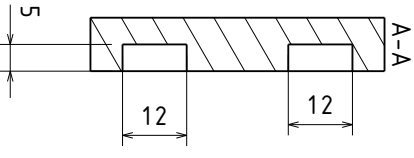
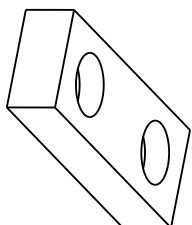
DESIGNED BY: Krijn de Kievit	DATE: 07/01/2021	<h1>Aft Leg Support</h1>	
CHECKED BY: Krijn de Kievit	DATE: 07/01/2021		
Thesis TU Delft			
SCALE: 1:1	WEIGHT (kg): XXX	DRAWING NUMBER: STR-02	SHEET: 1/1
This drawing is our property; it can't be reproduced or communicated without our written agreement.			
I	—	A	—
H	—	B	—
G	—	C	—
F	—	D	—
E	—	E	—
D	—	F	—
C	—	G	—
B	—	H	—
A	—	I	—



DESIGNED BY: Krijn de Kievit	DATE: 07/01/2021	CHECKED BY: Krijn de Kievit	DATE: 07/01/2021		SIZE A3		WEIGHT [kg]
					SCALE 1:1		DRAWING NUMBER STR-01
					SHEET 1/1		

Floor Clamp		Thesis TU Delft						
		STR-01						
I	H	G	F	E	D	C	B	A

This drawing is our property; it can't be reproduced or communicated without our written agreement.



DESIGNED BY:	Krijn		
DATE:	11/01/2021		
MATERIAL:	Steel		
SIZE:	A3	AMOUNT:	4
SCALE:	1:1	DRAWING NUMBER:	STR-14
DASSAULT SYSTEMES		SHEET:	1/1
Floor Clamp Support			
I			
H			
G			
F			
E			
D			
C			
B			
A			

This drawing is our property; it can't be reproduced or communicated without our written agreement.

H G B A

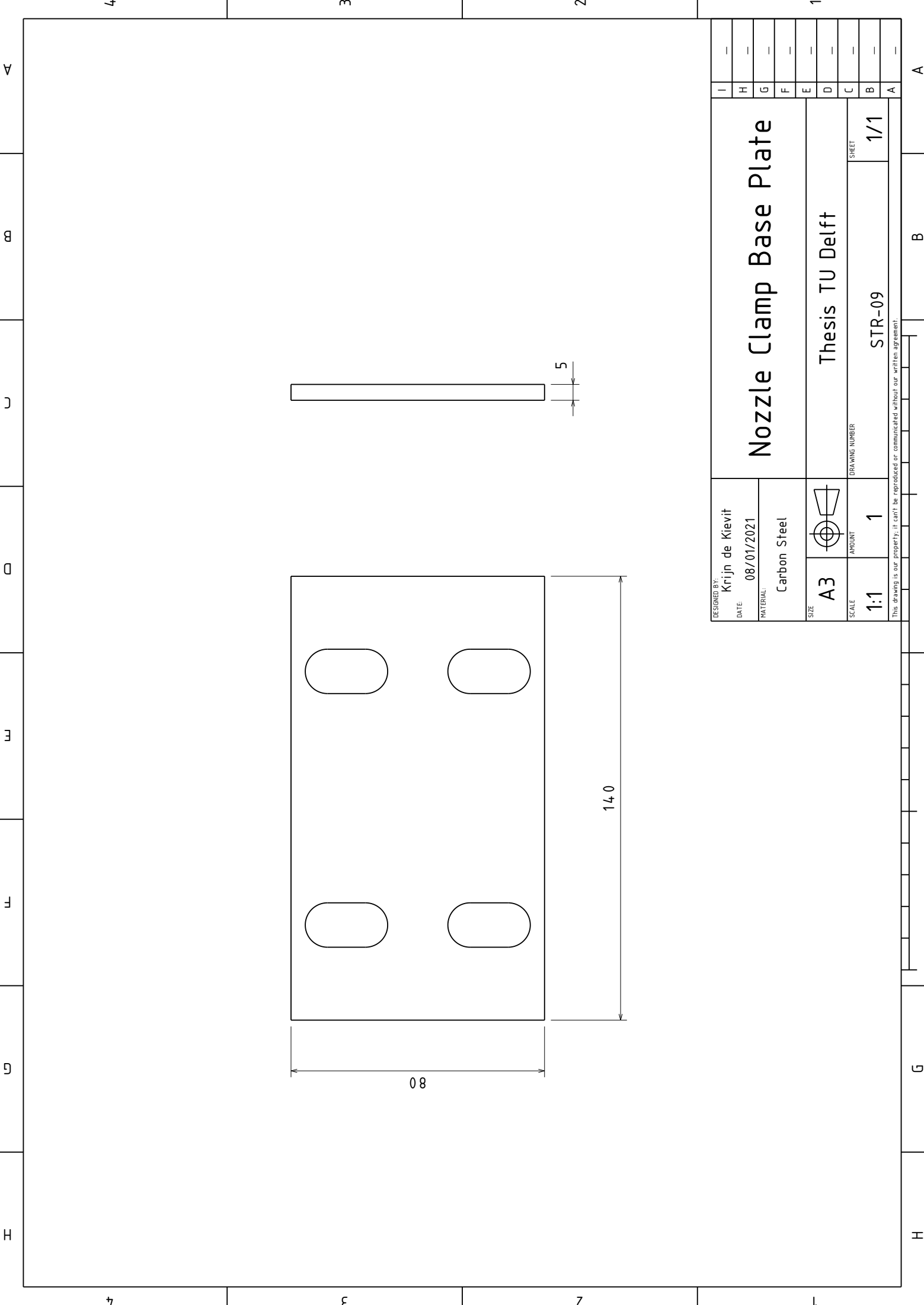
1

2

3

4

H G F E D C B A



DESIGNED BY: Krijn de Kievit	Nozzle Clamp Base Plate	
DATE: 08/01/2021	Thesis TU Delft	
MATERIAL: Carbon Steel	DRAWING NUMBER STR-09	
SIZE A3	SHEET 1/1	
SCALE 1:1	AMOUNT 1	
This drawing is our property; it can't be reproduced or communicated without our written agreement!		

4 3 2 1

A B C D E F G H

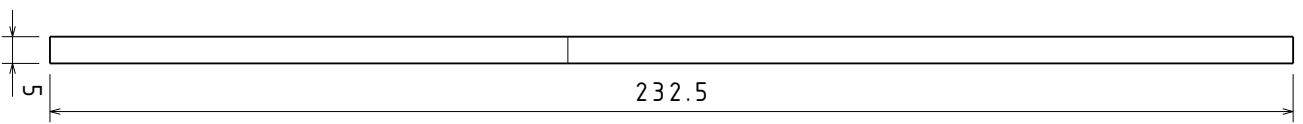
4 3 2 1

A B C D E F G H

1 2 3 4

H

H

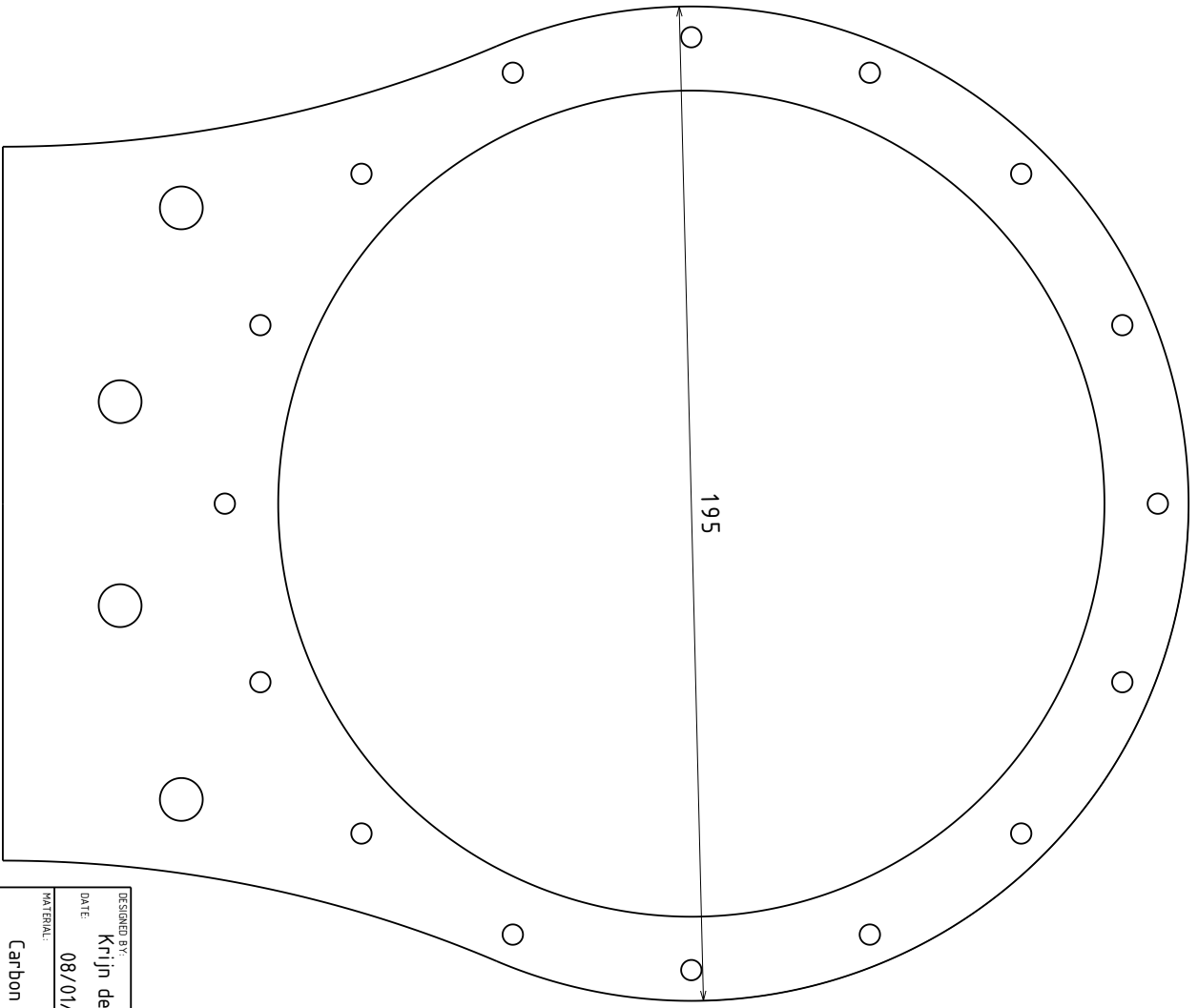


232.5

5

G

G



195

F

E

D

C

B

A

B

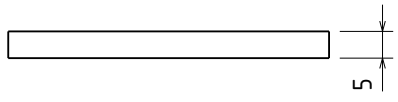
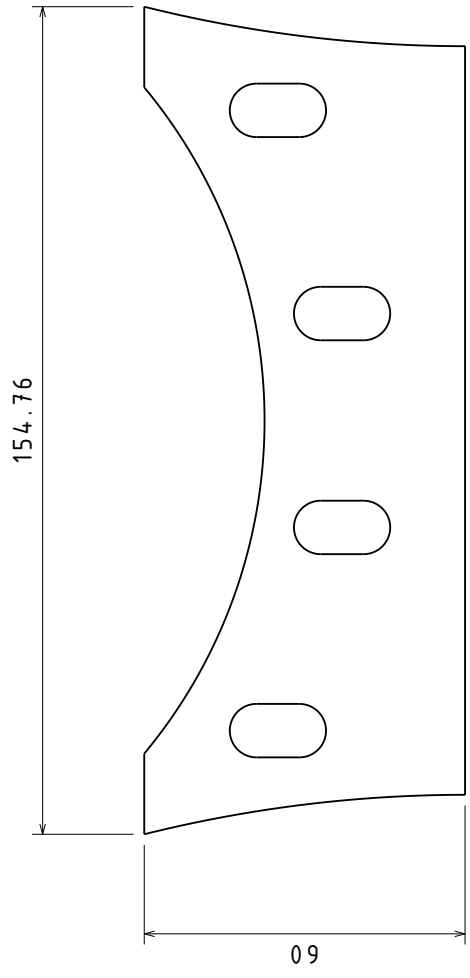
A


1 2 3 4

DESIGNED BY: Krijn de Kievit		Nozzle Clamp Main Plate		I	-
DATE: 08/01/2021	MATERIAL: Carbon Steel			H	-
SIZE: A3		DRAWING NUMBER: STR-11	G	-	
SCALE: 1:1	AMOUNT: 1		F	-	
This drawing is our property; it can't be reproduced or communicated without our written agreement.		Thesis TU Delft		E	-
		SHEET		D	-
		1/1		C	-
				B	-
				A	-

4 3 2 1

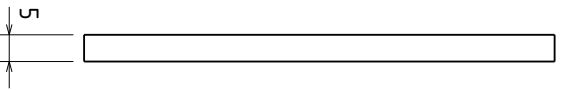
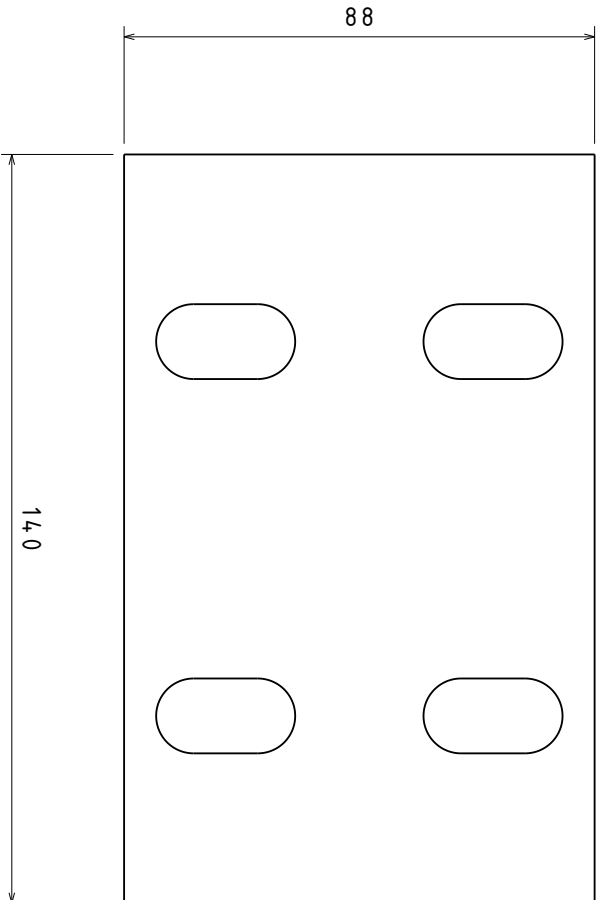
A B C D E F G H



DESIGNED BY:	Krijn de Kievit		
DATE:	08/01/2021		
MATERIAL:	Carbon Steel		
SIZE:	A3		Thesis TU Delft
SCALE:	1:1	AMOUNT:	1
		DRAWING NUMBER:	STR-10
		SHEET:	1/1
This drawing is our property; it can't be reproduced or communicated without our written agreement!			

H G B A

4 3 2 1



DESIGNED BY: Krijn de Kievit		DRAWING NUMBER STR-06		SHEET 1/1	
DATE: 08/01/2021					
MATERIALS: Carbon Steel		<h1 style="text-align: center;">Structure Clamp Base</h1> <p style="text-align: center;">Thesis TU Delft</p>			
SIZE: A3	AMOUNT: 2				
SCALE: 1:1					
<small>This drawing is our property; it can't be reproduced or communicated without our written agreement.</small>					

H
G
F
E
D
C
B
A

1

2

3

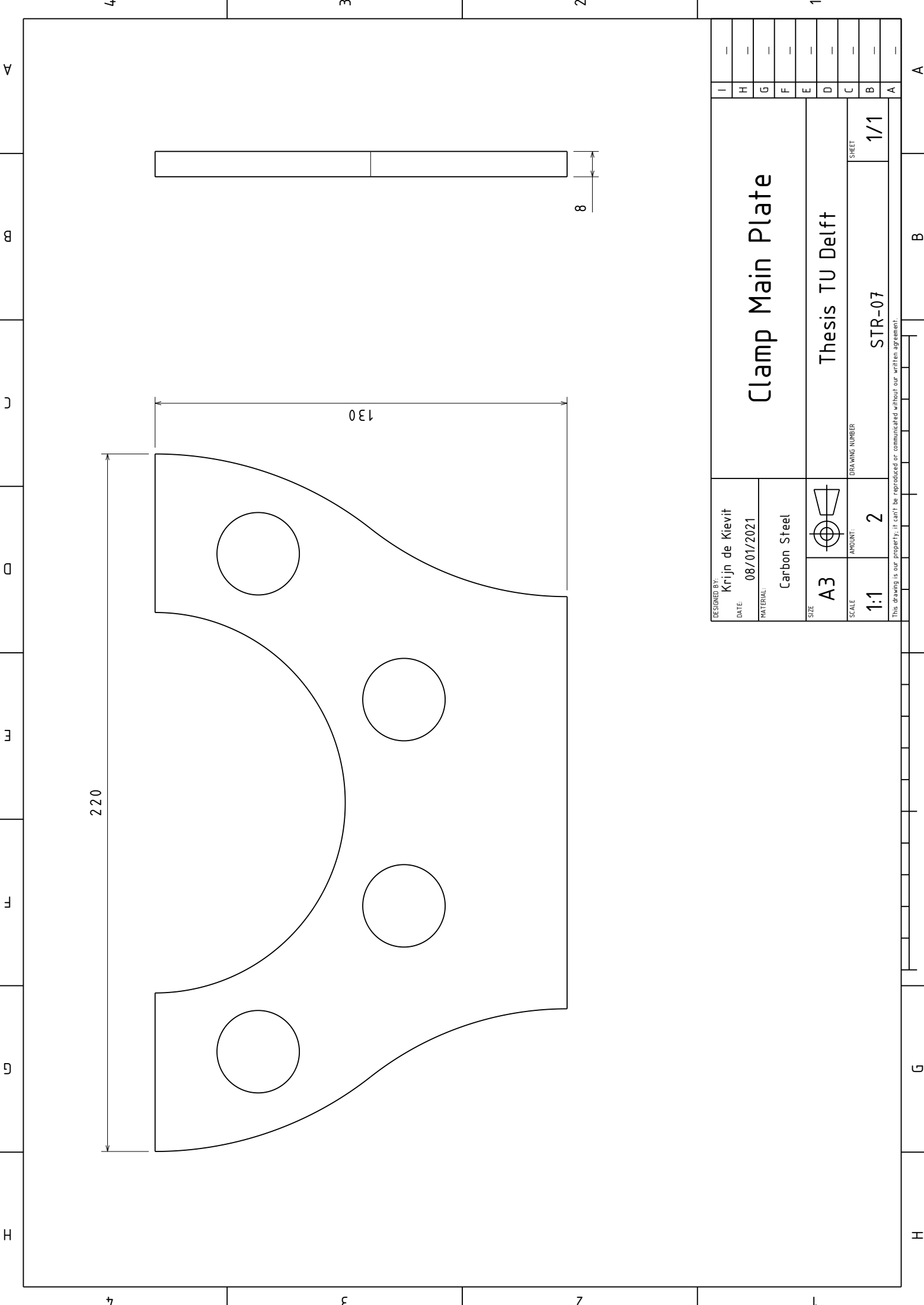
4

1

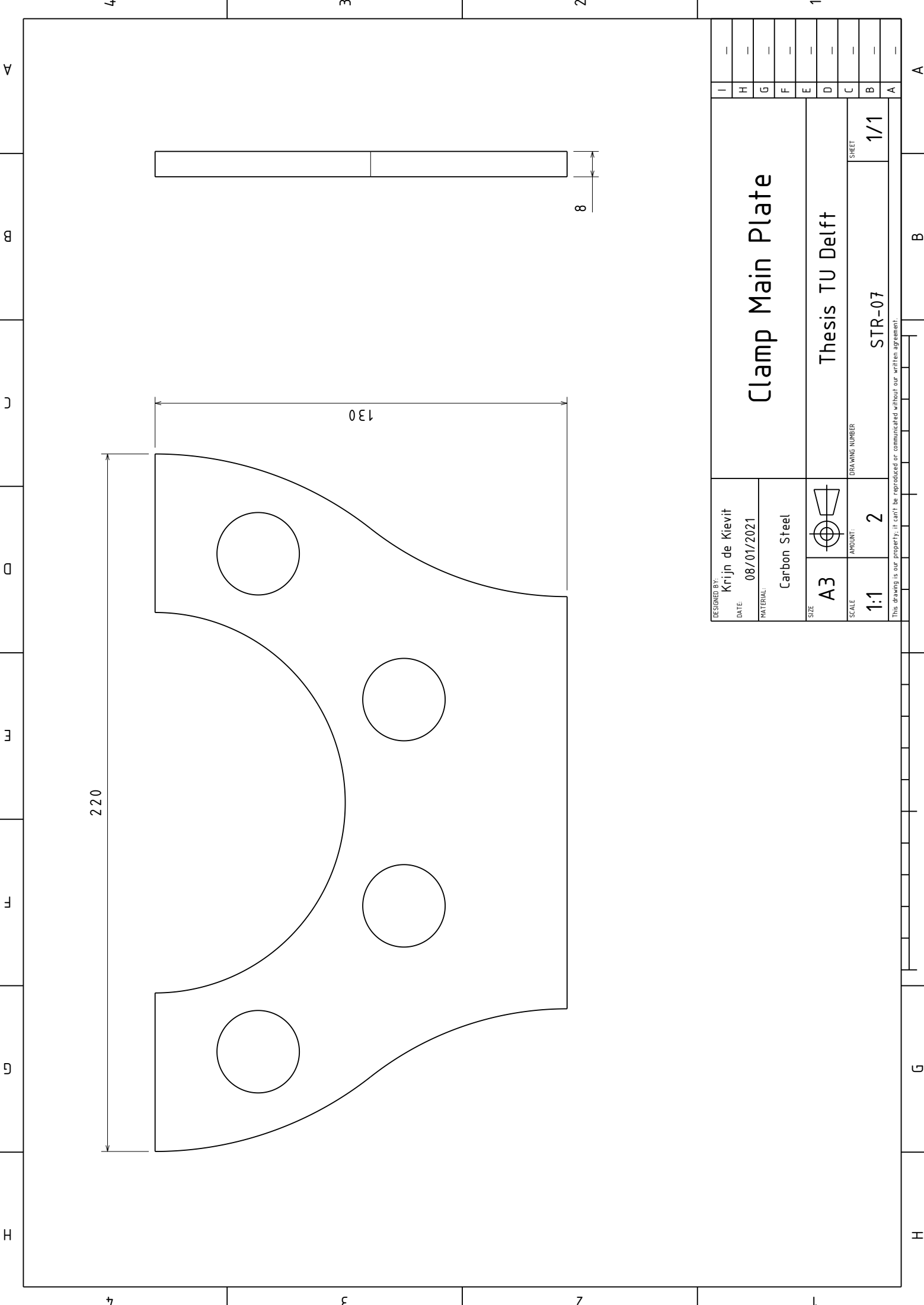
2

3

4



DESIGNED BY: Krijn de Kievit	Clamp Main Plate	
DATE: 08/01/2021	Thesis TU Delft	
MATERIAL: Carbon Steel	DRAWING NUMBER STR-07	
SIZE A3	SHEET 1/1	
SCALE 1:1	AMOUNT: 2	
This drawing is our property; it can't be reproduced or communicated without our written agreement!		



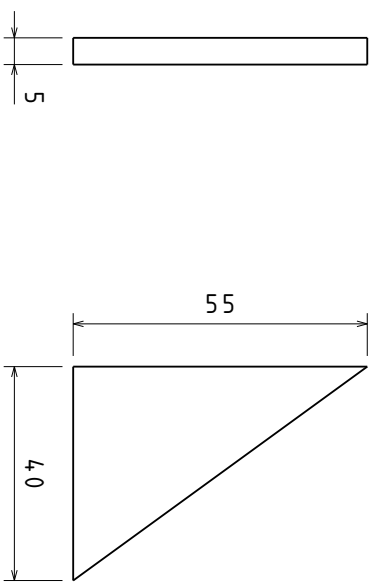
H
G
F
E
D
C
B
A

4

3

2

1



DESIGNED BY: Krijn de Kievit	Clamp Support			I	—
DATE: 08/01/2021				H	—
MATERIAL: Carbon Steel	Thesis TU Delft			G	—
SIZE: A3				E	—
SCALE: 1:1	AMOUNT: 2	DRAWING NUMBER: STR-08	D	—	
This drawing is our property; it can't be reproduced or communicated without our written agreement.			C	—	
			B	—	
			A	—	
			SHEET	1/1	

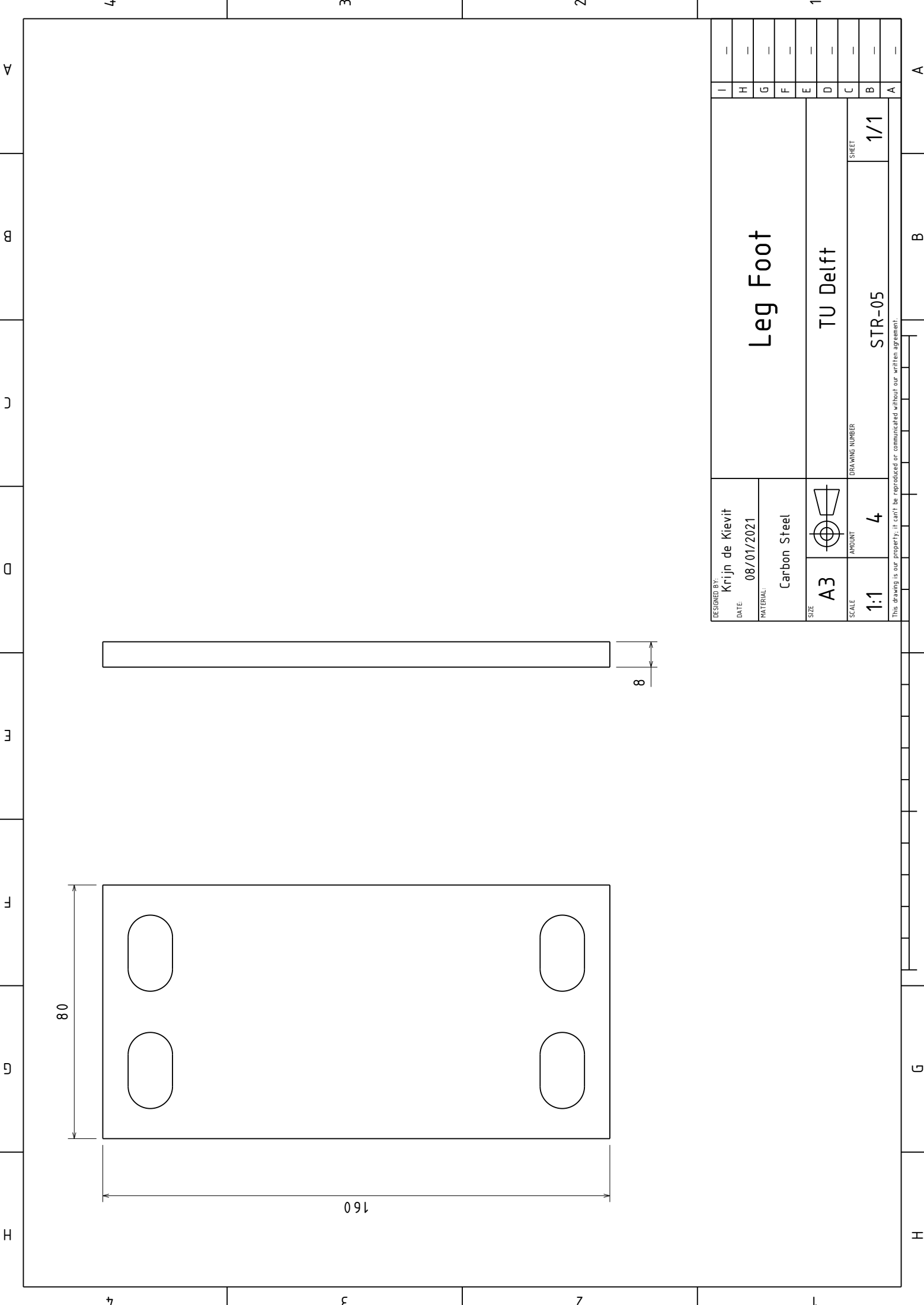
1

2

3

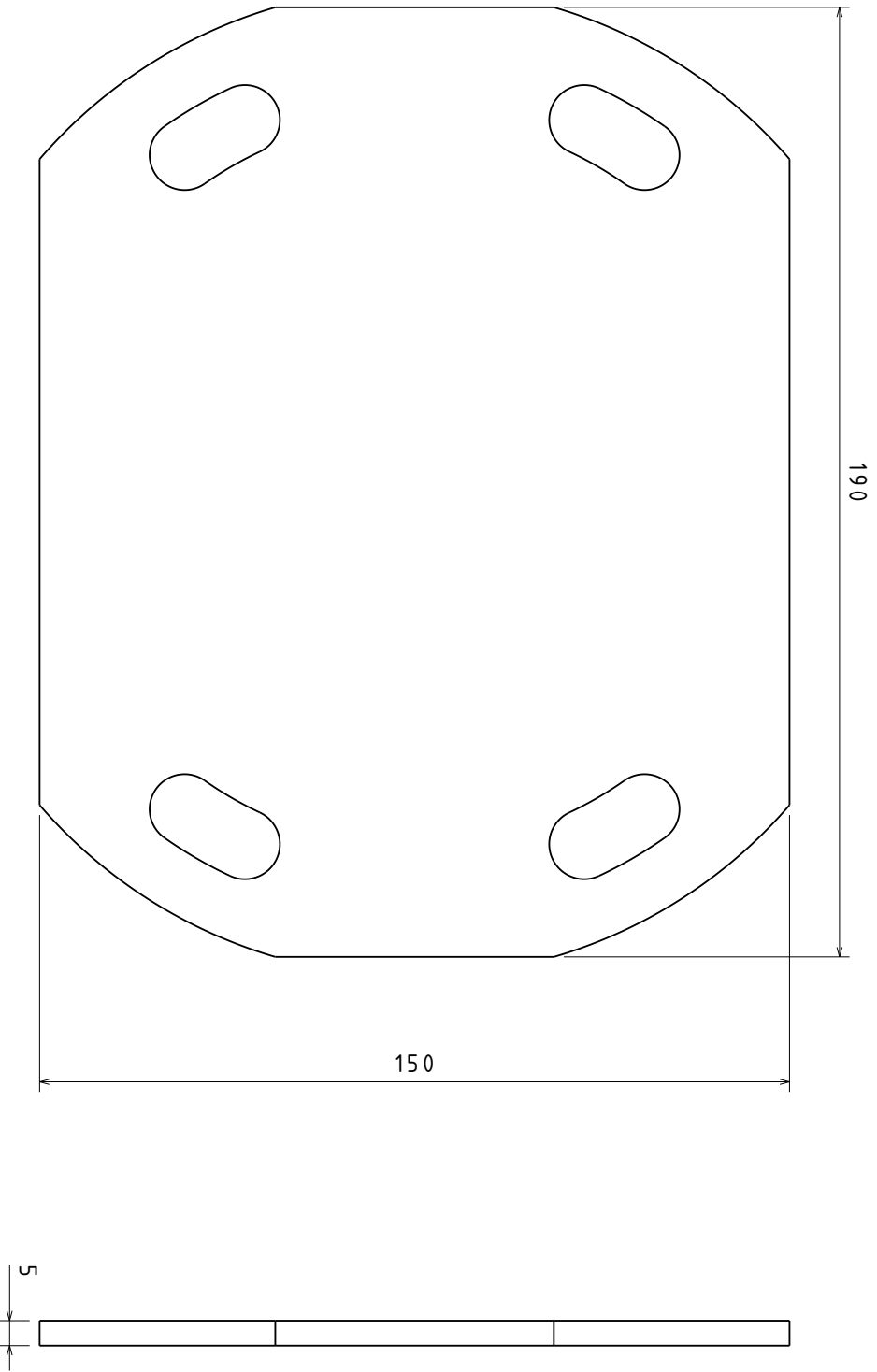
4

H
G
F
E
D
C
B
A



DESIGNED BY: Krijn de Kievit	Leg Foot	
DATE: 08/01/2021	TU Delft	
MATERIAL: Carbon Steel	STR-05	
SIZE: A3	1/1	
SCALE: 1:1	4	
	DRAWING NUMBER	
	SHEET	
	1/1	
	A	
	B	
	C	
	D	
	E	
	F	
	G	
	H	
	I	

This drawing is our property; it can't be reproduced or communicated without our written agreement.

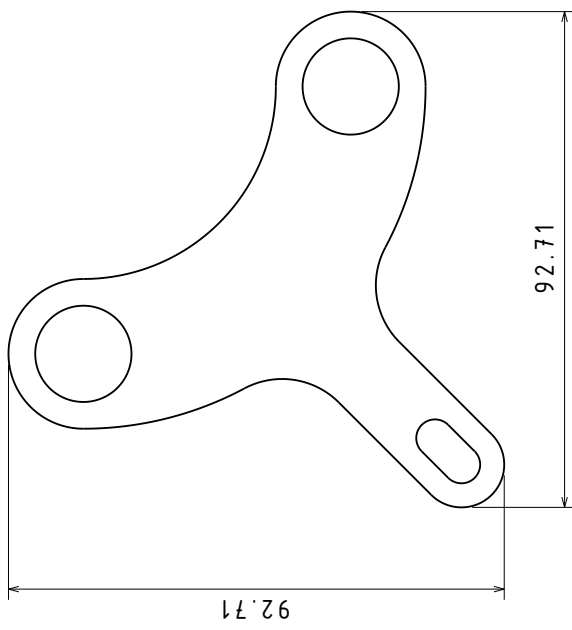
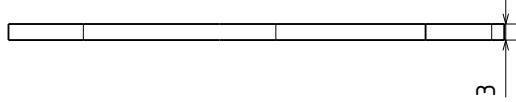


DESIGNED BY: Krijn de Kievit		DRAWING NUMBER STR-04		SHEET 1/1	
DATE: 08/01/2021		Front Leg Mount			
MATERIAL: Carbon Steel					
SIZE: A3	AMOUNT: 4				
SCALE: 1:1	This drawing is our property; it can't be reproduced or communicated without our written agreement.				

	1	2	3	4	
H					H
G					G
F					F
E					E
D					D
C					C
B					B
A					A
	1	2	3	4	

4 3 2 1

A B C D E F G H



DESIGNED BY:	Krijn		
DATE:	11/01/2021		
MATERIAL:	Carbon Steel		
SIZE:	A3		
SCALE:	1:1	AMOUNT:	1
		DRAWING NUMBER:	STR-12
		SHEET:	1/1

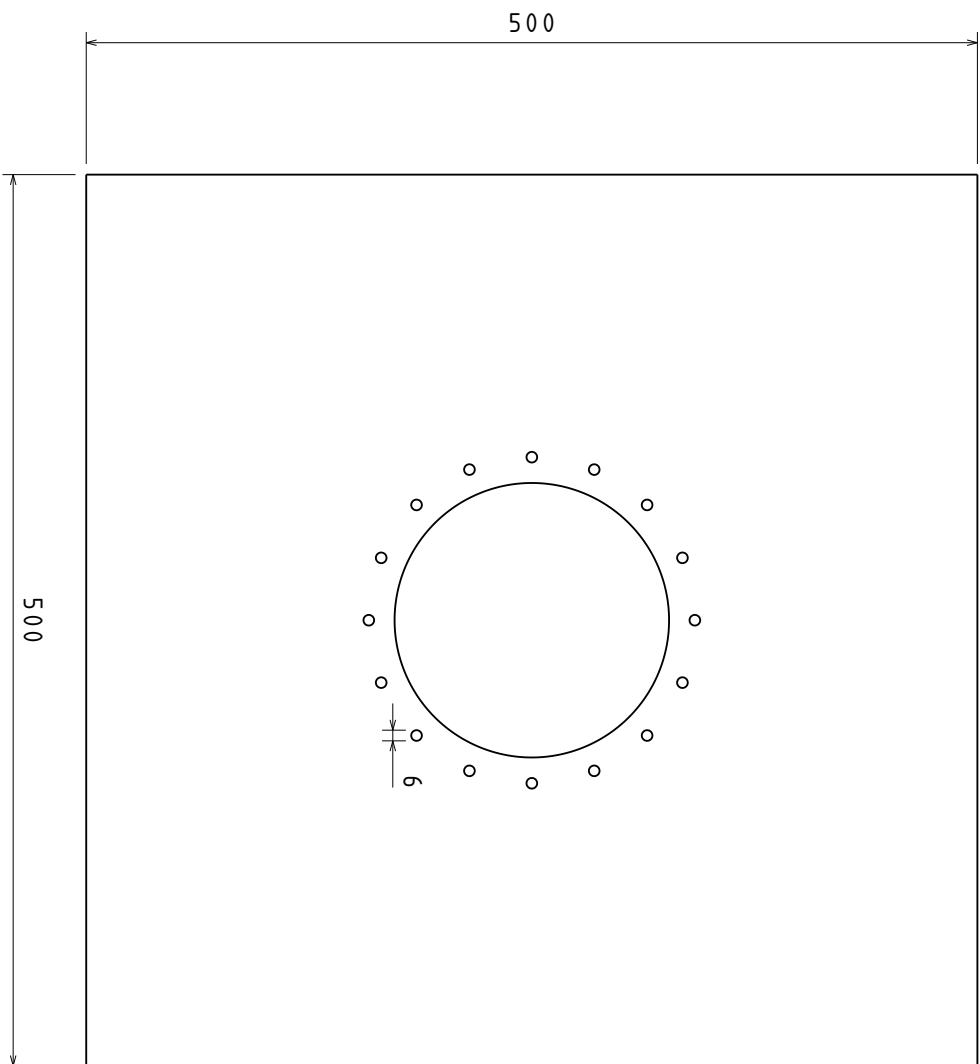
Nozzle Anti-Flight Clamp

DASSAULT SYSTEMES

I	—
H	—
G	—
F	—
E	—
D	—
C	—
B	—
A	—

4 3 2 1

A B C D E F G H



DESIGNED BY:	Krijn		
DATE:	11/01/2021		
MATERIAL:	Carbon Steel		
SIZE:	A3		
SCALE:	1:3	AMOUNT:	1
DRAWING NUMBER:		STR-13	
SHEET:		1/1	
Vent Back Plate			
Thesis TU Delft			
I			
H			
G			
F			
E			
D			
C			
B			
A			

This drawing is our property; it can't be reproduced or communicated without our written agreement.

4

3

2

1

A

B

C

D

E

F

G

H

4

3

2

1

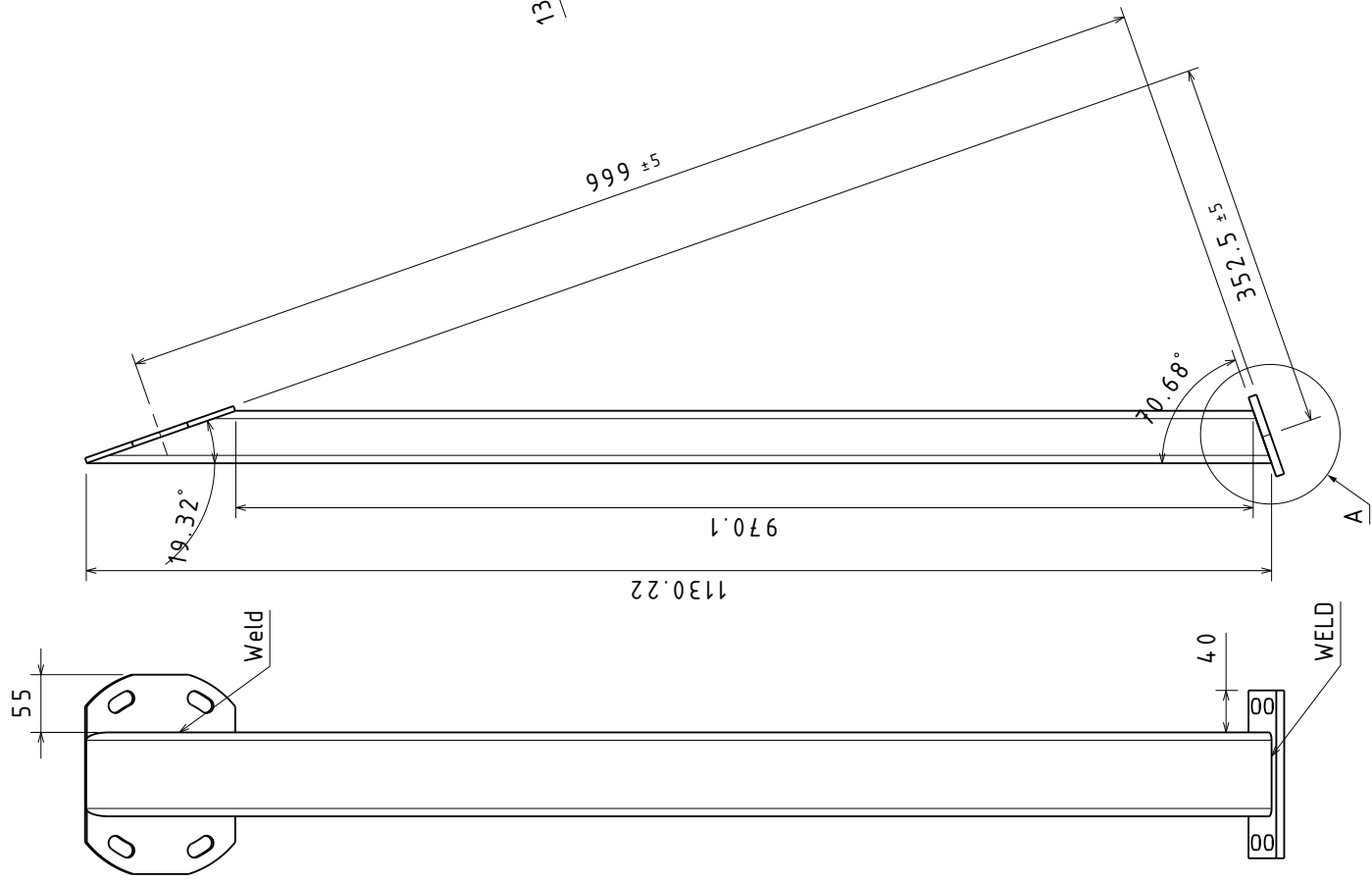
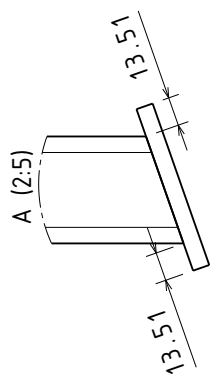
A

B

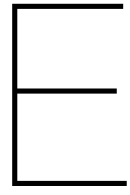
G

H

DESIGNED BY:	Krijn		DRAWING NUMBER STR-15	SHEET 1/1
DATE:	11/01/2021			
MATERIAL:	Steel	SCALE 1:5	AMOUNT 4	
SIZE:	A3			
Thesis TU Delft				
Front Leg				



This drawing is our property; it can't be reproduced or communicated without our written agreement.



Test Procedures

In case of emergency: +31 (0)15 27 81226

Low risk	Medium risk	High risk
<ul style="list-style-type: none"> • Test-setup is safe to approach • No safety gear required 	<ul style="list-style-type: none"> • Only authorized personnel in test area • Wear appropriate safety gear 	<ul style="list-style-type: none"> • Clear all personnel from test area • Do not approach the test-setup



Abbreviations

MV	Main Valve
CV	Control Valve
DV	Diffuser Valve

In case of emergency: +31 (0)15 27 81226

Test Location:
ST-15 Room HSL
Kluyverweg 2
2629 HT Delft

Monday 1st January, 1900
MSc. Thesis
Test ID: Nozzle Cold Flow Test

Summary of the setup

The test-setup consists of a feed line that is hooked up to the main supply tank of the HSL facility. This tank will be pressurised to maximum pressure (approx. 40 bar). The feed line connects to a diffuser that decelerates the gas into the settling chamber. At the front of the settling chamber a honeycomb mesh straightens the flow. The total pressure and temperature are measured in the settling chamber.

A contraction decreases the flow area after which the flow passes through a strain tube. This is a tube with 0.75 mm thick walls that has two full bridge strain gauge arrays, such that lateral nozzle loads can be measured in 2D.

The flow then passes through the nozzle, at which the following conditions are present:

Parameter	Value	Unit
Maximum Total Pressure	40	bar
Total Temperature	288	K
Maximum Mass Flow Rate	2.0	kg/s
Working Fluid	Dry air	-

Table 1: Operating conditions

Parameter	Value	Unit
Pressure	0.2	bar
Temperature	63.5	K
Mach Number	4.2	-
Fluid Velocity	623.9	m/s

Table 2: Nozzle exit conditions

A schlieren system is used to visualize the shock structure downstream of the nozzle exit. An additional camera is pointed directly at the nozzle exit to perform DIC of the nozzle lip.

Test Summary

Test Goals and Operations

The following primary and secondary goals were set before the test campaign:

Primary Goals:

Secondary Goals:

Emergency and Unpowered System States

When the emergency button is pressed the main valve will move to the unpowered position, which means it will close. This will also happen if the power is cut to the system. The control valve is hand actuated, and therefore does not rely on electrical power to be closed.

Feed System Chart

Below a diagram of the feed system is shown.

In case of emergency: +31 (0)15 27 81226

Test Location:
ST-15 Room HSL
Kluyverweg 2
2629 HT Delft

Monday 1st January, 1900

MSc. Thesis
Test ID: Nozzle Cold Flow Test

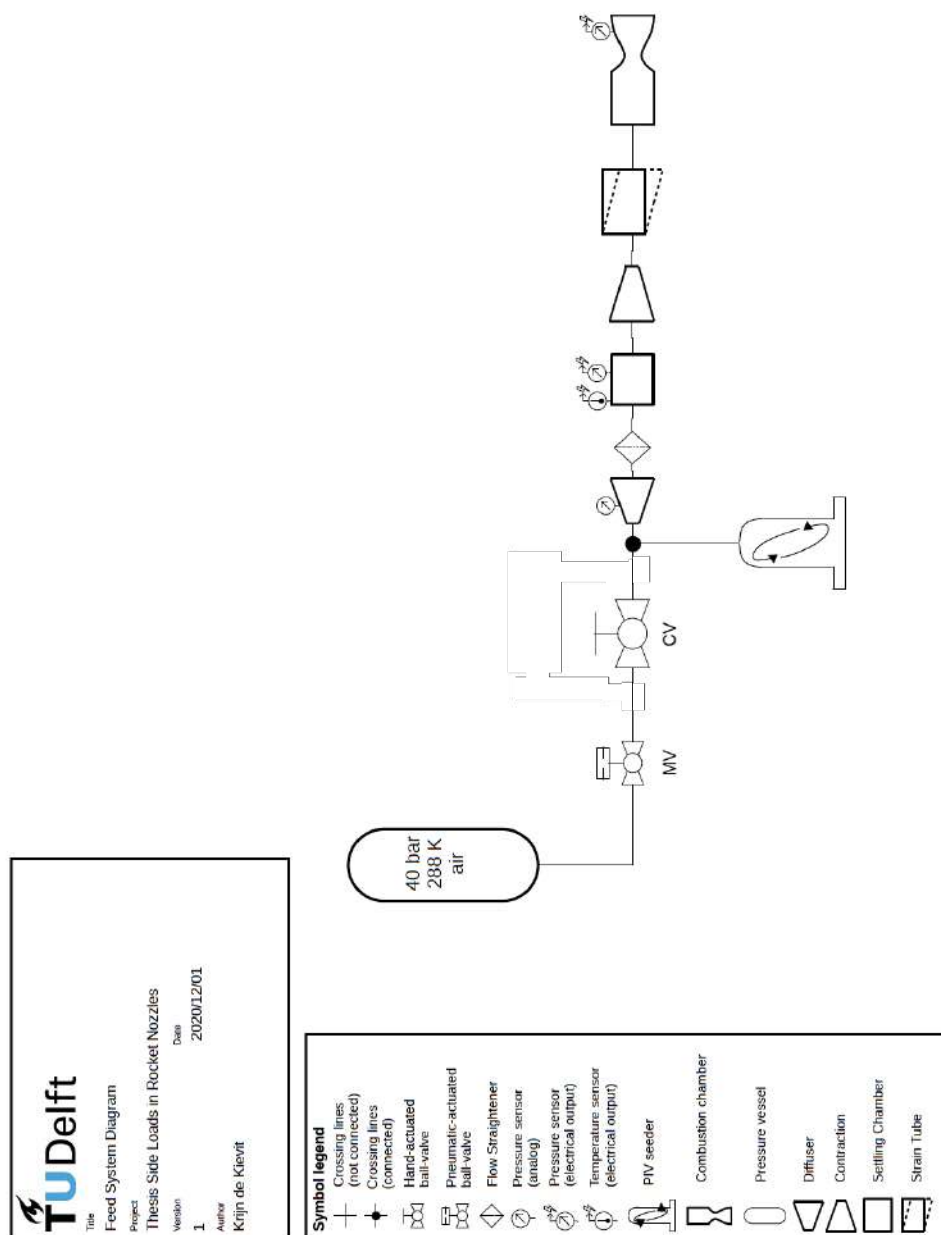


Figure 1: Feed system chart

In case of emergency: +31 (0)15 27 81226

Test Location:
 ST-15 Room HSL
 Kluyverweg 2
 2629 HT Delft

Monday 1st January, 1900
 MSc. Thesis
 Test ID: Nozzle Cold Flow Test

A - System Checks			
ID	Check	Description	Comments
A1		Check that all M12 bolts on the structure are properly tightened	
A2		Check that the system is properly connected to the facility floor by pushing on it.	
A3		Check that the supply hose is properly attached to the flange downstream of the CV. (hand tight + 1/4 turn)	
A4		Check that the supply hose is properly attached to the diffuser. (hand tight + 1/4 turn)	
A5		Make sure that the plug or the PIV seeder are properly tightened in the diffuser	
A6		Check that the flange bolts on the settling chamber are properly tightened	
A7		Check that the pressure and temperature sensor are properly tightened in the settling chamber	
A8		Check that the bolts connecting the contraction to the strain tube are properly tightened	
A9		Check that the bolts connecting the strain tube to the strain tube clamp are properly tightened	
A10		Check that the bolts connecting the strain tube and the nozzle are properly tightened	
A11		Check that the nozzle anti flight cable is properly attached to the floor and the setup	
A12		Check that the nozzle back plate is properly attached.	
A13		Make sure that the diffuser valve (DV) of the ST-15 is open	

B - Sensor and Actuator Checks			
ID	Check	Description	Comments
Hardware Checks at Setup			
B1		Ensure that all 45 pressure tap hoses are properly attached to the nozzle and the ScaniValves	
B2		Make sure that the power, trigger and ethernet cables are properly connected to the ScaniValves	
B3		Check that the trigger line is connected to the NI DAQ module (Module 2 Channel 1)	
Continued			

In case of emergency: +31 (0)15 27 81226

Test Location:
ST-15 Room HSL
Kluyverweg 2
2629 HT Delft

Monday 1st January, 1900

MSc. Thesis
Test ID: Nozzle Cold Flow Test

ID	Check	Description	Comments
B4		Check that all ScaniValve trigger lines are properly connected to the dividing connector	
B5		Power up all scanivalves	
B6		Check that the cable of the pressure sensor is properly connected to the sensor and the NI module (Module 5 AI Channel 8)	
B7		Check that the cable of the temperature sensor is properly connected to the sensor and the NI module (Module 3 Channel 0)	
B8		Check that the Main Valve cable is connected to the NI DAQ module (Module 2 Channel 0)	
B9		Check that both strain gauges are properly attached to the strain tube	
B10		Check that both strain gauges are connected to the NI DAQ module (Module 1 Channel 0 & 1)	
B11		Make sure that the NI DAQ module is plugged into power	
B12		Make sure the electronics box is turned on	
B13		Make sure that the webcam is in the correct spot	
B14		Turn on the schlieren light source to full power	
B15		Check that the razor is properly aligned with the light source	
B16		Make sure that the Photron camera is plugged in	
B17		Make sure that the Photron camera is connected through ethernet	
B18		Turn the Photron camera on	
ScaniValve Setup (in case of aluminium nozzle)			
B19		Check that all Ethernet cables of the ScaniValves are sending a signal on the Ethernet switch.	
B20		On one computer: Open 3 instances of ScanTel	
B21		Connect to all of the scanivalves. Use the UDP port settings 21, 22 and 23 in the configuration settings.	
B22		Check that the port in the host of the scanivalve module is the same as the UDP receive port. Do this by typing "list i" and checking that the port value "SET HOST x.x.x.x <port> <protocol>" is set to the same value as the UDP receive port you connected with.	
Continued			

In case of emergency: +31 (0)15 27 81226

Test Location:
ST-15 Room HSL
Kluyverweg 2
2629 HT Delft

Monday 1st January, 1900

MSc. Thesis
Test ID: Nozzle Cold Flow Test

ID	Check	Description	Comments
B23		Make sure that the protocol of the host is set to U (UDP)	
B24		Make sure that the IP address is set to the IP address of the computer	
B25		Type "list s" in each instance of ScanTel and make sure the following settings are entered and saved: <ul style="list-style-type: none"> • SET PERIOD 125 • SET AVG 1 • SET FPS 1000 • SET XSCANTRIG 1 • SET FORMAT 0 • SET TIME 1 • SET EU 1 • SET ZC 1 • SET BIN 1 • SET SIM 0 • SET QPKTS 0 • SET UNITSCAN BAR • SET CVTUNIT 0.068947 • SET PAGE 0 	
B26		type <save>	
B27		Set XSCANTRIG to 0	
B28		Start a binary capture file for each ScaniValve module	
B29		Do a test scan on each of the ScaniValve modules (check that the byte count in the bottom right corner is increasing)	
B30		Close all binary capture files (you can also check the data by converting the files)	
B31		Set XSCANTRIG to 1	
Pressure, Temperature, Strain Gauge and Main Valve Setup			
B32		Make sure that the NI DAQ module is connected to the computer via USB	
B33		Make that the main valve cable is properly connected to the main valve	
B34		Make sure that the webcam is showing live footage	
B35		Make sure that the main valve is NOT connected to pressurized air	
B36		Open the LabView Program	
Continued			

In case of emergency: +31 (0)15 27 81226

Test Location:
ST-15 Room HSL
Kluyverweg 2
2629 HT Delft

Monday 1st January, 1900

MSc. Thesis
Test ID: Nozzle Cold Flow Test

ID	Check	Description	Comments
B37		Make sure that all input ports in the LabView program are correct	
B38		Make sure the following settings are used <ul style="list-style-type: none"> • Measurement time: 2000 • Measurement rate: 1000 	
B39		Make sure the atmospheric pressure is correct	
B40		Make sure the file path is correct	
B41		Make a test file name	
B42		Start a binary file capture for each of the Scani-Valve modules	
B43		Set ScaniValves to scanning mode by typing "SCAN" and pressing <enter>	
Schlieren System Setup			
B44		Open Photron FPV on the computer	
B45		Check that the live function is working	
B46		Take a test measurement	
B47		Set the following settings <ul style="list-style-type: none"> • Frame rate = 1000 Hz • Shutter speed = 1/12000 	
B48		Turn on the signal generator	
B49		Make sure the signal generator outputs a square wave at 500 Hz	
B50		Run the LabView program	
Test Measurement			
B51		Check that all sensors are working properly	
B52		Cycle the main valve and listen if the namur valve actuates	
B53		Set the Photron cameras to recording mode	
B54		Take a test measurement, check that the byte count of the scanivalves is increasing	
B55		Close the binary capture files	
B56		Open the labview measurement file and check if it is correct	
Emergency Test			
B57		Open the main valve	
B58		Count down and press the emergency button, listen if the namur valve actuates	
Continued			

In case of emergency: +31 (0)15 27 81226

Test Location:
ST-15 Room HSL
Kluyverweg 2
2629 HT Delft

Monday 1st January, 1900
MSc. Thesis
Test ID: Nozzle Cold Flow Test

ID	Check	Description	Comments
Finished Emergency Test			
B59		Close the Main Valve in the LabView program	
B60		Disengage the emergency button	
System will now be pressurized			
B61		Make sure that the control valve is fully closed	
B62		Make sure the main valve is closed in LabView	
B63		Connect the main valve to pressurized air of 4.5 bar	
B64		Count down and open the main valve, wait a few seconds and close the main valve again.	
Pressurized Emergency Shutdown Test			
B65		Open the main valve	
B66		Count down and close the main valve with the emergency button	
B67		Close the main valve in the LabView program	
B68		Disengage the emergency button	
B69		Slowly open the control valve to let out the built up pressure	

C - Measurement Campaign			
ID	Check	Description	Comments
C1		Make sure there is a blast screen between the operating position and the setup	
C2		Make sure that the room is clear apart from necessary personnel	
C3		Inform any people present in the W-tunnel that tests are	
C4		Make sure all doors are closed	
C5		Turn the "beveiliging" key in the ST-15 control room	
C6		Make sure the room entry indicator is set to "WARNING"	
C7		Make sure that everyone is wearing hearing protection	
C8		Make sure LabView program is running with correct settings	
C9		Make sure 3 instances of ScanTel are running with correct settings	
C10		Make sure the signal generator is on	
Continued			

In case of emergency: +31 (0)15 27 81226

Monday 1st January, 1900

Test Location:
ST-15 Room HSL
Kluyverweg 2
2629 HT Delft

MSc. Thesis
Test ID: Nozzle Cold Flow Test

ID	Check	Description	Comments
C11		Make sure the control valve is closed	
The following sequence must be repeated each measurement point			
C12		Insert correct measurement file name in Lab-View	
C13		Start binary capture file for each ScaniValve module	
C14		Set ScaniValve modules to scanning mode	
C15		Set Photron camera to recording mode	
C16		Open main valve	
System will now be live			
C17		Slowly start opening the control valve and increase NPR to required value	
C18		Click "Start Measurement"	This will automatically start the ScanValves and Photron camera as well
C19		Stop recording on Photron camera	
C20		Close main valve	Leave control valve in same position
C21		Close binary capture files on ScanTel	
C22		Save Photron camera recording	
C23		Cycle back to step C5 for next measurement	

In case of emergency: +31 (0)15 27 81226

Test Location:
ST-15 Room HSL
Kluyverweg 2
2629 HT Delft

Monday 1st January, 1900
MSc. Thesis
Test ID: Nozzle Cold Flow Test

Bibliography

- [1] Joseph H Ruf, David M McDaniels, and Andrew M Brown. Nozzle Side Load Testing and Analysis at Marshall Space Flight Center. *AIAA Journal*, page 14, 2009.
- [2] Gerald Hagemann, Jan Alting, and Dieter Prelik. Scalability for Rocket Nozzle Flows Based on Subscale and Full-Scale Testing. *Journal of Propulsion and Power*, 19(3):321–331, May 2003. ISSN 0748-4658, 1533-3876. doi: 10.2514/2.6123. URL <https://arc.aiaa.org/doi/10.2514/2.6123>.
- [3] Krijn de Kievit. Side Loads in Overexpanded Rocket Nozzles - Literature Survey. Technical Report, Delft University of Technology, Delft, The Netherlands, October 2020.
- [4] George P. Sutton and Oscar Biblarz. *Rocket propulsion elements*. John Wiley & Sons, New York, 7th ed edition, 2001. ISBN 978-0-471-32642-7.
- [5] J.D. Anderson. *Fundamentals of Aerodynamics*. McGraw-Hill, New York, USA, 6th edition edition, 2017.
- [6] H. Babinsky and J. Harvey. *Shock wave-boundary-layer interactions*. Cambridge aerospace series. Cambridge University Press, Cambridge ; New York, 2011. ISBN 978-0-521-84852-7. OCLC: ocn701672464.
- [7] Christopher A Mouton. *Transition between Regular Reflection and Mach Reflection in the Dual-Solution Domain*. PhD thesis, California Institute of Technology, Pasadena, USA, 2007.
- [8] Woutjin J. Baars, Charles E. Tinney, Joseph H. Ruf, Andrew M. Brown, and David M. McDaniels. Wall Pressure Unsteadiness and Side Loads in Overexpanded Rocket Nozzles. *AIAA Journal*, 50(1):61–73, January 2012. ISSN 0001-1452, 1533-385X. doi: 10.2514/1.J051075. URL <https://arc.aiaa.org/doi/10.2514/1.J051075>.
- [9] M. Terhardt, G. Hagemann, and M. Frey. Flow separation and side-load behavior of truncated ideal rocket nozzles. In *37th Joint Propulsion Conference and Exhibit*, Salt Lake City, UT, U.S.A., July 2001. American Institute of Aeronautics and Astronautics. doi: 10.2514/6.2001-3686. URL <http://arc.aiaa.org/doi/10.2514/6.2001-3686>.
- [10] Ralf H. Stark. Flow Separation in Rocket Nozzles - An Overview. In *49th AIAA/ASME/SAE/ASEE Joint Propulsion Conference*, San Jose, CA, July 2013. American Institute of Aeronautics and Astronautics. ISBN 978-1-62410-222-6. doi: 10.2514/6.2013-3840. URL <http://arc.aiaa.org/doi/10.2514/6.2013-3840>.
- [11] Jan Ostlund. *Flow Processes in Rocket Engine Nozzles with Focus on Flow Separation and Side Loads*. Licentiate Thesis, Royal Institute of Technology, Stockholm, Sweden, 2002.
- [12] Manuel Frey and Gerald Hagemann. Restricted Shock Separation in Rocket Nozzles. *Journal of Propulsion and Power*, 16(3):478–484, May 2000. ISSN 0748-4658, 1533-3876. doi: 10.2514/2.5593. URL <https://arc.aiaa.org/doi/10.2514/2.5593>.
- [13] M. Frey and G. Hagemann. Flow separation and side-loads in rocket nozzles. In *35th Joint Propulsion Conference and Exhibit*, Los Angeles, CA, U.S.A., June 1999. American Institute of Aeronautics and Astronautics. doi: 10.2514/6.1999-2815. URL <http://arc.aiaa.org/doi/10.2514/6.1999-2815>.
- [14] Emanuele Martelli, Francesco Nasuti, and Marcello Onofri. Numerical calculation of FSS/RSS transition in highly overexpanded rocket nozzle flows. *Shock Waves*, 20(2):139–146, April 2010. ISSN 0938-1287, 1432-2153. doi: 10.1007/s00193-009-0244-4. URL <http://link.springer.com/10.1007/s00193-009-0244-4>.

- [15] M. Terhardt, G. Hagemann, and M. Frey. Flow separation and side-load behavior of the Vulcain engine. In *35th Joint Propulsion Conference and Exhibit*, Los Angeles, CA, U.S.A., June 1999. American Institute of Aeronautics and Astronautics. doi: 10.2514/6.1999-2762. URL <http://arc.aiaa.org/doi/10.2514/6.1999-2762>.
- [16] M. Frey. *Behandlung von Strömungsproblemen in Raketendüsen bei Überexpansion*. Ph.D. Thesis, Stuttgart University, Stuttgart, January 2001.
- [17] Marc Ramsey, Robert Pitz, Thomas Jenkins, Yu Matsutomi, Changjin Yoon, and William Anderson. Experimental Velocity Profiles in the Cap Shock Pattern of a Thrust Optimized Rocket Nozzle. In *49th AIAA Aerospace Sciences Meeting including the New Horizons Forum and Aerospace Exposition*, Orlando, Florida, January 2011. American Institute of Aeronautics and Astronautics. ISBN 978-1-60086-950-1. doi: 10.2514/6.2011-1167. URL <http://arc.aiaa.org/doi/10.2514/6.2011-1167>.
- [18] G. Hagemann, M. Frey, and W. Koschel. Appearance of Restricted Shock Separation in Rocket Nozzles. *Journal of Propulsion and Power*, 18(3):577–584, May 2002. ISSN 0748-4658, 1533-3876. doi: 10.2514/2.5971. URL <https://arc.aiaa.org/doi/10.2514/2.5971>.
- [19] Ten-See Wang, Xiang Zhao, Sijun Zhang, and Yen-Sen Chen. Development of an Aeroelastic Modeling Capability for Transient Nozzle Flow Analysis. *Journal of Propulsion and Power*, 30(6):1692–1700, November 2014. ISSN 0748-4658, 1533-3876. doi: 10.2514/1.B35277. URL <http://arc.aiaa.org/doi/10.2514/1.B35277>.
- [20] C. Génin, R. Stark, and S. Jack. Flow separation in out-of-round nozzles, a numerical and experimental study. In D. Knight, I. Lipatov, and P. Reijasse, editors, *Progress in Flight Physics – Volume 7*, pages 269–282, Munich, Germany, 2015. EDP Sciences. ISBN 978-5-94588-165-5. doi: 10.1051/eucass/201507269. URL <http://www.eucass-proceedings.eu/10.1051/eucass/201507269>.
- [21] J. Östlund and B. Muhammad-Klingmann. Supersonic Flow Separation with Application to Rocket Engine Nozzles. *Applied Mechanics Reviews*, 58(3):143–177, May 2005. ISSN 0003-6900, 2379-0407. doi: 10.1115/1.1894402. URL <https://asmedigitalcollection.asme.org/appliedmechanicsreviews/article/58/3/143/443735/Supersonic-Flow-Separation-with-Application-to>.
- [22] Joanna A. Zhang, Babak Shotorban, and Sijun Zhang. Numerical Experiment of Aeroelastic Stability for a Rocket Nozzle. *Journal of Aerospace Engineering*, 30(5):04017041, September 2017. ISSN 0893-1321, 1943-5525. doi: 10.1061/(ASCE)AS.1943-5525.0000746. URL <http://ascelibrary.org/doi/10.1061/%28ASCE%29AS.1943-5525.0000746>.
- [23] R.H. Schmucker. Flow Processes in Overexpanded Chemical Rocket Nozzles. Part 2: Side Loads due to Asymmetric Separation. Technical Report NASA TM-77395, NASA, Santa Barbara, USA, February 1984.
- [24] NASA. Acoustic Loads Generated By the Propulsion System. Technical Report SP-8072, NASA, Hampton, VA, USA, June 1971.
- [25] Charles E. Tinney, Kenneth Scott, Mandi Routon, Jayant Sirohi, and Joseph Ruf. Effect of Aeroelasticity on Vibroacoustic Loads during Startup of Large Area Ratio Nozzles. In *23rd AIAA/CEAS Aeroacoustics Conference*, Denver, Colorado, June 2017. American Institute of Aeronautics and Astronautics. ISBN 978-1-62410-504-3. doi: 10.2514/6.2017-3361. URL <https://arc.aiaa.org/doi/10.2514/6.2017-3361>.
- [26] H Kronmüller, K Schäfer, H Zimmermann, and R Stark. Cold Gas Subscale Test Facility P6.2 at DLR Lampoldshausen. In *6th international Symposium on Propulsion for Space Transportation in the 21st century*, page 8, Versaille, France, 2002. DLR.
- [27] R.D. Mehta and P. Bradshaw. Design rules for small low speed wind tunnels. *Aeronautical Journal*, pages 443–449, November 1979.

- [28] Peter Fasogbon, Luc Duvieubourg, and Ludovic Macaire. Scheimpflug Camera Calibration Using Lens Distortion Model. In Balasubramanian Raman, Sanjeev Kumar, Partha Pratim Roy, and Debashis Sen, editors, *Proceedings of International Conference on Computer Vision and Image Processing*, volume 459, pages 159–169, Singapore, 2017. Springer Singapore. ISBN 978-981-10-2103-9 978-981-10-2104-6. doi: 10.1007/978-981-10-2104-6_15. URL http://link.springer.com/10.1007/978-981-10-2104-6_15. Series Title: Advances in Intelligent Systems and Computing.
- [29] A. Criminisi, I. Reid, and A. Zisserman. A plane measuring device. *Image and Vision Computing*, 17(8):625–634, June 1999. ISSN 02628856. doi: 10.1016/S0262-8856(98)00183-8. URL <https://linkinghub.elsevier.com/retrieve/pii/S0262885698001838>.
- [30] F. Scarano. Experimental Aerodynamics. Course Reader, Delft University of Technology, Delft, The Netherlands, February 2013.
- [31] John Shi. Rocket Engine Nozzle Side Load Transient Analysis Methodology- a Practical Approach. In *46th AIAA/ASME/ASCE/AHS/ASC Structures, Structural Dynamics and Materials Conference*, Austin, Texas, April 2005. American Institute of Aeronautics and Astronautics. ISBN 978-1-62410-065-9. doi: 10.2514/6.2005-1860. URL <http://arc.aiaa.org/doi/10.2514/6.2005-1860>.
- [32] Yasuhide Watanabe, Norio Sakazume, and Masanori Tsuboi. LE-7A Engine Nozzle Problems during Transient Operations. In *38th AIAA/ASME/SAE/ASEE Joint Propulsion Conference & Exhibit*, Indianapolis, Indiana, July 2002. American Institute of Aeronautics and Astronautics. ISBN 978-1-62410-115-1. doi: 10.2514/6.2002-3841. URL <http://arc.aiaa.org/doi/abs/10.2514/6.2002-3841>.
- [33] Andrew Brown, Russell Keanini, Joseph Ruf, Darren Reed, and Mark D’Agostino. Characterization of Side Load Phenomena Using Measurement of Fluid/Structure Interaction. In *38th AIAA/ASME/SAE/ASEE Joint Propulsion Conference & Exhibit*, Indianapolis, Indiana, July 2002. American Institute of Aeronautics and Astronautics. ISBN 978-1-62410-115-1. doi: 10.2514/6.2002-3999. URL <http://arc.aiaa.org/doi/abs/10.2514/6.2002-3999>.
- [34] Joseph Ruf, David McDaniels, and Andrew Brown. Details of Side Load Test Data and Analysis for a Truncated Ideal Contour Nozzle and a Parabolic Contour Nozzle. In *46th AIAA/ASME/SAE/ASEE Joint Propulsion Conference & Exhibit*, Nashville, TN, July 2010. American Institute of Aeronautics and Astronautics. ISBN 978-1-60086-958-7. doi: 10.2514/6.2010-6813. URL <http://arc.aiaa.org/doi/abs/10.2514/6.2010-6813>.
- [35] Xiang Zhao, Sami Bayyuk, and Sijun Zhang. Aeroelastic response of rocket nozzles to asymmetric thrust loading. *Elsevier Computer and Fluids Journal*, 76:128–148, 2013.
- [36] E.M. Greitzer, C.S. Tan, and M.B. Graf. *Internal Flow: Concepts and Applications*. Cambridge Engine Technology Series. Cambridge University Press, 2007. ISBN 978-1-139-45111-6. URL <https://books.google.nl/books?id=z7z22pmYRjIC>.
- [37] B.T.C. Zandbergen. *Thermal Rocket Propulsion - Course Reader*. Delft University of Technology, Delft, The Netherlands, 2.05 edition, February 2016.
- [38] B Edney. Anomalous heat transfer and pressure distributions on blunt bodies at hypersonic speeds in the presence of an impinging shock. FFA Report 115, Aeronautical Research Institute of Sweden, Stockholm, Sweden, 1968.
- [39] G.V.R. Rao. Approximation of Optimum Thrust Nozzle Contour. *ARS Journal*, 30(6):561, 1960.
- [40] R.H. Schmucker. Flow Processes in Overexpanded Chemical Rocket Nozzles. Part 1: Flow Separation. Technical Report NASA-77396, NASA, Redwood City, USA, January 1984.
- [41] D. Dolling. Wall pressure fluctuations in a supersonic separated compression ramp flowfield. In *3rd Joint Thermophysics, Fluids, Plasma and Heat Transfer Conference*, St. Louis, MO, U.S.A., June 1982. American Institute of Aeronautics and Astronautics. doi: 10.2514/6.1982-986. URL <http://arc.aiaa.org/doi/10.2514/6.1982-986>.

- [42] David S. Dolling. Fifty Years of Shock-Wave/Boundary-Layer Interaction Research: What Next? *AIAA Journal*, 39(8):1517–1531, August 2001. ISSN 0001-1452, 1533-385X. doi: 10.2514/2.1476. URL <https://arc.aiaa.org/doi/10.2514/2.1476>.
- [43] A. L. Kistler. Fluctuating Wall Pressure under a Separated Supersonic Flow. *The Journal of the Acoustical Society of America*, 36(3):543–550, March 1964. ISSN 0001-4966. doi: 10.1121/1.1918998. URL <http://asa.scitation.org/doi/10.1121/1.1918998>.
- [44] D. S. Dolling and C. T. Or. Unsteadiness of the shock wave structure in attached and separated compression ramp flows. *Experiments in Fluids*, 3(1):24–32, 1985. ISSN 0723-4864, 1432-1114. doi: 10.1007/BF00285267. URL <http://link.springer.com/10.1007/BF00285267>.
- [45] Mehmet E. Erengil and David S. Dolling. Unsteady wave structure near separation in a Mach 5 compression ramp interaction. *AIAA Journal*, 29(5):728–735, May 1991. doi: 10.2514/3.10647.
- [46] S. J. Beresh, N. T. Clemens, and D. S. Dolling. Relationship Between Upstream Turbulent Boundary-Layer Velocity Fluctuations and Separation Shock Unsteadiness. *AIAA Journal*, 40(12):2412–2422, December 2002. ISSN 0001-1452, 1533-385X. doi: 10.2514/2.1609. URL <https://arc.aiaa.org/doi/10.2514/2.1609>.
- [47] B. Ganapathisubramani, N. T. Clemens, and D. S. Dolling. Effects of upstream boundary layer on the unsteadiness of shock-induced separation. *Journal of Fluid Mechanics*, 585:369–394, August 2007. ISSN 0022-1120, 1469-7645. doi: 10.1017/S0022112007006799. URL https://www.cambridge.org/core/product/identifier/S0022112007006799/type/journal_article.
- [48] B. Ganapathisubramani, N.T. Clemens, and D.S. Dolling. Low-frequency dynamics of shock-induced separation in a compression ramp interaction. *Journal of Fluid Mechanics*, 636:397–425, 2009.
- [49] Muzio Grilli, Peter J. Schmid, Stefan Hickel, and Nikolaus A. Adams. Analysis of unsteady behaviour in shockwave turbulent boundary layer interaction. *Journal of Fluid Mechanics*, 700:16–28, June 2012. ISSN 0022-1120, 1469-7645. doi: 10.1017/jfm.2012.37. URL https://www.cambridge.org/core/product/identifier/S0022112012000377/type/journal_article.
- [50] Noel T. Clemens and Venkateswaran Narayanaswamy. Low-Frequency Unsteadiness of Shock Wave/Turbulent Boundary Layer Interactions. *Annual Review of Fluid Mechanics*, 46(1):469–492, 2014. doi: 10.1146/annurev-fluid-010313-141346. URL <https://doi.org/10.1146/annurev-fluid-010313-141346>. _eprint: <https://doi.org/10.1146/annurev-fluid-010313-141346>.
- [51] D.S. Dolling. Fluctuating Loads in Shock Wave/Turbulent Boundary Layer Interaction: Tutorial and Update. In *31st Aerospace Sciences Meeting*, Reno,NV,U.S.A., January 1993. American Institute of Aeronautics and Astronautics. doi: 10.2514/6.1993-284. URL <http://arc.aiaa.org/doi/10.2514/6.1993-284>.
- [52] Jean-Paul Dussauge, Pierre Dupont, and Jean-François Debiève. Unsteadiness in shock wave boundary layer interactions with separation. *Aerospace Science and Technology*, 10(2):85–91, March 2006. ISSN 12709638. doi: 10.1016/j.ast.2005.09.006. URL <https://linkinghub.elsevier.com/retrieve/pii/S1270963805001495>.
- [53] M.E. Erengil and D.S. Dolling. Physical causes of separation shock unsteadiness in shock wave turbulent boundary layer interactions. In *AIAA 24th Fluid Dynamics Conference*, Orlando, FL, USA, January 1993. AIAA 93-3134.
- [54] O. Ünalms and D. Dolling. Decay of wall pressure field and structure of a Mach 5 adiabatic turbulent boundary layer. In *Fluid Dynamics Conference*, Colorado Springs,CO,U.S.A., June 1994. American Institute of Aeronautics and Astronautics. doi: 10.2514/6.1994-2363. URL <http://arc.aiaa.org/doi/10.2514/6.1994-2363>.

- [55] S. Piponniau, J. P. Dussauge, J. F. Debiève, and P. Dupont. A simple model for low-frequency unsteadiness in shock-induced separation. *Journal of Fluid Mechanics*, 629:87–108, June 2009. ISSN 0022-1120, 1469-7645. doi: 10.1017/S0022112009006417. URL https://www.cambridge.org/core/product/identifier/S0022112009006417/type/journal_article.
- [56] Stephan Priebe and M. Pino Martín. Low-frequency unsteadiness in shock wave–turbulent boundary layer interaction. *Journal of Fluid Mechanics*, 699:1–49, May 2012. ISSN 0022-1120, 1469-7645. doi: 10.1017/jfm.2011.560. URL https://www.cambridge.org/core/product/identifier/S002211201100560X/type/journal_article.
- [57] M. Summerfield, C. Foster, and W. Swan. Nozzle Flow Separation. *Jet Propulsion*, 24(9):319–321, 1954.
- [58] Guillaume Daviller, Jérôme Dombard, Gabriel Staffelbach, Julien Herpe, and Didier Saucereau. Prediction of Flow Separation and Side-loads in Rocket Nozzle Using Large-eddy Simulation. *International Journal of Computational Fluid Dynamics*, pages 1–11, July 2020. ISSN 1061-8562, 1029-0257. doi: 10.1080/10618562.2020.1786540. URL <https://www.tandfonline.com/doi/full/10.1080/10618562.2020.1786540>.
- [59] E. Martelli, L. Saccoccio, P. P. Ciottoli, C. E. Tinney, W. J. Baars, and M. Bernardini. Flow dynamics and wall-pressure signatures in a high-Reynolds-number overexpanded nozzle with free shock separation. *Journal of Fluid Mechanics*, 895:A29, July 2020. ISSN 0022-1120, 1469-7645. doi: 10.1017/jfm.2020.280. URL https://www.cambridge.org/core/product/identifier/S0022112020002803/type/journal_article.
- [60] Ten-See Wang. Transient three-dimensional startup side load analysis of a regeneratively cooled nozzle. *Shock Waves*, 19(3):251–264, July 2009. ISSN 0938-1287, 1432-2153. doi: 10.1007/s00193-009-0201-2. URL <http://link.springer.com/10.1007/s00193-009-0201-2>.
- [61] Allamaprabhu Yaravintelimath, Raghunandan B.N., and José A. Morfífigo. Numerical prediction of nozzle flow separation: Issue of turbulence modeling. *Aerospace Science and Technology*, 50:31–43, March 2016. ISSN 12709638. doi: 10.1016/j.ast.2015.12.016. URL <https://linkinghub.elsevier.com/retrieve/pii/S1270963815300183>.
- [62] V. Jaunet, S. Arbos, G. Lehnasch, and S. Girard. Wall Pressure and External Velocity Field Relation in Overexpanded Supersonic Jets. *AIAA Journal*, 55(12):4245–4257, December 2017. ISSN 0001-1452, 1533-385X. doi: 10.2514/1.J055874. URL <https://arc.aiaa.org/doi/10.2514/1.J055874>.
- [63] Ragnar Larusson, Niklas Andersson, and Jan Östlund. Hybrid RANS-LES Simulation of Separated Nozzle Flow. In *52nd AIAA/SAE/ASEE Joint Propulsion Conference*, Salt Lake City, UT, July 2016. American Institute of Aeronautics and Astronautics. ISBN 978-1-62410-406-0. doi: 10.2514/6.2016-4670. URL <http://arc.aiaa.org/doi/10.2514/6.2016-4670>.
- [64] Ph. Reijasse, L. Morzenski, D. Blacodon, and J. Birkemeyer. Flow separation experimental analysis in overexpanded subscale rocket-nozzles. In *37th Joint Propulsion Conference and Exhibit*, Salt Lake City, UT, U.S.A., July 2001. American Institute of Aeronautics and Astronautics. doi: 10.2514/6.2001-3556. URL <http://arc.aiaa.org/doi/10.2514/6.2001-3556>.
- [65] C.E. Campbell and J.M. Farley. Performance of Several Conical Convergent-Divergent Rocket-Type Exhaust Nozzles. Technical Report TND-467, NASA, Cleveland, USA, September 1960.
- [66] J. Mattsson, U. Högman, and L. Torngren. A Sub-Scale Test Programme on Investigation of Flow Separation and Side-Loads in Rocket Nozzles. In *Proceedings of the 3rd European Symposium on Aerothermodynamics of Space Vehicles*, The Netherlands, November 1998. ESA-ESTEC.
- [67] F Nasuti, M Onofri, and E Pietropaoli. The Influence of Nozzle Shape on the Shock structure in Separated Flows. In *Proceedings of the 5th European Symposium on Aerothermodynamics for Space Vehicles*, volume SP-563, pages 353–358. ESA, 2005.

- [68] T.W. Schilling. Flow Separation in Rocket Nozzle. Master's thesis, University of Buffalo, New York, USA, 1962.
- [69] S. Kalt and D. Badal. Conical Rocket Nozzle Performance Under Flow Separated Condition. *Journal of Spacecraft and Rockets*, 2(3):447–449, 1965.
- [70] P. Carrière, M. Sirieix, and J.-L. Solignac. Propriétés de similitude des phénomènes de décollement laminaires ou turbulents en écoulement supersonique non uniforme. In *Proceedings of the 12th International Congress of Applied Mechanics*, Stanford, USA, August 1968. Stanford University.
- [71] D.R. Chapman, D.M. Kuhen, and H.K. Larson. Investigation of separated flows in supersonic and subsonic streams with emphasis on the effect of transition. Technical Report 1356, NACA, 1957.
- [72] Ph. Reijasse and J Birkemeyer. Semi-Empirical Flow Separation Model for Subscale Nozzles. In *Proceedings of the 4th European Symposium on Aerothermodynamics for Space Applications*, pages 407–414, Capua, Italy, October 2001. ESA.
- [73] L. Nave and G. Coffey. Sea level side loads in high-area-ratio rocket engines. In *9th Propulsion Conference*, Las Vegas, NV, U.S.A., November 1973. American Institute of Aeronautics and Astronautics. doi: 10.2514/6.1973-1284. URL <http://arc.aiaa.org/doi/10.2514/6.1973-1284>.
- [74] M. Frey and G. Hagemann. Status of flow separation prediction in rocket nozzles. In *34th AIAA/ASME/SAE/ASEE Joint Propulsion Conference and Exhibit*, Cleveland, OH, U.S.A., July 1998. American Institute of Aeronautics and Astronautics. doi: 10.2514/6.1998-3619. URL <http://arc.aiaa.org/doi/10.2514/6.1998-3619>.
- [75] José Antonio Morfiño and José Juan Salvá. Numerical study of the start-up process in an optimized rocket nozzle. *Aerospace Science and Technology*, 12(6):485–489, September 2008. ISSN 12709638. doi: 10.1016/j.ast.2007.11.003. URL <https://linkinghub.elsevier.com/retrieve/pii/S127096380700140X>.
- [76] F. Nasuti and M. Onofri. Viscous and inviscid vortex generation during start-up of rocket nozzles. *AIAA Journal*, 36(5):809–815, 1998.
- [77] V. Zmijanović, B. Rasuo, and A. Chpoun. Flow Separation Modes and Side Phenomena in an Overexpanded Nozzle. *FME Transactions*, 40:111–118, 2012.
- [78] G. Hagemann, M. Terhardt, M. Frey, Ph. Reijasse, M. Onofri, F. Nasuti, and J. Östlund. Flow separation and side-loads in rocket nozzles. In *35th Joint Propulsion Conference and Exhibit*, Los Angeles, CA, U.S.A., June 1999. American Institute of Aeronautics and Astronautics. doi: 10.2514/6.1999-2815. URL <http://arc.aiaa.org/doi/10.2514/6.1999-2815>.
- [79] Wiehan Kwan and Ralf Stark. Flow Separation Phenomena in Subscale Rocket Nozzles. In *38th AIAA/ASME/SAE/ASEE Joint Propulsion Conference & Exhibit*, Indianapolis, Indiana, July 2002. American Institute of Aeronautics and Astronautics. ISBN 978-1-62410-115-1. doi: 10.2514/6.2002-4229. URL <http://arc.aiaa.org/doi/abs/10.2514/6.2002-4229>.
- [80] Anh Thi Nguyen, H. Deniau, S. Girard, and T. Alziary de Roquefort. Unsteadiness of Flow Separation and End-Effects Regime in a Thrust-Optimized Contour Rocket Nozzle. *Flow, Turbulence and Combustion (formerly Applied Scientific Research)*, 71(1-4):161–181, 2003. ISSN 1386-6184. doi: 10.1023/B:APPL.0000014927.61427.ad. URL <http://link.springer.com/10.1023/B:APPL.0000014927.61427.ad>.
- [81] Ralf Stark, Wiehan Kwan, Fabien Quessard, Gerald Hagemann, and Michael Terhardt. Rocket Nozzle Cold-Gas Test Campaigns for Plume Investigations. In *Proceedings of the 4th European Symposium on Aerothermodynamics for Space Applications*, Capua, Italy, October 2001. ESA.

- [82] Changjin Yoon, Yu Matsutomi, William Anderson, and Charles Merkle. Investigation of the Cap-Shock Pattern in a Thrust-Optimized Rocket Nozzle. In *47th AIAA/ASME/SAE/ASEE Joint Propulsion Conference & Exhibit*, San Diego, California, July 2011. American Institute of Aeronautics and Astronautics. ISBN 978-1-60086-949-5. doi: 10.2514/6.2011-5685. URL <http://arc.aiaa.org/doi/abs/10.2514/6.2011-5685>.
- [83] S. B. Verma and Oskar Haidn. Unsteady Side-Load Evolution in a Liquid Rocket Engine Nozzle. *Journal of Spacecraft and Rockets*, 57(2):391–397, March 2020. ISSN 1533-6794. doi: 10.2514/1.A34556. URL <https://arc.aiaa.org/doi/10.2514/1.A34556>.
- [84] Takeo Tomita, Hiroshi Sakamoto, Takuo Onodera, Masaki Sasaki, Mamoru Takahashi, Yasuhide Watanabe, and Hiroshi Tamura. Experimental Evaluation of Side-Load Characteristics on TP, CTP and TO Nozzles. In *40th AIAA/ASME/SAE/ASEE Joint Propulsion Conference and Exhibit*, Fort Lauderdale, Florida, July 2004. American Institute of Aeronautics and Astronautics. ISBN 978-1-62410-037-6. doi: 10.2514/6.2004-3678. URL <http://arc.aiaa.org/doi/10.2514/6.2004-3678>.
- [85] Takeo Tomita, Mamoru Takahashi, Masaki Sasaki, Hiroshi Sakamoto, Masahiro Takahashi, and Hiroshi Tamura. Experimental evaluation of side-loads in LE-7A prototype engine nozzle. *Shock Waves*, 19(3):213–228, July 2009. ISSN 0938-1287, 1432-2153. doi: 10.1007/s00193-009-0191-0. URL <http://link.springer.com/10.1007/s00193-009-0191-0>.
- [86] Jan Ostlund and Mikael Bigert. A sub scale investigation on side loads in sea level rocket nozzles. In *35th Joint Propulsion Conference and Exhibit*, Los Angeles, CA, U.S.A., June 1999. American Institute of Aeronautics and Astronautics. doi: 10.2514/6.1999-2759. URL <http://arc.aiaa.org/doi/10.2514/6.1999-2759>.
- [87] M. Onofri and F. Nasuti. The physical origins of side loads in rocket nozzles. In *35th Joint Propulsion Conference and Exhibit*, Los Angeles, CA, U.S.A., June 1999. American Institute of Aeronautics and Astronautics. doi: 10.2514/6.1999-2587. URL <http://arc.aiaa.org/doi/10.2514/6.1999-2587>.
- [88] B. Gribben, F. Cantariti, K. Badlock, and B. Richards. Numerical Study of an Underexpanded Jet. In *Proceedings of the 3rd European Symposium on Aerothermodynamics of Space Vehicles*, pages 111–118, ESA-ESTEC, December 1998. ESA.
- [89] F. Welsh. Electron Beam Fluorescence Measurements of Shock Reflection Hysteresis in an Underexpanded Supersonic Jet. In *Proceedings of the 21st International Symposium on Shock Waves*, pages 863–868, Canberra, Australia, July 1997. Panther Publishing.
- [90] Shashi Bhushan Verma, Ralf Stark, and Oskar Haidn. Relation between shock unsteadiness and the origin of side-loads inside a thrust optimized parabolic rocket nozzle. *Aerospace Science and Technology*, 10(6):474–483, September 2006. ISSN 12709638. doi: 10.1016/j.ast.2006.06.004. URL <https://linkinghub.elsevier.com/retrieve/pii/S1270963806000782>.
- [91] A.K. Chopra. *Dynamics of Structures - Theory and Applications to Earthquake Engineering*. Prentice Hall, Berkeley, CA, USA, 1st edition, 1995.
- [92] Genin C. and S. Jack. Flow separation study in stiff ovalized rocket nozzles, Part I: Experimental approach. In *51st AIAA/SAE/ASEE Joint Propulsion Conference*, Orlando, FL, July 2015. American Institute of Aeronautics and Astronautics. ISBN 978-1-62410-321-6. doi: 10.2514/6.2015-4153. URL <http://arc.aiaa.org/doi/10.2514/6.2015-4153>.
- [93] C. Génin, S. Jack, and R. Stark. Flow Visualization in Out-of-Round Rocket Nozzles. In *30th International Symposium on Shock Waves I*, pages 83–87. Springer International Publishing, Cham, 2017. ISBN 978-3-319-46211-0 978-3-319-46213-4. doi: 10.1007/978-3-319-46213-4_13. URL http://link.springer.com/10.1007/978-3-319-46213-4_13.

- [94] Earl H. Dowell. *A Modern Course in Aeroelasticity*, volume 217 of *Solid Mechanics and Its Applications*. Springer International Publishing, Cham, 2015. ISBN 978-3-319-09452-6 978-3-319-09453-3. doi: 10.1007/978-3-319-09453-3. URL <http://link.springer.com/10.1007/978-3-319-09453-3>.
- [95] Jan Östlund, Tomas Damgaard, and Manuel Frey. Side-Load Phenomena in Highly Overexpanded Rocket Nozzles. *Journal of Propulsion and Power*, 20(4):695–704, July 2004. ISSN 0748-4658, 1533-3876. doi: 10.2514/1.3059. URL <https://arc.aiaa.org/doi/10.2514/1.3059>.
- [96] L.-O. Pekkari. Aeroelastic stability of supersonic nozzles with separated flow. In *29th Joint Propulsion Conference and Exhibit*, Monterey, CA, U.S.A., June 1993. American Institute of Aeronautics and Astronautics. doi: 10.2514/6.1993-2588. URL <http://arc.aiaa.org/doi/10.2514/6.1993-2588>.
- [97] L. Pekkari. Aeroelastic Analysis of Side Load in Supersonic Nozzles with Separated Flow. In *30th Joint Propulsion Conference and Exhibit*, Indianapolis, IN, U.S.A., June 1994. American Institute of Aeronautics and Astronautics. doi: 10.2514/6.1994-3377. URL <http://arc.aiaa.org/doi/10.2514/6.1994-3377>.
- [98] E. Lefrançois. Numerical validation of a stability model for a flexible over-expanded rocket nozzle. *International Journal for Numerical Methods in Fluids*, 49(4):349–369, October 2005. ISSN 0271-2091, 1097-0363. doi: 10.1002/flid.1000. URL <http://doi.wiley.com/10.1002/flid.1000>.
- [99] E Lefrancois. A numerical investigation of side loads resulting from rigid body motions of an overexpanded engine nozzle. *International Journal for Numerical Methods in Fluids*, 66:671–689, 2010.
- [100] Eric Blades, Edward Luke, and Joseph Ruf. Fully Coupled Fluid-Structure Interaction Simulations of Rocket Engine Side Loads. In *48th AIAA/ASME/SAE/ASEE Joint Propulsion Conference & Exhibit*, Atlanta, Georgia, July 2012. American Institute of Aeronautics and Astronautics. ISBN 978-1-60086-935-8. doi: 10.2514/6.2012-3969. URL <http://arc.aiaa.org/doi/abs/10.2514/6.2012-3969>.
- [101] Sijun Zhang, Babak Shotorban, Jeremy Pohly, and Joanna A. Zhang. Aeroelastic Response of Rocket Nozzles Subected to Combined Thrust and Side Loads. In *22nd AIAA Computational Fluid Dynamics Conference*, Dallas, TX, June 2015. American Institute of Aeronautics and Astronautics. ISBN 978-1-62410-366-7. doi: 10.2514/6.2015-3414. URL <http://arc.aiaa.org/doi/10.2514/6.2015-3414>.
- [102] N. Bekka, M. Sellam, and A. Chpoun. Aeroelastic stability analysis of flexible overexpanded rocket nozzle. *Shock Waves*, 26(4):513–527, July 2016. ISSN 0938-1287, 1432-2153. doi: 10.1007/s00193-015-0575-2. URL <http://link.springer.com/10.1007/s00193-015-0575-2>.
- [103] N. Bekka, M. Sellam, and A. Chpoun. New Modified Pekkari Model to Analyse the Aeroelastic Stability Behaviour for a Flexible Overexpanded Rocket Nozzle. In *30th International Symposium on Shock Waves 1*, pages 67–70. Springer International Publishing, Cham, 2017. ISBN 978-3-319-46211-0 978-3-319-46213-4. doi: 10.1007/978-3-319-46213-4_10. URL http://link.springer.com/10.1007/978-3-319-46213-4_10.
- [104] Luciano Garelli, Rodrigo R. Paz, and Mario A. Storti. Fluid–structure interaction study of the start-up of a rocket engine nozzle. *Computers & Fluids*, 39(7):1208–1218, August 2010. ISSN 00457930. doi: 10.1016/j.compfluid.2010.03.005. URL <https://linkinghub.elsevier.com/retrieve/pii/S0045793010000563>.
- [105] Sijun Zhang and T. Fuchiwaki. Aeroelastic Coupling and Side Loads in Rocket Nozzles. In *38th Fluid Dynamics Conference and Exhibit*, Seattle, Washington, June 2008. American Institute of Aeronautics and Astronautics. ISBN 978-1-60086-989-1. doi: 10.2514/6.2008-4064. URL <http://arc.aiaa.org/doi/10.2514/6.2008-4064>.

- [106] W J Tuovila and Norman S Land. Experimental study of aeroelastic instability of overexpanded rocket nozzle extensions. NASA Technical Note TN D-4471, NASA, Washington DC, USA, 1968.
- [107] Anh Nguyen, H. Deniau, S. Girard, and T. Alziary de Roquefort. Wall Pressure Fluctuations in an Over-Expanded Rocket Nozzle. In *38th AIAA/ASME/SAE/ASEE Joint Propulsion Conference & Exhibit*, Indianapolis, Indiana, July 2002. American Institute of Aeronautics and Astronautics. ISBN 978-1-62410-115-1. doi: 10.2514/6.2002-4001. URL <http://arc.aiaa.org/doi/abs/10.2514/6.2002-4001>.
- [108] Raymundo Rojo, Charles E. Tinney, and Joseph H. Ruf. Effect of Stagger on the Vibroacoustic Loads from Clustered Rockets. *AIAA Journal*, 54(11):3588–3597, November 2016. ISSN 0001-1452, 1533-385X. doi: 10.2514/1.J055017. URL <http://arc.aiaa.org/doi/10.2514/1.J055017>.
- [109] Takeo Tomita, Mamoru Takahashi, Masahiro Takahashi, Shuichi Ueda, Hiroshi Tamura, and Kenji Aoki. Visualization of the formation of separation bubbles on a bell-shaped nozzle surface in relation to serious side-load. In *37th Joint Propulsion Conference and Exhibit*, Salt Lake City, UT, U.S.A., July 2001. American Institute of Aeronautics and Astronautics. doi: 10.2514/6.2001-3559. URL <http://arc.aiaa.org/doi/10.2514/6.2001-3559>.
- [110] Michael M. James, Alexandria R. Salton, Kent L. Gee, Tracianne B. Neilsen, and Sally A. McInerney. Full-scale rocket motor acoustic tests and comparisons with empirical source models. In *Proceedings of Meeting on Acoustics*, pages 1–13, Kansas City, MO, USA, 2014. doi: 10.1121/1.4870984. URL <http://asa.scitation.org/doi/abs/10.1121/1.4870984>.
- [111] M A Eitner, J Sirohi, and C E Tinney. Modal parameter estimation of a reduced-scale rocket nozzle using blind source separation. *Measurement Science and Technology*, 30(9):095401, September 2019. ISSN 0957-0233, 1361-6501. doi: 10.1088/1361-6501/ab228f. URL <https://iopscience.iop.org/article/10.1088/1361-6501/ab228f>.
- [112] Stratasys. AFP3400. Data Sheet, Stratasys, Rehovot, Israel, 2015.
- [113] Stratasys. E1095AB. Technical Report Data Sheet, Stratasys, Rehovot, Israel, May 2017.
- [114] Stratasys. E1090AB. Data Sheet, Stratasys, Rehovot, Israel, May 2017.
- [115] Elia Efraim. Accurate formula for determination of natural frequencies of FGM plates basing on frequencies of isotropic plates. *Procedia Engineering*, 10:242–247, 2011.
- [116] A. Pope and K.L. Goins. *High-speed Wind Tunnel Testing*. Robert E. Krieger Pub., 1978. URL <https://books.google.nl/books?id=eUxyswEACAAJ>.
- [117] T.-L. Ho and G. Emanuel. Design of a Nozzle Contraction for Uniform Sonic Throat Flow. *AIAA Journal*, 38(4):720–723, April 2000. ISSN 0001-1452, 1533-385X. doi: 10.2514/2.1019. URL <https://arc.aiaa.org/doi/10.2514/2.1019>.
- [118] B.W. Van Oudheusden. Viscous Flows Lecture Slides, 2019.
- [119] Gerald Hagemann and Manuel Frey. Shock pattern in the plume of rocket nozzles: needs for design consideration. *Shock Waves*, 17(6):387–395, May 2008. ISSN 0938-1287, 1432-2153. doi: 10.1007/s00193-008-0129-y. URL <http://link.springer.com/10.1007/s00193-008-0129-y>.
- [120] W. J. Baars and C. E. Tinney. Transient wall pressures in an overexpanded and large area ratio nozzle. *Experiments in Fluids*, 54(2):1468, February 2013. ISSN 0723-4864, 1432-1114. doi: 10.1007/s00348-013-1468-8. URL <http://link.springer.com/10.1007/s00348-013-1468-8>.
- [121] Jitang Fan and Ang Chen. Studying a Flexible Polyurethane Elastomer with Improved Impact-Resistant Performance. *Polymers*, 11(3):467, March 2019. ISSN 2073-4360. doi: 10.3390/polym11030467. URL <https://www.mdpi.com/2073-4360/11/3/467>.